

# **The Three-Dimensional Structure of Magnetic Reconnection in SSX**

---

**Matt Landreman**

mlandre1@swarthmore.edu  
Swarthmore College Department of Physics and Astronomy  
500 College Avenue, Swarthmore, PA 19081

Senior Honors Thesis  
March 22, 2003

## Abstract

In plasma physics it is a commonly cited and often valid approximation that magnetic fieldlines are “frozen” to the plasma fluid. However, in certain situations in solar and astrophysics, as well as in fusion engineering, this approximation of “ideal magnetohydrodynamics” leaves out important physical processes. Large gradients in the field can arise, causing effects that were previously negligible to become significant, and allowing the fieldlines to slip through the plasma. Mysteriously, this “magnetic reconnection” effect appears to be much more significant than a back-of-the-envelope calculation would suggest. Reconnection is investigated in the Swarthmore Spheromak Experiment (SSX), a laboratory plasma device. The reconnecting field configuration in SSX is both largely reproducible and also more three-dimensionally complicated than in previous experiments elsewhere. The principle diagnostic discussed herein utilizes an array of small pick-up loops to measure the magnetic field. Use is made of a novel inexpensive high-speed multiplexing data acquisition system, which for the first time permits observations of a plasma’s complicated dynamics in all three dimensions and their variation from shot to shot. Custom visualization software has been developed to explore the complicated four-dimensional datasets. The magnetic probe exhibits an uncertainty of 2%, and it correctly reproduces the theoretical expected fields for simple known current geometries. The probe provides evidence that both a driven and a slower steady-state variety of reconnection do in fact occur in SSX, and several unique three-dimensional properties distinguish the plasma configuration from previous “two-dimensional” experiments. An unfortunate inherent curvature in the geometry prevents conclusive testing of a magnetic quadrupole phenomenon reported in recent computational studies of collisionless reconnection. Various higher-order terms in the generalized plasma Ohm’s law can be computed, suggesting that the  $\mathbf{J} \times \mathbf{B}$  Hall force and the pressure gradient force may be the key phenomena in SSX among those neglected in ideal magnetohydrodynamics. Reconnection is correlated with the detection of high-energy ions emanating from the site of spheromak collision. Recent modifications to the SSX device to permit “full-merging” of the plasma have produced images of a more tempestuous and less controlled reconnection geometry, although the physical processes involved seem to be the same as those in the original configuration.

# Contents

<b>1</b>	<b>Introduction</b>	<b>1</b>
<b>2</b>	<b>The Theory of Magnetic Reconnection</b>	<b>4</b>
2.1	Plasma Physics . . . . .	4
2.1.1	A Few Basic Ideas for Our Toolbox . . . . .	4
2.1.2	Magnetohydrodynamics . . . . .	7
2.1.3	MHD Equilibrium and the Spheromak . . . . .	9
2.1.4	The Frozen-In Flux Conditions . . . . .	11
2.2	Evidence from Nature that Reconnection is Significant . . . . .	14
2.2.1	Coronal Heating and Solar Flares . . . . .	14
2.2.2	Cosmic Ray Acceleration . . . . .	15
2.2.3	Instabilities in Tokamaks . . . . .	16
2.3	Magnetic Reconnection - The Theoretical Basis . . . . .	16
2.3.1	Beyond the Ideal Ohm's Law . . . . .	16
2.3.2	2D Reconnection in Resistive MHD . . . . .	18
2.3.3	Could Shocks Be Involved in Reconnection? . . . . .	23
2.3.4	Turbulence and Particle Acceleration . . . . .	23
2.3.5	Collisionless Reconnection . . . . .	24
2.3.6	Three-Dimensional Reconnection . . . . .	27
2.3.7	What Remains to Be Done? . . . . .	29
2.4	Previous Experiments . . . . .	30
2.4.1	UCLA Experiments . . . . .	30
2.4.2	Tokyo Experiments . . . . .	32
2.4.3	Princeton Experiments . . . . .	35
<b>3</b>	<b>The Swarthmore Spheromak Experiment</b>	<b>37</b>
3.1	SSX Operation . . . . .	37
3.2	3D Magnetic Measurements . . . . .	38
3.2.1	Magnetic Probe Theory and Design . . . . .	42
3.2.2	Calibration and Analysis . . . . .	45
3.2.3	Previous Magnetic Measurements in SSX . . . . .	49
3.2.4	Data Visualization . . . . .	50
3.2.5	Data Analysis Methods . . . . .	50
3.3	Particle Measurements . . . . .	52

<b>4 Results and Discussion</b>	<b>54</b>
4.1 3D Magnetic Field Probe Functionality . . . . .	54
4.2 Plasma Measurements . . . . .	55
4.2.1 Overview of a Typical Shot . . . . .	57
4.2.2 Magnetic Evidence for Reconnection . . . . .	59
4.2.3 Decay-Epoch Reconnection . . . . .	65
4.2.4 The Significance of Each Term in Ohm's Law . . . . .	69
4.2.5 Particle Acceleration . . . . .	73
4.2.6 Full Merging of Spheromaks . . . . .	74
<b>5 Future Directions and Concluding Remarks</b>	<b>84</b>
<b>A Why the Displacement Current can be Neglected</b>	<b>86</b>
<b>B Derivation of Ohm's Law for Plasmas</b>	<b>88</b>
<b>C Multiplexer timing circuitry</b>	<b>97</b>
<b>D Demonstration of 3D probe on simple vacuum fields</b>	<b>100</b>
<b>E Visualization Software</b>	<b>104</b>
<b>F Additional Details of Shot Evolution</b>	<b>113</b>
F.1 Single-Bank Shots . . . . .	113
F.2 Full Merging of Spheromaks . . . . .	116
<b>G Acknowledgements</b>	<b>118</b>
<b>H Notation</b>	<b>119</b>
<b>Bibliography</b>	<b>120</b>

# Chapter 1

## Introduction

One of the outstanding problems in plasma physics today is to understand the process of *magnetic reconnection*. Reconnection is one of Nature’s reminders that the models created by physicists are often so simple (“assume a frictionless surface and no gravity, etc.”) that they leave out significant processes.

In plasmas – gases so hot that the electrons and protons become dissociated – physicists have tried to build a tractable dynamical theory known as “ideal magnetohydrodynamics” by making a certain canonical set of simplifying assumptions. One of the consequences of these assumptions is that magnetic fieldlines and the plasma fluid should be fixed to each other; where one moves, the other follows. We can imagine fieldlines as threads embedded in the plasma, dragged and stretched by the fluid as it flows. In many cases this simplified theory works very well, but in certain situations it fares surprisingly poorly. The observed *rate* of reconnection appears to be much faster in many situations than the most naive calculation would suggest. For example, the typical lifetime of a solar flare is 15 minutes to 1 hour, and solar physicists were surprised when their first theoretical prediction for this number (the “resistive decay time”) came out to be  $3.2 \times 10^6$  years!. Somewhere in the sequence of simplifying assumptions that leads to the frozen-in flux prediction, an important term was mistakenly thrown out. But which one? Scientists dispute which terms in the equations are the most important to keep, and it is hard to keep *any* without producing a theory so complicated that analytical methods become impossible.

Figure 1.1 depicts a typical reconnection configuration. Two plasmas with oppositely directed magnetic fields (**B**) converge, here from above and below. This could be caused by two coalescing loops on the solar surface, as shown here, or by many other systems with dynamic magnetic fields. If the field is perfectly frozen to the fluid, the two converging plasmas should be able to sit next to each other. However, when reconnection becomes significant, the field between the plasmas grows weak in a region with some non-zero width. There is some residual component to the field (vertical in this figure) from the large-scale curvature of the incoming fields, so the fieldlines near the sides now pass *between* the two plasmas. This is a topological change, since before reconnection each fieldline was associated with only one of the two masses of plasma. The fieldlines have “reconnected” so that they attach to different regions. A pair of fieldlines called the *separatrix* partitions the region into four parts based on the topology of the fieldlines (from top to top plasma, from top to bottom plasma, etc.) At the *X-point* or *null point* where the separatrices cross, the field is exactly zero. If we extrude the picture into the third dimension, the separatrices become surfaces, and the X-point becomes an X-line.

Reconnection can be thought of as a process of energy conversion. As the plasmas converge from above and below in our figure, fluid is squeezed out the sides from the reconnection region. This fluid has a weaker magnetic field than the incoming plasma, so  $B^2/2\mu_0$  energy has disappeared. The energy must show up somewhere: heat, high kinetic energy of the out-flowing plasma, super-thermal particles, or EM radiation. One of the problems in reconnection theory is to predict the partitioning of the incoming energy into these forms.

Reconnection is important to understand, as it seems to be a common process. It is known or suspected to participate in many astrophysical phenomena, including the dynamics of the solar corona and the Earth’s magnetosphere, and

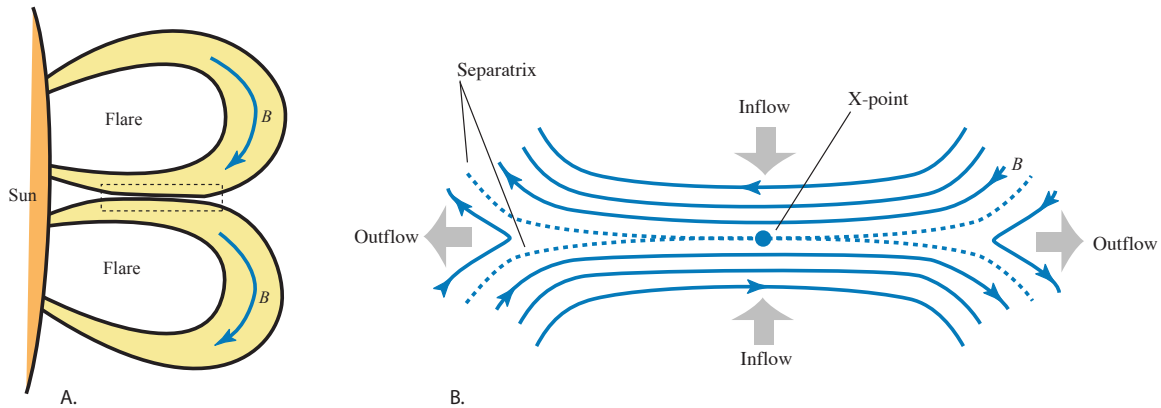


**Figure 1.1:** A typical reconnection configuration. We can imagine this configuration arising when two loops of plasma on the solar surface move towards each other (A). The  $B$  fields point in opposite directions, giving approximately the 2D arrangement shown in B around the region of contact.

acceleration of cosmic rays. It is also thought to underlie one of the instabilities in tokamak fusion reactors that has complicated their development. There is much incentive, then, to discover how our ideal theory fails when reconnection takes place.

One problem that confronts those studying this phenomenon is that it is hard to put probes into the typical and important places where reconnection seems to occur. We cannot send probes inside the sun's corona, to intergalactic regions, or into the center of a  $100,000,000$  °C fusion plasma. Satellites in the Earth's magnetosphere cannot survey the entire three-dimensional volume in which reconnection occurs. Laboratory experiments *have* been able to produce reconnection in very smooth and reproducible two-dimensional plasmas. But these measurements do not show the process in the geometrically complicated, three-dimensional flows that appear in natural phenomena.

The Swarthmore Spheromak Experiment (SSX) is an attempt to overcome these problems. It is a “laboratory astrophysics” experiment – a scaled-down model of real disordered astrophysical reconnection. With the novel magnetic field diagnostic discussed in this thesis, we are able to see the geometrical complexity of the plasma under investigation.

## Note To the Selective Reader

This thesis can be divided into two parts, each of which serves a different mission. The first of these missions is to tell the story of magnetic reconnection: what is it exactly, why is it an interesting problem, and how does it relate to other problems in plasma physics? These questions are addressed in Chapter 2, with some more mathematical details in Appendices A and B. A basic introduction to reconnection can be found by a bit of selective reading: It is first good to see the precise statement of the frozen-in flux conditions by reading the two Theorems of Section 2.1.4 without worrying about the details of the proofs. Section 2.2 relates some cases in which reconnection appears in nature. Sections 2.3.1 and 2.3.2 describe the quantitative statement of the reconnection “problem,” present the canonical Sweet-Parker approach, and explain why this model is incomplete. A reader with more time might want to get more background in plasma physics (Section 2.1), read about other theoretical approaches to the reconnection problem (Section 2.3), or see results from other laboratories concerning reconnection (Section 2.4).

The second basic mission of this thesis is to serve as a record of the 3D magnetic probe device and of the results of analysis on the data it obtained. This information is recorded in Chapters 3 through 5, with some technical details and further images in Appendices C through F. The key findings from analysis of 3D probe data are summarized in Section 4.2.

## A Few Conventions

It will be useful throughout this discussion to distinguish between the velocities of particular particles and the velocity field of a fluid. We will use the convention that  $\mathbf{v}$  refers to the former and  $\mathbf{u}$  refers to the latter. In other words,  $\mathbf{u}(\mathbf{x}) = (\text{mean of } \mathbf{v} \text{ for particles near } \mathbf{x})$ .

In this thesis we will also distinguish between “2D” and “3D” vector fields. By these categories we do *not* mean the number of *components* of the vectors, but rather *in how many dimensions the vectors vary*. For example, the vector field  $\mathbf{F}(x, y, z) = (xy, x^2 - y, y/\exp(x))$  would be considered 2D, for even though it defines a three-dimensional vector on a three-dimensional space, it has no  $z$ -dependence, and therefore varies in only two directions.

# Chapter 2

# The Theory of Magnetic Reconnection

## 2.1 Plasma Physics

It takes some patience and preparation in order to understand reconnection because it is the *unexpected failure* of a prediction that is itself non-trivial to understand, the prediction of frozen-in flux. In this first chapter, we tackle this initial step of explaining why we *expect* flux freezing (i.e., no reconnection). We will begin with a crash course in some important concepts from plasma physics, and then quickly present the theory of ideal plasma dynamics. We take a moment to discuss a valuable result of this theory: its ability to describe spheromaks, the parcels of plasma made to converge in SSX. Finally, we provide a formal derivation of the frozen-in-flux condition.

### 2.1.1 A Few Basic Ideas for Our Toolbox

Prepare yourself for a bit of hopping about from topic to topic in this first section as we embark on a crash course in plasma physics. It will be worth the effort, however, for the following concepts of Larmor gyration, beta, the convective derivative, and the Alfvén speed will all figure prominently in the analysis ahead.

#### Larmor Orbits

For the discussion of this thesis, a *plasma* is a fully ionized fluid of charged particles. We will principally be concerned with plasmas for which there is rough net neutrality, and which are typically embedded with a significant magnetic field. As a consequence of this field, the Lorentz force law implies that the particles will tend to be trapped in helical orbits about the fieldlines. This fact introduces anisotropy, and plasmas can thus have different temperatures or pressures in the direction parallel to  $\mathbf{B}$  compared with the perpendicular direction. A particle can jump from an orbit of one fieldline to another if it collides with another particle. In this *single-particle picture*, we can see already that *plasma particles tend not to move across fieldlines unless there are collisions*. When we develop a model that treats a plasma as a fluid instead of as individual particles, this fact will appear again.

The radius of a particle's orbit around a fieldline is known as the Larmor radius or gyroradius, and can be found by equating the centripetal force with the Lorentz force:

$$\frac{mv^2}{r} = qvB \quad \Rightarrow \quad r_{\text{Larmor}} \equiv r = \frac{mv}{qB} \quad (2.1)$$

## Beta

A dimensionless number often used to describe a configuration of plasma is the  $\beta$  parameter.  $\beta$  conveys something about the “confinement efficiency” of a configuration. It is useful because in laboratory experiments it happens to be fairly constant for a particular geometry of machine ( $\beta_{\text{tokamak}} \sim 0.05$ ,  $\beta_{\text{stellarator}} \sim 0.01$ ,  $\beta_{\text{spheromak}} \sim 0.1$ ) across different device sizes and plasma parameters. Consider that magnetic energy density  $B^2/2\mu_0$  has the dimensions of pressure.  $\beta$  is the ratio of these two kinds of forces acting on the plasma - thermal and magnetic pressure:

$$\beta \equiv \frac{p}{B^2/2\mu_0} = \frac{2\mu_0 p}{B^2} \quad (2.2)$$

If one’s goal is to confine a plasma of some given pressure, different machine geometries will require different levels of magnetic field. Inefficient geometries will require a large  $B$ , and thus have a low  $\beta$ . Tokamaks and most other laboratory plasma devices have  $\beta$  values of a few percent at most. Configurations with higher  $\beta$  tend to expend less energy creating imposed magnetic fields, so they are attractive for fusion research. Space plasmas often have  $\beta$  values approaching 1, or even higher.

## The Convective Derivative

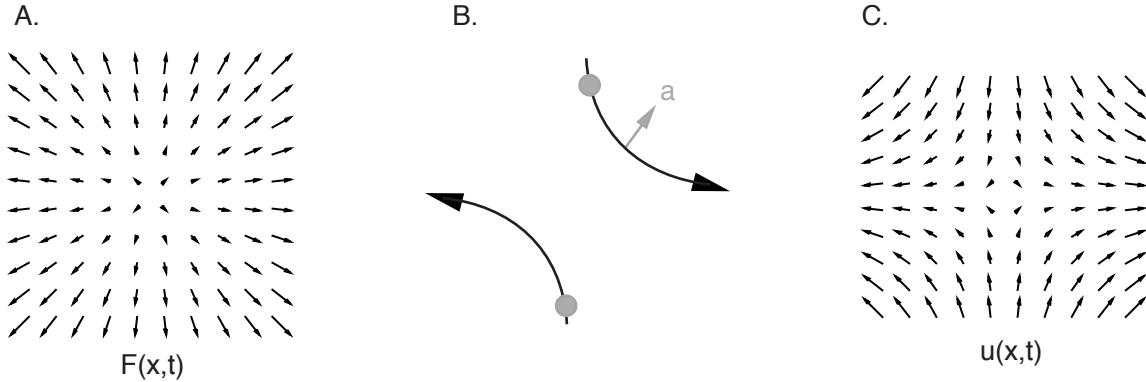


**Figure 2.1:** A position-dependent force  $\mathbf{F}(\mathbf{x})$  (A) causes fluid elements to accelerate (B) during their trajectories. However, the velocity field of this fluid  $\mathbf{u}(\mathbf{x})$  is constant in time (C), so  $\partial \mathbf{u} / \partial t \neq \mathbf{a}$ . Here,  $\mathbf{F} = (x, y)$  and  $\mathbf{u} = (x, -y)$ .

One particularly subtle concept in plasma physics – or really in fluid mechanics in general – is the “convective derivative.” Let us motivate it with a quick thought experiment. Suppose we have a position-dependent force  $\mathbf{f}(\mathbf{x})$  that acts on a fluid. Then for each fluid element<sup>1</sup> (a differentially small packet of fluid)  $\alpha$  (with velocity  $\mathbf{u}_\alpha$  and location  $\mathbf{x}_\alpha$ ) we can write Newton’s second law:

$$m \frac{d\mathbf{u}_\alpha}{dt} = \mathbf{f}(\mathbf{x}_\alpha(t)). \quad (2.3)$$

Now, let us look at the “big picture” and consider the velocity field of the whole fluid  $\mathbf{u}(\mathbf{x})$  instead of the velocity of each *individual fluid element*. Can we simply promote all of the parameters for element  $\alpha$  above to overall fluid parameters and say that

$$\rho \frac{\partial \mathbf{u}}{\partial t} = \mathbf{F}(\mathbf{x}) \quad (2.4)$$

---

<sup>1</sup>For this discussion, you can pretend that we have a perfectly continuous (i.e., infinitely divisible) fluid. The fact that a real fluid has internal thermal particle motion can be accounted for by simply including the pressure gradient force  $-\nabla p$  as part of  $\mathbf{F}$ . Appendix B goes through a more thorough derivation of the convective derivative, showing how this term arises.

where  $\rho$  is the mass density and  $\mathbf{F}$  is the force density? The answer – counterintuitively – is *no!* As an example, consider  $\mathbf{F}$  and  $\mathbf{u}$  as given in Figure 2.1. The left-hand side of the *fluid element's* equation (2.3) is clearly nonzero, for the elements follow curved trajectories and thus must accelerate. However, the left-hand side of the *overall* fluid equation is zero, since  $\mathbf{u}$  is constant with time! What is going on? The explanation is that the time derivatives in Equations 2.3 and 2.4 mean different things. Let us appropriate an underutilized notation from statistical mechanics in which we put a subscript on derivatives to indicate what is being held constant. The fluid element's equation (2.3) uses

$$\left( \frac{d\mathbf{u}}{dt} \right)_{(\text{fluid element } \alpha)} \quad (2.5)$$

while the fluid equation (2.4) uses

$$\left( \frac{\partial \mathbf{u}}{\partial t} \right)_x \quad (2.6)$$

Time derivatives are being taken with different things being held constant! In the overall fluid case we consider the velocity's change with time *while our position is fixed*. In the element's case we consider the velocity's change with time *while our position is changing with the fluid element*. The relationship between these two derivatives, component-wise, is given by the chain rule:

$$\left( \frac{\partial u_i}{\partial t} \right)_\alpha = \left( \frac{\partial u_i}{\partial t} \right)_x + \sum_{j=1}^3 \left( \frac{\partial x_j}{\partial t} \right)_\alpha \left( \frac{\partial u_i}{\partial x_j} \right) = \left( \frac{\partial u_i}{\partial t} \right)_x + \mathbf{u} \cdot \nabla u_i$$

We can put all three components ( $i = 1, 2, 3$ ) of the above equation together by saying

$$\left( \frac{\partial \mathbf{u}}{\partial t} \right)_\alpha = \left( \frac{\partial \mathbf{u}}{\partial t} \right)_x + (\mathbf{u} \cdot \nabla) \mathbf{u} \quad (2.7)$$

Thus, the correct fluid equation of motion is not (2.4) but rather:

$$\rho \left( \frac{\partial}{\partial t} + (\mathbf{u} \cdot \nabla) \right) \mathbf{u} = \mathbf{F}(\mathbf{x}). \quad (2.8)$$

The term in the big parentheses on the left-hand side is called the “convective derivative” of  $\mathbf{u}$ .

Unfortunately, physicists have chosen a confusing notation for this concept:  $\frac{d\mathbf{u}}{dt}$ . The use of  $d$  over  $\partial$  is not meant to signify that  $\mathbf{u}$  is somehow not a function of multiple variables (it is:  $t$  and  $\mathbf{x}$ ) and thus that we no longer need to do *partial* differentiation. The convective derivative is a concept unique to fluid mechanics, and it would be preferable not to use a notation that seems to refer back to single-variable calculus. Consequently, in this thesis we will use a new notation for emphasis:  $\frac{d\mathbf{u}}{dt}$ . Thus,

$$\rho \frac{d\mathbf{u}}{dt} = \mathbf{F}(\mathbf{x}) \quad (2.9)$$

Also, it should be noted that although we will only use the convective derivative of  $\mathbf{u}$  in this thesis, elsewhere in fluid physics the convective derivatives of other quantities are sometimes used as well, in which case:

$$\frac{d\mathbf{A}}{dt} = (\text{Convective derivative of } \mathbf{A}(\mathbf{x}, t)) \equiv \left( \frac{\partial}{\partial t} + (\mathbf{u} \cdot \nabla) \right) \mathbf{A} \quad (2.10)$$

## The Alfvén Speed

A characteristic speed appears often in discussions of reconnection, known as the Alfvén speed. Most students of plasma physics, however, encounter this speed in a seemingly unrelated situation, in the context of special types of

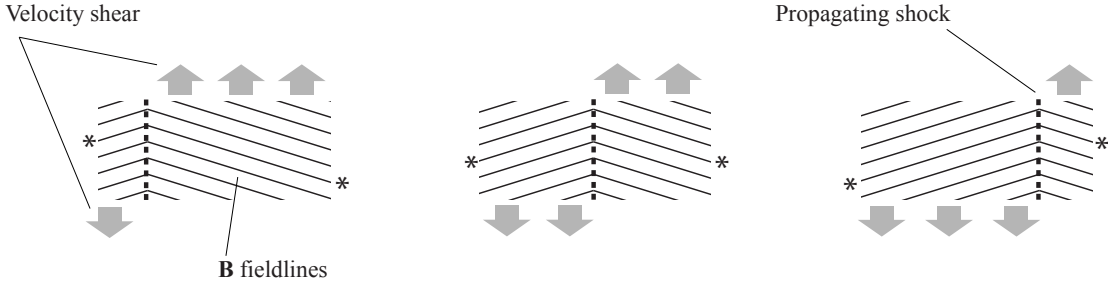


**Figure 2.2:** A propagating Alfvén shock wave. There is a velocity shear in the plasma. Since the fieldlines move with the fluid (as we will see shortly) the kink in the fieldlines must propagate to the right, as you can see by following the starred fieldline. The speed at which the kink (or shock) moves is the *Alfvén speed*.

waves that appear in plasmas (but not other fluids). In particular, consider the situation of Figure 2.2. A “kink” in the magnetic field propagates to the right. We have noted that plasma “sticks” to magnetic fieldlines, so there is also a vertical shear in the motion of the plasma to accompany the motion of the magnetic kink. It turns out that the kink propagates at the speed

$$u_{Alf} \equiv \frac{B}{\sqrt{\rho \mu_0}} \quad (2.11)$$

where  $\rho$  is the mass density. This kind of wave is known as a “magnetoacoustic” wave (the “acoustic” part of the name comes from the fact that one of the varying quantities in this wave is the fluid velocity, just like in a sound wave). Smooth oscillations are also possible, but in the case of the sharp discontinuity depicted here it is considered a “shock” (like the traveling pressure discontinuity associated with supersonic travel).

When we again see the Alfvén speed in the context of reconnection we should not be surprised even though there are no waves present; for reconnection is also an instance of *magnetic discontinuities associated with gradients in fluid velocity*, just as in Figure 2.2.

### 2.1.2 Magnetohydrodynamics

In trying to describe the dynamics of a plasma we are confronted with an overwhelmingly complex system. We clearly cannot write down  $\mathbf{F} = m\mathbf{a}$  for each of the  $> 10^{20}$  particles, so to make any progress we will need to make some simplifying assumptions. The first step is to recognize that a plasma is similar to a standard gas, so we can appropriate concepts like temperature and pressure from the kinetic theory of gases, assuming the plasma is in thermal equilibrium. However, plasmas are a bit more complicated than gases because all of the charged species interact with the electric and magnetic fields. Thus, we really need a separate copy of the fluid equations for each particle species, and we also need Maxwell’s equations. It would take too much time to fully discuss the meaning of each equation, but we will list

them here for you to see:

$$m_\alpha n_\alpha \left( \frac{\partial \mathbf{u}_\alpha}{\partial t} + (\mathbf{u}_\alpha \cdot \nabla) \mathbf{u}_\alpha \right) = n_\alpha q_\alpha (\mathbf{E} + \mathbf{u}_\alpha \times \mathbf{B}) - \nabla \cdot \underline{\mathbf{P}}_\alpha + \sum_\beta \mathbf{R}_{\alpha\beta} \quad \text{Newton's second law} \quad (2.12)$$

$$\frac{\partial n_\alpha}{\partial t} = -\nabla \cdot (n_\alpha \mathbf{u}_\alpha) \quad \text{mass conservation} \quad (2.13)$$

$$\mathbf{J} = \sum_\alpha n_\alpha \mathbf{u}_\alpha q_\alpha \quad \text{definition of current} \quad (2.14)$$

$$\nabla \times \mathbf{B} = \mu_0 \mathbf{J} + \mu_0 \epsilon_0 \frac{\partial \mathbf{E}}{\partial t} \quad \text{full Ampère's law} \quad (2.15)$$

$$\nabla \cdot \mathbf{B} = 0 \quad \text{no magnetic monopoles} \quad (2.16)$$

$$\nabla \times \mathbf{E} = -\frac{\partial \mathbf{B}}{\partial t} \quad \text{Faraday's law} \quad (2.17)$$

$$\nabla \cdot \mathbf{E} = \frac{1}{\epsilon_0} \sum_\alpha n_\alpha q_\alpha \quad \text{Gauss's law} \quad (2.18)$$

$\alpha$  and  $\beta$  are indices over the different species of particles, and  $\mathbf{R}_{\alpha\beta}$  represents the transfer of momentum between species in collisions. In addition, an equation of state is needed for each of the six independent components of the symmetric tensor  $\underline{\mathbf{P}}_\alpha$ , the pressure tensor of species  $\alpha$  (see Appendix B). When considering the number of unknowns this set represents, remember that vector quantities count threefold and  $\underline{\mathbf{P}}_\alpha$  has six degrees of freedom. If there are  $s$  species of particles, then there are  $10s + 9$  unknowns:  $\mathbf{B}, \mathbf{E}, \mathbf{J}$  (current density),  $\underline{\mathbf{P}}_\alpha$ ,  $n_\alpha$  (number density), and  $\mathbf{u}_\alpha$  (velocity). For even a simple plasma, fully ionized hydrogen (which has only two species), this is 29 unknown fields.

Even if we are working with fully ionized hydrogen we can still whittle away at this list of equations by making a canonical set of assumptions. The result is a set of equations known as Ideal Magnetohydrodynamics, or “Ideal MHD”. The assumptions of MHD include the following:

- The electron mass is insignificant compared to the proton mass
- The electron and ion densities are approximately equal, but need not be exactly so
- None of the particles are relativistic
- Collisions are frequent enough to achieve local thermal equilibrium but not frequent enough to introduce significant dissipation
- The Larmour orbits (see Section 2.1.1) are much smaller than the size of the system in question

The plasma is considered to be a fluid with a single velocity, mass density, and pressure at any point, although in fact there are two species of particles that each have a different velocity distribution. Ideal MHD has 14 unknowns:  $p, \rho$  (mass density),  $\mathbf{B}, \mathbf{J}, \mathbf{u}$ , and  $\mathbf{E}$ . Here are the corresponding 14 equations:

$$\nabla \cdot \mathbf{B} = 0 \quad \text{no magnetic monopoles} \quad (2.19)$$

$$\nabla \times \mathbf{B} = \mu_0 \mathbf{J} \quad \text{shortened Ampère's law} \quad (2.20)$$

$$\nabla \times \mathbf{E} = -\frac{\partial \mathbf{B}}{\partial t} \quad \text{Faraday's law} \quad (2.21)$$

$$\frac{\partial \rho}{\partial t} + \nabla \cdot (\rho \mathbf{u}) = 0 \quad \text{mass conservation} \quad (2.22)$$

$$\rho \frac{d\mathbf{u}}{dt} = -\nabla p + \mathbf{J} \times \mathbf{B} \quad \text{“equation of motion”} \quad (2.23)$$

$$\mathbf{E} + \mathbf{u} \times \mathbf{B} = 0 \quad \text{“ideal Ohm’s law”} \quad (2.24)$$

Note that we have dropped the displacement current from Ampère’s law. We will henceforth indicate this shortened form when we say “Ampère’s law.” Because this approximation is used frequently in this thesis, and because it is a

good illustration of the form of argument used to drop terms in deriving MHD, a “proof” that the displacement current is negligible is provided in Appendix A.

MHD can be a very powerful theory – where it applies. We will soon see that it is MHD, and the last equation above in particular, that implies the freezing of magnetic fieldlines to the plasma from the fluid viewpoint. For this reason, we will be particularly interested in this “Ohm’s law” equation in future sections.

Why is this equation called “Ohm’s law?” You are probably familiar with  $V = IR$  as Ohm’s law, which looks quite different from what appears above in the MHD equations. However, there is in fact a connection between the two equations. First, we put  $V = IR$  into a equivalent expression about densities by adding some factors of length  $L$  and cross-sectional area  $A$  of a particular volume element, where  $L$  is in some coordinate direction  $i$ :

$$\frac{V}{L} = \frac{I}{A} \frac{AR}{L} \Rightarrow E_i = J_i \eta \Rightarrow \mathbf{E} = \eta \mathbf{J} \quad (2.25)$$

$\eta$  is the *resistivity* of the material. Next, suppose our material is *moving* relative to our lab frame. Even if Ohm’s law is perfectly correct in the frame moving with the fluid, when we Lorentz transform to the lab frame the  $\mathbf{E}$  causes a magnetic field to appear. In the  $u \ll c$  limit this Lorentz transformation gives:

$$\mathbf{E} + \mathbf{u} \times \mathbf{B} = \eta \mathbf{J} \quad (2.26)$$

Plasmas move faster and are more typically permeated with significant magnetic fields than the resistors used as electrical components, so in plasma physics we must keep the  $\mathbf{u} \times \mathbf{B}$  term around. Thus, the MHD ideal Ohm’s law is really the same as the familiar Ohm’s law in the case where there is *no resistivity* – this is what makes the law “ideal.” The resistivity of plasmas is typically as low as copper or other metals, making  $\eta = 0$  an often valid approximation.

We sometimes want to back off from some of the assumptions of these ideal MHD equations to discuss “non-ideal” plasma behavior. Often this is done by modifying the ideal Ohm’s law. Many of the last and weakest assumptions made in the MHD derivation involve eliminating terms in the derivation of this particular equation, making it a good place for scrutiny. However, there are other significant terms besides  $\eta \mathbf{J}$  which appear when we formally derive Ohm’s law from the full fluid equations for each species. For example, about halfway through the simplifications we have:

$$\mathbf{E} + \mathbf{u} \times \mathbf{B} = \eta \mathbf{J} - \frac{1}{ne} \nabla p_e + \frac{1}{ne} \mathbf{J} \times \mathbf{B} + \frac{m_e}{ne^2} \frac{\partial \mathbf{J}}{\partial t} \quad (2.27)$$

We will see this “generalized” Ohm’s law extensively in later sections.

### 2.1.3 MHD Equilibrium and the Spheromak

One of the most useful reasons for making the simplifying assumptions of magnetohydrodynamics is that the equations become simple enough to admit analytical solutions. In particular, we are often interested in equilibria, systems of  $\mathbf{B}$ ,  $\mathbf{J}$ , etc. for which all time derivatives are zero and there is no bulk flow. These solutions are interesting because they should persist for a “long” time – much longer than a similar density gradient would persist in a non-ionized gas. Solar flares – or a tokamak plasma held far from the reactor wall – are such examples of structure that can persist longer in a plasma than in a non-ionized gas.

The word “spheromak” in the title of this thesis refers to one particular such MHD equilibrium solution. Although we will skip most of the mathematical derivation of this equilibrium, a few steps are worthy of discussion. This analysis closely follows Geddes [20]. We start with one of the MHD equations we wrote down in the previous section, the

“plasma equation of motion” (Equation 2.23)<sup>2</sup>:

$$\rho \frac{d\mathbf{u}}{dt} = -\nabla p + \mathbf{J} \times \mathbf{B} \quad (2.29)$$

We are interested in flow-free equilibrium, so  $\mathbf{u} = 0$ , and the left-hand side therefore vanishes. Next, recall that the  $\beta$  parameter reflects the relative importance of thermal pressure to magnetic pressure, and that almost all laboratory plasmas have  $\beta \ll 1$  (see Section 2.1.1). Thus, it is often a good approximation that  $\nabla p \rightarrow 0$ . Thus,  $0 = \mathbf{J} \times \mathbf{B}$ , and so

$$\mathbf{J} \parallel \mathbf{B}.$$

We next apply Ampère’s law to the left-hand side:

$$\nabla \times \mathbf{B} \parallel \mathbf{B}$$

or equivalently,

$$\nabla \times \mathbf{B} = \lambda \mathbf{B} \quad (2.30)$$

for some scalar  $\lambda$ . This is the equation of *force-free equilibrium*, so called since both the pressure and  $\mathbf{J} \times \mathbf{B}$  forces were taken to be 0. In general,  $\lambda$  can be a *position-dependent* scalar field, but the solutions for which  $\lambda$  does *not* depend on space are particularly interesting for the following reason.

We first define a quantity called *magnetic helicity*

$$K \equiv \int_V \mathbf{A} \cdot \mathbf{B} dV \quad (2.31)$$

where  $A$  is the vector potential<sup>3</sup>. It turns out that for all ideal and even for a large class of non-ideal MHD dynamics, the total magnetic helicity of the plasma volume does not change. Thus, the process by which a real laboratory plasma reaches an equilibrium is the *minimization of its energy* subject to the constraint of a fixed  $K$ . This minimization subject to a constraint can be performed with Lagrange multipliers, and the result is none other than Equation 2.30 with  $\lambda$  constant over space. Thus, the constant- $\lambda$  approximation is a reasonable one.

With this simplification, Equation 2.30 at last has analytical solutions. Let us take the boundary condition to be that  $\mathbf{B}$  is parallel to the surface along a closed cylindrical volume of radius  $R$  and length  $L$ . The reason for this choice will not be clear until a later section, when we will see that magnetic fields cannot penetrate good conductors. The boundary condition thus describes a plasma produced inside a cylindrical metal can, since  $\mathbf{B}$  will not (on the relevant timescale) be able to point into the conducting wall. Schaffer [48] derives the solutions to this boundary-value problem. The lowest-order (and thus dominant) solution is:

$$\begin{aligned} B_r &= B_0 \frac{k_z}{k_r} J_1(k_r r) \cos(k_z z) \\ B_\theta &= B_0 \lambda J_1(k_r r) \sin(k_z z) \\ B_z &= -B_0 J_0(k_r r) \sin(k_z z) \end{aligned} \quad (2.32)$$

where the  $J_n$  are Bessel functions,  $B_0$  is an arbitrary overall scale factor, and

$$k_z = \frac{\pi}{L}, \quad k_r = \frac{z_{1,1}}{R}, \quad \lambda = \pm \sqrt{\frac{k_z^2}{k_r^2} + 1}$$

---

<sup>2</sup>A good way to think about this equation is that it is something like Newton’s second law, divided by volume:

$$\frac{ma}{V} = \frac{F}{V} \quad (2.28)$$

The left-hand side of Equation 2.29 is  $m/V$  times the convective derivative of velocity (Section 2.1.1)- the acceleration of a fluid element as it moves in space. The terms on the right-hand side are the fluid and electromagnetic forces acting on that fluid element.

<sup>3</sup>We can use  $A$  in any gauge to calculate the helicity. It turns out that as long as we perform the integration over a magnetic surface (a surface with no perpendicular component of  $B$ ) then  $K$  is gauge-invariant [45]

Here,  $z_{1,1} \approx 3.8317$  is the first root of  $J_1$ .

This is a spheromak! Actually, qualitatively similar  $\mathbf{B}$  solutions for other geometries (e.g., spherical) can also be considered spheromaks. Also, other methods exist to find equilibria that are more accurate than the method shown here.

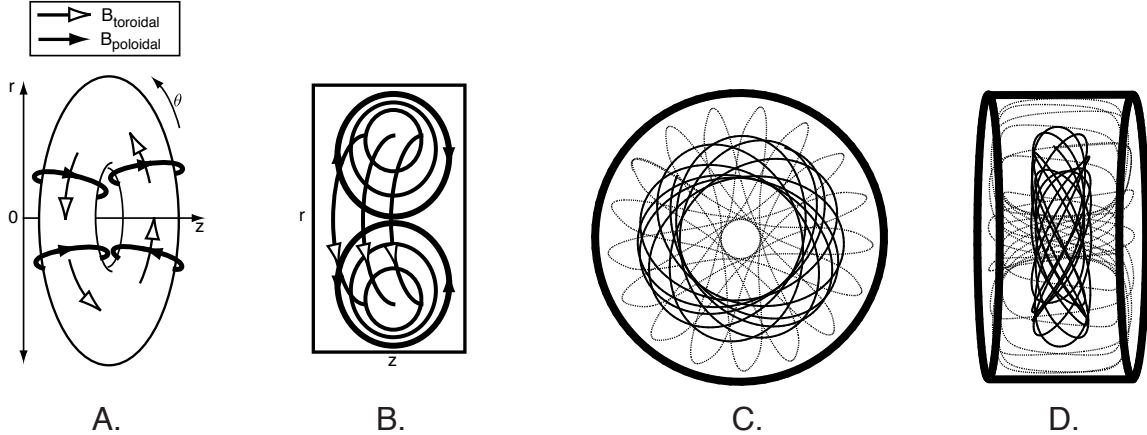


**Figure 2.3:** A-B: The helical field of a spheromak can be thought of as a sum of toroidal and poloidal components. C and D show two actual fieldlines calculated from Equations 2.32.

The fieldlines of a spheromak follow a helix-like path around the axis of the cylindrical container (Figure 2.3). The  $\theta$  component of  $\mathbf{B}$  is referred to as the “toroidal field”, as a purely  $\theta$ -directed fieldline bundle would look like a torus. The  $r$  and  $z$  components are known as the “poloidal field”<sup>4</sup>. Note that given the container dimensions  $R$  and  $L$ , a spheromak is determined uniquely up to an overall scale factor  $B_0$  and the *sign* of  $\lambda$ . The two choices of sign correspond to “left-handed” and “right-handed” spheromaks, whose fieldlines are right-handed and left-handed helices, respectively. Also, the total magnetic helicity of the two configurations differs by a minus sign.

## 2.1.4 The Frozen-In Flux Conditions

Let us now formally state what it means for the magnetic field to be “frozen” to the plasma. In fact, there are actually two closely related but non-equivalent senses of this idea, known as “flux conservation” and “fieldline conservation.” We first describe flux conservation, following Griffiths’ derivation [23].

**Theorem 1.** *Consider an imaginary loop  $\mathcal{C}$  that is “drawn” into an ideal MHD plasma fluid, and which moves with the fluid in time. Then the magnetic flux through that loop will be constant in time*

The statement is subtle. In other words, we pick a particular surface in the plasma and watch how it evolves with time. Since the fluid velocity may vary for the various regions comprising the surface, the surface may get very twisted and distorted in time. Yet, the “number of field lines” which pass through that surface - i.e. the amount of magnetic flux through it - will remain constant.

*Proof.* First, note that only since  $\mathbf{B}$  is divergence-free is it well-defined to talk about the “flux through the loop”, since *any* surface integral of  $\mathbf{B}$  over a surface  $\mathcal{S}$  bounded by  $\mathcal{C}$  will give the same number by Stokes’ theorem:

$$\int_{\mathcal{S}} \mathbf{B} \cdot d\mathbf{a} = \int_{\mathcal{S}} (\nabla \times \mathbf{A}) \cdot d\mathbf{a} = \oint_{\mathcal{C}} \mathbf{A} \cdot dl = \begin{pmatrix} \text{Only depends on} \\ \text{boundary } \mathcal{C} \end{pmatrix} \quad (2.33)$$

---

<sup>4</sup>It is because the  $r$  and  $z$  field components together resemble the field of a dipole? Or because they vary with the *polar* and not azimuthal angle? We may endlessly speculate...

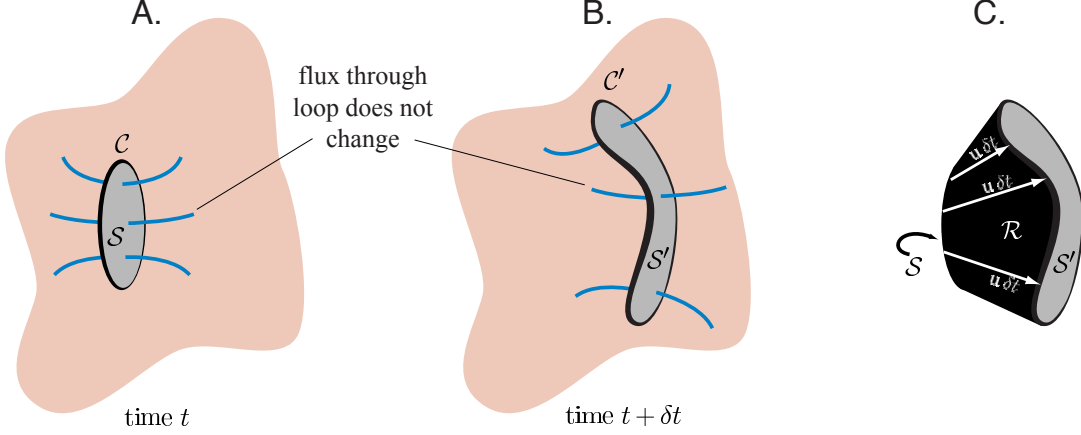


**Figure 2.4:** Notation for the proof of flux conservation.

Above,  $\mathbf{A}$  is the vector potential, and  $d\mathbf{a}$  is a differential area element. Now, consider the loop  $C'$ , which is obtained by moving each point  $\mathbf{x}$  on  $C$  to  $\mathbf{x} + \mathbf{u}(\mathbf{x})\delta t$ , as shown in Figure 2.4. In other words,  $C'$  is where  $C$  ends up after a moment of time  $\delta t$ . We would like to show that the flux  $\Phi + \delta\Phi$  through  $C'$  at time  $t + \delta t$  equals the flux  $\Phi$  through  $C$  at time  $t$ . Letting  $\mathcal{R}$  denote the thin ribbon of surface between  $C$  and  $C'$ , we can note that the flux through  $C'$  at any particular time equals the sum of the flux through the loop  $C$  and that through the surface  $\mathcal{R}$ . This is because any surface bounded by  $C$ , when “glued” to  $\mathcal{R}$ , gives a surface whose boundary is  $C'$ , and flux integrals only depend on the boundary curve as we have noted. To put these ideas into symbols, let  $S$  be any surface bounded by  $C$ , and let  $S'$  be any surface bounded by  $C'$ :

$$\begin{aligned}\delta\Phi &= \int_{S'} \mathbf{B}(t + \delta t) \cdot d\mathbf{a} - \int_S \mathbf{B}(t) \cdot d\mathbf{a} \\ &= \int_{\mathcal{R}} \mathbf{B}(t + \delta t) \cdot d\mathbf{a} + \int_S \mathbf{B}(t + \delta t) \cdot d\mathbf{a} - \int_S \mathbf{B}(t) \cdot d\mathbf{a}\end{aligned}\quad (2.34)$$

Since  $\delta t$  is very small, then what is this difference  $\delta\Phi$  to first order in  $\delta t$ ? The last two of the three integrals above are over the same surface, so we may combine them and recognize the small change in  $\mathbf{B}$  as a time derivative:

$$\begin{aligned}\int_S \mathbf{B}(t + \delta t) \cdot d\mathbf{a} - \int_S \mathbf{B}(t) \cdot d\mathbf{a} &= \int_S (\mathbf{B}(t + \delta t) - \mathbf{B}(t)) \cdot d\mathbf{a} \\ &\approx \int_S \left( \delta t \frac{\partial \mathbf{B}}{\partial t} \right) \cdot d\mathbf{a} \\ &= \delta t \int_S \frac{\partial \mathbf{B}}{\partial t} \cdot d\mathbf{a}\end{aligned}\quad (2.35)$$

Now that we have simplified the latter two of the three integrals in equation 2.34, let us consider the first one. We can note that any integral over  $\mathcal{R}$  is already first-order (not zeroth!) in  $\delta t$ , because the ribbon  $\mathcal{R}$  is only as wide as the distance  $\mathbf{u} \delta t$  that the fluid moves in time. Thus, the only first-order contribution from this term involves a *zeroth*-order approximation for  $\mathbf{B}(t + \delta t)$ :

$$\begin{aligned}\int_{\mathcal{R}} \mathbf{B}(t + \delta t) \cdot d\mathbf{a} &= \int_{\mathcal{R}} \left( \mathbf{B}(t) + \delta t \frac{\partial \mathbf{B}}{\partial t} + \dots \right) \cdot d\mathbf{a} \\ &= \left( \int_{\mathcal{R}} \mathbf{B} \cdot d\mathbf{a} \right) + \mathcal{O}(\delta t^2)\end{aligned}\quad (2.36)$$

Combining equations 2.34, 2.35, and 2.36, we see that

$$\delta\Phi = \delta t \int_S \frac{\partial \mathbf{B}}{\partial t} \cdot d\mathbf{a} + \int_{\mathcal{R}} \mathbf{B}(t) \cdot d\mathbf{a}\quad (2.37)$$

Next, we will convert the last term above into a *path* integral around  $\mathcal{C}$ . For each bit of length  $d\mathbf{l}$  around  $\mathcal{C}$ , we accumulate a small area  $d\mathbf{a}$  of  $\mathcal{R}$ . The area is approximately a rectangular patch with one side of length  $d\mathbf{l}$  and the other side of length  $\delta t \mathbf{u}$ . Following the convention of equation 2.34 as to which side of  $\mathcal{R}$  is the “positive” one, we obtain  $d\mathbf{a} = -\delta t \mathbf{u} \times d\mathbf{l}$ . We now rewrite the last integral in 2.37 as

$$\begin{aligned}\delta\Phi &= \delta t \int_S \frac{\partial \mathbf{B}}{\partial t} \cdot d\mathbf{a} - \oint_{\mathcal{C}} \mathbf{B}(t) \cdot (\delta t \mathbf{u} \times d\mathbf{l}) \\ &= \delta t \int_S \frac{\partial \mathbf{B}}{\partial t} \cdot d\mathbf{a} - \delta t \oint_{\mathcal{C}} (\mathbf{B}(t) \times \mathbf{u}) \cdot d\mathbf{l}\end{aligned}$$

where the cyclic permutability of the triple product was used in the last equality. Dividing by  $\delta t$  and using Stokes’ theorem,

$$\frac{d\Phi}{dt} = \int_S \frac{\partial \mathbf{B}}{\partial t} \cdot d\mathbf{a} - \int_S \nabla \times (\mathbf{u} \times \mathbf{B}) \cdot d\mathbf{a} = \int_S \left[ \frac{\partial \mathbf{B}}{\partial t} - \nabla \times (\mathbf{u} \times \mathbf{B}) \right] \cdot d\mathbf{a} \quad (2.38)$$

What is the term in brackets above? Plugging the ideal MHD Ohm’s law into Faraday’s law, we find

$$\frac{\partial \mathbf{B}}{\partial t} = -\nabla \times \mathbf{E} = \nabla \times (\mathbf{u} \times \mathbf{B}) \quad (2.39)$$

and so the term in brackets in equation 2.38 is 0! Thus  $d\Phi/dt = 0$ , so the flux through  $\mathcal{C}$  is constant in time.  $\square$

*Fieldline conservation* is another sense in which the field is “frozen” into the plasma.

**Theorem 2.** *If the points  $\mathbf{x}_1(t), \mathbf{x}_2(t), \dots$  move with the fluid in an ideal MHD plasma, and if at some time  $t$  a field line of  $\mathbf{B}$  passes through all the  $\mathbf{x}_i$ , then a single field line passes through the  $\mathbf{x}_i$  at all other times as well.*

The proof for ideal MHD plasmas follows from the theorem we just proved<sup>5</sup>. This argument is due to Cowley [13].

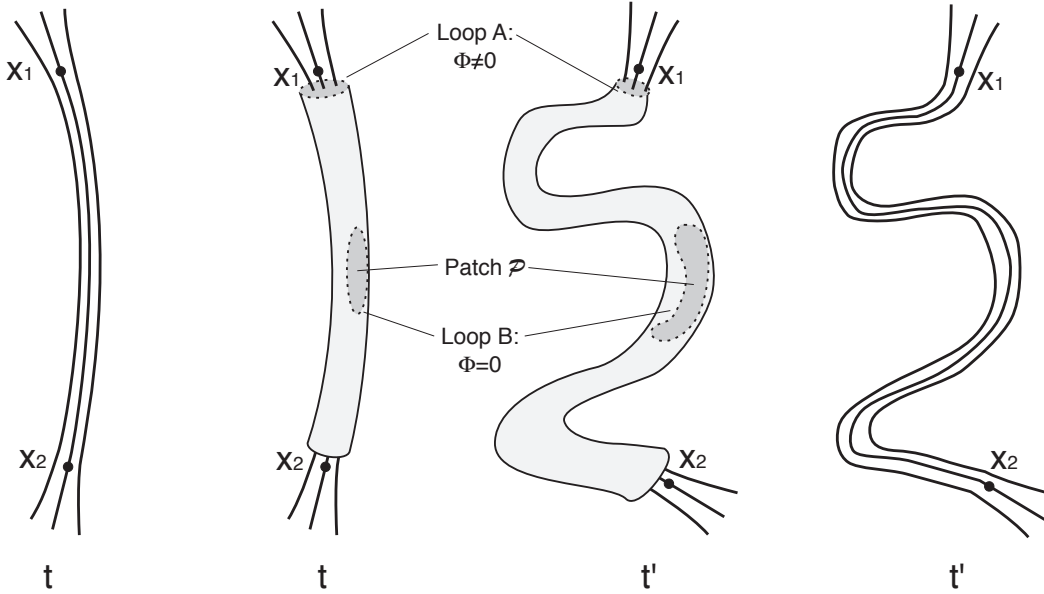


**Figure 2.5:** Proof of the second sense of the frozen-in flux condition.

---

<sup>5</sup>A special class of non-ideal effects can result in a plasma for which fieldline conservation applies, but not flux conservation.

*Proof.* Consider an imaginary thin tube surrounding the field line at time  $t$ , as in Figure 2.5. Since the tube follows  $\mathbf{B}$ , then there is no flux through any patch  $\mathcal{P}$  of surface along the tube, such as the patch surrounded by loop B in the figure. At some other time  $t'$ , consider where the tube will have moved to if it follows the fluid. It still surrounds the  $\mathbf{x}_i$ , and by our first theorem each patch  $\mathcal{P}$  *still* contains no flux. If we follow the end “caps” of the tube, such as the patch surrounded by loop A in the figure, they still contain as many field lines as they did at time  $t$ . Thus, the field *still* runs through the tube at time  $t'$ , and the tube flows with the fluid.  $\square$

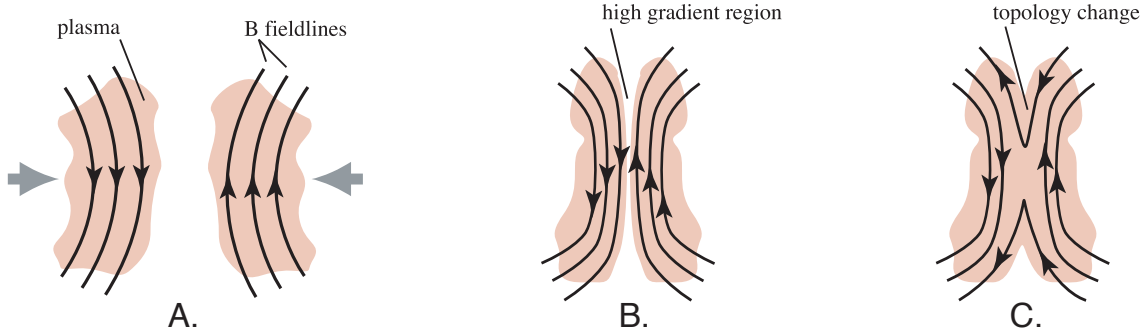


**Figure 2.6:** The canonical picture of reconnection. A: A converging flow can drag together oppositely directed fieldlines. B: In pure MHD an arbitrarily sharp gradient should be achievable, since fieldline topology can never change. C: In practice, however, non-ideal effects take over and fieldlines reconnect.

## 2.2 Evidence from Nature that Reconnection is Significant

MHD is a useful approximation to reality. It simplifies the world of plasma phenomena to the point where some very powerful results can be derived. Alas, the world does not always seem to be as ideal as Ideal MHD would have us believe. A number of situations unambiguously indicate a breakdown of MHD, such as the simple fact that flares in the solar corona evolve and die out. The breakdown of MHD occurs when a *large gradient in the magnetic field* develops. The fieldlines are then said to *reconnect*, because points in the fluid that the lines previously linked together become unlinked, and previously unlinked points become linked (Figure 2.6). The fact that MHD seems to break down in regions of large gradients is not too surprising. Large gradients in the magnetic field cause otherwise negligible terms in the plasma equations – those with spatial derivatives – to become important. These great changes in  $\mathbf{B}$  over small distances tend to bring out the non-idealness in a plasma.

There is nothing in the equations of ideal MHD to prevent such gradients from arising. If two bundles of fluid with oppositely-directed  $\mathbf{B}$  happen to move towards each other, they will carry their fieldlines with them and produce a large shear.

The fact that ideal MHD *does* break down where there are large gradients is not in itself surprising; of course the assumptions going into ideal MHD will break down in extreme regimes. What *is* mysterious is that *it does not take as large a gradient as you would expect* for the breakdown to occur. Reconnection is seen to occur over gradient regions that are much wider than the simplest theories predict. This fact is directly related to the previously mentioned fact that reconnection is *much faster* than simple theories predict.

We now mention a few contexts in which reconnection is thought to occur.

### 2.2.1 Coronal Heating and Solar Flares

The surface of the sun is roughly 5770 K, as we might expect considering how hot a blackbody would have to be to produce a spectrum peaked in the visible region. However, x-ray images of the sun show bright regions in the corona, the

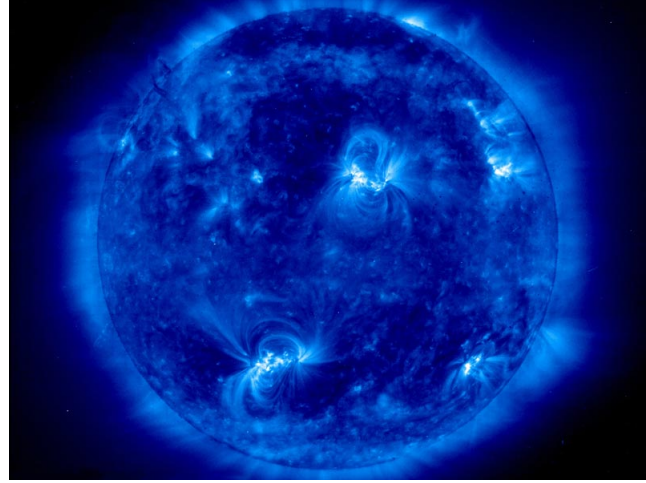


**Figure 2.7:** An x-ray image of the sun, taken by the SOHO satellite.

“atmosphere” above the sun’s surface (Figure 2.7). The gas must be in the million-Kelvin range to produce radiation of such small wavelength, and the hottest regions can reach more than 1000 times the surface temperature. Imagine if the atmosphere of the Earth were 1000 times the Earth’s surface temperature! This is a highly non-equilibrium situation, so there must be some source of energy fueling these hot regions. The probable explanation is that energy is stored in the magnetic field inside the sun through a dynamo process. The magnetic fields rise to the corona and reconnect. Reconnection implies a loss of magnetic energy, and this lost energy turns up as heat.

## 2.2.2 Cosmic Ray Acceleration

Reconnection may also help to explain the astrophysical problem concerning the origin of cosmic rays. It has been well established that the stream of cosmic ray particles impacting the Earth contains some particles with energies of over  $10^{20}$  eV - that is, single protons with the energy of a 1 kg mass that has fallen 1 m! These energies greatly exceed those possible in modern accelerators ( $\sim 1\text{TeV}$ ); there are only a few possible sources in the universe that could generate such particles.

The possible sources are further restricted due to a phenomenon known as the Greisen-Zatsepin-Kuzmin (GZK) Cutoff. To an observer on Earth the cosmic background radiation has a typical energy in the microwave band, but to a particle with  $> 10^{19}$  eV, Doppler shifting becomes important. Such a particle sees not microwaves ahead but gamma waves. If these photons are above a certain critical energy, photodisintegration reactions become significant which scatter and slow the protons [55] over a length scale of about 20 Mpc. The fact that we see significant numbers of cosmic rays with energies above the critical value ( $\sim 10^{19}$  eV) indicates that the source of the acceleration is within a few multiples of this distance from Earth. An additional complication is that the distribution of high-energy cosmic rays is isotropic; they seem to come from every direction. There are not many possible sources that could be both nearby and also isotropic.

One possible answer is that the particles are accelerated locally (within 100 Mpc) by magnetic reconnection. Reconnection turns magnetic energy into other forms, and we will see in later sections that one of these forms is accelerated particles. Furthermore, reconnection can be a source of energy wherever there is magnetic field - including the interstellar medium - possibly explaining the isotropy of the distribution of particles.

If reconnection is to account for the observed flux of cosmic rays, then it must be a significant process, more significant than you would predict with the simplest reconnection models.

### 2.2.3 Instabilities in Tokamaks

In order to achieve economical nuclear fusion energy, we must be able to create *stable* plasmas: stable so they can produce power for a significant duration of time, and stable so they do not move to contact the reactor wall and lose their thermal energy to collisions. Tokamaks – the vanguard of fusion reactor designs today – have been plagued by a number of instabilities involving reconnection [45]. Consequently, a better understanding of reconnection will be helpful in realizing the promise of fusion power.

One such instability, known as the sawtooth, causes the plasma temperature (and consequently other related parameters) to rise slowly (over  $\sim 0.2$  seconds in the largest machines) and then to suddenly decrease. The rise-fall pattern can repeat many times during a shot. In the best supported explanation for this behavior, a well-understood ideal MHD instability known as the “kink” affects that plasma which is farther than some threshold distance from the vessel walls (i.e., minor radius  $< r_0$ ). This core of the plasma tries to blow outward, but instead it reconnects with the surrounding tube of stable plasma (in which minor radius  $> r_0$ ) leaving a configuration like that before the kink developed, and the cycle repeats. If we truly understand what is happening in this reconnection phase, we should be able to predict the duration of the crash phase of the sawtooth oscillation. However, the simplest model proposed by Kadomtsev predicts a time which is too long by a factor of ten. Attempts are being made to modify the Kadomtsev model to account for this discrepancy.

Reconnection has been implicated in other tokamak instabilities as well, such as “Mirnov oscillations” and “major disruptions.”[45]

## 2.3 Magnetic Reconnection - The Theoretical Basis

Nature has spoken. Ideal MHD is applicable in many circumstances, but not all. There do seem to be important situations in which the field becomes unlinked from the fluid in an otherwise ideal situation. Somewhere in the assumptions of MHD we threw out the baby with the bathwater - but in which assumption? Specifically, the following questions can be asked:

- Which non-ideal physical effects are important in allowing reconnection to occur? Which assumptions of MHD break down?
- What determines the *rate* of reconnection? How fast does magnetic flux change its connectivity?
- If the magnetic field gradient cannot get arbitrarily sharp, then how small *does* the field-reversal region get?
- Magnetic energy is turned into heat, fluid flow, and high-energy particles. How is the original energy partitioned into these three forms?

Let us look at some of the ideas that have been generated by researchers so far in response to these questions.

### 2.3.1 Beyond the Ideal Ohm's Law

One good place to look for non-ideality in the plasma equations is in Ohm's law. When we introduced magnetohydrodynamics, we presented this tidy equation:

$$\mathbf{E} + \mathbf{u} \times \mathbf{B} = 0 \tag{2.40}$$

This equation is obtained by starting with the 100% true equations of electromagnetism and making a *very long* sequence of assumptions. The derivation can be seen in Appendix B (if you want to see the gory details). But if reconnection does in fact happen, this simple equation cannot be completely correct. Recall that in the proof of the frozen-in flux condition, the only two equations of MHD we needed were  $\nabla \cdot \mathbf{B} = 0$ , Faraday's law, and Ohm's “law”.

The former two are certainly true even in a non-ideal plasma, for they are fundamental rules of electrodynamics. Ohm's "law", however, is not similarly fundamental. We needed to make many simplifying assumptions to derive it, and thus there must be *other* relevant terms in it which were thrown out! Let us take a few steps back in the derivation, and reinstate the last four terms which we at first thought to be negligible:

$$\mathbf{E} + \mathbf{u} \times \mathbf{B} = \eta \mathbf{J} - \frac{1}{ne} \nabla p_e + \frac{1}{ne} \mathbf{J} \times \mathbf{B} + \frac{m_e}{ne^2} \frac{\partial \mathbf{J}}{\partial t} \quad (2.41)$$

Perhaps it is one of these new terms which is allowing reconnection to happen<sup>6</sup>. In fact, it could certainly be the case that different terms are responsible for reconnection in different circumstances.

We can make some educated guesses about which terms in this "generalized Ohm's law" are important using some clever reasoning. First, note that each term is either a gradient or else contains  $\mathbf{J}$ .  $\mathbf{J}$  is also approximately a spatial derivative,  $(1/\mu_0) \nabla \times \mathbf{B}$ , according to Ampère's law. Thus, the situations of steep gradients in  $\mathbf{B}$  that result in reconnection will make each term grow larger (just as we claimed earlier- sharp shears bring out non-ideal behavior). However, the terms will not all grow large at the same rate. Imagine two ideal masses of plasma flowing towards each other, producing a steeper and steeper gradient. As soon as *one* non-ideal term causes the fieldlines to start reconnecting, the gradient will not grow any sharper. It has become standard in the lore of reconnection to talk about these terms as being associated with a length, in the following sense. Given  $|\mathbf{B}|$ ,  $T$ , and  $n$ , over how small a distance must  $\mathbf{B}$  reverse its direction so that the term becomes as large as the *ideal* terms in Ohm's law? Among the non-ideal terms, the one with the greatest associated length in this sense "wins." Once this leading term allows the incoming field to diffuse away, the gradient will not get any tighter and the remaining terms will not grow significant.

Let us then find formulas for the distance associated with each term. For example, consider the term  $\eta \mathbf{J}$ , which we henceforth will call the resistivity term. Suppose a typical velocity magnitude for our plasma is  $u_0$ , and that a typical magnetic field magnitude is  $B_0$ . If we call the distance over which the  $\mathbf{B}$ -field reverses  $L_{\text{resistivity}}$ , then we can "approximate" the curl operator  $\nabla \times$  with  $1/L_{\text{resistivity}}$ . We then set the magnitude of our resistivity term equal to the  $\mathbf{u} \times \mathbf{B}$  term in the ideal part of Ohm's law:

$$u_0 B_0 \sim \eta J = \eta \left| \frac{1}{\mu_0} \nabla \times \mathbf{B} \right| \sim \frac{\eta}{\mu_0} \frac{B_0}{L_{\text{resistivity}}}$$

Solving for our length we find:

$$L_{\text{resistivity}} \sim \frac{\eta}{\mu_0 u_0} \quad (2.42)$$

Although  $\eta$  is not always easy to measure directly, a formula was derived by Spitzer to estimate it based on the temperature. Consequently, we can estimate  $L_{\text{resistivity}}$  for any interesting plasma.

Next, consider the  $(1/ne) \mathbf{J} \times \mathbf{B}$  term. This term is often called the Hall Term, since  $\mathbf{J} \times \mathbf{B}$  is the Hall force in standard electrodynamics. Introducing the typical density  $n_0$  we repeat our order-of-magnitude trick from above and find:

$$u_0 B_0 \sim \frac{1}{n_0 e} \left( \frac{B_0}{\mu_0 L_{\text{Hall}}} \right) B_0 \Rightarrow L_{\text{Hall}} \sim \frac{B_0}{\mu_0 u_0 n_0 e} \quad (2.43)$$

As we have already foreshadowed, it will turn out that flow speeds in reconnection contexts are often of the order of the Alfvén speed. Plugging in  $u_{Alf}$  for  $u_0$  gives us

$$L_{\text{Hall}} \sim \frac{B_0}{\mu_0 (B_0 / \sqrt{\rho_0 \mu_0}) n_0 e} = \sqrt{\frac{m_i}{\mu_0 n_0 e^2}} \quad (2.44)$$

This same length happens to appear in other plasma physics contexts, in which it is known as the "ion-inertial length" and often denoted by<sup>7</sup>  $c/\omega_{pi}$ . We will use this common notation in coming sections when we discuss the relevance of the Hall term to reconnection.

<sup>6</sup>Here,  $p_e$  represents the *electron pressure*, which is *not* the same as the pressure  $p$  we have seen in the equation of motion.  $p_e$  is a function of the *electron* velocity distribution about the average *electron* velocity, while  $p$  is computed from the momentum distribution of *all* particles about the *center-of-mass* velocity.

<sup>7</sup>Here  $\omega_{pi}$  is called the "ion plasma frequency." We will shortly see  $\omega_{pe}$ , the "electron plasma frequency."

Parameter	Dimension	Laboratory experiments	Earth's Magnetosphere	Solar Corona	Solar Interior
$L$	m	$10^{-1}$	$10^7$	$10^8$	$10^7$
$B_0$	T	$10^{-1}$	$10^{-8}$	$10^{-2}$	$10^1$
$n_0$	$\text{m}^{-3}$	$10^{20}$	$10^5$	$10^{15}$	$10^{29}$
$T_0$	K	$10^5$	$10^7$	$10^6$	$10^6$
$L_{\text{resistivity}}$	m	$10^{-4}$	$10^{-7}$	$10^{-7}$	$10^{-3}$
$L_{\text{Hall}} = \frac{c}{\omega_{pi}}$	m	$10^{-2}$	$10^6$	$10^1$	$10^{-6}$
$L_{\text{pressure}} = \beta \frac{c}{\omega_{pi}}$	m	$10^{-3}$	$10^5$	$10^{-3}$	$10^{-2}$
$L_{\text{inertia}} = \frac{c}{\omega_{pe}}$	m	$10^{-4}$	$10^4$	$10^{-1}$	$10^{-8}$
$S$	1	$10^3$	$10^{14}$	$10^{14}$	$10^{13}$

**Table 2.1:** Typical physical parameters and characteristic Ohm's law length scales for several reconnection regimes. Laboratory values apply to TS-3, MRX, and SSX (see later sections). In the bottom row,  $S$  denotes the Lundquist number (see Section 2.3.2.) Adapted from Priest and Forbes [45].

Similarly, for the pressure term  $(1/ne)\nabla p_e$  we introduce the characteristic temperature  $T_0$  and obtain:

$$u_0 B_0 \sim \frac{n_0 k T_0}{n_0 e L_{\text{pressure}}} \Rightarrow L_{\text{pressure}} \sim \frac{k T_0}{u_0 B_0 e} \sim \frac{k T_0}{(B_0 \sqrt{\rho_0 \mu_0}) B_0 e} \sim \frac{2\mu_0 k T_0}{B_0^2} \sqrt{\frac{m_i}{\mu_0 n_0 e^2}} = \beta \frac{c}{\omega_{pi}} \quad (2.45)$$

$\beta$  is the thermal to magnetic pressure ratio discussed earlier. We have made the assumption here that the  $\mathbf{B}$  gradient occurs over roughly the same distance as the  $p_e$  gradient, and allowed the 2 to be inserted since it does not greatly affect the order of magnitude. Note that since  $\beta$  is typically a bit less than one, the pressure term will typically be slightly less relevant than the Hall term.

Lastly we consider the  $(m_e/ne^2)\partial\mathbf{J}/\partial t$  term. Its existence is related to the fact that electrons have non-zero inertia (as opposed to MHD's assumption of negligible electron mass). This connection is evidenced by the  $m_e$  in the expression and can be seen in the generalized Ohm's law derivation. To approximate  $\partial/\partial t$  here we take it to be on the order of  $u_0/L$ :

$$u_0 B_0 \sim \frac{m_e}{ne^2} \frac{u_0}{L_{\text{inertia}}} \frac{B_0}{\mu_0 L_{\text{inertia}}} \Rightarrow L_{\text{inertia}} \sim \sqrt{\frac{m_e}{\mu_0 ne^2}} \quad (2.46)$$

This expression, like  $L_{\text{Hall}}$ , turns up in other contexts in plasma physics, so it too has a name already: the electron inertial length. It is customary in the field of reconnection to denote this length by  $c/\omega_{pe}$ .

Table 2.1 shows the order of magnitude for each of these lengths for several contexts in which reconnection is known to occur. The term whose characteristic length is the greatest should be the dominant term. Since the Hall term has the greatest magnitude in all environments except for the solar interior, we might be tempted to conclude that it is generally the important term for reconnection. However, our order-of-magnitude estimation here cannot be taken without a grain of salt;  $\mathbf{B}$  tends to zero in the center of the reconnection region, so its importance is probably overestimated by this procedure. Also, it should be remembered that our argument here completely ignored the *direction* of each Ohm's law term, which might be of importance.

### 2.3.2 2D Reconnection in Resistive MHD

Suppose we take the equations of ideal MHD and add the resistivity term to the Ohm's law equation:

$$\mathbf{E} + \mathbf{U} \times \mathbf{B} = \eta \mathbf{J} \quad (2.47)$$

The resulting model is known as “Resistive MHD.” Quite surprisingly, most analytical treatments of reconnection focus on resistive MHD, not on versions of MHD in which other non-ideal terms have been included. This choice is hard to understand, since  $\eta\mathbf{J}$  is only the second largest term in the solar interior, and in the remaining cases in Table 2.1 it is the *least* important term (by 13 orders of magnitude in the magnetosphere!). However, theoreticians have focused on this term for several reasons. First, it is the easiest to understand of the non-ideal effects; there is a clear connection between resistivity and *heating*, one of the known by-products of reconnection. If magnetic energy is to be transformed into other forms of energy, “Ohmic dissipation” in a plasma can convert it into heat for the same reason that resistors grow warm in electrical circuits: currents cause energetic collisions between the current-carrying particles, and previously free energy is converted into heat. It is not nearly as clear that the addition of any of the other terms to Ohm’s law would result in the necessary dissipation of energy. Also, there are several reasons to suspect that the effective values for resistivity are much higher than the values used in the table above. First, the Spitzer formula we used to estimate the resistivity above does not take into account certain types of scattering that occur not by the conventional method of Coulomb collisions but rather by resonant interactions between the particles and waves. Secondly, a related study of *turbulence* in liquids suggests that the  $\eta\mathbf{J}$  term can be greatly magnified by an “energy cascade” to small scale lengths, which we will discuss later. Some researchers believe these “anomalous resistivity” processes can boost  $\eta$  enough to make resistivity the dominant non-ideal effect. Thus, perhaps the resistivity term is the one responsible for reconnection in some cases even if our order-of-magnitude estimates suggest otherwise. In this section, we summarize some of the results that have been obtained for reconnection in resistive MHD.

## The Sweet-Parker Model

Suppose resistivity is the only non-ideal effect in a plasma. Let us impose some boundary conditions on a region of space characteristic of reconnection situations and investigate what follows from the resistive MHD equations. What will result will be a prediction for the flow speeds and for the width of the reconnection region. This model was first described by Sweet and Parker [42] almost 50 years ago. Our derivation here follows the discussion of Brown [7] and Kornack [29].

Figure 2.8 illustrates our scenario. The  $\mathbf{B}$  field is antiparallel on two long edges, forming a large gradient. We make a simplifying assumption that none of the quantities change as you move in the third dimension. Recall that from our definition in the Introduction, this makes our model “2D.” The two masses of plasma coalesce at some speed  $u_{in}$ . You might imagine that the simplest reconnection model would consider *perfectly straight* incoming fields that extended to infinity (i.e., the box in Figure 2.8 would be infinitely wide.) However, then there would be nowhere for the incoming fluid to go! Instead, we allow the incoming fields to have some very small curvature - small enough that the fields are approximately in the  $\pm\hat{x}$ -direction, but enough that only a finite length of the two field bundles makes contact. By convention, this length of interaction is denoted by  $2L$ . We also define  $2\delta$  to be the length over which we move from one ideal field bundle, through the non-ideal interaction region, and into the other ideal bundle. Our earlier qualitative statement that the curvature was “small” can now be more precisely restated as the condition that  $\delta/L \ll 1$ .

We must also make a simplification that the fluid is incompressible. If this assumption can be believed, there are several results that follow. First, conservation of mass implies that

$$u_{in}L = u_{out}\delta \quad (2.48)$$

Since  $L \gg \delta$ , then  $u_{out} \gg u_{in}$ .

Secondly, we can write an expression for the outflow speed using conservation of energy. The incoming fluid has some kinetic energy density due to its motion, some magnetic energy density due to the field there, and some thermal energy density. The outgoing fluid also has kinetic energy, but much more since  $u_{out} \gg u_{in}$ . Also, there is virtually no magnetic energy density in the outflow. While the temperature of the outgoing fluid is probably higher than in the incoming fluid, we assume that the difference in thermal energy is small enough that the difference is negligible compared with the other energy differences. Since the fluid is incompressible, conservation of *energy* will imply

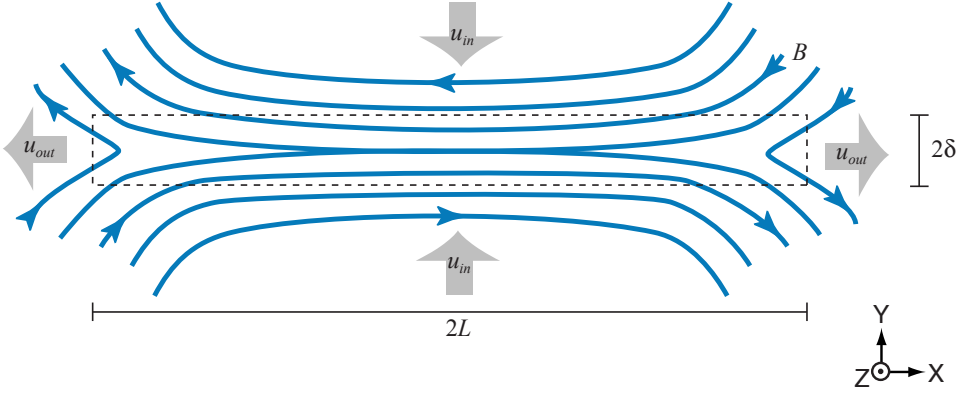


**Figure 2.8:** The canonical 2D Sweet-Parker reconnection configuration. Plasma flows into the reconnection region (dashed box) from above and below, and is rapidly ejected. Local physics somehow determines  $\delta$ ,  $u_{in}$ , and  $u_{out}$  from  $B$  and  $L$ .

conservation of *energy density*. Thus, we can write down the following:

$$\frac{1}{2}\rho u_{in}^2 + \frac{B_{in}^2}{2\mu_0} = \frac{1}{2}\rho u_{out}^2 + \frac{B_{out}^2}{2\mu_0} \quad (2.49)$$

$$\frac{B_{in}^2}{2\mu_0} \approx \frac{1}{2}\rho u_{out}^2 \quad (2.50)$$

so, dropping the subscript on  $B_{in}$  (since we will no longer consider the much smaller  $\mathbf{B}_{out}$ ):

$$u_{out} = \frac{B}{\sqrt{\rho\mu_0}} \quad (2.51)$$

This happens to be the same velocity discussed in section 2.1.1, the *Alfvén speed*  $u_{Alf}$ . We will continue to use this name for the speed in this reconnection context.

Now let us begin a new thread of argument. Consider Ohm's law outside the reconnection region. Spatial variation in  $B$  is very small there, so  $\eta\mathbf{J} = \eta\nabla \times \mathbf{B} = 0$  and we find:

$$\begin{aligned} E_x &= 0 \\ E_y &= 0 \\ E_z - u_{in}B_x &= 0 \end{aligned} \quad (2.52)$$

so  $\mathbf{E} = u_{in}B_x\hat{\mathbf{z}}$ . Could  $\mathbf{E}$  be something different inside the reconnection region? Since  $u$  is small in the region then  $\mathbf{E} = \eta\mathbf{J}$  there.  $\mathbf{E}$  cannot have a  $y$ -component there, for  $E_y$  would have to change signs across the layer by symmetry, and the resulting  $\hat{\mathbf{y}}$ -directed current would result in accumulation of charge, disallowed by our steady-state assumption. What about the  $x$  and  $z$  components of  $\mathbf{E}$ ? Since we are assuming the problem to be constant in time,  $\frac{\partial \mathbf{B}}{\partial t} = 0$ . If we apply Faraday's law to a square loop of side length  $\sim L$  in the  $xy$  plane and whose top edge is in the reconnection region, we find  $E_x = 0$ . If we again apply the law to a similar loop in the  $yz$  plane we find that  $E_z$  inside the reconnection region is the same as  $E_z$  far from the region. Thus,  $\mathbf{E}$  is the same everywhere. Combining our knowledge of  $\mathbf{E}$  in the region with Ohm's law, we find that there is a  $\hat{\mathbf{z}}$ -directed current there:

$$\mathbf{J} = \frac{1}{\eta}u_{in}B_x\hat{\mathbf{z}} \quad (2.53)$$

Now, one last line of reasoning. Consider an Ampèrean loop around the reconnection region (following the dotted line in Figure 2.8). Integrating  $\mathbf{B} \cdot d\mathbf{l}$  around it we obtain  $4LB_x$ , since we can neglect the very short lengths in the  $\hat{\mathbf{y}}$  direction. Ampère's law says there must be a current  $I = \Phi/\mu_0$  through the loop. However, we know what the current density is, and  $I = 4\delta LJ_z$ . Thus,

$$B_x = \mu_0 J_z \delta \quad (2.54)$$

Eliminating  $\mathbf{J}$  from Equations 2.53 and 2.54 gives:

$$\delta\mu_0 u_{in} = \eta \quad (2.55)$$

We have arrived at a set of three equations (2.48, 2.48, and 2.48) relating the fundamental properties of our system ( $B$ ,  $u_{in}$ ,  $u_{out}$ ,  $L$ ,  $\delta$ ,  $\eta$ , and  $\rho$ ). Rearranging these three equations slightly, then for a situation of reconnection with known  $B$ ,  $L$ ,  $\eta$ , and  $\rho$  the Sweet-Parker model makes a testable prediction for the values of  $\delta$ ,  $u_{in}$ , and  $u_{out}$ :

$$u_{out} = u_{Alf} = \frac{B}{\sqrt{\rho\mu_0}} \quad (2.56)$$

$$u_{in} = \sqrt{\frac{B\eta}{L\sqrt{\rho\mu_0^3}}} \quad (2.57)$$

$$\delta = \sqrt{\frac{L\eta}{B}\sqrt{\frac{\rho}{\mu_0}}} \quad (2.58)$$

## The Dimensionless Reconnection Rate

We can reformulate the results of the Sweet-Parker model and compare them to the results of other reconnection models in an elegant way using dimensionless quantities. Our principle point of comparison will be a value which is something like a *reconnection rate* – how rapidly the magnetic field is annihilated. Using the notation from Figure 2.8,  $u_{in}$  is one quantification of this rate, so we can obtain a dimensionless rate by normalizing by the Alfvén speed:

$$M \equiv \left( \begin{array}{c} \text{Reconnection} \\ \text{Rate} \end{array} \right) \equiv \frac{u_{in}}{u_{Alf}} \quad (2.59)$$

Equations 2.56-2.58 can be combined to yield:

$$M = \sqrt{\frac{\eta}{u_{Alf}\mu_0 L}} \quad (2.60)$$

Let us take a momentary digression to give some meaning to this quantity under the square root above.

When is it a good approximation to say that resistive effects are negligible in a plasma? One measure of the applicability of the frozen-in flux condition is a dimensionless value called the “magnetic Reynolds number”, which tells you if any significant diffusion *would* occur if you *did* allow for non-zero resistivity. Let us fix a point in space and consider what can cause the magnetic field to change with time at that point. Both convection of  $\mathbf{B}$  with the motion of the plasma and also diffusion of  $\mathbf{B}$  through the plasma can contribute. If we plug the resistive Ohm’s law into Faraday’s law and assume that  $\eta$  is roughly constant in space we get

$$\frac{\partial \mathbf{B}}{\partial t} = -\nabla \times \mathbf{E} \approx \nabla \times (\mathbf{u} \times \mathbf{B}) - \nabla \times (\eta \mathbf{J}) \approx \nabla \times (\mathbf{u} \times \mathbf{B}) - \eta(\nabla \times \mathbf{J}) \quad (2.61)$$

Using Ampère’s law, we can substitute for  $\mathbf{J}$  in Equation 2.61.

$$\frac{\partial \mathbf{B}}{\partial t} = \nabla \times (\mathbf{u} \times \mathbf{B}) + \frac{\eta}{\mu_0} \nabla \times \nabla \times \mathbf{B} \quad (2.62)$$

$$= \nabla \times (\mathbf{u} \times \mathbf{B}) + \frac{\eta}{\mu_0} \nabla^2 \mathbf{B} \quad (2.63)$$

where we have used a vector identity to get the last equation. This expression, known as the magnetic induction equation, expresses the rate of change of  $\mathbf{B}$  as a sum of convective and diffusive parts, exactly as we were expecting. To see this, observe that if we set  $\eta = 0$  we obtain Equation 2.39, the key result of ideal MHD that led to the frozen-in flux condition. Consequently, it is the former term that leads to convection of  $\mathbf{B}$  with the fluid. The second term

Author(s)	Normalized Reconnection Rate ( $M$ )
Dere 1996	0.001-0.1
Tsuneta 1996	0.07
Tsuneta <i>et al.</i> 1997	0.06
Ohyama and Shibata 1997	0.0002-0.13
Ohyama and Shibata 1998	0.02
Forbes and Lin 2000	0.03
Yokoyama <i>et al.</i> 2001	0.001-0.03
Isobe <i>et al.</i> 2002	0.001-0.01

**Table 2.2:** Calculation of normalized reconnection rates ( $M$ ) by several groups for various events in the solar corona. These values are much faster than the Sweet-Parker prediction of  $M = 10^{-7}$ . Values are from Isobe *et al* [26].

is proportional to  $\eta$  and thus represents the deviation from the frozen-in condition due to collisions. The magnetic Reynolds number is an estimate of the ratio of the magnitudes between these convection and diffusion terms:

$$\frac{|\nabla \times (\mathbf{u} \times \mathbf{B})|}{|\eta/\mu_0 \nabla^2 \mathbf{J}|} \sim \frac{(1/l)uB}{(\eta/mu_0)(1/l)^2 B} = \frac{\mu_0 u l}{\eta} \equiv R_M \quad (2.64)$$

Here we have “approximated”  $\nabla$  with  $1/l$ , where  $l$  is some characteristic length over which the quantities change. If  $R_M \gg 1$ , then the resistive part of the induction equation – and consequently any resistive effects in MHD – are negligible, and ideal MHD is as good an approximation as *resistive* MHD.

Lastly, we plug in for  $u$  and  $l$  the typical velocity and length scales, which are  $u_{Alf}$  and  $L$  respectively. Another dimensionless number that comes up in plasma physics, the *Lundquist number*, is defined to be  $R_M$  with  $u$  set to  $u_{Alf}$ , and so it is a bit more precise to say now that the ratio we have computed is this Lundquist number:

$$S \equiv \frac{\mu_0 u_{Alf} L}{\eta} \quad (2.65)$$

Returning at last to our discussion of the Sweet-Parker model, we see that we can write the reconnection rate elegantly as:

$$M_{S-P} = \frac{1}{\sqrt{S}} \quad (2.66)$$

Other reconnection theories often predict the reconnection rate as some other function of  $S$ . Table 2.1 shows typical values of  $S$ . As you might imagine from our earlier discussion of how negligible resistive effects are,  $S$  is usually much larger than 1.

## Our Simplest Model is Too Slow!

How does the Sweet-Parker model’s prediction of the reconnection rate compare with data? Table 2.2 shows values of  $M$  calculated by various groups for flares in the solar corona. Recall from Table 2.1 that a typical Lundquist number  $S$  for this region is  $10^{14}$ . Thus, the Sweet-Parker prediction is  $1/\sqrt{10^{14}} = 10^{-7}$ , many orders of magnitude too slow!

Reconnection rates have been measured not only in the solar corona but also in the Earth’s magnetosphere, tokamak reconnection-related instabilities, and other laboratory reconnection experiments like SSX. Curiously, across these wide ranges of parameters the rate  $M$  is almost always observed to be in the range  $0.01 - 0.1$ ! It is perhaps not too surprising that these observed rates are *so* much faster than the Sweet-Parker predictions, for as we saw in Table 2.1 the resistivity term which this model depends on is usually insignificant compared to other non-ideal terms. However, we present next several more advanced models that are able to achieve rates as fast as  $M = 0.1$  while still relying only on resistivity.

### 2.3.3 Could Shocks Be Involved in Reconnection?

Another class of 2D resistive reconnection theories exist which are able to predict a faster reconnection rate than the Sweet-Parker model, and which do not even need to invoke *anomalous* resistivity. However, these theories are not the end of the story on reconnection, for they predict the existence of *shocks*, a feature which has never been experimentally observed.

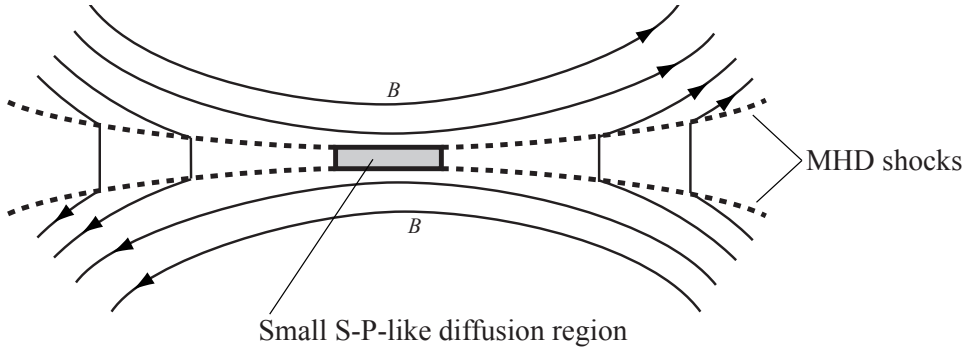


**Figure 2.9:** Petschek’s model of reconnection. A small Sweet-Parker region exists in the center, but most of the magnetic flux is annihilated by the four standing shocks.

The most-cited example from this class of theories is the original one developed by Petschek in 1963 [44]. In Petschek’s model, a small Sweet-Parker region exists in the center of a larger reconnection region. Only a small amount of the incoming magnetic flux is annihilated in the Sweet-Parker region. Rather, most of it is converted into fluid kinetic energy by four *magnetoacoustic shock waves* that develop, as shown in Figure 2.9. We saw in the plasma physics introduction (Section 2.1.1) that this kind of wave is associated with discontinuities in the magnetic field and fluid velocity. In essence, the shocks are doing most of the reconnecting, and resistivity is only doing a small part. Since we saw that resistivity is an insignificant phenomenon in most reconnection contexts, we should expect that the Petschek model would predict a faster reconnection rate than Sweet-Parker. In fact, the Petschek model allows for a continuum of reconnection rates, the maximum of which is approximately

$$M_{\text{Petschek}} \approx \frac{\pi}{8 \ln S} \quad (2.67)$$

For the magnetosphere and corona this works out to around the correct value of 0.1! However, there is a major problem with the Petschek theory: no one has ever observed magnetoacoustic shocks around a reconnection zone! The Petschek model, while tempting, thus cannot be easily accepted.

### 2.3.4 Turbulence and Particle Acceleration

It was mentioned earlier that *turbulence* is one of the reasons that resistivity might play a larger role than then Lundquist number suggests. This lesson can be learned through a remarkable connection between MHD and classical fluid mechanics. Incompressible fluids – such as water flowing slower than the water sound speed – are described by the *incompressible Navier-Stokes equation*. This equation can take several forms, one of which is

$$\frac{\partial \omega}{\partial t} = \nabla \times (\mathbf{u} \times \omega) + \nu \nabla^2 \omega \quad (2.68)$$

where  $\nu$  is the *viscosity* and  $\omega \equiv \nabla \times \mathbf{u}$  is the *vorticity*. But wait – this is just the magnetic induction equation (2.63) we saw a few pages earlier, with the substitutions  $\mathbf{B} \rightarrow \omega, \eta/\mu_0 \rightarrow \nu$ ! Since  $\omega$ , like  $\mathbf{B}$ , is divergence-free, any results we find for incompressible fluids can be related to resistive MHD by the reverse substitutions (although not exactly, since  $\omega$  and  $\mathbf{u}$  are related in a way that  $\mathbf{B}$  and  $\mathbf{u}$  are not). Also, just as the ratio of the convection to diffusion terms in the induction equation gave us the magnetic Reynolds number, the ratio of the convection to diffusion terms in

the Navier-Stokes equation defines the (original) *Reynolds number*, which of course really came before its magnetic cousin:

$$R \equiv \frac{u_0 L_o}{\nu} \quad (2.69)$$

where  $u_0$  and  $L_o$  are a typical speed and length respectively.  $R$  is often quite large for human-scale situations – for a 1.0 m hot tub with 0.1 m/s water we get  $R = 10^5$ . Since  $R$  is so large (i.e.,  $\nu$  is so small) we might be tempted to drop the right-most term in the Navier-Stokes equation. However, a simple experiment in your bathtub (or a precise simulation on a supercomputer) can show that almost any initial flow pattern rapidly degenerates into a chaotic swarm of vortices *at all scales*, which is precisely what we mean when we say “turbulence”. In particular, the nonlinear  $\nabla \times (\mathbf{u} \times \omega)$  term in the Navier-Stokes equation seems capable of driving an “energy cascade” to smaller and smaller scales [18]. Since the viscosity term  $\nu \nabla^2 \omega$  involves a *second derivative*, eventually these scales will become so small that the viscosity term dominates!  $\nu$  may be small, but  $\nabla$  “grows larger” until the term becomes relevant. It is certainly our everyday experience that the fluid motion in a bathtub or sink rapidly dies out, even though these systems have huge Reynolds numbers – viscous dissipation here is clearly non-negligible.

There are profound implications for non-ideal MHD. Since the equations look the same, we expect the solutions to look the same. Even though  $R_M$  and the closely related  $S$  can be  $10^{14}$ , dissipation (here due to resistivity rather than viscosity) might be non-negligible. Energy may get transferred to smaller and smaller scales until resistivity dominates other non-ideal effects.

Turbulence is actually one of a number of processes that can cause the effective resistivity to be much larger than the Spitzer value. Certain interactions between particles and waves are other such processes. Any situation in which  $\eta_{\text{effective}} > \eta_{\text{Spitzer}}$  is said to have *anomalous resistivity*.

One of the few ways to theoretically investigate the complicated effects of turbulence on a plasma’s dynamics is to do a computer simulation. A model by Matthaeus *et al.* has produced some interesting results[38]. The code simulates incompressible resistive MHD (the same set of equations used in the Sweet-Parker model) but unlike Sweet-Parker it allows the fine turbulent structure of the flow pattern to be resolved. The model is also two-dimensional. Turbulence is introduced by modifying the incoming fields with a small random perturbation, and the computer evolves the system in time. Remarkably, the resulting turbulence produces an anomalous resistivity that increases the normalized reconnection rate to around the experimentally observed value of 0.1 [38].

Also, while the Sweet-Parker model assumed a simple X-point at the reconnection layer, the Matthaeus model exhibits a layer of both X- and O-points. Just as it would be hard to theoretically predict the development of vortices in a bathtub from looking at the Navier-Stokes equation, it would be hard to predict the development of these O-points by looking only at the resistive MHD equations.

A useful consequence of simulating reconnection on a computer is that the trajectories of individual particles can be traced as they move through the system, with a surprising and promising result. Several thousand particles were “placed” in the above model at random locations. Their trajectories were followed as they were acted upon by the Lorentz  $\mathbf{E} + \mathbf{v} \times \mathbf{B}$  force, with the fields defined by the computational model discussed above. Figure 2.10 shows the final energies of the particles. Most did not gain much energy, but a few were accelerated to hundreds of times their original velocity. These highly accelerated particles had become trapped inside the magnetic islands (O-points) in the center of the reconnection layer. The fieldlines of O-points - unlike those of X-points - stay inside the reconnection region. Thus, a particle which begins to orbit such a fieldline will stay in the layer where there is a large electric field and continue to increase in energy, unlike those particles orbiting X-point fieldlines that are carried away from the  $\mathbf{E}$  field by the outflow. This discovery of a particle acceleration mechanism is quite noteworthy, for as we saw in earlier sections, reconnection has been cited as a mechanism for accelerating particles in some astronomical settings.

### 2.3.5 Collisionless Reconnection

Even though turbulence might magnify the effect of resistivity, it initially seemed like resistivity was not nearly the most important non-ideal effect. Not surprisingly, then, other researchers have looked at non-resistive non-ideal effects,

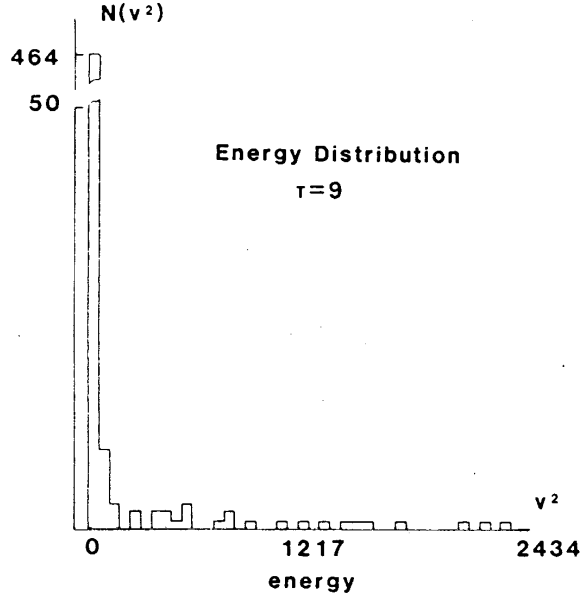


**Figure 2.10:** A histogram of particle energies from the Matthaeus turbulent reconnection simulation. Most particles have close to their original energy, but the velocities of a few have increased several thousand fold. Figure from Matthaeus *et al.* [37].

and a few very promising results have been obtained. Since classical resistivity is the result of collisions, the term “collisionless reconnection” has been used to describe this regime in which  $\eta\mathbf{J}$  is ignored.

One significant change that occurs when we move to collisionless reconnection is that we make the frozen-in flux conditions slightly more precise: rather than moving with the fluid velocity  $\mathbf{u}$ , the fieldlines move with the *electron fluid* velocity  $\mathbf{u}_e$ . To see this fact, consider the Ohm’s law with the Hall term added:

$$\mathbf{E} + \mathbf{u} \times \mathbf{B} = \frac{1}{ne} \mathbf{J} \times \mathbf{B} \quad (2.70)$$

Bringing the Hall term to the left,

$$\mathbf{E} + \left( \mathbf{u} - \frac{1}{ne} \mathbf{J} \right) \times \mathbf{B} = 0 \quad (2.71)$$

Since the current density  $\mathbf{J}$  for our fully ionized hydrogen plasma<sup>8</sup> is  $\mathbf{J} = ne(\mathbf{u} - \mathbf{u}_e)$ , then the term in parentheses above is just the electron velocity  $\mathbf{u}_e$ . Thus,

$$\mathbf{E} + \mathbf{u}_e \times \mathbf{B} = 0 \quad (2.72)$$

From the *ideal* Ohm’s law we found that fieldlines move with velocity  $\mathbf{u}$ , so if we rework the derivation with this modified Ohm’s law we find that fieldlines more precisely move with velocity  $\mathbf{u}_e$ .

This fact has ramifications for the structure of the reconnection region. Ions, having more inertia than electrons, take a greater distance to turn a corner. Consequently, when the inflowing fluid in a reconnection region turns to be expelled, the ions turn in a larger arc than the electrons do (Figure 2.11). Since as we saw above it is the electron fluid to which the  $B$  field is frozen, then the ions “de-couple” from the field due to the Hall term in an “ion diffusion region” surrounding the x-point. As we discussed in Section 2.3.1, this region has width  $c/\omega_{pi}$ .

Of course, the electrons too must de-couple from the field for reconnection to occur. This decoupling happens in a small layer inside the ion diffusion region, since the electrons are less massive than the ions. One of the other non-ideal effects, such as the “electron inertia” ( $m_e/e^2n)\partial\mathbf{J}/\partial t$  term, would be responsible in this “electron diffusion” region.

<sup>8</sup>Since the ions are much heavier than the electrons, the plasma’s overall fluid velocity is taken to be the ion velocity, and  $\mathbf{J}$  is just a relative velocity difference between ions and electrons.

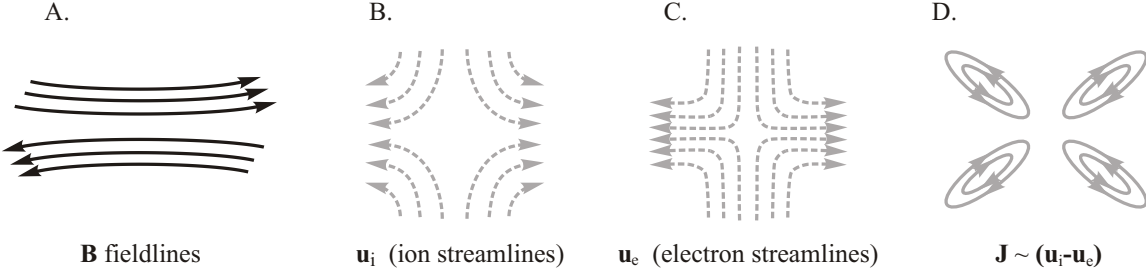


**Figure 2.11:** Velocities of the electrons and ions in a reconnection region when the Hall correction is considered. B-C. Since the electrons are less massive than the ions, they turn the corner over a smaller radius. D. The difference in velocities leads to looping currents that create the out-of-plane magnetic quadrupole.

Thus, both the Hall term and at least one more non-ideal term need to be included in a collisionless reconnection model, making analytical results hard to come by. We must resort to computational models in this case. A particularly noteworthy body of work has come from a series of such models from Shay, Drake, Rogers, Denton, Bhattacharjee, and Ma [52, 51, 53, 54, 2]. These groups have used several categories of models:

- A system can be evolved using the MHD equations with a more complete version of Ohm's law
- The electrons can be treated as an MHD-like fluid, while the ions are treated like particles (obeying the Lorentz force). This arrangement is known as a "hybrid" model.
- Both the electrons and ions can be treated as particles

As the models get more precise, they also require more computational power. The group has also tested their models in various parameter regimes to vary which terms in Ohm's law are the most relevant. The significant finding is that across a wide range of parameters and across different models, the observed reconnection rate is *always* about  $M \approx 0.1$ ! Recall that  $M \approx 0.1$  in almost all observations and experiments of reconnection. The reason for this stability is that the reconnection rate is determined solely by the ion dynamics – the effect with the largest associated length – and so the smaller-scale non-ideality that decouples the electrons in the electron diffusion region does not change  $M$ .

Also, the thickness of the region over which  $\mathbf{B}$  reverses direction in the simulations is on the order of twice the ion-inertial length  $c/\omega_{pi}$ . You can think of the ion-inertial length as the distance it takes the ions to turn the corner in the ion-diffusion region, so it makes sense that twice this distance should be the total layer thickness.

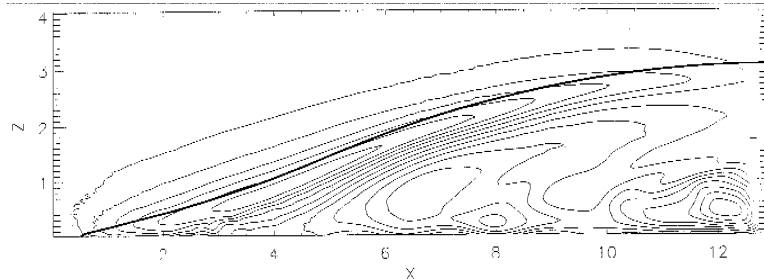


**Figure 2.12:** Contours of the out-of-plane  $B$  component, which are streamlines of the in-plane  $J$ . Only the top-right quarter of the reconnection region is shown. Distance units are normalized by the ion-inertial length  $c/\omega_{pi}$ . The dark line is the "separatrix," topologically dividing the  $B$  fieldlines. From a simulation by Shay *et al* [54].

One particular feature observed in these models is of particular note, as it will be relevant to SSX experiments in a later section. Observe in Figure 2.11 that in the ion diffusion region there is a significant velocity difference between

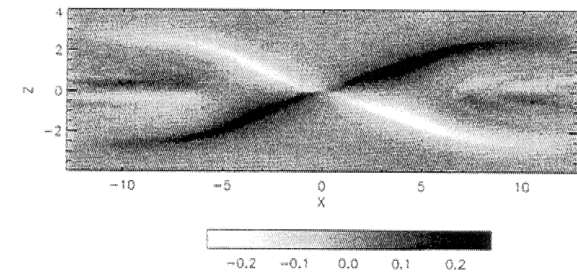


**Figure 2.13:** Out-of-plane  $B$  component for a hybrid simulation by Shay *et al* [54]. Black means  $B$  points into the paper and white means out of the paper. Distance units are normalized by the ion-inertial length  $c/\omega_{pi}$ . Figure from [54]

the electrons and ions. Consequently, there will be an in-plane current  $\mathbf{J} \approx (\mathbf{u}_i - \mathbf{u}_e)/ne$ , unlike in the Sweet-Parker model. A bit of vector subtraction can show that this in-plane current makes loops in the four corners of our picture. Figure 2.12 shows these current streamlines for the top-right quarter for one of the models by Shay *et al* [54]. By Ampère's law, these currents cause an out-of-plane  $B$ -field component. Figure 2.13 shows this component in another Shay *et al* model. This structure is known as a "magnetic quadrupole," and it is one of several important testable predictions to come out of the group's models. Satellite observations in the Earth's magnetosphere may have observed this quadrupole signature[39], but it is hard to be certain since these satellites can only record data along a 1D path.<sup>9</sup>

### 2.3.6 Three-Dimensional Reconnection

Many papers ([34, 47, 46]) have been published in the past 15 years on "3D magnetic reconnection," but these papers refer to something different from what is investigated in the SSX laboratory. We will see that the geometry of the SSX magnetic field configuration is largely 2D, much like Figure 1.1 extended neatly into the third dimension, with only a bit of gentle curving and a small out-of-plane component added to make the situation truly 3D. These recent papers, however, have focused more on *topologically unique* magnetic field configurations – configurations that depart from Figure 1.1 much more than the field of SSX does. This theoretical work is more about finding geometrically interesting solutions to the resistive MHD equations – taking for granted that resistivity is the cause of reconnection – rather than exploring which non-ideal effects might truly be the mechanism. Although this work does not bear directly on the experiments performed in SSX, we give here a summary of some popular concepts in 3D reconnection theory just to give a taste for the sort of work that has been done.

### 3D Nulls

"Null points," locations where  $\mathbf{B} = 0$ , are interesting for several reasons. At these points, the non-ideal terms in Ohm's law become more significant since the  $\mathbf{u} \times \mathbf{B}$  term is zero. Also, it turns out that the fieldlines connecting null points – known as *separators*, tend to be locations of large velocity gradients – and hence places where non-ideal effects become significant [34]. So what does  $\mathbf{B}$  look like near these null points? The condition  $\nabla \cdot \mathbf{B}$  restricts the possibilities to those illustrated in Figure 2.14. The field is directed into the null along a line (the "spine") and outward along a plane (the "fan"), or vice-versa (in the fan and out the spine). Fieldlines in the fan may spiral, and the fan may lie at any angle to the spine.

---

<sup>9</sup>By 2006 NASA hopes to launch the Magnetospheric Multiscale Mission, an array of five satellites traveling together which will be able to better understand the 3D spatial variation of the magnetospheric field[14]. Observations from this project may provide more conclusive evidence for the quadrupole.

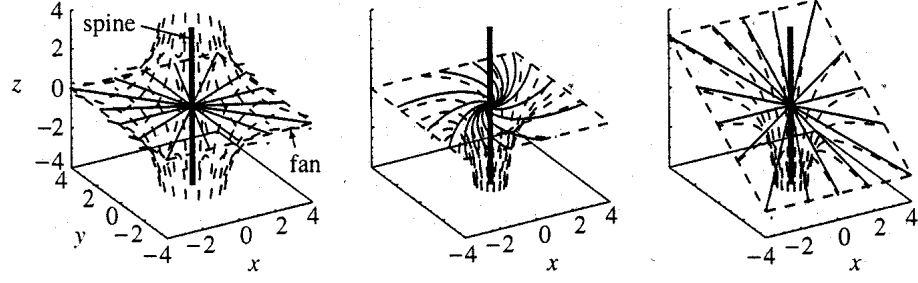


**Figure 2.14:** Possible configurations of  $\mathbf{B}$  at a 3D null, showing the spines and fans. The field points inward along one, and outward along the other. Figure from Lau and Finn[34].

## Reconnection Near Nulls

We mentioned above that reconnection tends to happen near null points, and we can begin to see why with the following simple example. Consider the 3D null described by

$$\mathbf{B} = (x, y, -2z) \quad (2.73)$$

This field is shown in Figure 2.15 in a cylinder coaxial with the spine. Priest and Titov [47] noted the following interesting fact about this configuration. Suppose the plasma moves to the left above the fan and to the right below the fan, as shown in the figure, while  $\mathbf{B}$  is constant. If the field is frozen to the plasma, the flow will have to be very fast near the null to keep  $\mathbf{B}$  constant. In fact, there will be a discontinuity in  $\mathbf{u}$  along the fan: it is arbitrarily fast to the left at  $z$  just above 0, and arbitrarily fast to the right at  $z$  just below 0. At this infinitely large gradient in  $\mathbf{u}$ , non-ideal effects will become significant. The conclusion is that reconnection can occur along fans. A different velocity pattern results in a discontinuous  $\mathbf{u}$  along the spine, so reconnection can occur there as well.

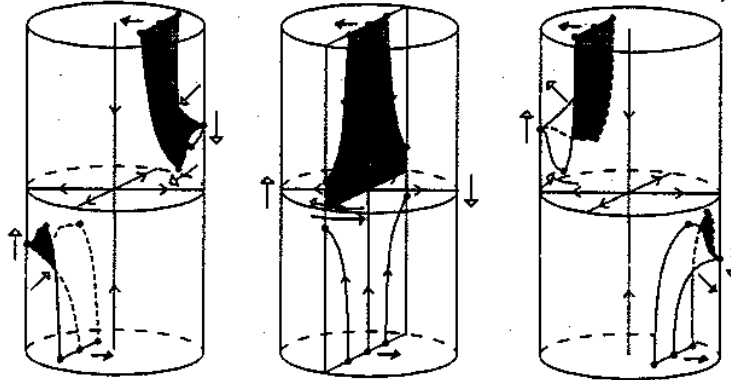


**Figure 2.15:** Fan reconnection. Figure from Priest and Titov[47].

## A Taxonomy of Topologies

Another major direction in 3D reconnection theory has nothing to do with the physics of reconnection at all: the classification of field topologies that can result from various sources or sinks of magnetic flux. While there are no magnetic monopoles, the surface of the sun can be thought of as dotted with various sources and sinks where magnetic loops generated by internal dynamo effects have bubbled through. The literature of 3D reconnection is filled with diagrams like Figure 2.16 depicting the topological possibilities.

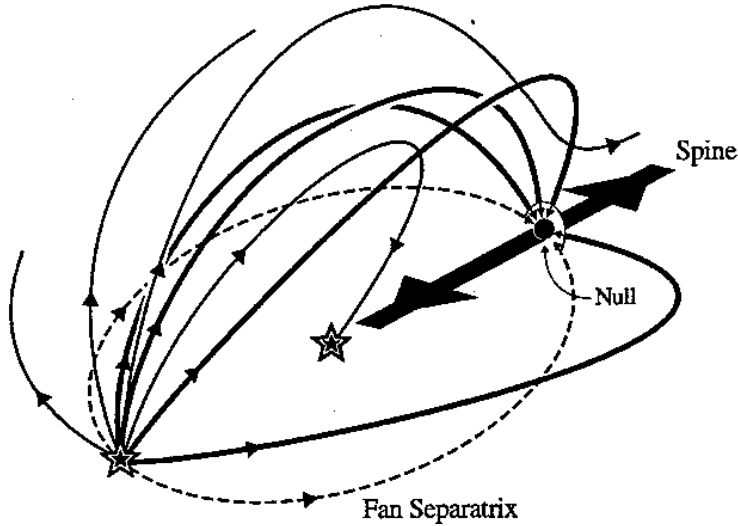


**Figure 2.16:** An illustration of the magnetic topology resulting from a strong source and a weak sink (stars). Figure from Priest and Schrijver[46].

### Sweet-Parker in 3D

One piece of 3D reconnection theory that does pertain to the SSX configuration is an extension of the Sweet-Parker analysis by Priest and Schrijver [46]. Suppose, as in Figure 2.17, that we have two converging masses of plasma, each with a uniform  $\mathbf{B}$  field, and that the angles between the fields of the two masses is  $\theta$ . Also, suppose that the fields are in fact curled away somewhat at the edges (as in our 2D picture, Figure 2.8) so that the effective area of interaction is a *circle* of thickness  $2\delta$  and *diameter*  $2L$ . Assuming (as Sweet and Parker did) incompressible resistive MHD, Priest and Schrijver derive

$$M_{3DS-P} = \frac{1}{\sqrt{S}} \sqrt{2 \sin \frac{\theta}{2}} \quad (2.74)$$

Thus, no reconnection occurs if the fields are aligned, and the maximum reconnection rate occurs when the fields are antialigned (as you would expect). For antialigned fields, the rate is faster than the Sweet-Parker result by  $\sqrt{2}$ , since there is relatively more area over which the plasma can escape in three dimensions.

### 2.3.7 What Remains to Be Done?

The simulations by Shay *et al.* begin to answer many of the questions we originally posed about reconnection. They can predict the reconnection rates observed in nature ( $\sim 0.1$ ) over a wide range of parameters. Electron inertia is implicated as the ultimate cause of reconnection, although the Hall term plays an important role in the surrounding ion diffusion region. The simulations by Matthaeus *et al.* indicate that particle acceleration can occur as well, and suggest that turbulence is important in the acceleration mechanism.

Although we do have these important results, there is work left to be done in the study of reconnection. To what extent do our 2D models apply to the complicated 3D geometries of natural reconnection? Also, a camp still holds, in opposition to Biskamp and Shay *et al.*, that anomalous resistivity is the non-ideality that causes reconnection. The Shay group's models have made testable predictions that should be verified by experimentalists and observationalists. The fact that we have *an* explanation does not mean that it is *the* explanation or at least the complete one. The true test of our understanding of reconnection will be to compare theoretical models to experiments, which allow much finer measurements to be made than the relatively inaccessible solar corona or magnetosphere.

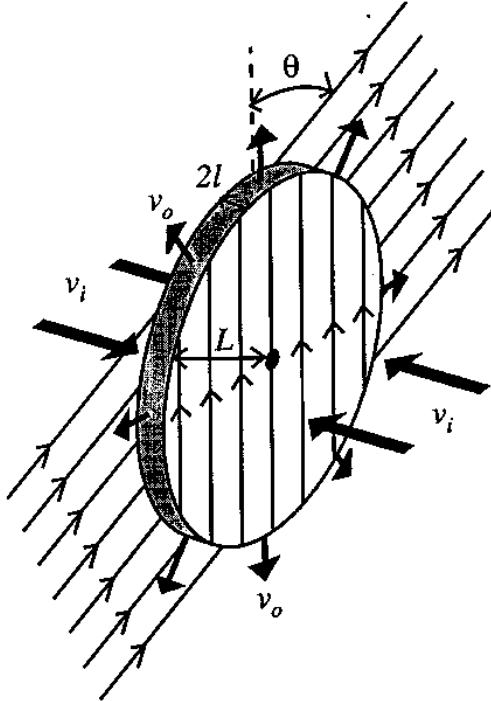


**Figure 2.17:** The configuration for the 3D Sweet-Parker analysis. From Priest and Schrijver[46].

## 2.4 Previous Experiments

Laboratory reconnection experiments have been performed for over 20 years [6]. The pioneering work was done at UCLA through the early 1980s by Stenzel and Gekelman ([21, 57, 56]). More recently, groups at the University of Tokyo ([60, 41, 40]) and at Princeton ([59, 27, 25, 24]) have also studied the phenomenon. As with any field of science, no two experimental setups are identical, and each group has focused their investigation on slightly different types of measurements and parameter regimes.

### 2.4.1 UCLA Experiments

The philosophy behind the UCLA experiment was to amass detailed spatial information about as many quantities as possible ( $\mathbf{B}$ ,  $\mathbf{E}$ ,  $\mathbf{u}$ , etc.) [56, 57, 21]. As we will discuss later, it is quite challenging and expensive to acquire many “channels” of data in a single experiment. In plasma physics, unfortunately, it would be ideal to know all the relevant quantities at many locations. Suppose we wanted to know  $\mathbf{B}$ ,  $\mathbf{E}$ ,  $\mathbf{u}$ ,  $\mathbf{J}$ , and  $T$ :

$$(13 \text{ quantities}) \times (20 \text{ by } 20 \text{ grid of points}) \times (\$1000 \text{ per channel}) = \$5,200,000 \quad (2.75)$$

The UCLA group got around this problem by making their plasma highly reproducible - from one shot to the next there was minimal change in any quantity ( $\delta$  density between shots / density  $< 5\%$ ). They constructed a movable robotic probe that would automatically move to the next location in a grid of points between pulses of the machine (every 2 s). Also, for each grid location, data from 10 to 80 pulses was averaged together to produce a very smooth result. As a consequence, any turbulence or other chaotic feature that varied from one shot to the next was averaged out, but they succeeded in acquiring a detailed picture of their “average” reconnection event.

The UCLA device consisted of a 1.5 m diameter cylinder, 2 m long, containing two 75 cm wide plates running the length of the tube (Figure 2.18.A). A uniform ( $\delta$  density over the volume / density  $< 10\%$ ) plasma was generated

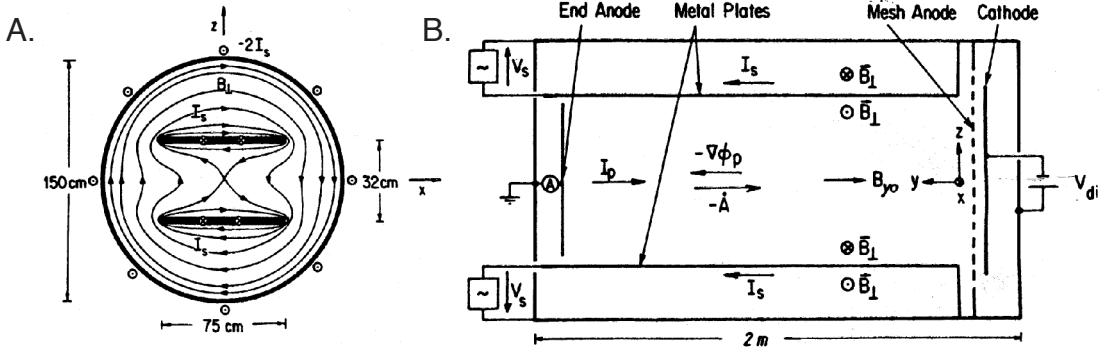


**Figure 2.18:** Stenzel and Gekelman’s reconnection experiment at UCLA. A: Cross section showing vacuum magnetic field. B: Side view showing currents. Figure from [21].

by a large disk cathode at one end of the chamber. The canonical reconnection geometry of the magnetic fields was generated not by flows of pre-magnetized plasma, as it is in astrophysical settings, but rather by a *linearly increasing external current* flowing down the length of the large plates (Figure 2.18.B). In the *absence of plasma*, the field near the axis of the chamber looks like hyperbolas, with an x-shaped separatrix (Figure 2.19.A). However, when plasma is present, it freezes (mostly) to the fieldlines, which are trying to push inwards because the plate current is increasing. As the fluid is frozen to the field, it is pushed inwards (Figure 2.20.A) and forms a double-Y-shaped reconnection geometry (Figure 2.19.B). The large width and length of the plates results in a relatively two-dimensional system; the axial component of the magnetic field is less than 10% of the transverse components. Typical parameters were  $n \sim 10^{12} \text{ cm}^{-3}$ ,  $T_e \sim 4 \text{ eV}$  and  $|\mathbf{B}| \sim 20 \text{ Gauss}$ . For these values, the ion Larmour radius is about the same as the machine size, so it is not considered to be in the MHD regime.

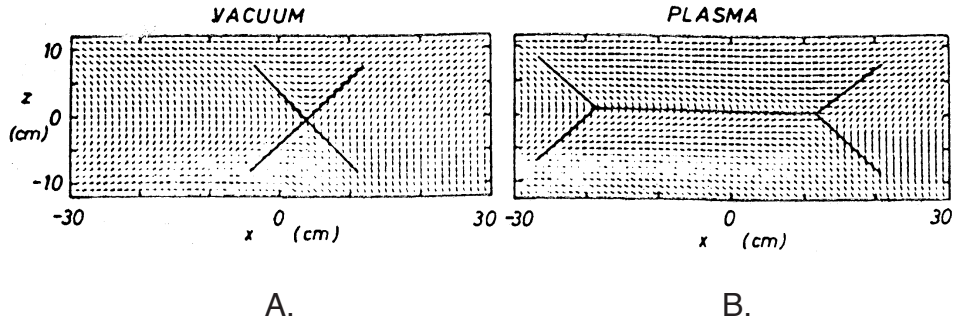


**Figure 2.19:** Transverse magnetic fields in the reconnection region, with the separatrix superimposed. A: In the absence of plasma, an even X-type separatrix forms. B: With plasma, frozen-in plasma resists reconnecting, and the separatrix flattens into a double-Y shape. Figure from [57].

By Ampère’s law, a curling magnetic field indicates a perpendicular current; thus, the double-Y-shaped magnetic field indicates a broad, flat current sheet at its center (Figure 2.20.B). Under certain conditions this current grows so strong that its magnetic field dominates that of the large plates, resulting in “magnetic islands” - closed fieldlines that do not circle either of the plates.

Good measurements were known for every variable in the generalized Ohm’s law except for the resistivity  $\eta$ :

$$\mathbf{E} + \mathbf{u} \times \mathbf{B} = \eta \mathbf{J} + \frac{1}{ne} \mathbf{J} \times \mathbf{B} - \frac{1}{ne} \nabla p_e + \frac{m_e}{ne^2} \frac{\partial \mathbf{J}}{\partial t}$$

Thus, they could solve for  $\eta$ . Stenzel and Gekelman found  $\eta/\eta_{Spitzer} \approx 25$ , demonstrating the presence of significant anomalous resistivity.

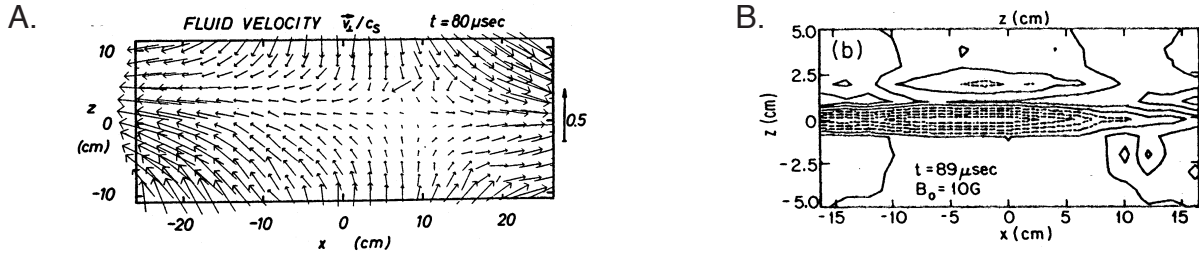


**Figure 2.20:** A: The velocity field of the plasma shows that it freezes to the incoming fieldlines, is forced into the null region, and expelled at nearly the Alfvén speed ( $c_s \approx v_{Alf}$ ). From [21]. B: Contours of axial current density show the central flat current sheet. From [56].

Stenzel and Gekelman's work was quite thorough, but it was not the end of the story. The UCLA experiments were unsurpassed in their detailed spatial maps of so many relevant plasma quantities. However, even in their parameter regime which was optimized for reproducibility, some measurements were found to vary from shot-to-shot by an amount on the order of the average measurement. Although they did perform correlation studies with two probes recording from different points during the same shot, their large maps of *averaged* plasma quantities leave out the shot-to-shot structure. Also, it is rare that nature produces as two-dimensional a reconnection geometry as that created in the UCLA device. Finally, space plasmas fall well into the MHD regime ( $S > 10^{10}$ ), while the UCLA plasma did not. Thus, more work remained to be done.

## 2.4.2 Tokyo Experiments

The first fully MHD-regime reconnection experiments (and also the groundbreaking work in spheromak merging) began at the University of Tokyo in the late 1980s [60]. Figure 2.21 illustrates the experimental setup, the TS-3 device. Coils produced toroidal and poloidal fields before the gas was ionized. After formation, the spheromaks were pushed together by variable magnetic fields that allowed the “collision velocity” to be controlled. Typical parameters for TS-3 were  $n \sim 10^{14} \text{ cm}^{-3}$ ,  $T_e \sim 5 - 15 \text{ eV}$ , and  $|\mathbf{B}| \leq 1 \text{ kG}$ . Consequently,  $\rho_i = 2 - 5 \text{ mm} \ll L$  and  $S \sim 300$ , so the plasma is in the MHD regime. A 2D grid of magnetic probes was used to map out the reconnection region, and Doppler shifts and broadening of ion emission lines were used to determine the ion temperature and drift velocity at various locations.

One effect studied by the Tokyo researchers was an increase in the velocity and temperature of ions in the reconnection region [41]. One would expect that the heating of a plasma could be accounted for by the  $\eta J^2$  power dissipated due to resistivity. However, here the ion temperature grew too large to be explained by this “Ohmic heating”. In fact, from knowledge of the size and magnitude of the reconnection-layer current, of the ion kinetic energy, and of the rate of magnetic field annihilation, the group could trace the flow of energy. Of 230 J lost in  $B^2/2\mu_0$  magnetic energy, 20 J appeared as Ohmic heating, but 180 J appeared as increased ion kinetic energy. Thus, resistivity (the  $\eta \mathbf{J}$  term in Ohm's law) is small compared to the effect of electric and magnetic fields “directly” accelerating the ions.

Another line of investigation on the TS-3 device was the effect of the out-of-reconnection-plane component of  $\mathbf{B}$  on reconnection [40]. The experimenters had separate control over the poloidal and toroidal fields and thus were able to create left handed - left handed spheromak pairs, left handed - right handed spheromak pairs, etc. The case of two equal-handedness spheromaks is known as co-helicity, while the case of two opposite-handed spheromaks is termed counter-helicity. With a bit of spatial reasoning one can see that in counter-helicity merging the incoming spheromak magnetic fields are antiparallel, but in co-helicity merging the fields are only (roughly)  $90^\circ$  apart (Figure 2.22.A-B). In the former case there is a plane ( $45^\circ$  out of the page in Figure 2.22) in which the 2D reconnection picture applies, but in the co-helicity case there is not. Only the poloidal *components* of the fields can reconnect, not *all* of the incoming

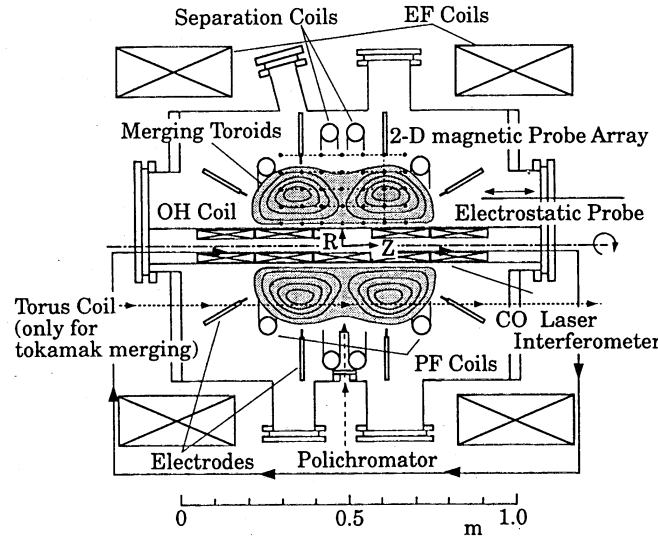


**Figure 2.21:** Schematic of the Tokyo TS-3 device. Figure from [40].

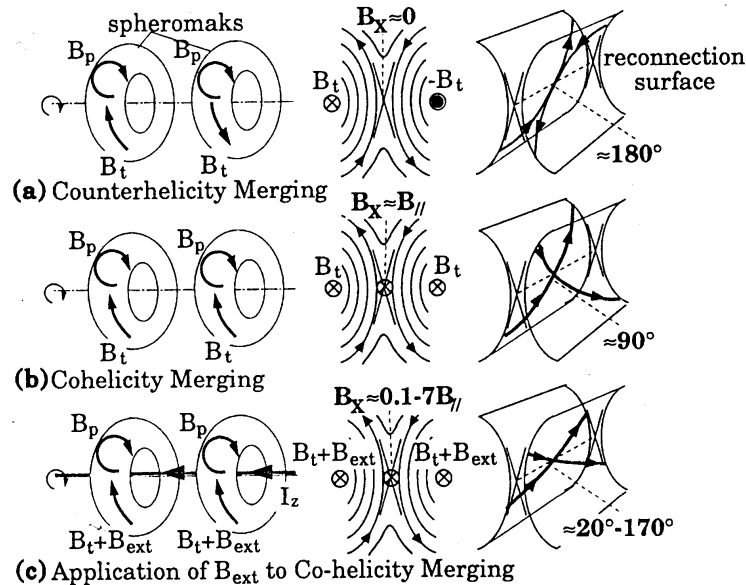


**Figure 2.22:** The Tokyo device could arbitrarily vary the angle at which the reconnecting fields met.  $B_X$  refers to the out-of-reconnection-plane component of the fields, while  $B_{\parallel}$  denotes the in-plane component. Figure from [40].

field. Furthermore, the Tokyo team could vary this “reconnection angle” to *any* value from  $20^\circ - 170^\circ$  using a current channel that ran through the central axis of the device. Current running through this path created an additional toroidal field that could add to or subtract from the existing spheromak toroidal fields, modifying their angles relative to each other (Figure 2.22.C).

Figure 2.23 shows the results of these experiments. The reconnection rate was fastest for antiparallel fields, and gradually slows for less “ideal” angles. Note also in Figure 2.23.B that the reconnection rate is also roughly proportional to the collision velocity of the incoming spheromaks. Thus, the Tokyo group demonstrated that reconnection is affected by the third dimension of the problem and also by distant forces on the incoming plasma, two factors ignored in simple models like Sweet-Parker.

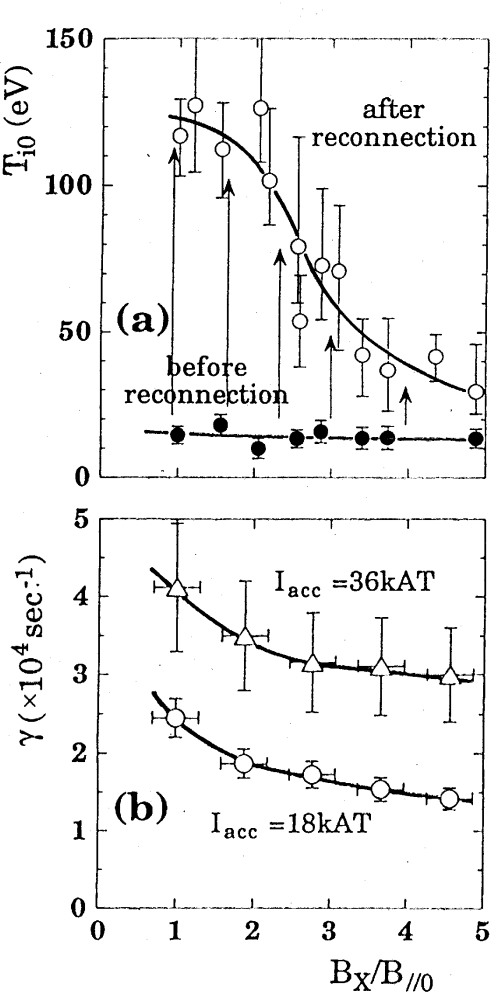


**Figure 2.23:** Evidence from TS-3 that reconnection is fastest when the fields are antiparallel. The X-axis is  $-1 \times$  the tangent of the angle between the fields. In  $B_\perp$ ,  $\gamma$  is the reconnection rate.  $I_{acc}$  is the current applied to the coils that accelerate the spheromaks together, and is roughly proportional to the collision velocity. Figure from [40].

A hypothesis of the Tokyo group is that fast reconnection occurs when the central current sheet - which arises “spontaneously” to keep the flux frozen to the incoming plasma - grows thinner than the ion Larmor radius. For antiparallel fields in a counter-helicity merging, there is very little  $B_\perp$  in the reconnection region, and so the ion Larmor radius is large - larger than the current sheet. At angles much less than  $180^\circ$ ,  $B_\perp$  grows sizable, and the ion Larmor radius remains thinner than the current sheet. Exactly why the large size of the ions’ Larmor radius leads to a fast reconnection

rate is unclear.

### 2.4.3 Princeton Experiments

Princeton's entry to the field of reconnection science is the Magnetic Reconnection Experiment (MRX). Its researchers have collaborated extensively with those of TS-3, and the two projects have reached similar findings. MRX, pictured in Figure 2.24, has similar parameters to TS-3 ( $n \sim 10^{14} \text{ cm}^{-3}$ ,  $|\mathbf{B}| \sim 0.5 \text{ kG}$ ,  $T_e \sim 10 - 20 \text{ eV}$ ,  $S \sim 700$ ). MRX has yet another method for producing reconnection. Before the gas is ionized large currents are initiated in two rings inside the vacuum, called "flux cores." After ionization, the currents are reduced, pulling flux towards the cores. This in turn pulls flux that is common to both cores towards a reconnection region between the cores (Figure 2.24.B).

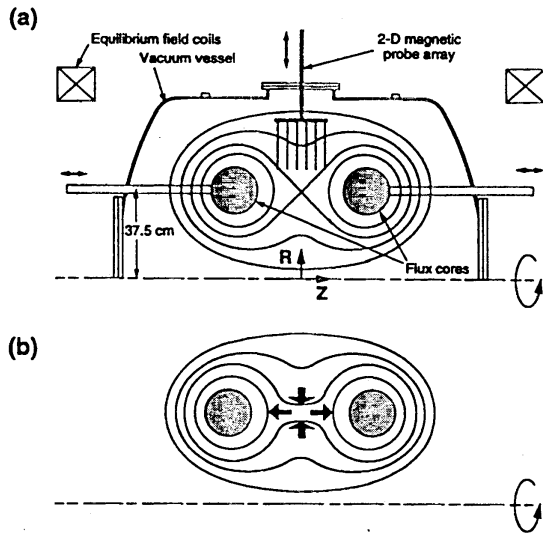


**Figure 2.24:** A: The MRX device at Princeton. B: During the reduction of the initial current in the flux cores, common flux reconnects to become local to one or the other of the cores. Figure from [59].

As MRX does not use spheromaks, reconnection of antiparallel fields can occur in the R-Z plane (unlike TS-3, in which there is always a toroidal component to the fields as well). MRX does have the ability to add toroidal field using other coils, allowing them to also produce co- and counter-helicity reconnection. While  $B_\theta = 0$  produces the usual double-Y-shaped reconnection region, O-points are observed (as in the UCLA device) during counter-helicity merging.

A study of ion heating in the reconnection layer was done on MRX, using Doppler spectroscopy techniques similar to those used in TS-3, and the findings were quite similar[25]. A region of high-temperature ions was found local to the reconnection layer. The energy of the hot ions cannot be accounted for by Ohmic heating, and its time dependence precisely mirrors the energy *lost* from magnetic field annihilation (Figure 2.25). The group suggests that wave-particle interactions or collisionless inertial effects are perhaps responsible for this ion heating, as well as for determining the reconnection rate.

The MRX group also investigated the validity of the Sweet-Parker model[27]. A series of shots were taken varying only  $B_z$  (which should vary the reconnection rate), and the results can be seen in Figure 2.26.A. Recall that the Sweet-Parker model predicts  $v_{in}/v_{Alf} = 1/\sqrt{S}$ . The data did not support this result. Instead, the data were found to fit well to a modified Sweet-Parker theory that was generalized to include compressibility of the fluid and a pressure differential between inflow and outflow. Additionally, a good fit required using an experimental value for the resistivity  $\eta$  that was roughly 10 times the Spitzer prediction.

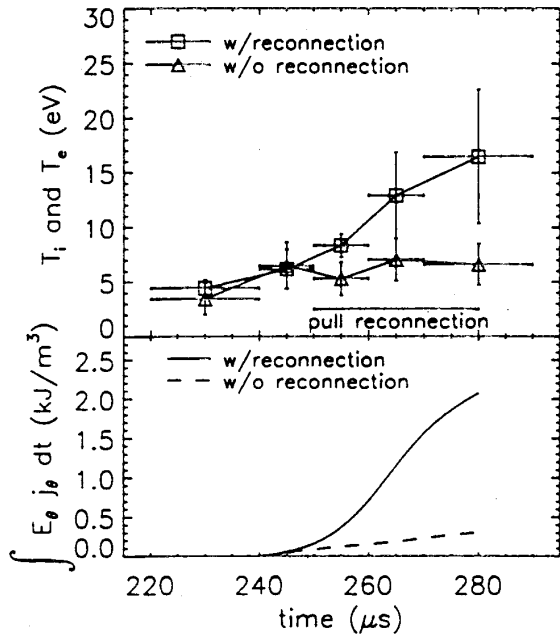


**Figure 2.25:** Time evolution of ion temperature (above) and total lost magnetic energy (below) in MRX, showing the close relationship. Figure from [25].

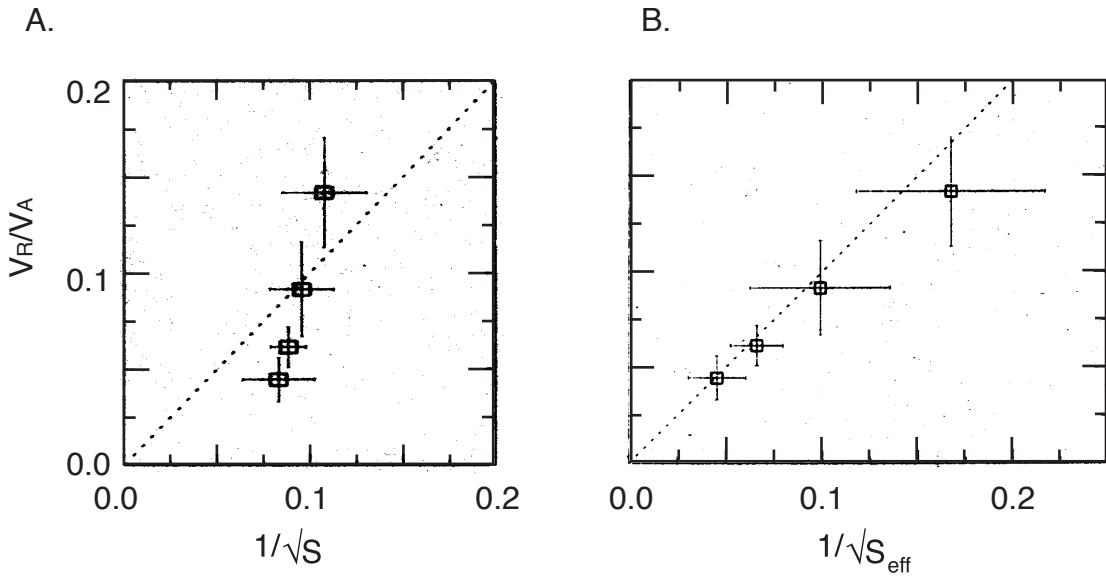


**Figure 2.26:** MRX experiment to test the Sweet-Parker model. The data do not lie on the  $y = x$  line as predicted by the model (A), although with modifications the model can be made to fit well (B). Figure from [27].

# Chapter 3

## The Swarthmore Spheromak Experiment

### 3.1 SSX Operation

The Swarthmore Spheromak Experiment was designed to allow easy measurements of reproducible reconnection events. Spheromaks are a good magnetofluid configuration for this purpose for several reasons. Unlike tokamaks, they are topologically unlinked to the magnets and electrodes needed to produce them. As a result, they can be translated from the initial ionization region so that very little neutral gas is present in the measurement region. Spheromaks also provide an interesting 3D reconnection geometry. Finally, their temperature,  $\beta$ , and  $B$  field strength can be made comparable to those of solar flares. Consequently, results learned from spheromak research can be quite relevant to solar observations.

Spheromak formation in SSX has been extensively documented in previous papers [29, 20, 49]. In SSX, two spheromaks are produced at opposite ends of the vacuum chamber by a pair of “coaxial plasma guns.” The formation process is illustrated in Figure 3.1. (a) A small amount of hydrogen gas is introduced into the evacuated chamber at the end of the gun, between the coaxial electrodes. The gas is propelled by a mechanism similar to that of a rail gun, as follows. (b) High voltage pulsed power supplies are discharged across the electrodes, resulting in a radial ionizing current through the hydrogen. The current through the central electrode concurrently creates a toroidal magnetic field. A  $\mathbf{J} \times \mathbf{B}$  force results in the plasma and pushes it out of the gun. Meanwhile, a separate “stuffing flux” magnet outside the device creates an additional magnetic field. The central electrode is constructed of highly magnetically permeable metal to concentrate this “stuffing field” in a radial direction at its end. (c) The accelerated plasma enters this concentrated field region as it exits the gun. The frozen-in flux constraint must be overcome if the plasma is to cross this field. If the force of the moving plasma exceeds a certain formation threshold, the stuffing fieldlines reconnect around the plasma and a spheromak is formed (d). The plasma’s magnetic field now contains a toroidal component originating from the discharge current, and a poloidal component from the stuffing field. The process may be thought of as similar to that of blowing a soap bubble. The stuffing field has a magnetic tension analogous to surface tension, which is overcome by the magnetic pressure of the incoming plasma.

Figure 3.2 shows the SSX laboratory. The spheromaks are created in a roughly  $1\text{ m}^3$  vacuum chamber. A schematic illustration of the chamber can be seen in Figure 3.3, and some rendered 3D illustrations are shown in Figure 3.4. Each spheromak is confined within a copper cylinder known as a flux conserver. The high conductivity of the copper prevents magnetic flux from penetrating, for the same reasons that fieldlines are normally locked into a perfectly conducting plasma. The conservers provide the necessary boundary condition for the spheromak equilibrium, and effectively confine the plasma for the duration of the experiment.

For most experiments discussed in this paper the conservers were configured as follows. Each plasma gun fed into a separate cylindrical conserver, each of radius 25.4 cm and length 30.8 cm. The conserver walls were separated by 2.5 cm at the midplane of the vacuum chamber. Two holes (referred to as “chevrons”) were cut in the midplane-side walls of each conserver, as shown in Figure 3.5. These openings allowed a small amount of plasma from each

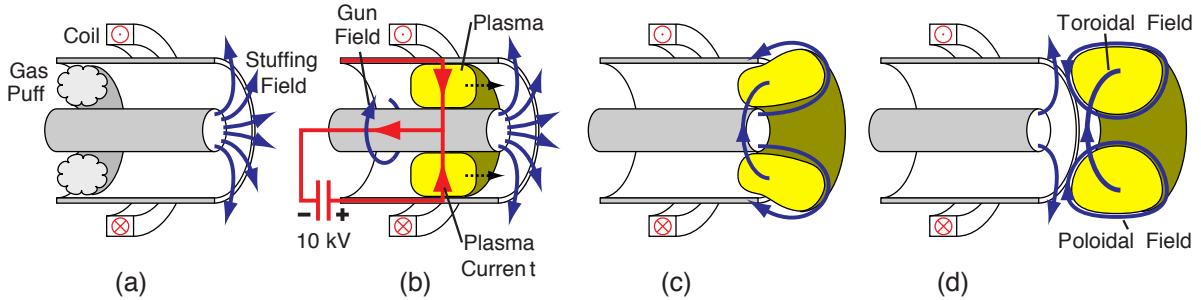


**Figure 3.1:** Spheromak formation using a magnetized coaxial plasma gun.

density	$n_e \approx n_i$	$10^{14} \text{ cm}^{-3}$
temperature	$T_e \approx T_i$	20 eV
magnetic field	$B_{typical}$	0.05 - 0.1 T
length scale	$L$	0.1 m
Beta	$\beta$	0.1
Alfvén speed	$v_{Alf}$	$10^5 \text{ m/s}$
Lundquist Number	$S$	$\sim 10^3$
Larmor radius	$r_L$	0.9 cm
Sweet-Parker thickness	$\delta_{S-P}$	0.15 cm
Collisionless thickness	$2\frac{c}{\omega_{pi}}$	4.6 cm

**Table 3.1:** SSX Plasma Parameters

spheromak to bow out from the conservers at the midplane and converge, so that reconnection can occur. However, the holes were small enough that a spheromak-like equilibrium could be reached inside each conserver, and that the plasma was largely still well contained. This divided setup was advantageous for a number of reasons. Had the spheromaks been fired into a single conserver the resulting configuration would be relatively unstable, as will be discussed further in the next chapter. With separate conservers, the spheromaks remained very stable for the duration of the experiment because they were largely isolated. Also, this design allowed for better measurement of particles accelerated in the reconnection region. Diagnostics for such particles were located around the midplane of the vacuum chamber. Particles exiting the reconnection zone were free to travel towards the surrounding diagnostics without interference from surrounding plasma, because the conserver walls kept the gap region relatively empty. The presence of other magnetic fields would have diverted the particles and prevented reliable measurements of these particles.

Power to each plasma gun is provided by capacitor banks. With a capacitance of 0.5 mF and maximum voltage of 10 kV (a charge of 5 C), the maximum energy stored in each of the two supplies works out to 25 kJ. Peak discharge currents are around 60 kA. The stuffing field electromagnets are powered by a separate system, capable of 600 V (0.05 C). Peak stuffing flux is approximately 3 mWb. In a typical shot, each system is charged to roughly half of its maximum capacity. Other SSX parameters are listed in Table 3.1 [29]. In general, the plasma parameters are quite similar to those of the Tokyo and Princeton experiments. Values for density, temperature, and  $B$  have been obtained by various diagnostics (interferometry, Langmuir probe, Mach probe, etc.), and the other numbers in the table can be computed from these three and the length scale.

## 3.2 3D Magnetic Measurements

Perhaps the most unique diagnostic tool used on SSX is a system for measuring the 3D structure of the magnetic field in the reconnection region. Recall that the UCLA, Tokyo, and Princeton experiments all used magnetic probes to map

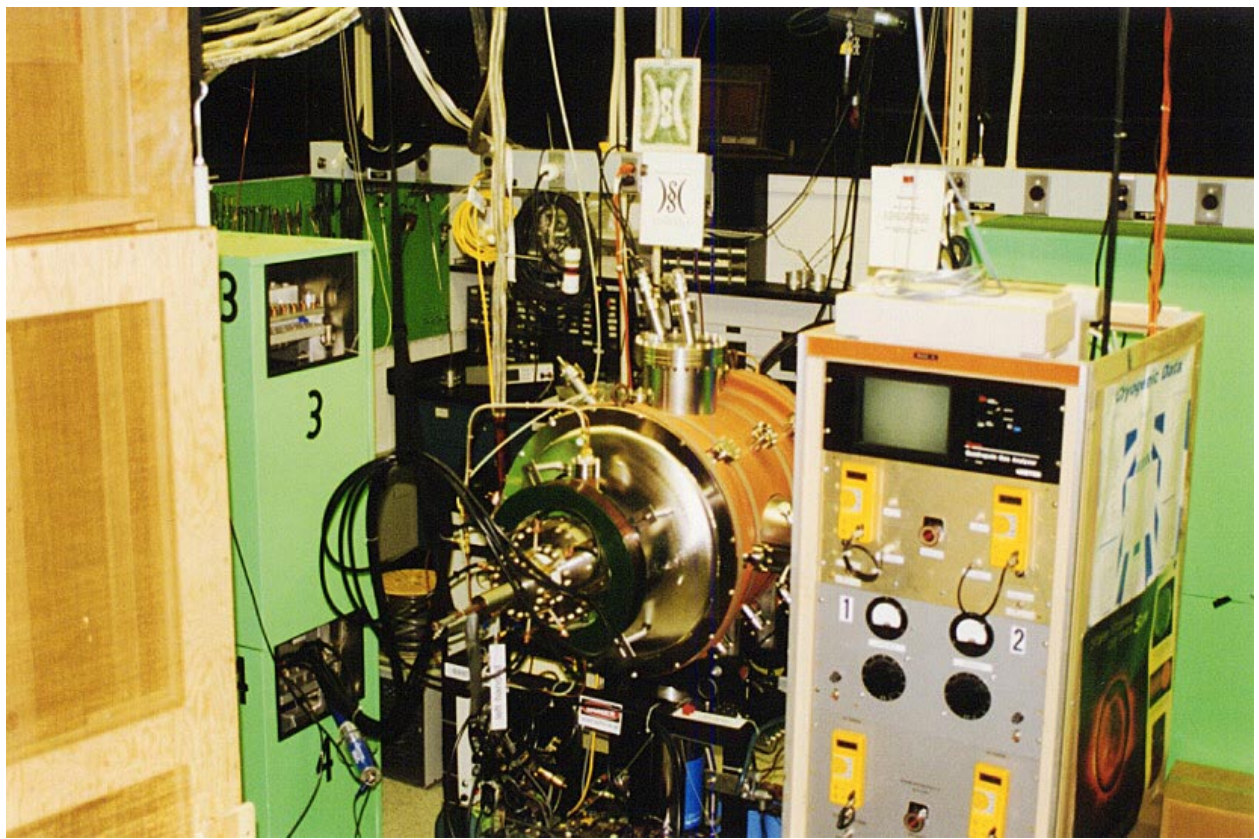


**Figure 3.2:** The SSX laboratory. The vacuum chamber is in the center. The 3D magnetic probe is not visible in this image, but it attaches to a large port on the right of the chamber.

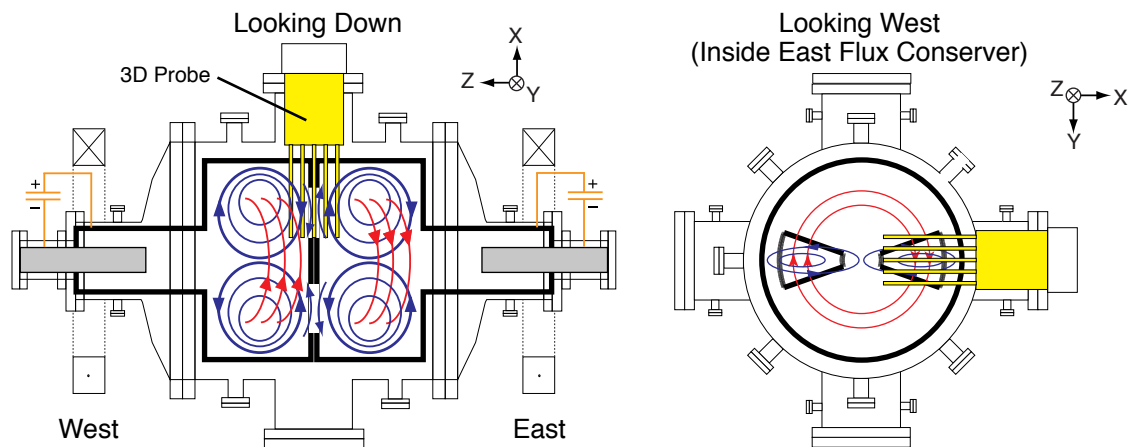


**Figure 3.3:** Schematic illustration of the SSX vacuum chamber. The thick line represents the flux conserver, which is the effective boundary for the spheromaks.

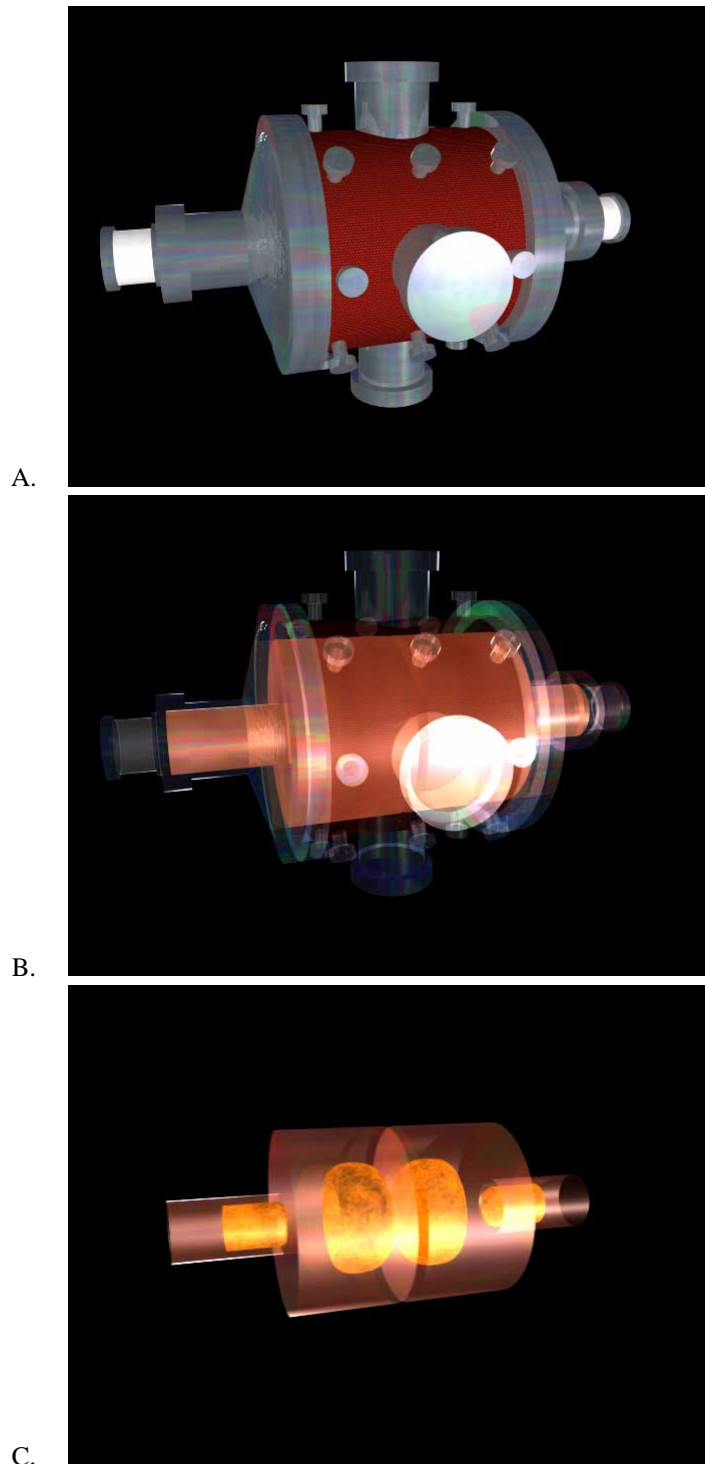


**Figure 3.4:** A 3D rendering of the SSX device. The outer walls of the vacuum chamber are shown in A. B: Inside the vacuum walls are two separate copper flux conservers. C: A separate plasma gun fires a spheromak into each conserver. These graphics were rendered by Nicholas Ouellette and Casey Smith (both Swarthmore '02) using the Maya application.

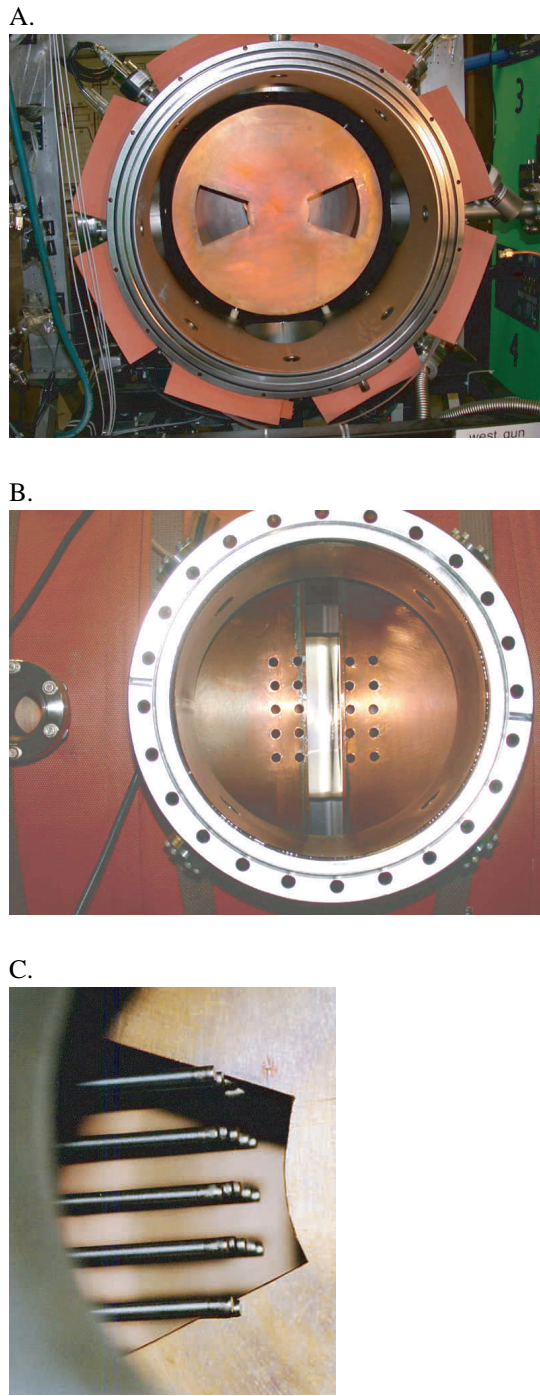


**Figure 3.5:** The flux conservers. A. The vacuum chamber split down the midplane reveals the conservers inside. The conservers's two "chevron" holes can be seen. B. Looking into the port in which the 3D magnetic probe is attached. The holes visible in the conservers allow four of the five vertical planes of probe stalks (discussed in Section 3.2.1) to reach inside the spheromaks. The central plane of probes lies between the conservers. C. The 3D probe, now installed, is viewed from inside one of the conservers.

the  $\mathbf{B}$  field in the reconnection region. However, no group has yet mapped  $\mathbf{B}$  in a *three-dimensional volume in a single shot*. The UCLA device mapped  $\mathbf{B}$  in a three-dimensional volume, but averaged over many (10-80) shots. The Tokyo and Princeton experiments used a rectangular array of probes to detect  $\mathbf{B}$  in the reconnection plane in a single shot. The assumption was made that because the machine was axisymmetric, then there would be little more to see by adding more probes in the third dimension.

In SSX, however, axisymmetry is broken by the chevron holes in the flux conservers. The canted equilibrium spheromak fields bulge through these holes, making for a complicated geometry that is hard to fully appreciate from a two-dimensional slice. The fact that SSX plasmas are generated far away and then shot towards the reconnection region, rather than generated already on top of the probes, makes the experiment particularly dynamical and tumultuous. Thus, unpredictable three-dimensional effects are sure to arise that *differ from shot to shot*. While this means that it is harder to diagnose and comprehend the field dynamics, it is also perhaps the experiment that most realistically reproduces plasma dynamics on the Sun or in space. SSX gives us a chance to see the kind of chaotic asymmetric reconnection that actually happens in nature.

The reason no one has implemented a three-dimensional probe array so far is largely due to cost, as discussed above in Section 2.4.1. Each *channel*, or one-variable analog timeseries measured in the experiment, costs roughly \$1000 to feed into a computer (using a device called a “digitizer”). Thus, an  $8 \times 5 \times 5$  array of probes, each measuring a *three-component vector*, is prohibitively expensive to digitize:

$$(8 \times 5 \times 5 \text{ probes}) \times (3 \text{ components per probe}) \times (\$1000) = \$600,000,$$

or about the current value of the entire SSX laboratory. In the instrument developed for SSX, the number of channels of digitization has been kept low without sacrificing the detail of shot-to-shot differences through the use of electronic multiplexers. Magnitudes of one magnetic field component along a row of probe locations are sequentially fed into the same digitizer. During data processing, a software routine sorts the information into a separate time sequence for each probe location. A cost reduction approaching a factor of ten can be accomplished with this approach over separate digitization of each signal.

The author was responsible for the construction of some of the 3D probe hardware, development of the data acquisition, processing, and visualization software, and operation of the data acquisition system during experiments.

### 3.2.1 Magnetic Probe Theory and Design

To measure the magnetic field vector at a point, one needs no more than three small loops of wire, oriented orthogonally to each other. By Faraday’s law, as the magnetic field changes near a loop, an EMF will be induced proportional to the rate of change of magnetic flux through the loop and the number of turns of wire  $N$ :

$$\mathcal{E} = -N \frac{\partial \Phi}{\partial t} \quad (3.1)$$

If the loops are small relative to the scale of variation in  $\mathbf{B}$ , then we can take  $\mathbf{B}$  to be constant over the region. Flux is just the area  $A$  of the loop times the component of  $\mathbf{B}$  perpendicular to the loop. Thus, if we integrate the EMF over time we get a component of the magnetic field:

$$B_{\perp}(t) = B_{\perp}(0) + \frac{1}{NA} \int_0^t \mathcal{E}(\tau) d\tau \quad (3.2)$$

If we start the integration at a time before the plasma is created we can take  $B_{\perp}(0) = 0$ . Three orthogonal loops can give us the three components of  $\mathbf{B}$ .

In the SSX magnetic probe array, each probe location consists of three small coils of #34 magnet wire (Figure 3.6.A). Eight such triplets of coils are wound on 25 delrin rods, or “probe stalks” (Figure 3.6.B). The stalks are arranged in a five by five grid (Figure 3.6.D). Loops normal to the stalk axis (the X direction) consist of 10 turns of wire, while those normal to the vertical direction (Y) or those normal to the other horizontal direction (Z) consist of five turns.

The outermost six probe triplets are spaced at 0.6" in the X direction, with the remaining two triplets spaced at 1.5". This allows for higher resolution at the end of the probe in the heart of the reconnection zone, but also allows for a baseline to be taken near the flux conserver walls where we expect to see little field. The probe stalks are inserted into a vacuum-welded thin stainless steel module for protection from the plasma. The high resistance of the stainless steel permits rapid penetration of magnetic flux compared to the time scale of the phenomena under study ( $\tau_{soak} \leq 0.1\mu s$ ) [29]. This property ensures that the impact of the probes on the magnetic field dynamics will be minimal. A pin runs through the back end of each row of five stalks to ensure they are aligned in the X direction. These pins also prevent stalk rotation, ensuring that the Y and Z coils are properly oriented.

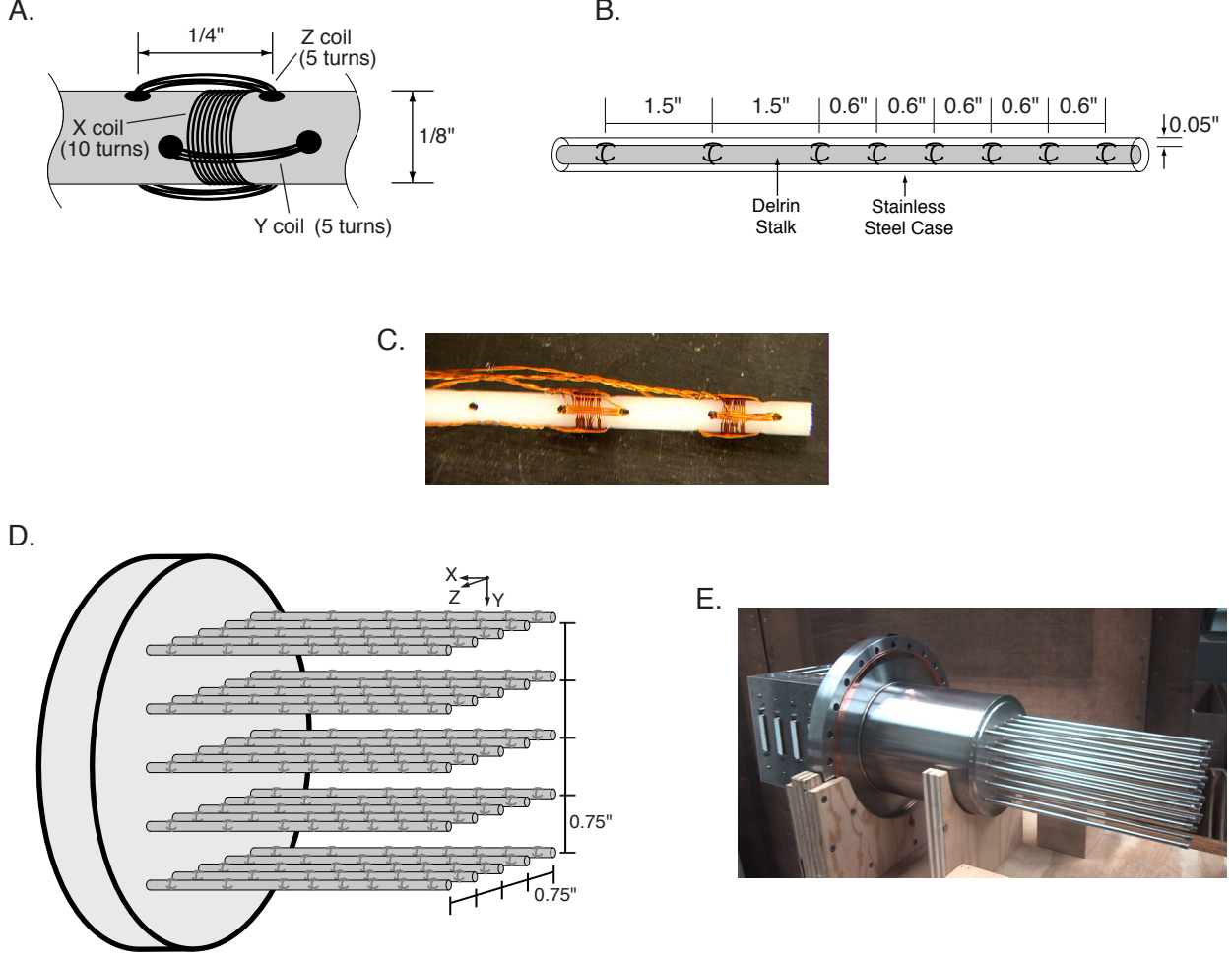


**Figure 3.6:** Magnetic field probe design. A: A triplet of coils measures the vector  $\partial\mathbf{B}/\partial t$  at one location. B: Each probe stalk consists of eight such coil triplets. C. Photograph of a partially wound probe stalk. D: 25 probe stalks are arranged in a  $5 \times 5$  array. E. Photograph of the probe housing.

The probe is inserted at the midplane of the vacuum chamber (Figure 3.7). Two vertical planes of probes lie within the East flux conserver, and two within the West conserver. The central vertical plane lies in the 1 inch gap between the copper walls. The radially innermost plane of probes is slightly inside the chevron holes in the conservers, while the radially outermost plane of probes is roughly flush with the conservers' outer wall. The relation between the probe and the conservers can also be seen in the photographs of Figure 3.5.

The 48 wire ends from each probe stalk (8 probe locations  $\times$  3 wire loops per location  $\times$  2 ends of each wire) are soldered to a 50-pin D connector on the probe. 25 large shielded cables plug into these D connectors to carry the signals to the instrument room via twisted-pair wires. The signals proceed to a set of 25 custom-designed integrator / multiplexer circuit boards, one for each probe stalk. The boards were developed in collaboration with the University

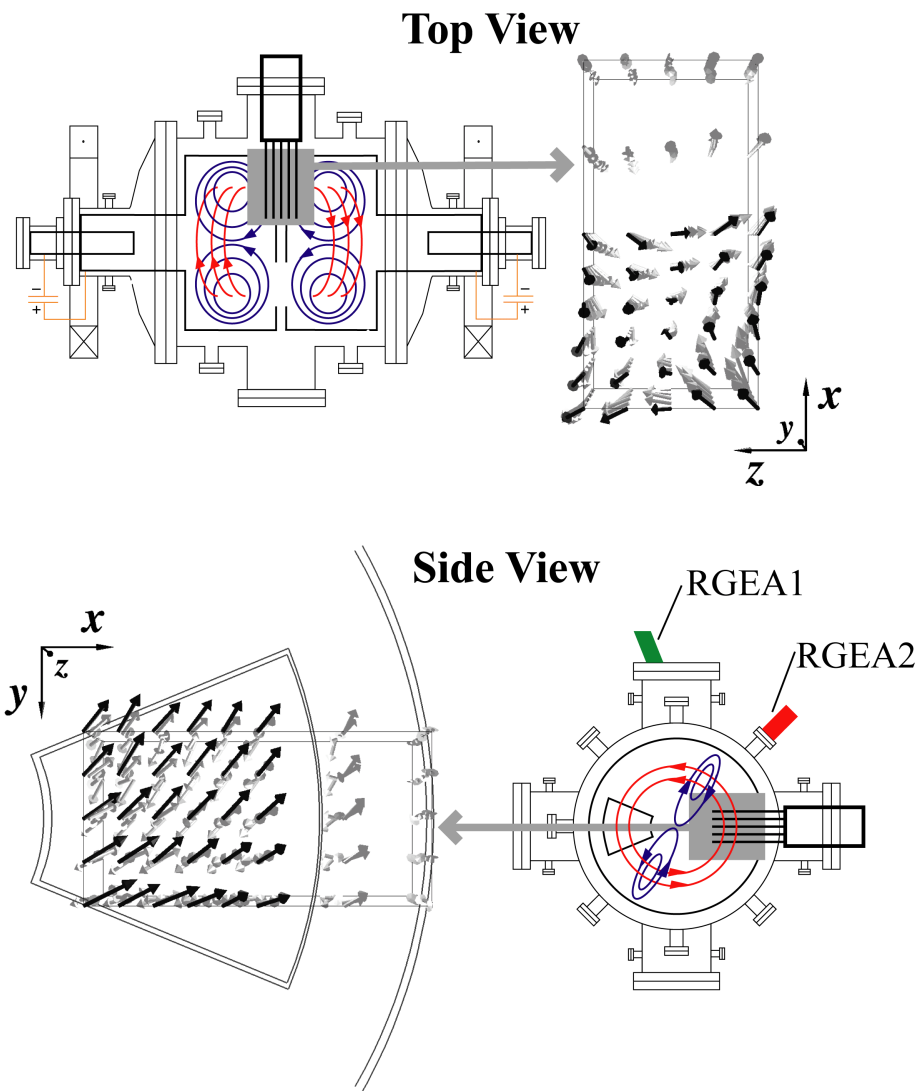


**Figure 3.7:** Placement of the 3D probe within the SSX vacuum chamber, showing its relation to the spheromaks and the flux conservers. The RGEAs are discussed in the section on particle measurements (3.3).

of Washington's Redmond Plasma Physics Laboratory. RPPL is using boards of the same design to collect data for a separate plasma physics experiment there.

The schematic for each board can be seen in Figure 3.8.A. The first stage in the circuit is an active electronic integrator to turn  $\partial\mathbf{B}/\partial t$  into  $\mathbf{B}$ . There are 24 integrators on each board, one for each component of  $\mathbf{B}$  at each of the eight positions we wish to measure it. The integration time constant is fixed at 100  $\mu s$ . Since the integrators are reset by a fixed bleed resistor the maximum integration time is limited to about 1 or 2 ms before there is noticeable droop in the output signal, but this is far longer than the duration of a plasma experiment ( $\sim 150 \mu s$ ).

As a result of the integrators, each of the 600 signals has a unique offset voltage. To compensate, several  $\mu s$  of data are recorded for each shot before any field is created. During software data processing, the average value of these points is subtracted from the rest of the signal.

The 24 integrated signals are multiplexed 8:1 to produce the three output signals. Multiplexing is done by Maxim MAX440 high-speed video multiplexer / amplifier chips. There are three multiplexer chips per board, one for each set of eight signals. Figure 3.9.A illustrates the synchronization and data acquisition system. A gate signal and 10 MHz clock is fanned out by custom-built electronics to synchronize the 25 multiplexer boards and 10 digitizers. Appendix C describes the details of this timing system. Since multiplexing divides the sample rate by eight, the true time resolution of the instrument is 800 ns per sample. The outputs of the multiplexers are terminated in a  $50\Omega$  input at the digitizer. At  $50\Omega$  the output range is about  $\pm 1V$ .

After multiplexing, the data are transferred to a computer. The 75 multiplexer output channels are fed into a bank of DSP Technology Inc. model 2028 10MHz CAMAC digitizers. A custom LabVIEW application running on a Macintosh G3 downloads the data to a file over a GPIB interface with the CAMAC crate controller. Before processing and analysis, a software routine de-multiplexes each data channel into its eight components. Figure 3.10 illustrates typical output of the multiplexing system and how it is de-multiplexed to isolate the signal from each magnetic pickup loop.

Due to the nature of the experiment for which our instrument was used, special effort was necessary to obtain clean signals. The 100 kA discharge currents that ionize the plasma fill the laboratory with electronic noise, from which our signals must be protected. As a precautionary measure the integrator/multiplexer boards, digitizers, and computer equipment are all located in a Faraday cage. The power supply to these devices is isolated. In addition, all wiring between the probes and computer is either coaxial cable or shielded twisted-pair leads. Typical multiplexer output showed little noise above the 2 mV resolution of our digitizers, indicating that the noise had been adequately suppressed.

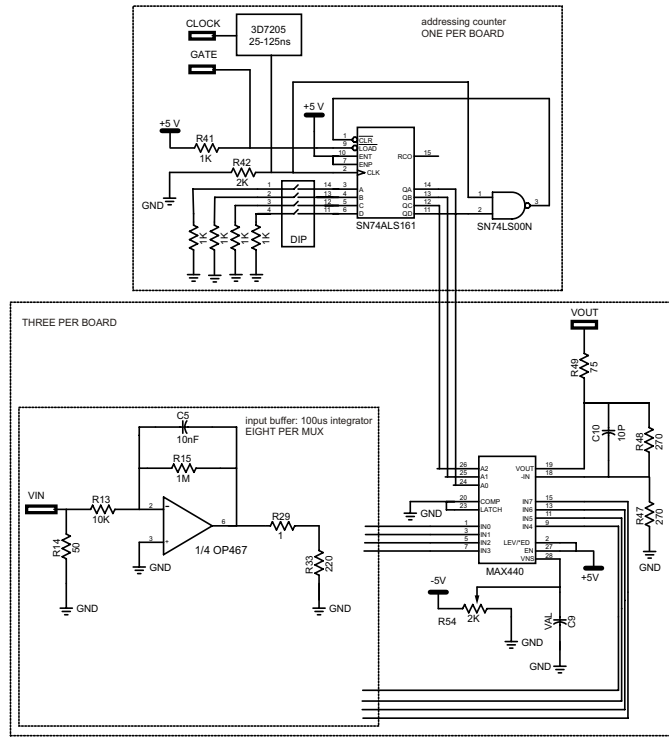
### 3.2.2 Calibration and Analysis

Without calibration, the probes would vary slightly in sensitivity. Each wire loop is small enough that fluctuations in winding affect the total enclosed area, and therefore the induced current, for a given  $\partial\mathbf{B}/\partial t$ . There may be occasional mistakes in the number of loops wound in a loop, or a coil's leads might be soldered to the D-connector backwards. Also, it is difficult to align the thin probes such that the Y-coils lie perfectly horizontally; each probe stalk may be rotated several degrees about its axis and thus may be measuring the components of  $\mathbf{B}$  in a slightly different coordinate system.

These problems seem inevitable and overwhelming. However, a calibration process was devised that can compensate for *all* these errors *simultaneously!* It requires only a trick of matrix algebra, and a few preliminary tests with a known magnetic field. For this purpose, a Helmholtz coil ( $r = 12$  cm, 2 turns per coil) was constructed to fit around the probe, as in Figure 3.11.A. A mounting device positions the sensor array at a known location within the coil, which can be oriented along three perpendicular axes. High voltage pulsed power supplies at 2.2 kV discharged roughly 11 kA through the coil, creating a peak field intensity near 1500 gauss. This is comparable to the 500-1000 gauss fields inside the SSX plasma device. The current was measured by a Rogowski pickup on the power supply that was calibrated with a precision resistor.

For each orientation of the Helmholtz coil, uncalibrated magnetic field data was recorded with the normal data ac-

A.



B.

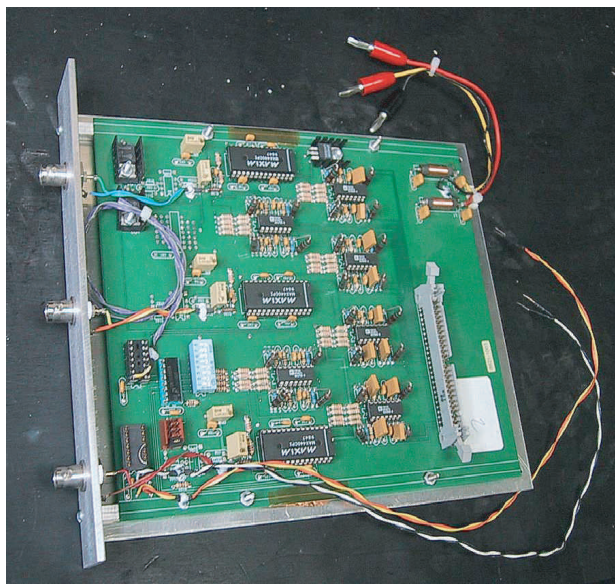
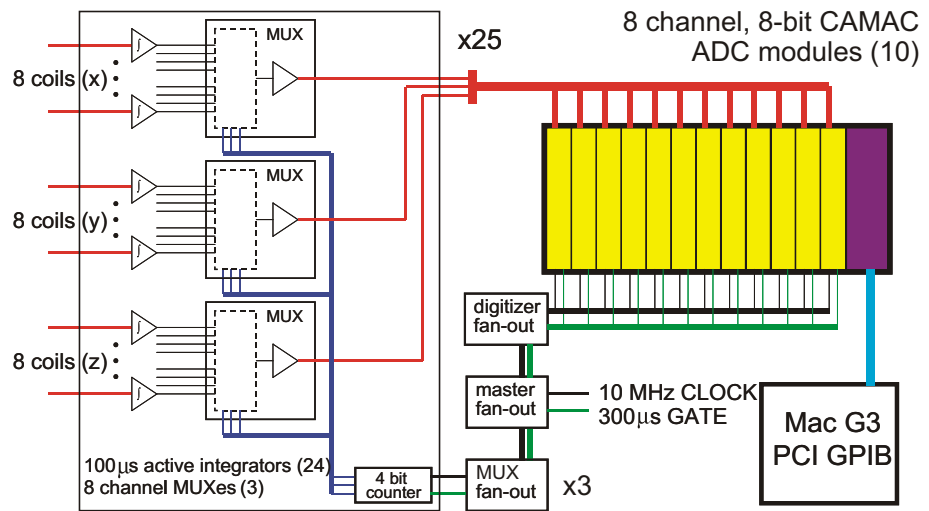


**Figure 3.8:** A. Electrical schematic of the multiplexer boards. B. Photograph of one of the boards.

A.



B.

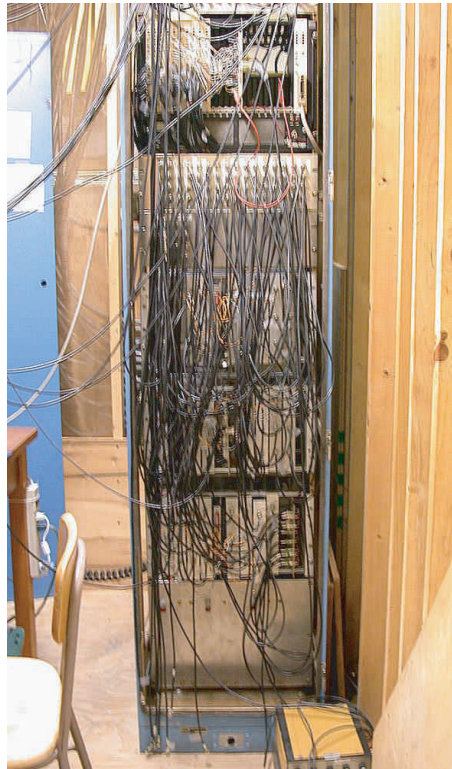


**Figure 3.9:** A. Block diagram of multiplexer and timing system. B. The cabinet housing three crates of MUX boards, power supplies, and the timing circuitry.

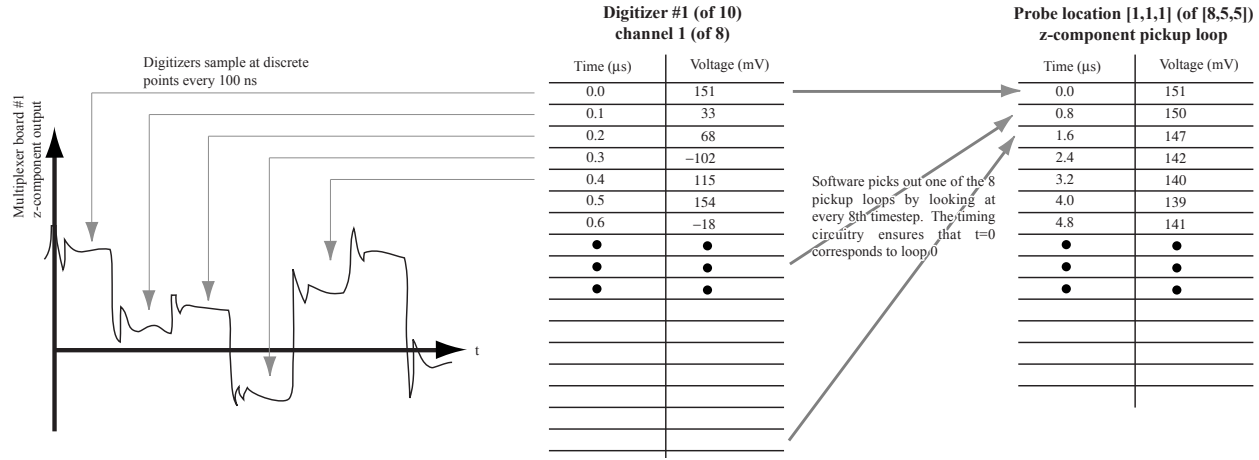


Figure 3.10: Digitization and de-multiplexing of data.

quisition system. An IDL routine calculates the theoretical field vectors for the location of each coil triplet using a numerical integration of the Biot-Savart law for the moment of peak current. Such a calculation is possible because the Helmholtz coil uses a simple current geometry (two rings). Figure 3.11.B shows the theoretical Helmholtz field for one of the three shots.

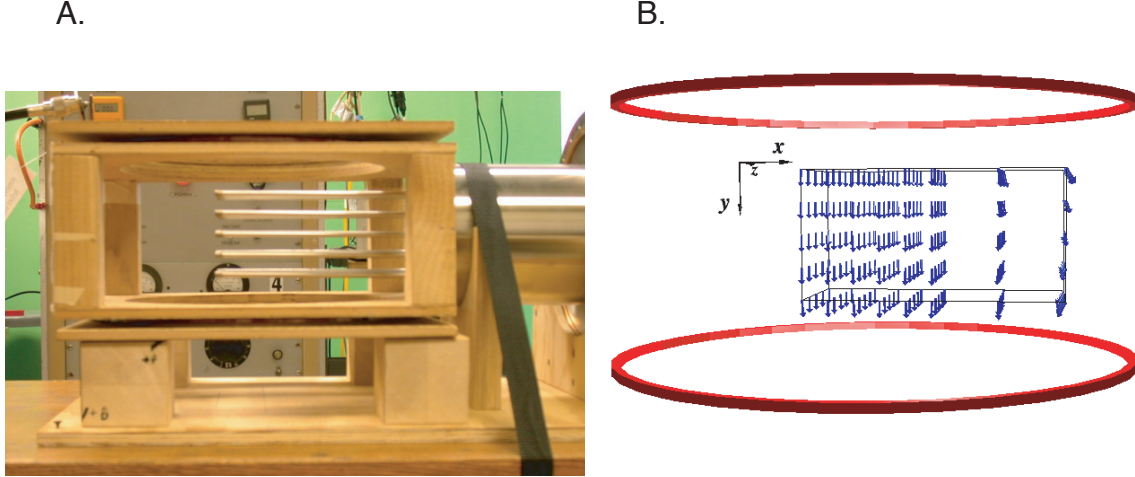


Figure 3.11: Calibration setup. A) Helmholtz coil positioned around magnetic probe array, oriented normal to the y direction. B) Theoretical  $\mathbf{B}$  fields for the setup pictured in A, calculated from the Biot-Savart law. The large loops represent the Helmholtz coils. The actual  $\mathbf{B}$  measurements were calibrated to fit this field, based on this and two similar tests in the x and z directions.

Next comes the matrix algebra step. First, note that all of the factors we have discussed that make the vector of measured voltages different from the  $\mathbf{B}$  vector (variations in loop area, rotation, etc.) effect a *linear transformation* on the  $\mathbf{B}$  vector. For example, coil lead reversal multiplies one component of  $\mathbf{B}$  by  $-1$ , or probe stalk rotation multiplies the  $\mathbf{B}$  vector by a rotation matrix. We can thus describe *all* such linear “errors” by stating that the vector  $\mathbf{M}$  of measured voltages is related to the true components of  $\mathbf{B}$  by some matrix  $\underline{\mathbf{E}}$ :

$$\mathbf{M} = \underline{\mathbf{E}}\mathbf{B}. \quad (3.3)$$

$\underline{\mathbf{E}}$  should be nearly the identity matrix (times a unit conversion constant), but the aforementioned factors will cause it to be somewhat different. Inverting this relation, we can solve for the physical information we wish to extract:

$$\mathbf{B} = \underline{\mathbf{E}}^{-1}\mathbf{M}. \quad (3.4)$$

If we can do some calibration experiments to find  $\underline{\mathbf{E}}^{-1}$ , it will be easy to correct all future data. There are nine unknowns in the matrix. From each of the *three* orientation shots with the Helmholtz coil we get a *vector* equation  $(\mathbf{B}^{(i)}) = \underline{\mathbf{E}}^{-1} \mathbf{M}^{(i)}$ ,  $i = x, y, z$ , giving us the necessary nine equations. An IDL routine solves the system of nine resulting linear equations for each vector location. The 200  $\underline{\mathbf{E}}^{-1}$  matrices are saved and recalled for all subsequent data acquisition to transform the measured  $\mathbf{M}$  before data analysis.

In a custom-built device to measure 600 signals, there will inevitably be a few hard-to-trace problems that make a few detectors non-functional. There are diminishing returns to fixing every channel: repairing the last 10 or 20 of the broken probe loops won't tell you much more about the plasma dynamics, but it will take a *very* long time. Thus, 16 probe loops in the three-dimensional array remain broken. Most of these problems are known to be the result of broken wires inside the probe housing, between the D-connector and the delrin rod. The thin wire breaks easily, and it is hard to re-solder without breaking at least one new wire.

However, some form of compensation for these errors must be performed, because even a single stray vector looks glaringly out-of-place in any graphical representation of the measured vector field. In addition, subsequent analysis which involves taking spatial derivatives of the data would cause the error to propagate. A compensation procedure was devised that relies on interpolation. A list of the dead probe loops is maintained and recorded in a computer file. During data processing, the software replaces the timeseries for this component with an interpolation of the data for its neighbors. As the measured fields are quite smooth, this replacement looks extremely natural. It makes the vector fields look much more comprehensible, and it should not significantly detract from the data accuracy.

### 3.2.3 Previous Magnetic Measurements in SSX

Previous studies have been conducted on SSX using smaller arrays of magnetic pickup loops, and have been reported by Kornack *et al*[29, 28]. The most detailed experiments had been performed using a single probe stalk, consisting of 10 coil triplets at a 1 cm spacing (=30 digitizer channels). The single stalk was not oriented in the  $x$  direction, as the stalks for the 3D probe array are, but rather in the  $z$  direction so that it crossed the reconnection layer.

The single-probe studies established a basic outline for the magnetic evolution of an SSX shot. Plasma first reaches the machine midplane roughly 25  $\mu\text{s}$  after the high-voltage discharge. There is some motion of the fields for the next 15  $\mu\text{s}$  as reconnection occurs and as the spheromaks recoil from their collision with the flux conserver endplate. After 50  $\mu\text{s}$  there is a slow decay of the equilibrium fields. We will see this pattern in more detail in Figure 4.4 when the 3D probe measurements are discussed.

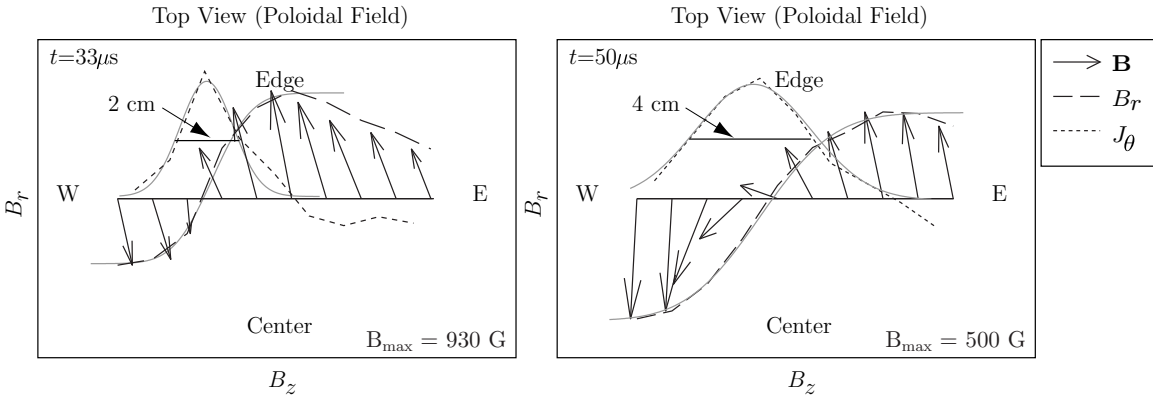


**Figure 3.12:** Previous linear probe measurements on SSX indicate a layer thickness of 2-4 cm.  
Figure from Kornack[29].

Much of this information could have been gleaned from other diagnostic methods, but the linear probe more importantly provided the first quantitative measure of the reconnection layer thickness (Figure 3.12). Kornack *et al.* found that immediately after the arrival of the two spheromaks, the current sheet width at half maximum was approximately

2 cm. After equilibrium is established later in the shot, the sheet thickness had grown to roughly 4 cm. These numbers accord much better with the 4.6 cm thickness predicted by the collisionless two-fluid model than with the Sweet-Parker prediction of 0.15 cm.

### 3.2.4 Data Visualization

The mass of three-dimensional data from even a single shot is essentially impossible to interpret without the aid of some software tool to display it visually. Also, although there are a number of quantitative calculations we performed on the data, the purpose of the 3D magnetic probe was largely qualitative and visual in nature - to make visible the dynamics of spheromak collision. Thus, custom 3D visualization software was a necessary component of the 3D magnetic probe program.

IDL provides a powerful set of 3D graphics rendering functions, and was chosen as the platform for the software. Several applications were written for the 3D magnetic probe data. The first was developed concurrently with the timing circuitry for the multiplexers - long before any plasma data were taken - so that readings from the Helmholtz and straight-line currents could be interpreted as soon as the multiplexers were completed. A screen shot from this application can be seen in Figure 3.13. The application allowed for displaying the measured  $\mathbf{B}$  field arrows at an arbitrary angle which could be rotated in real time. The user could scan through time while displaying this information in order to “replay” the shot on a human timescale. Other features included the ability to crop the field of vectors which were displayed, to export movies, and to display other information calculated from the  $\mathbf{B}$  field (discussed in the next section).

As anticipated, once real plasma data were obtained there were many new analyses we thought of to perform which had not been coded into the original visualization application. Also, the first application, while well suited for interactive exploration of the data and for rapidly building a qualitative feel for it, was not ideal for creating images for publication. Consequently, a second set of applications was developed, also in IDL. For each function of the  $\mathbf{B}$  field we wished to compute, a copy of the original program template could be made, and this new function added to the program.

A more thorough description of the various visualization programs developed for SSX can be found in Appendix E.

### 3.2.5 Data Analysis Methods

Although the probe measures only  $\mathbf{B}$ , there are many other objects and quantities that can be computed numerically from the  $\mathbf{B}$  data if certain assumptions are made.

Magnetic fieldlines can be approximated by integrating the measured  $\mathbf{B}$  field. More precisely, fieldlines are solutions of the differential equation for  $\mathbf{l}(s)$  given by<sup>1</sup>  $\partial\mathbf{l}/\partial s = \mathbf{B}/|\mathbf{B}|$ . A fourth-order Runge-Kutta integration routine is used, and trilinear interpolation is used to approximate the value of the  $\mathbf{B}$  field at arbitrary locations within the probed volume. Figure 3.13 shows a  $\mathbf{B}$  field and the fieldlines calculated from it.

Another quantity we can calculate from the  $\mathbf{B}$  measurements in the current density field. To see how this can be done, consider Ampère’s law:

$$\mathbf{J} = 1/\mu_0 \nabla \times \mathbf{B} \quad (3.5)$$

Thus, we can infer what the  $\mathbf{J}$  field looks like in the probe region by taking the curl of the  $\mathbf{B}$  field we measure. To take the curl numerically, on our discrete lattice of probe locations, we do the following. Consider probe location  $(0,0,0)$  and  $(1,0,0)$ . If we take the y-components of  $\mathbf{B}$  at these two points, subtract them, and divide by the distance between these probe locations (0.75 in), we will have computed an approximation to  $\partial B_y / \partial x$  at  $(0.5,0,0)$ . Similarly, comparing  $B_x$  at  $(0,0,0)$  and  $(0,1,0)$  gives us  $\partial B_x / \partial y$  at  $(0,0.5,0)$ . Subtraction of these two derivatives gives us the z-component of  $\nabla \times \mathbf{B}$  at  $(0.5,0.5,0.5)$  – this point is the center of the cube with corners at the points used to compute

---

<sup>1</sup>It is true that it is not mathematically necessary to normalize  $\mathbf{B}$ , i.e.,  $\partial\mathbf{l}_1/\partial s = \mathbf{B}$  will give you a curve  $\mathbf{l}_1(s)$  that is simply a reparameterization of  $\mathbf{l}(s)$ . However, it makes sense numerically to normalize  $\mathbf{B}$  in order to have a uniform step size.

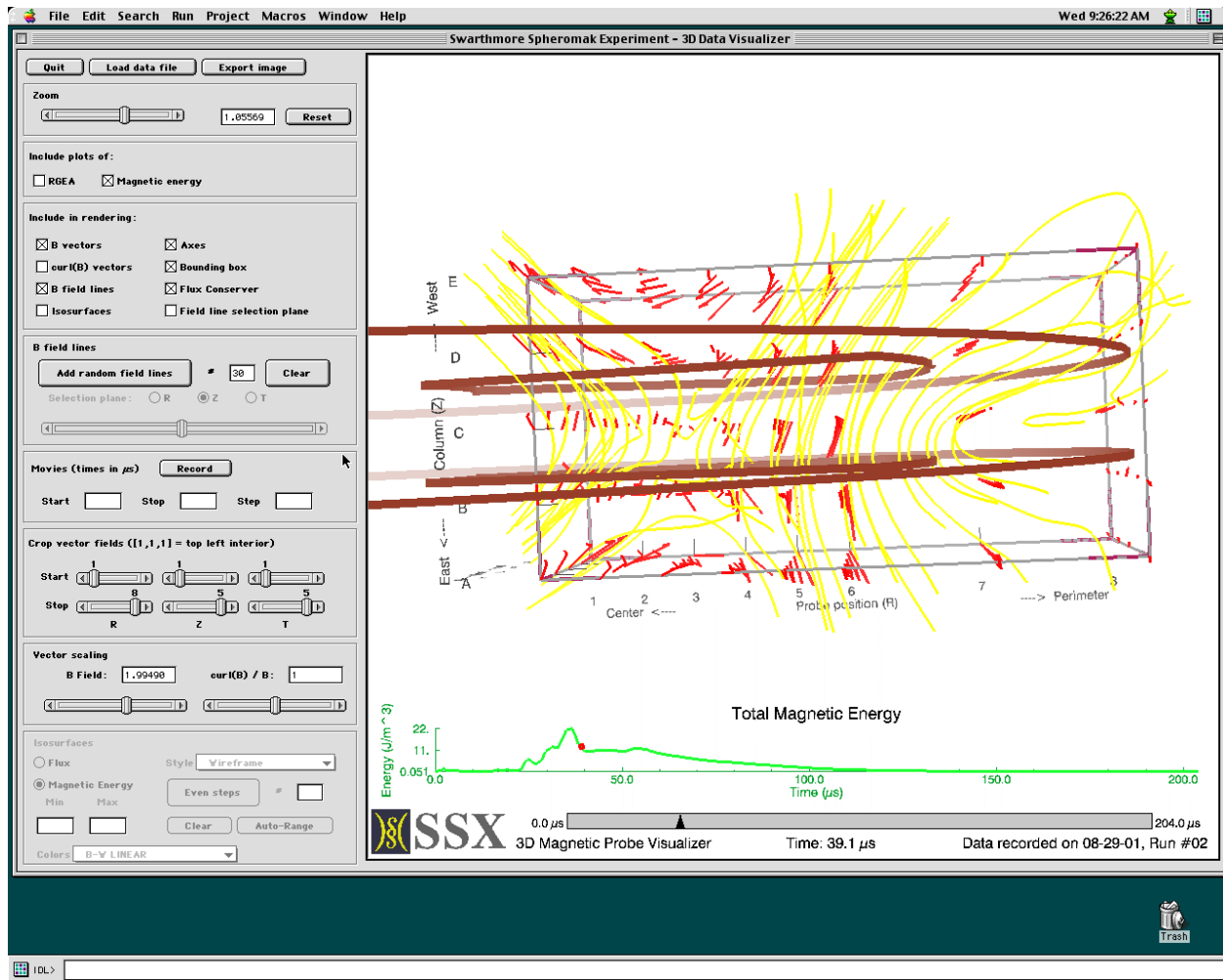


**Figure 3.13:** Screen shot from the first custom IDL visualization package. The display currently shows reconnected fieldlines leading between the two spheromaks. The flattened rings through the data are an end-on representation of the end disks of the flux conservers, together with the annular-wedge holes that allow reconnection.

this and the other components. Note that we need a pair of points to compute any one derivative, so our *five* columns of probe stalks will only give us *four* z-derivatives for each x- and y-coordinate. Thus, when we compute  $\mathbf{J}$ , we only know it for a  $7 \times 4 \times 4$  grid. We can interpret this grid of points to be the center of each “cube” of  $\mathbf{B}$  measurements.

Yet another computable quantity is the magnetic energy density, which is defined to be  $B^2/2\mu_0$ . From this field, we can also approximate the *pressure gradient field*,  $\nabla p$ , from a “pressure-balance” condition as follows. Start with the MHD equation of motion (Equation 2.23):

$$\rho \widetilde{\frac{d\mathbf{u}}{dt}} = \rho \left( \frac{\partial \mathbf{u}}{\partial t} + (\mathbf{u} \cdot \nabla) \mathbf{u} \right) = -\nabla p + \mathbf{J} \times \mathbf{B} \quad (3.6)$$

Using Ampère’s law to substitute for  $\mathbf{J}$  and applying a vector identity we get:

$$\rho \left( \frac{\partial \mathbf{u}}{\partial t} + (\mathbf{u} \cdot \nabla) \mathbf{u} \right) = -\nabla p + \frac{1}{\mu_0} (\nabla \times \mathbf{B}) \times \mathbf{B} \quad (3.7)$$

$$= -\nabla p - \frac{1}{2\mu_0} \nabla(B^2) + \frac{1}{\mu_0} (\mathbf{B} \cdot \nabla) \mathbf{B} \quad (3.8)$$

In SSX,  $\mathbf{B}$  is more or less perpendicular to  $\nabla B_i$ , so we drop the last term on the right<sup>2</sup>. Lastly, we wish to show that the velocity terms on the left can be ignored. Let us plug in some typical values, using the Alfvén speed for  $u$  (a generously large estimate) and the Alfvén crossing time between probe locations  $2 \text{ cm}/u_{Alf}$  for the time scale (generously small).

$$\rho \frac{\partial \mathbf{u}}{\partial t} \sim (1.67 \times 10^{-27} \text{ kg})(10^{20} \text{ m}^{-3}) \frac{10^5 \text{ m/s}}{2 \times 10^{-7} \text{ s}} \sim 8.4 \times 10^4 \text{ kg/m}^2 \text{s}^2 \quad (3.9)$$

$$\rho(\mathbf{u} \cdot \nabla) \mathbf{u} \sim (1.67 \times 10^{-27} \text{ kg})(10^{20} \text{ m}^{-3}) \frac{(10^5 \text{ m/s})^2}{0.02 \text{ m}} \sim 8.4 \times 10^4 \text{ kg/m}^2 \text{s}^2 \quad (3.10)$$

$$\frac{1}{2\mu_0} \nabla(B^2) \sim \frac{1}{8\pi \times 10^{-7} \text{ Tm/A}} \frac{(0.1 \text{ T})^2}{0.02 \text{ m}} \sim 2.0 \times 10^5 \text{ kg/m}^2 \text{s}^2 \quad (3.11)$$

Thus, the velocity terms are about 40% as significant as the  $B^2$  term when the flow speeds are greatest. This is not small enough that we can ignore the terms. However, if we suspect that the flow speeds are less than  $u_{Alf}$  then the velocity terms – which go like  $u^2$  – rapidly fall to the range in which we can neglect them compared to  $B^2$ . In this case, once we compute  $B^2/2\mu_0$  we find the pressure gradient field by:

$$\nabla p = -\frac{1}{2\mu_0} \nabla(B^2) \quad (3.12)$$

Conceptually, you can think of this condition as stating that there is a balance between magnetic pressure and conventional thermal pressure. It is a shaky approximation that cannot be used when we expect rapid flows, but when it is valid it gives us a remarkable ability to find *spatial variation in pressure* from our magnetic field measurements.

### 3.3 Particle Measurements

Diagnostics known as a “Retarding Grid Energy Analyzers” (RGEAs) are used in SSX to measure high-energy particles. The devices point into the vacuum chamber and use an electrical potential barrier to block all particles below some energy  $V$ .  $V$  can be set to different values between shots. The RGEAs then measure the current of particles that make it past the potential barrier (i.e., the number of particles above that energy).

SSX is equipped with two RGEAs (Figure 3.7). RGEA1 sits atop the vacuum chamber and points normal to the reconnecting fields. RGEA2 sits on the side of the chamber and is directed parallel to the reconnecting fields. Recall

---

<sup>2</sup>It would have been easy enough for us to keep this term, since it can be easily computed from our  $\mathbf{B}$  data, but this fact was not discovered until the writing of this thesis when much analysis had already been completed.

that Matthaeus *et al.* found super-Alfvénic acceleration of particles normal to the reconnection layer in simulations. Thus, the two RGEAs are situated to detect two kinds of particle acceleration: RGEA1 detects acceleration due to the reconnection electric field normal to the incoming  $\mathbf{B}$  fields, while RGEA2 detects acceleration due to bulk flow out of the reconnection region.

The RGEAs have been in operation since before the 3D probe array was installed. It was indeed found that particles of super-Alfvénic energies were seen by RGEA1 while RGEA2 detected only Alfvénic energies. The RGEA1 measurements suggest the distribution of particles accelerated by reconnection possesses a drift energy of about 90 eV and a peak energy of 200 eV. These numbers are consistent with the expected reconnection EMF ( $uBL \sim 500$  V). These and other RGEA results have been documented by Schlossberg[49] and by Brown *et al.*[8, 9]. RGEA measurements will be related to magnetic measurements in the following chapter.

# Chapter 4

## Results and Discussion

### 4.1 3D Magnetic Field Probe Functionality

Several analyses were conducted using known magnetic fields to ensure the accuracy of the probe before its use in the SSX plasma. We first tested fields created by the Helmholtz calibration apparatus. One check is to compute  $\nabla \cdot \mathbf{B}$ , which should equal zero within experimental uncertainty (Fig. 4.1.A). Numerical computation of  $\nabla \cdot \mathbf{B}$  requires a comparison of adjacent values of the measured  $\mathbf{B}$ . Consequently, it was computed on a smaller grid of  $4 \times 4 \times 5$  points, the centers of each cube of  $\mathbf{B}$  values in the closely spaced probe region. We can thus compute the mean square deviation of  $\nabla \cdot \mathbf{B}$  from 0. This test suggests an uncertainty in  $|\mathbf{B}|$  of less than 25 gauss, in accord with expectations from digitizer resolution and other known sources of experimental error. A similar  $\chi^2$  test can be performed for  $\nabla \times \mathbf{B}$ . This quantity should be zero for the Helmholtz field since there are no moving charges in the measurement volume (Figure 4.1.B). Note that  $\nabla \times \mathbf{B}$  need not be zero for shots with plasma, in which there will be currents within the volume. This  $\nabla \times \mathbf{B}$  least-squares test suggests a similar level of error.

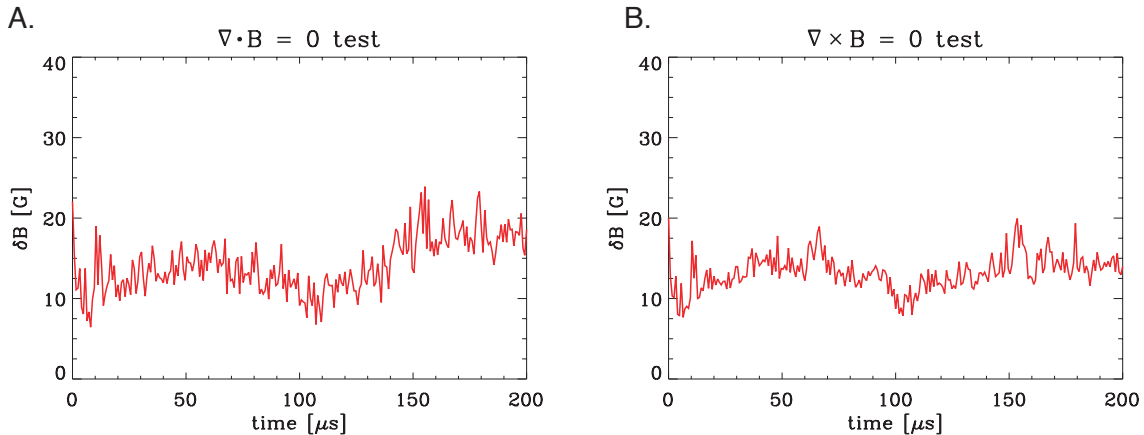


**Figure 4.1:** Analysis of probe accuracy for Helmholtz field.  $\chi^2$  analysis indicates if  $\nabla \cdot \vec{B} = 0$  then the uncertainty in  $|\vec{B}|$  is a reasonable 25 gauss. Since there are no current sources within the measurement volume,  $\nabla \times \mathbf{B} = 0$ .  $\chi^2$  analysis of  $\nabla \times \vec{B}$  results in a similar uncertainty.

For the following additional tests, a different simple field was generated by a long straight wire in the Z direction attached to the same high voltage pulsed power supply (Figure 4.3). The return loop had a radius of over 3 m, so the probe experienced approximately the field of an infinite line current:  $B(r) = \mu_0 I / 2\pi r$ .

One test performed on the wire field was to compute the current from the observed  $\mathbf{B}$  data to compare with the

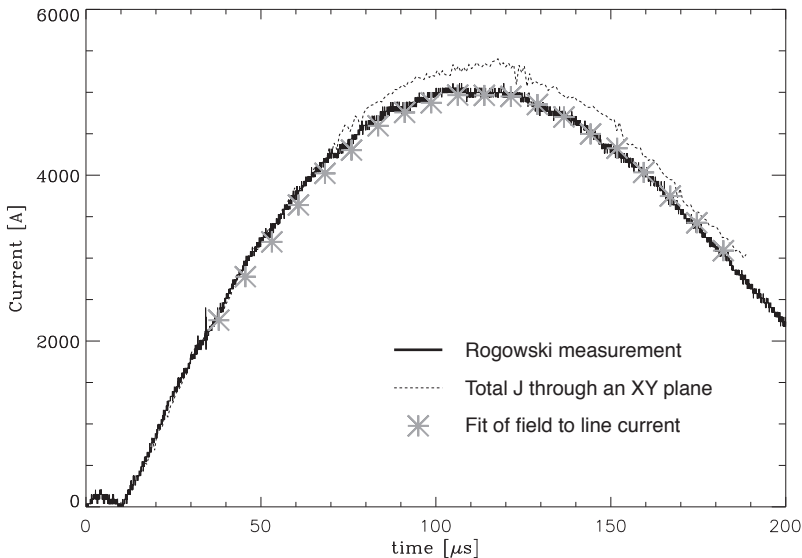


**Figure 4.2:** Analysis of probe accuracy for line current. The current in the wire was calculated by two methods from the probe data: by adding up  $\int (\nabla \times \mathbf{B}) \cdot d\mathbf{a}$ , and by fitting  $\mathbf{B}$  to a line current. These values compare well with the current measured by a Rogowski loop.

Rogowski current measurement.  $\mathbf{J} = (\nabla \times \mathbf{B})/\mu_0$  was computed on the  $4 \times 4 \times 5$  grid mentioned above. Since  $I = \int \mathbf{J} \cdot d\mathbf{a}$ , then summing  $J_Z$  over a given X-Y plane yields the total current  $I$  through that plane. For each such X-Y plane this value should equal the Rogowski measurement. Figure 4.2 shows the mean of these four computed  $I$  values versus the Rogowski value. Again, the measurements agree within the expected uncertainty.

Since we know the field for this configuration is due to a line current, we can also perform a fit to obtain another estimate of the current. The data were fit to infinite wire fields of variable position, direction, and current. The best fit position and direction qualitatively correspond to the actual position of the wire. Figure 4.2 illustrates the best fit current magnitude over time, which corresponds to the Rogowski current measurement within reasonable error.

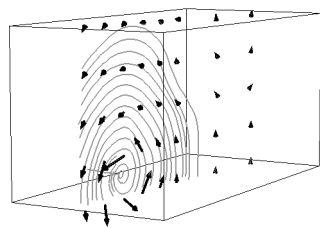
## 4.2 Plasma Measurements

This section describes analysis of SSX data that was performed by the author during Summer 2002. This analysis was rather open-ended, not a test of any particular hypothesis. It was rather a series of loosely connected computational experiments to see what sort of interesting information could be gleaned from the 3D  $\mathbf{B}$  vector field. Among the noteworthy results are the following, which will be discussed in further detail in the coming sections:

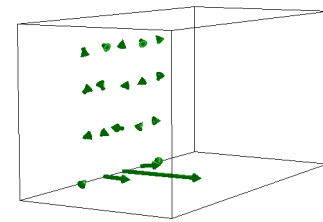
- There are two time periods of interest: the initial high-velocity impact between the spheromaks, and a quasi-equilibrium period of slow decay.
- Fieldlines clearly run from one spheromak to the other, conclusively demonstrating that reconnection has occurred.
- The geometry of the incoming spheromak fields turns out to produce a configuration somewhat resembling the 2D picture, but skewed so that the “plane” of reconnection is at a roughly  $45^\circ$  angle in the  $xy$  plane.
- The actual fields differ to a small degree from a “skewed 2D” configuration in two ways. First, there is an out-of-plane component of  $\mathbf{B}$  unique to the *center* of the field null region (i.e., the X-line). Secondly, the geometry of spheromak fieldlines causes the reconnection “planes” to be slightly curved.



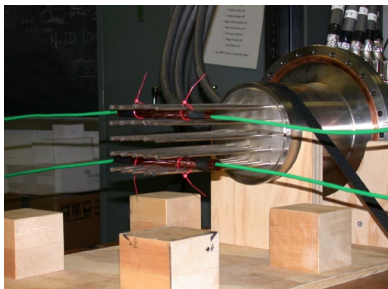
A.



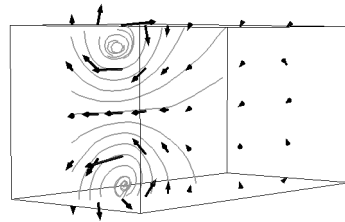
B.



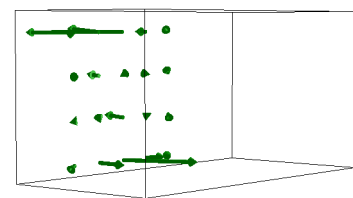
C.



D.



E.



F

**Figure 4.3:** Demonstration of the 3D magnetic probe measuring a line current. The experimental setup is shown in A. B shows the measured field as seen from the same perspective. One plane of  $\mathbf{B}$  vectors is shown along with several fieldlines. In C,  $\mathbf{J}$  is numerically computed from  $\nabla \times \mathbf{B}$ . D-F show the results for two antiparallel line currents.

- This inherent curvature of the fields prevents us from conclusively testing for the existence of the quadrupole moment predicted by the computational studies of collisionless reconnection.
- Comparisons with shots in which only one spheromak is produced suggest that reconnection is still occurring in the equilibrium/decay period.
- It is mathematically possible to compute the vector field of *convective derivative of velocity*, and this field is consistent with the occurrence of reconnection late in the shot.
- We can estimate the magnitudes of each term in the generalized Ohm's law. Resistivity seems far less significant than the Hall and pressure forces.
- We observe a momentary upward-directed current that is likely related to the observation of accelerated particles by the RGEA.
- “Full-merging” experiments were conducted in which the spheromaks were allowed to reconnect along a much larger surface. The physics seems identical with the earlier (“partial-merging”) shots.
- The 3D probe seems to have a non-negligible slowing effect on the plasma.

We now proceed to discuss each of these lines of analysis in more detail.

### 4.2.1 Overview of a Typical Shot

The 3D magnetic field probe was inserted into SSX to measure the field of a two-spheromak merging event. Figure 4.4 shows a typical measurement. This figure introduces a convention that will be used frequently, in which thick vertical lines on an overhead magnetic energy plot indicate the times in the shot represented by the accompanying frames. The second row in the figure presents the  $\mathbf{B}$  vectors. The bottom row shows fieldlines traced through these vector fields. The density of fieldlines in these images is proportional to the field strength, and the color of each line is chosen randomly so the lines can be distinguished. The computation of fieldlines is somewhat tricky, and is discussed in more detail on page 110.

The field activity can be divided up into several epochs of qualitatively different behavior. We will henceforth refer to times in microseconds after the high-voltage ionizing pulse is triggered. In the first  $20 \mu\text{s}$  the field is zero to within the precision of the probe. During this time the spheromaks are forming and moving away from the plasma guns towards the machine midplane.

In the next “driven epoch,” from  $20 \mu\text{s}$  to about  $40 \mu\text{s}$ , we observe the arrival of the spheromaks. They usually do not arrive at the exact same moment due to slight variation from shot to shot in the charge on each capacitor bank and the chaotic nature of the plasma evolution. Thus, often we see the field in the probe region first dominated by one spheromak. The other one then arrives and pushes the first out of the center, producing a reconnection X-point. After a few microseconds the jostling dies down and the probe volume is roughly equally divided between the two spheromaks.

The third and longest period is an “equilibrium/decay epoch,” during which this structure fades away. The field’s decay follows a roughly exponential time course, with a time constant close to  $40 \mu\text{s}$ . There is very little change in the fields during this period other than an overall scaling of all the field vectors by the  $\sim \exp(-t/40 \mu\text{s})$  factor.

## The Averaged Dataset

A series of 36 shots was conducted with identical equipment parameters. These shots were both examined individually, and also averaged together to produce a single file of the same format as each individual shot. Since the spatial and temporal variation is somewhat smoother in this file than in “real” shots, it was sometimes advantageous to employ this 36 shot average in some of the following analyses.

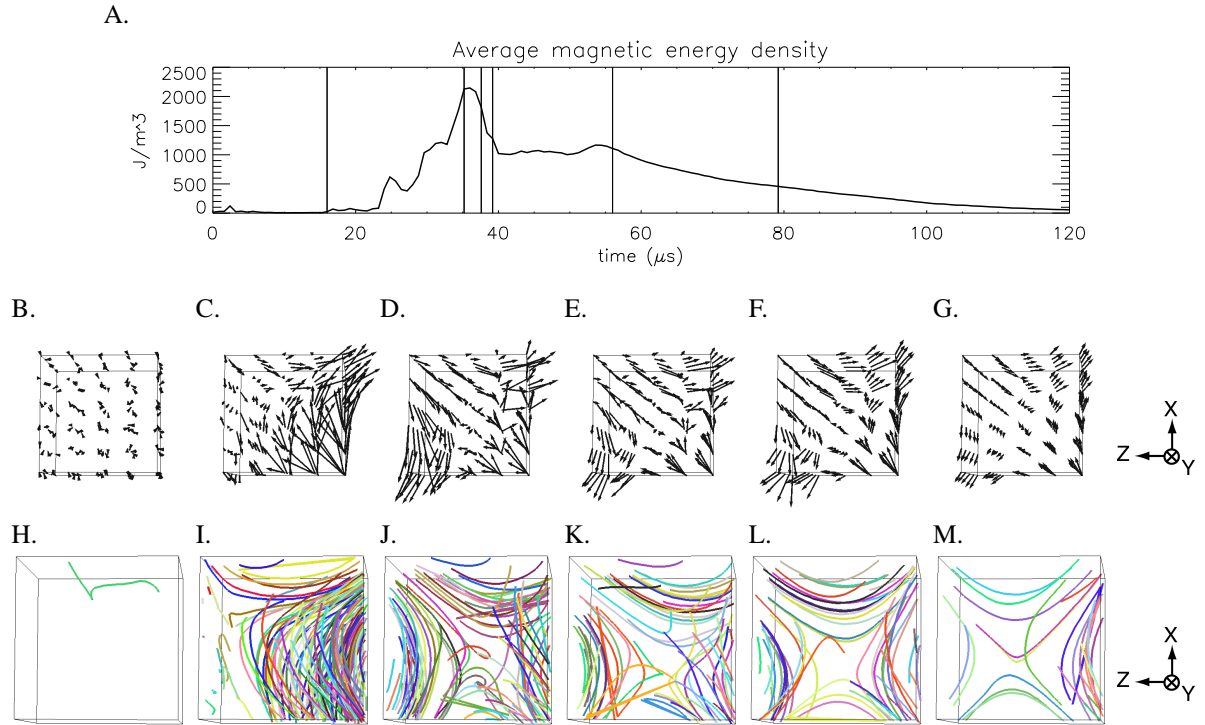


**Figure 4.4:** A typical spheromak merging shot in SSX. A: A plot of the average magnetic energy density in the volume ( $B^2/2\mu_0$ ) shows how the plasma arrives suddenly, “bounces around”, and then decays exponentially. Below are the magnetic field vectors looking down on the probe array, with the spheromak guns to the left and right. B: There is little signal before plasma arrives at the probe. C-E: The spheromak to the right arrives first, then the one on the left. F-G: There is little change except for exponential decay once equilibrium is established. H-M depict fieldlines for the same times.

## 4.2.2 Magnetic Evidence for Reconnection

Before the installation of the 3D magnetic probe there was ample evidence that reconnection of the spheromaks was happening – such as a burst of high-energy particles measured by the RGEAs concurrent with the peak in magnetic energy observed by the 2D array[28] – but there was always an alternate possibility. Perhaps the plasma really *was* ideal; perhaps the spheromaks simply ran into each other without the field topology changing, and the burst of particles was merely a coincidence. However, with the introduction of the 3D probe array we are able to further demonstrate the existence of reconnection in SSX.

### Inter-Spheromak Fieldlines

It was not possible to trace true fieldlines with only two-dimensional data. Data from the 3D array, however, demonstrates that many fieldlines in the equilibrium/decay epoch clearly lead from one spheromak to the other, as Figure 4.5 shows. No fieldlines initially connect the two halves of the machine, so reconnection must have occurred.

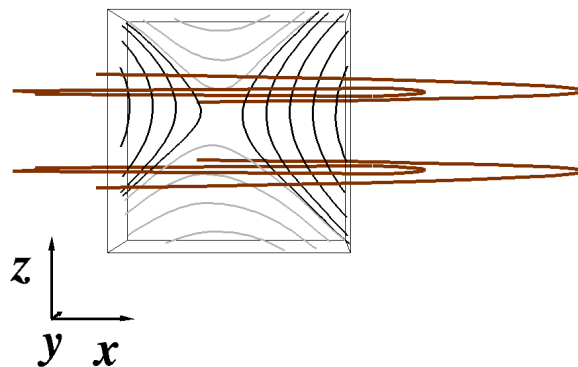


**Figure 4.5:** A view of some magnetic fieldlines looking down from above during the equilibrium/decay epoch demonstrates that reconnection has occurred. The gray lines “belong” to either one spheromak or the other, but the black lines connect the two spheromaks. The rings represent the flux conserver walls, and the chevron holes are barely visible due to the perspective.

### The Best-Fit Reconnection Plane

Spheromak fieldlines follow roughly helical paths around a torus, as discussed in Section 2.1.3. As Figure 4.6 shows, these fieldlines will thus cross the flux conserver holes at some angle that depends on the incline of the helix. If the two spheromaks are given opposite helicities, as they were for most shots, then this angle of the field should be roughly the same for each spheromak. This hypothesis is borne out in the observations. A view of the equilibrium/decay-epoch fields towards the  $+z$ -direction (figure 4.7) shows that the fields for much of the volume lie roughly along the same angle in the  $y$ - $z$  plane, around  $45^\circ$  on average. To more precisely determine the value of this angle, the following regression procedure can be used. We can consider the simple model that the  $y$ -component of  $\mathbf{B}$  is a linear function of the  $x$  and  $z$  components,  $B_y = \alpha B_x + \beta B_z$ . We expect roughly  $\alpha \approx -1.0$ ,  $\beta \approx 0.0$  (There might be some small  $z$ -coordinate dependence due to different absolute helicities between the two spheromaks, for example). Using the 200 measured  $\mathbf{B}$  vectors for some particular shot and time, we may use a linear fit to find the best values for  $\alpha$  and  $\beta$ . Typical results are  $\alpha = -0.9$  and  $\beta = -0.04$ .

If we were to look at a thin slice of data at this angle, it would look approximately like the pictures used by theorists to describe 2D reconnection. In Figure 4.8 we again see the same typical shot, but here we examine only the field in this best-fit plane. The measured  $\mathbf{B}$  data are interpolated along the plane and the view rotated so that we look normal to it. The density of measurements appears to be higher than it actually is because interpolation was being performed. From these slices the similarity in topology to 2D models can be seen.

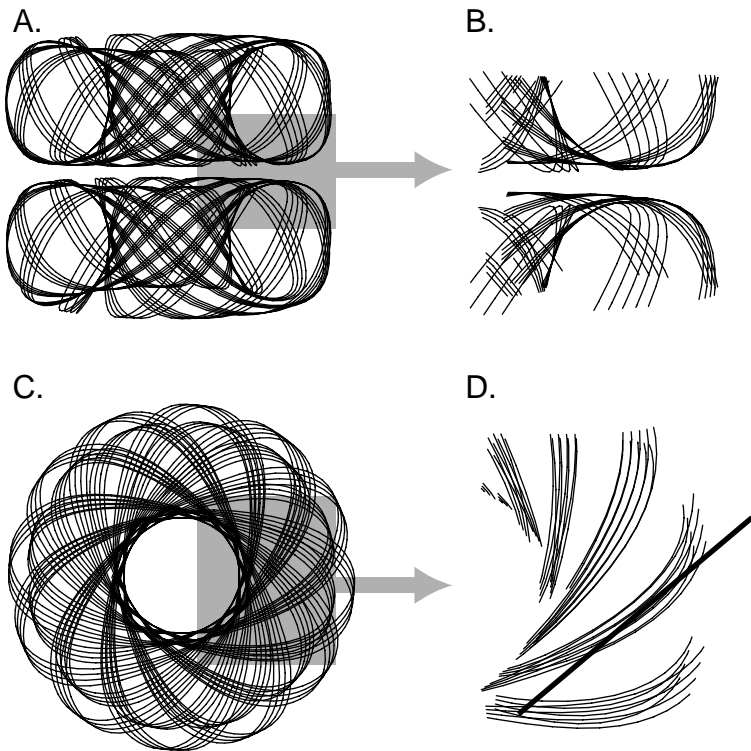


**Figure 4.6:** A and C are spheromak fieldlines, integrated from the analytical solution. If we zoom in near a region in which opposite helicity spheromaks are adjacent as in SSX, we see that the fieldlines lie at an inclined angle. Comparing the fieldlines with a straight line as in D, we also see that they are intrinsically curved. Note that in D, we have stripped away the fieldlines on the outside of the spheromak pair, which have opposite concavity from the inner lines. We do not have to choose the precise equations for the fieldlines that we did in Section 2.1.3 in order to see these angle and curvature effects. These effects also appear in just about any curve that cycles around in a bent helix (e.g., “torus knots”).

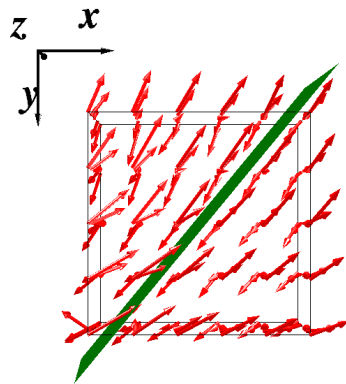


**Figure 4.7:** When viewed along the axis of the vacuum chamber, the equilibrium fields seem to lie in the plane normal to  $(1,1,0)$ .

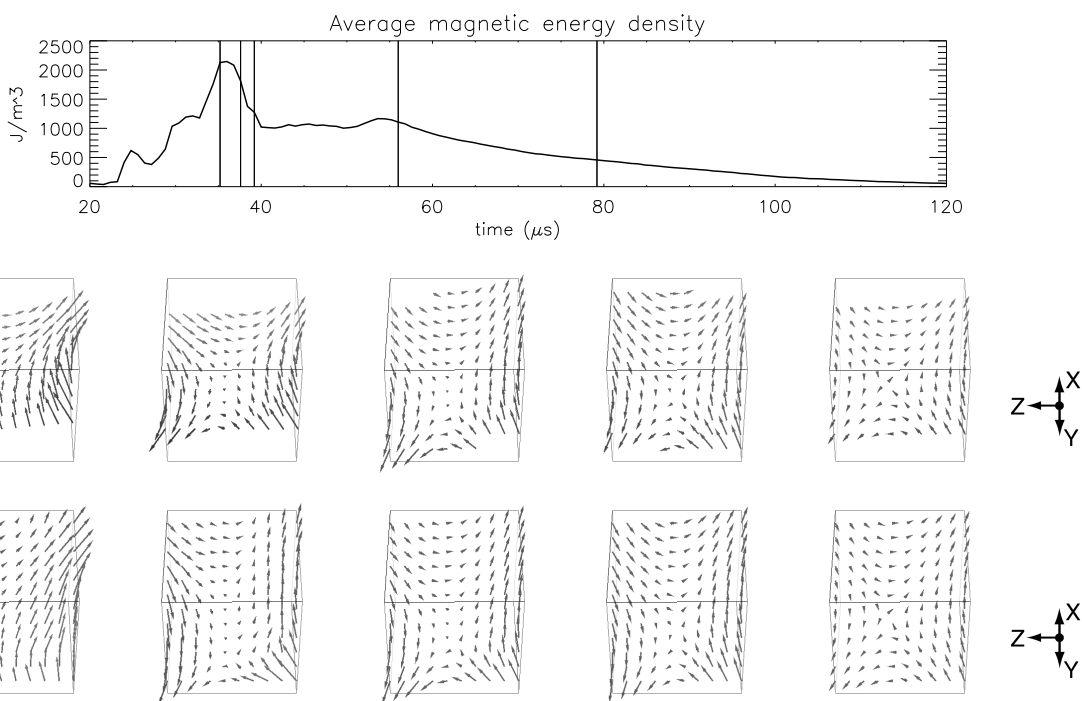


**Figure 4.8:** A slice through the magnetic field for a typical shot (run 2, 8/9/01). In A, a separate best-fit reconnection plane is calculated for each image, while every shot in B uses the same plane. The arrows shown are interpolated from the actual data, so the spatial resolution is not actually as good as it appears.

## Two Kinds of Reconnection?

The careful reader may have noticed that it is not clear when reconnection *stops* in our typical shot. When we show fieldlines leading from one spheromak to the other by  $40 \mu\text{s}$  into the shot, it is because reconnection happens when the two spheromaks impact on each other upon arriving at the machine midplane.

However, the slices shown in Figure 4.8 continue to show an x-point through the equilibrium/decay epoch, suggesting reconnection may still be occurring during this period. However, there is not necessarily any *inflow* this late into the shot, and this inflow may be crucial for driving reconnection. Clearly, reconnection happens when the spheromaks arrive, but does it continue even after this initial collision, when there may not be any bulk flow pushing the plasma together? Perhaps all the reconnection has occurred by  $t = 50 \mu\text{s}$  and the fields afterwards just *look* like a reconnection configuration, even though there is no further reconnection. Even if there is reconnection during this decay period, it may have a very different character than in the initial driven period. The relevant terms in Ohm's law might be different from one period to the other. We will keep this distinction in mind between the *driven* reconnection phase and the *steady-state* reconnection phase as we analyze the experimental results.

## Observation of Spheromak Equilibrium Fields

It is an interesting exercise to plot the measured equilibrium fields along with a theoretical prediction for spheromak fields. In Section 2.1.3 it was discussed that an analytical solution exists for a spheromak in a cylindrical flux conserver. The SSX spheromaks do not live in such ideal boundary conditions, due to the holes at the midplane and the extension of the conservers around the plasma guns. However, Geddes [20] found the latter to modify the equilibrium by very little in computational equilibrium calculations, and it is the effect of the former in which we are interested. Thus, inputting the flux conserver diameter and length into Equation 2.32 we can obtain a theoretical prediction for the  $\mathbf{B}$  field at each probe location - if there were no holes in the conservers. Figure 4.9 shows this comparison.

The theoretical model consistently predicts a shallower angle for the field in the xy-plane. This effect is largely due to the fact that the analytical spheromak solution (Equation 2.32) predicts a purely radial field up against the wall of the conserver, with an increasing theta-component as you move inwards from this wall<sup>1</sup>. The real spheromaks do not stop at the plane of the conserver wall, because the chevron holes allow them to protrude into the inter-conserver space. Thus, a better fit, as shown in Figure 4.9.C, is obtained by taking the edge of the spheromak to actually be the *beyond* the conserver wall by 1 in. However, neither positioning of the equilibrium gives an accurate model for the z-component of the fields. In the analytical solution this component is very small, and yet in SSX a z-component is observed that is on the order of the x- and y-components. It is likely that this large z-component is due to the flux conserver walls. Although the holes allow the spheromaks to protrude into the inter-conserver region near the probe volume, the fieldlines cannot cross the walls surrounding the region. Thus, they need to bend in the z-direction to form this "bulge" at the chevrons.

## Skewed Reconnection

In "2D" reconnection, it is understood that the plasma has a third dimension to it, but that nothing interesting happens in that direction. The world consists of planes such as those in Figure 4.8, all stacked *exactly* on top of each other. However, if one was to divide the probed volume in SSX into a stack of such planes, they would instead be *skewed*. This can be seen as follows.

In Figure 4.8, the central point of reconnection is distinguishable by the fact that the magnetic field is very weak at that point. The set of centers of each reconnection plane, then, is equal to the region of space with the lowest magnetic field magnitude - and thus the lowest magnetic energy density. Figure 4.10 shows an isosurface of magnetic energy density at a small value. It is evident that this "tube" of reconnection centers points more or less in the y-direction,

<sup>1</sup>This effect can also be seen in SSX shots, particularly for those in which only one plasma gun is fired. As there is no opposing spheromak to block it, the plasma moves far enough into the probe volume to observe the steepening of the fields further into the spheromak.

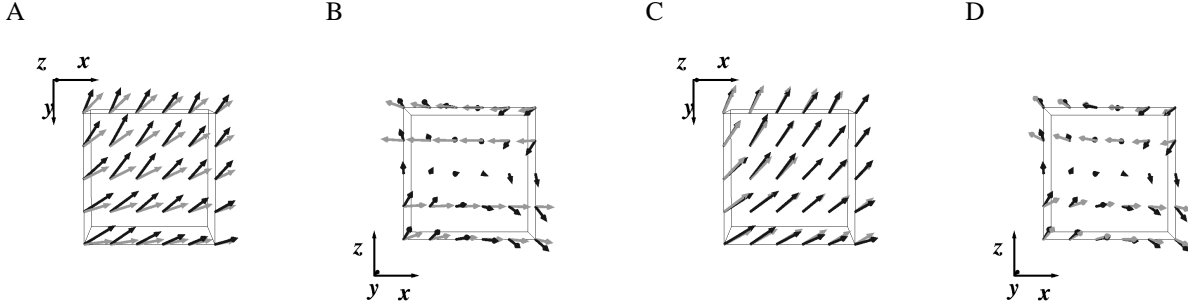


**Figure 4.9:** Comparing the measured magnetic field to the force-free equilibrium prediction. A: Only one vertical plane of vectors is shown - the West-most vertical plane of one spheromak. The theory correctly predicts that B is at an incline and concave up, but its quantitative prediction of the angle is incorrect. B: A bird's eye view shows that the theoretical model does not predict much  $B_z$ , although the data show a sizable z-component. C: Setting the edge of the analytical spheromak to be past the actual wall of the conserver produces a much better fit in the xy-plane. D: the z-component is still incorrect, however.

and *not* perpendicular to the  $\sim 45^\circ$ -inclined reconnection planes. If we think of each reconnection plane as a playing card, then the observed volume in SSX is like a skewed stack of such cards.

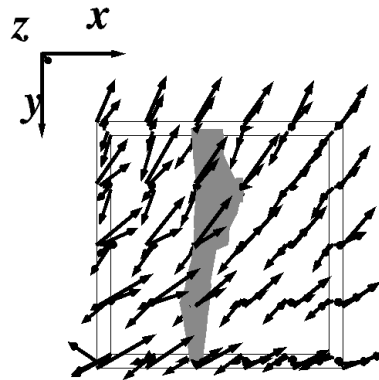


**Figure 4.10:** The shaded volume represents points with less than 2.5% of the maximum magnetic energy density - equivalently, the region of weakest magnetic field. In 2D reconnection models this region should lie perpendicular to the plane of reconnection, which was shown earlier in Figure 4.7. Here this is not the case.

This angle difference can be quantified. Recall that the  $\nabla p$  field can be constructed by taking the gradient of the magnetic energy density. Thus, the tube of energy-density-minima points perpendicular to these  $\nabla p$  vectors. A regression model just like the one described in the previous section can be used to construct an equation for the plane in which the  $\nabla p$  arrows tend to point. The normal to this plane would – if SSX reconnection were 2D – equal the normal to the best-fit reconnection plane. Instead, as Figure 4.11 shows, they differ by roughly  $45^\circ$ .

One possible explanation for this skewness is to image the spheromaks as two doughnuts being placed together so that they touch along a circle. In the region of the doughnuts analogous to where we place our magnetic probe, this circle of contact is approximately a vertical line. Since the spheromak fieldlines follow roughly toroidal surfaces like those of the doughnuts, we should expect that the x-line should follow a similar roughly vertical line.

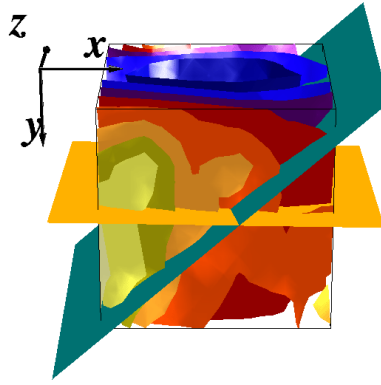


**Figure 4.11:** Another way to visualize the skewness of the reconnection in SSX. The diagonal plane is the best-fit reconnection plane, as before. The curved surfaces are surfaces of constant  $|\mathbf{B}|$ . Thus, the line of  $x$ -points is the central surface. All the surfaces are approximately vertical cylinders. The horizontal plane is a “best-fit null-line normal plane” It is obtained by applying linear regression to the  $\nabla(|\mathbf{B}|)$  vectors, which should make it normal to the axis of the cylindrical surfaces. The roughly  $45^\circ$  difference between the planes is apparent.

## Inherent Field Curvature

Another difference between ideal 2D reconnection and that observed in SSX is that the SSX reconnection “plane” cannot truly be planar because of the source of the reconnecting flux. A glance back at Figure 4.6 shows that not only should the fieldlines cross the measurement volume at an angle, but also that they should be *curved*. Indeed, when we look at the equilibrium fields towards  $+z$  (Figure 4.7) the fields are slightly steeper towards the top and left than they are at the bottom and right. Spheromak fields are inherently curved, so it is only an approximation to say that there is any reconnection *plane* at all.

This curvature poses a problem with one important test we attempted on SSX data. Recall that the computational models of Shay *et al.* predicted the formation of a quadrupole structure in the out-of-plane  $B$  field due to the Hall effect. We hoped to look for this theoretical prediction in our data. Unfortunately, the inherent curvature in the spheromak fields is *exactly* the same thing – a quadrupole in the out-of-plane  $B$  component! SSX data do unambiguously show a quadrupole, but it is impossible to disentangle the two possible causes. It happens that the inherent quadrupole has the same sense (i.e., the same direction in each quadrant) as the Hall effect prediction. Since we do have a fairly good fit between our observed fields and the theoretical spheromak equilibrium fields, we tried subtracting the theoretical  $\mathbf{B}$  from our measured  $\mathbf{B}$  to see if there was a significant *residual* quadrupole. Unfortunately, the fit was poor enough that there is too much noise to see any signal. This subtraction test was complicated by the fact that the fit has two free parameters – the overall scale of the field and how far past the flux conserver wall to translate it. Over the range of these two parameters that resulted in reasonable fits to SSX data, the data-minus-theory field could show a quadrupole of the right orientation, no quadrupole, or a quadrupole of the opposite orientation. In short, the inherent curvature and general asymmetry of the SSX geometry made it impossible to conclusively test for Shay’s quadrupole.

## Swept-Sheared Fieldlines

There appears to be a significant out-of-plane component of the magnetic field localized in the center of the reconnection region. This can be seen by tracing fieldlines forwards and backwards from various points in a single best-fit reconnection plane, as shown in Figure 4.12. The fieldlines generally remain within the plane, but the ones that go through the minimum- $B$  region clearly leave the plane a bit more than the others. We have termed this to be a “swept-sheared” structure. This observation has been discussed in several SSX publications[9, 8].

This structure is significant because, presuming there is an electric field normal to the reconnection plane as in 2D models, there is a non-zero component of  $\mathbf{B}$  along this  $\mathbf{E}$ . Consequently, the plasma particles will be held in the center

of the reconnection region longer than if  $\mathbf{E} \cdot \mathbf{B} = 0$  (as in the Sweet-Parker configuration), giving these particles more time to be accelerated by the electric field there. Thus, this normal component of  $\mathbf{B}$  may be closely related to the super-Alfvénic particles observed.

## Summary: SSX Is More 2D than 3D

The previous sections have discussed how the SSX magnetic field differs from the canonical 2D Sweet-Parker picture. However, it must be emphasized that by our original definition the SSX field is still basically 2D: nothing varies significantly in the  $y$  direction. True,  $\mathbf{B}$  has a *component* along  $\hat{\mathbf{y}}$  (whereas it had no out-of-plane component in the Sweet-Parker picture), but it does not *vary* along  $\hat{\mathbf{y}}$ . Despite our efforts to make SSX have an interesting 3D geometry, then, it turns out that by our strict definition the field ended up being 2D! We are not really getting our money's worth out of the 3D probe array, for a 2D grid of loop-triples (to measure *vector*  $\mathbf{B}$  on a *square* grid) would provide almost equal information (assuming we already knew to expect that nothing varied with  $y$ ).

### 4.2.3 Decay-Epoch Reconnection

The field patterns during the equilibrium/decay epoch look like a reconnection pattern, but we do not know if there is still inflow, and so we cannot tell directly how fast reconnection is proceeding. There is a sizeable radial current even during this period, and so there may be at least Ohmic dissipation. However, there are other ways we can attempt to show that reconnection is still occurring.

#### Comparison with One-Spheromak Shots

The most direct piece of evidence is that the spheromaks decay faster when there is another spheromak present to reconnect with. A decaying exponential function can be fit to the magnetic energy trace, both for shots in which only one plasma gun is fired (one spheromak), and also for normal shots (two spheromaks). Figure 4.13 illustrates a histogram of the decay constants for each type of shot. The mean decay constant for single-bank shots is more than two standard deviations from the mean for two-spheromak shots, indicating a significant effect. Something in the interaction between the two spheromaks is acting as a sink of energy, causing the two structures to decay faster when they interact than they would decay in isolation.

How much of the total energy dissipation is due to this spheromak-spheromak interaction effect, and how much is due to the normal effects which cause the decay of an isolated spheromak? We can model the situation as in Figure 4.14, as an inductor and two resistors in series. The spheromaks each act as an inductor, since they are in effect magnetic energy storage devices. Each resistor corresponds to one of the two dissipative processes. There are two numbers we can learn from Figure 4.13. One is  $\tau_G = 20.37 \mu\text{s}$ , the energy decay time for only the “general” decay effect – probably dominated by resistivity – which makes an isolated spheromak fade away. The other number is  $\tau_{G+R} = 17.07 \mu\text{s}$ , the energy decay time when both the general and reconnection decay effects are present. A bit of circuit analysis on the system in Figure 4.14 shows that if both resistors are included,

$$\left( \begin{array}{c} \text{Proportion of initial magnetic} \\ \text{energy dissipated by } R_R \end{array} \right) = 1 - \frac{\tau_{G+R}}{\tau_G} = 16\% \quad (4.1)$$

For SSX, the total magnetic energy in the spheromaks after the equilibrium/decay phase begins is approximately  $(0.2 \text{ m}^3) \times (500 \text{ J/m}^3) = 100 \text{ J}$ , so about 16 J is dissipated by the reconnection effect.

There is certainly a substantial current flowing in the radial direction even during the equilibrium/decay epoch. Is it the case that Ohmic dissipation from the current is responsible for the  $R_R$  effect? If we treat the reconnection regions as a pair of  $1'' \times 5'' \times 5''$  resistors, we can calculate how much energy they should dissipate during the equilibrium/decay epoch. Each resistor carries a roughly uniform  $\mathbf{J}$  of approximately  $5 \times 10^6 \text{ A/m}^2$  through a  $1'' \times 5''$  cross-section, for a total current of  $I = 1.6 \times 10^3 \text{ A}$ . Using the Spitzer resistivity of  $\eta \sim 1.2 \times 10^{-5} \Omega\text{m}$ , then each slab’s total

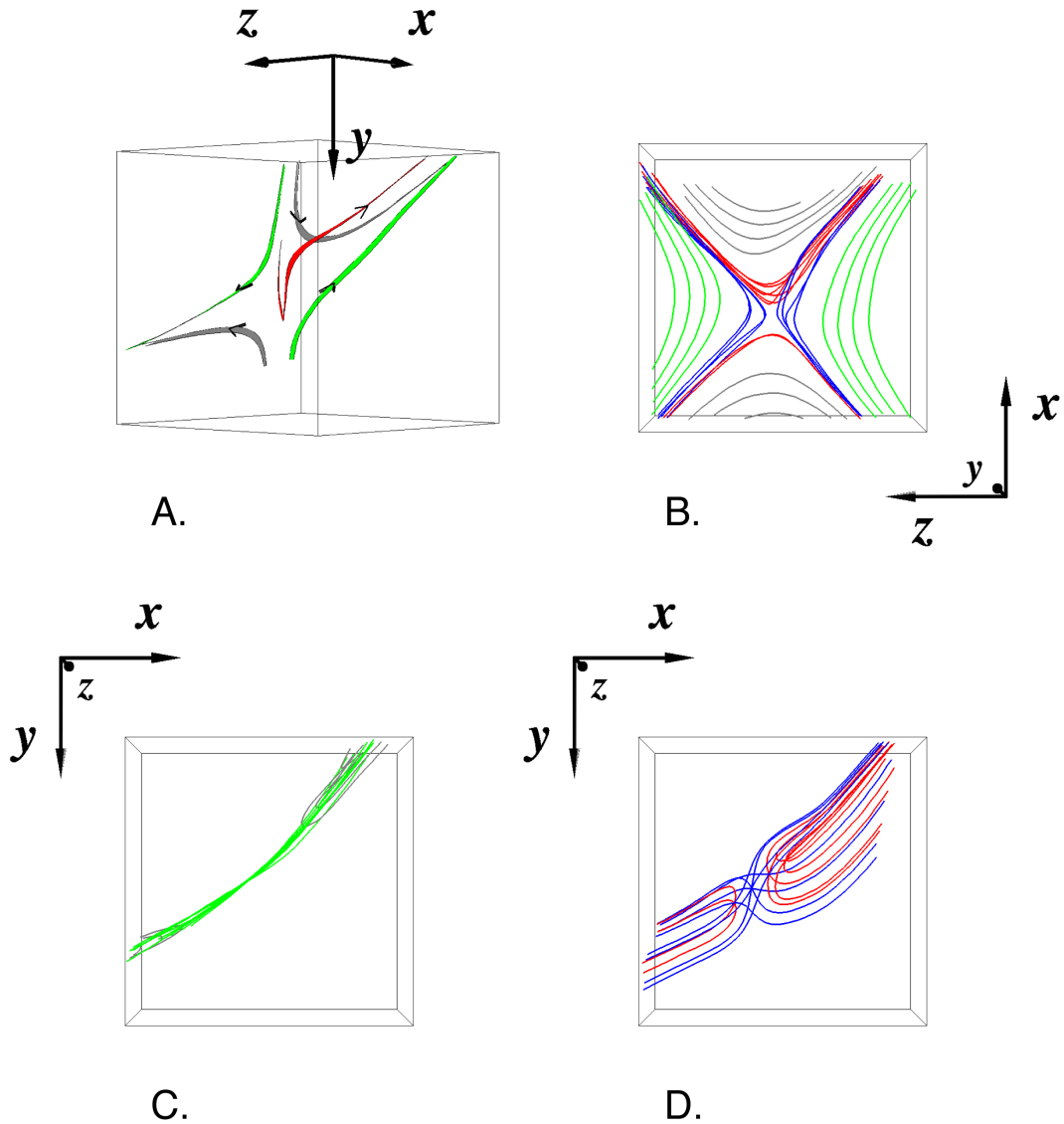


**Figure 4.12:** “Swept-sheared” fieldline structure. A. The fieldline in the center of the reconnection x-point has a significantly greater out-of-reconnection-plane component than for lines further from the point. This can also be seen by taking a set of fieldlines through a reconnection plane (seen from above in B) and dividing them into the ones far from (C) and near to (D) the x-point. When seen from the side (C-D) those near the x-point clearly have a greater out-of-plane component. From Cothran *et al.*[12]

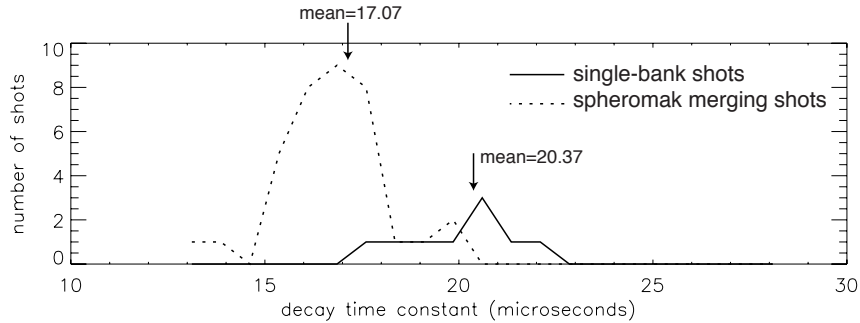


**Figure 4.13:** A histogram of magnetic energy density decay constants for single-bank and two-spheromak shots. Many more normal shots than single-bank shots were taken.

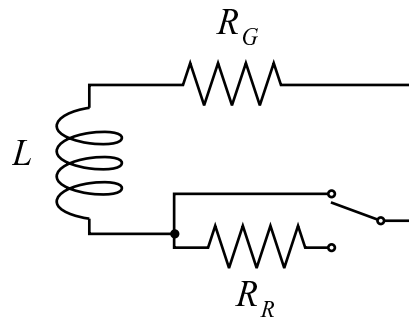


**Figure 4.14:** A circuit model of spheromak decay.  $L$  represents the inductive effect of the plasma,  $R_G$  is the general resistive decay process for isolated spheromaks, and  $R_R$  is an additional reconnection decay process present when the steep field gradient is produced in two-spheromak shots.

resistance is  $R = \eta L/A = 4.5 \times 10^{-4} \Omega$ . The current decays on a timescale of about  $\tau = 40 \mu\text{s}$ , so the total dissipated energy per ‘‘resistor’’ is  $E = P\tau = (I^2 R)\tau = 4.7 \times 10^{-2} \text{ J}$ . The total power dissipated by Ohmic heating in the two chevron reconnection regions then is twice this number, or roughly 0.1 J. We determined in the previous paragraph that approximately 16 J were dissipated by reconnection in order to produce the observed difference in decay rates between one- and two-spheromak shots, more than two orders of magnitude more energy. Thus, resistivity cannot account for the difference in decay rates. A non-ideal and non-resistive effect is indeed likely to be present in the equilibrium/decay epoch.

## Reconnection Flow Patterns?

The final piece of evidence supporting reconnection during the equilibrium/decay epoch comes from looking at the flow pattern during this period. Unfortunately, we have no way to calculate  $\mathbf{u}$ , but we *do* have a way to calculate its *convective derivative*. In Section 2.1.3 we introduced the plasma equation of motion:

$$\rho \frac{d\mathbf{u}}{dt} = -\nabla p + \mathbf{J} \times \mathbf{B} \quad (4.2)$$

where  $\frac{d}{dt}$  is the convective derivative (Section 2.1.1). During the equilibrium/decay epoch we can approximate the right-hand side. We do not know the spatial variation of the mass density  $\rho$  well but we know a line-averaged value from other diagnostics (interferometry and spectroscopy), so we at least know the *direction* of  $\frac{d\mathbf{u}}{dt}$ . Unfortunately, there are many fields  $\mathbf{u}$  consistent with a given  $\frac{d\mathbf{u}}{dt}$ , so we cannot ‘‘integrate’’ to find the flow pattern.

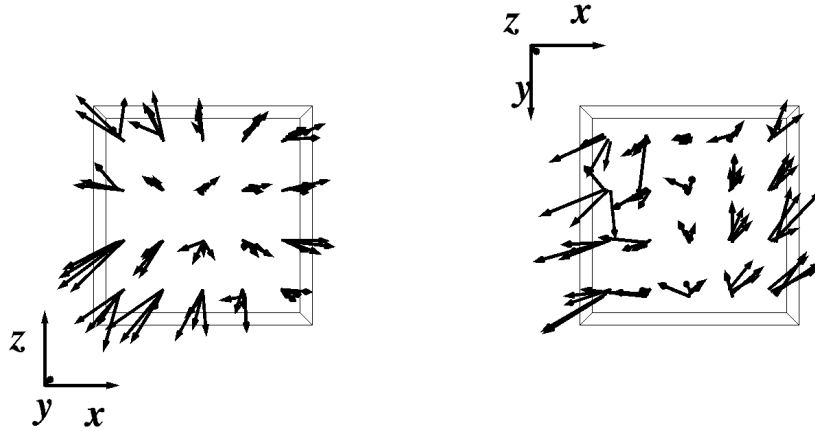


**Figure 4.15:** Calculation of the convective derivative of velocity at  $t = 64 \mu\text{s}$ .

Figure 4.15 shows  $\frac{d\mathbf{u}}{dt}$  if we take  $\rho$  to be uniform over space. These vectors - convective derivative of velocity - indicate the force that the fluid feels at a point in space. The most noteworthy feature is the radial field as seen in the bird’s eye view on the left. You can see that we did not pick just any field for Figure 2.1 when we introduced the convective derivative. We saw in that earlier figure that *one* possible flow pattern which can generate a radial convective derivative is a flow in from two sides and out the other two sides. Mapping this onto the SSX geometry, we see that this *could* indicate flow coming in from the spheromaks and out between the flux conservers. This is exactly what we would expect if reconnection were occurring during this period (recall the flow pattern of the Sweet-Parker model). Of course, the convective derivative is a many-to-one mapping; it is just as *mathematically* possible that the observed convective derivative would be caused by flow *in* from between the conservers and *out* into the bulk of the spheromaks. Thus, we have not found *proof* of a reconnection flow pattern. However, we do see that there is at least *some* flow:  $\frac{d\mathbf{u}}{dt} = 0$ , which is not what we observe. Thus, we see evidence that is not conclusive, but at least

consistent with the notion that reconnection is still occurring. Current mach probe studies will hopefully provide better information about flow patterns [16].

It is an interesting observation that there is a three-dimensional aspect to this field. It has a component upwards for most of the volume, especially at the chamber wall, and it points downwards towards the axis of the machine, as can be seen in the figure.

#### 4.2.4 The Significance of Each Term in Ohm's Law

One question we can address with SSX data is which terms become relevant in the generalization of Ohm's law. An order-of-magnitude estimation procedure shows that the Hall term should be dominant, although by another argument ( $\mathbf{B} \rightarrow 0$  at a null point) it should be small. We found that the characteristic width of a reconnection layer dominated by Hall forces should be roughly  $10^{-2}$  m for SSX, which does seem to be about the reconnection layer thickness (as measured by a high-resolution 1D array of pickup loops [28]). However, now that we have spatial data for  $\mathbf{B}$  (and therefore for some other quantities as well) we can attempt to be more precise about which terms are relevant. For this discussion we will distinguish between the “ideal” Ohm's law terms ( $\mathbf{E}$  and  $\mathbf{u} \times \mathbf{B}$ ) and the “non-ideal” terms (resistivity, Hall force, pressure, and electron inertia).

How well do we know each term? We know  $\mathbf{J}$  well, so by using the Spitzer resistivity we can approximate the resistivity term  $\eta\mathbf{J}$ . We do not need to make any approximations to get the Hall term, so if we know with particular precision. We also have good knowledge of  $\partial\mathbf{J}/\partial t$  to get the electron inertia term.

Our knowledge is weakest for the pressure term, which we calculate as follows. To the extent that  $T_i \approx T_e$  and  $n_e \approx n_i$ , then  $p_i = n_i k T_i \approx n_e k T_e = p_e$ . It follows that  $p \approx p_e + p_i \approx 2p_e$ , so if we know  $\nabla p$  we can divide by 2 to get  $\nabla p_e$ . During the equilibrium/decay epoch it may be valid to use the pressure-balance approximation  $p + B^2/2\mu_0 = \text{constant}$  (see section 3.2.5), so  $\nabla p = -(1/2\mu_0)\nabla(B^2)$ . However, this approximation is certainly wrong during the driven epoch when flow speeds are greater. For the equilibrium/decay epoch, however, it may be safe to assume that  $\nabla p_e \approx -(1/4\mu_0)\nabla(B^2)$ .

Also note that we have no knowledge of the ideal terms in Ohm's law:  $\mathbf{E}$  and  $\mathbf{u} \times \mathbf{B}$ . We know little of  $\mathbf{E}$  aside from a rough magnitude<sup>2</sup>, and without  $\mathbf{u}$  we cannot find  $\mathbf{u} \times \mathbf{B}$ . We cannot compare *all* the terms in Ohm's law, then, but we can compare the *non-ideal* terms in the equation. Figure 4.16 shows the vector sum of the non-ideal terms<sup>3</sup>:

$$\eta\mathbf{J} - \frac{1}{ne}\nabla p_e + \frac{1}{ne}\mathbf{J} \times \mathbf{B} + \frac{m_e}{ne^2}\frac{\partial\mathbf{J}}{\partial t} \quad (4.3)$$

Since the  $\nabla p_e$  formula is certainly invalid at early times, we choose  $t = 64 \mu\text{s}$ , during the equilibrium/decay epoch.

The first noteworthy aspect of Figure 4.16 is that it is almost identical to Figure 4.15, which is supposed to represent something *completely different*, the local force on the fluid. Observe that the two terms in the equation of motion (Equation 4.2), plotted in the earlier figure ( $\nabla p \approx 2\nabla p_e$  and  $\mathbf{J} \times \mathbf{B}$ ) both appear as non-ideal terms in Ohm's law, although their ratios between the equations differ by a factor of 2. Thus, the similarity in figures suggests that the Hall term and the pressure term – particularly the former – dominate the non-ideal terms in Ohm's law. Sure enough, when we look at the magnitudes of each term we find that this is exactly the case, as Table 4.1 shows. The contributions from the pressure and Hall terms are of the same order of magnitude, and they dominate the other terms. The resistivity is the next most significant term, coming in at about 1/30 of the total magnitude. The MRX group did find an anomalous

<sup>2</sup> Researchers at other magnetic probe experiments have been able to calculate  $\mathbf{E}$  from their  $\mathbf{B}$  measurements. However, this trick – which we will describe here – requires a symmetry that SSX does not have. First, one makes use of Faraday's law,  $\nabla \times \mathbf{E} = \partial\mathbf{B}/\partial t$  to get the curl of  $\mathbf{E}$  from their magnetic measurements. Secondly, in MHD the charge density is negligible so we also know  $\mathbf{E}$ 's divergence:  $\nabla \cdot \mathbf{E} = 0$ . Knowing these derivatives however does *not* uniquely define  $\mathbf{E}$  – it only does so up to a divergence- and curl-free field (analogous to a constant of integration). Such a field is exactly the gradient of a solution of Laplace's equation, and we know from electromagnetism that to find such a solution we need to know the boundary conditions. Axisymmetric experiments like MRX can assume symmetric boundary conditions, but in SSX we cannot. Thus, there are many conceivable  $\mathbf{E}$  fields in SSX that would be consistent with the  $\mathbf{B}$  we observe.

<sup>3</sup> Although our high-density grid for  $\mathbf{B}$  is  $6 \times 5 \times 5$ , we reduce our resolution by 1 when we take derivatives to get  $\mathbf{J}$  and  $\nabla p$ . Thus, our “non-idealness field” is known on a  $5 \times 4 \times 4$  grid. To compute  $\mathbf{J} \times \mathbf{B}$  we must interpolate  $\mathbf{B}$  down to a smaller grid so that we know it at the same locations for which we know  $\mathbf{J}$ .

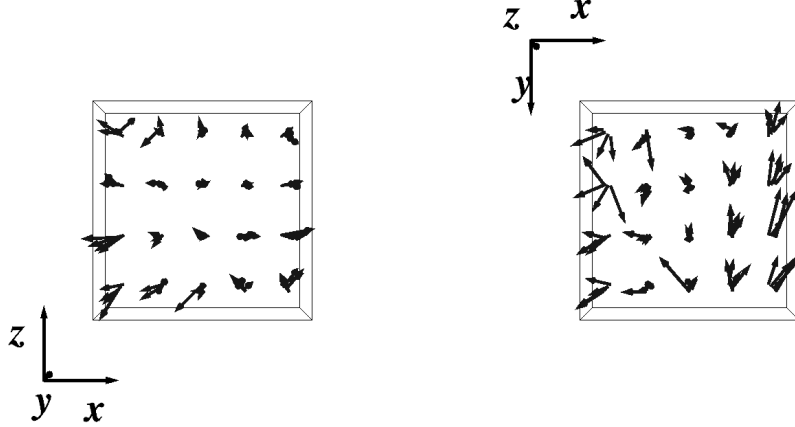


**Figure 4.16:** The vector sum of the non-ideal terms we can calculate in Ohm's law at  $t = 64 \mu\text{s}$ . Although this figure looks almost identical to Figure 4.15, it *is* different.

	Resistivity	Hall	Pressure	$e^-$ Inertia	Vector sum of non-ideal terms
	$\eta  \mathbf{J} $	$\frac{1}{ne}  \mathbf{J} \times \mathbf{B} $	$\frac{1}{ne}  \nabla p_e $	$\frac{m_e}{ne^2}  \frac{\partial \mathbf{J}}{\partial t} $	
36 shot average	$1.3 \times 10^1$	$4.7 \times 10^2$	$1.4 \times 10^2$	$3.2 \times 10^{-2}$	$3.5 \times 10^2$
run 2, 8/29/01	$1.3 \times 10^1$	$4.5 \times 10^2$	$3.4 \times 10^2$	$7.2 \times 10^{-2}$	$3.7 \times 10^2$

**Table 4.1:** The relative magnitudes in Volts/meter of the non-ideal terms in Ohm's law for the averaged data and for one particular shot. Values are the norm of the vector at the central grid location. Note the similarities in proportion to Table 2.1 for laboratory plasmas. The Spitzer resistivity and  $n = 10^{20} \text{ m}^{-3}$  are used.  $t = 64 \mu\text{s}$ .

resistivity of roughly 10 times the Spitzer value used here, and even the Spitzer value is somewhat uncertain since it depends on the poorly-known temperature. Thus, it may be possible for the resistivity term to become significant if both of these factors conspire to raise  $\eta$ . Recall that when we initially discussed the significance of each term we noted that the Hall term tends to zero in the center of the reconnection region if  $\mathbf{B}$  does as well. Here, we see that the Hall term is dominant *even considering* that  $B$  is smaller there. This is partially because in the SSX reconnection geometry there is no true null point (because of the out-of-plane field component) so  $B$  never grows very small.

Recall that we expected the pressure term to be roughly  $\beta$  times the Hall term. As  $\beta$  for SSX is about 0.1, the data suggest that the pressure term may in fact be slightly larger than this prediction.

Another way to approach the problem of which terms in Ohm's law are significant is to take the curl of the equation:

$$\nabla \times \mathbf{E} + \nabla \times (\mathbf{u} \times \mathbf{B}) = \eta \nabla \times \mathbf{J} + \frac{1}{ne} \nabla \times (\mathbf{J} \times \mathbf{B}) - \frac{1}{ne} \nabla \times \nabla p_e + \frac{m_e}{ne^2} \nabla \times \frac{\partial \mathbf{J}}{\partial t} \quad (4.4)$$

$$-\frac{\partial \mathbf{B}}{\partial t} + \nabla \times (\mathbf{u} \times \mathbf{B}) = \eta \nabla \times \mathbf{J} + \frac{1}{ne} \nabla \times (\mathbf{J} \times \mathbf{B}) + \frac{m_e}{ne^2} \nabla \times \frac{\partial \mathbf{J}}{\partial t} \quad (4.5)$$

Note that the pressure term disappears, since it is a curl of a gradient. This disappearance is helpful, since we did not know the pressure term well during the initial inflow of plasma. Also, we turned  $\mathbf{E}$ , a term which we did not have a way to calculate, into something computable from our  $\mathbf{B}$  data. At this point, the only thing we do not know is  $\mathbf{u}$  in the second term. This  $\nabla \times (\mathbf{u} \times \mathbf{B})$  expression we will call the “induction term”. Table 4.2 again presents the magnitudes

	E Field	Resistivity	Hall	$e^-$ Inertia	Induction
	$ \frac{\partial \mathbf{B}}{\partial t} $	$\eta  \nabla \times \mathbf{J} $	$\frac{1}{ne}  \nabla \times (\mathbf{J} \times \mathbf{B}) $	$\frac{m_e}{ne^2}  \nabla \times \frac{\partial \mathbf{J}}{\partial t} $	$ \nabla \times (\mathbf{u} \times \mathbf{B}) $
36 shot average ( $t = 37 \mu\text{s}$ )	$6.8 \times 10^3$	$7.6 \times 10^2$	$1.5 \times 10^5$	$4.2 \times 10^0$	$1.5 \times 10^5$
run 2, 8/29/01 ( $t = 37 \mu\text{s}$ )	$5.2 \times 10^4$	$1.7 \times 10^3$	$5.0 \times 10^5$	$4.5 \times 10^1$	$4.9 \times 10^5$
36 shot average ( $t = 64 \mu\text{s}$ )	$2.1 \times 10^3$	$1.4 \times 10^2$	$5.9 \times 10^4$	$5.5 \times 10^0$	$6.1 \times 10^4$
run 2, 8/29/01 ( $t = 64 \mu\text{s}$ )	$6.4 \times 10^3$	$2.9 \times 10^2$	$9.4 \times 10^4$	$7.2 \times 10^0$	$9.7 \times 10^4$

**Table 4.2:** Relative magnitudes for terms in the curl-of-Ohm’s-law for the averaged shot data and for one particular shot. The earlier time is during driven reconnection while the later time is during the equilibrium/decay epoch. Values are the norm of the vector at the central grid location. The terms that involve time derivatives are smaller for the averaged shot, since moment-to-moment noisy variation is averaged out.

of the terms we know at the center of the reconnection region<sup>4</sup>. Since our estimates are now good for all times, and not just the equilibrium/decay epoch, we also present values for  $t = 37 \mu\text{s}$ , at which time the two spheromaks have both arrived and are slamming together in driven reconnection. Plots of the magnitudes of each term over time at two locations are also shown<sup>5</sup> in Figure 4.17.

Several things are noteworthy in this table. First, the Hall term again dominates. In fact, it even dominates over the new term  $\nabla \times \mathbf{E}$  which was not in Table 4.1. This means (surprisingly) that the *non-ideal* Hall term is dominating over the *ideal*  $\partial \mathbf{B}/\partial t$  term deriving from  $\mathbf{E}$ ! The non-ideal effects seem to have grown strong here indeed, and the ideal MHD assumption of  $\mathbf{E} + \mathbf{u} \times \mathbf{B} = 0$  is very inaccurate here.

In Figure 4.17 we see that the electric field term is somewhat noticeable – although very small – during the initial driven phase. This presence of an electric field might be a noteworthy difference between the driven and equilibrium/decay epochs of reconnection.

While perhaps obvious, we should not forget that the ratio of terms in the curl-of-Ohm’s-law equation is not necessarily the same as the ratio in the original un-curved version. For example, the  $\mathbf{J}$  field tends to be fairly uniform in space, so its curl is smaller than one would expect given the scale-length of variation in  $\mathbf{B}$ . Consider the ratio of the Hall term to the resistivity term. In the un-curved Ohm’s law the ratio is about 36:1, but in the curved version the ratio is 421:1.

Also, note that the variation between run 2 (the individual shot) and the averaged data is much greater for the curved terms than for the un-curved terms. Taking the curl introduces greater uncertainty into the calculations, since the original error in  $\mathbf{B}$  is compounded.

To summarize, the Ohm’s law term comparisons reiterate (with some additional temporal and spatial detail) what a simple order-of-magnitude calculation easily shows: the significant terms in Ohm’s law for SSX are the induction, Hall, and pressure terms. The relevant version of the equation is:

$$\mathbf{u} \times \mathbf{B} = \frac{1}{ne} (\mathbf{J} \times \mathbf{B} - \nabla p_e) \quad (4.6)$$

Finally, using these numbers we can estimate the flow speed, though not its velocity. To estimate the velocity we would have to un-curl the  $\nabla \times (\mathbf{u} \times \mathbf{B})$  term, which we cannot do without better knowledge of the boundary conditions (see

<sup>4</sup>For the terms in the curl-of-Ohm’s-law, we need to take at most *two* spatial derivatives. Thus, we only know these terms on an even smaller  $4 \times 3 \times 3$  grid

<sup>5</sup>Similar plots were not shown for the un-curved Ohm’s law terms because our method for computing  $\nabla p$  is certainly invalid until the equilibrium/decay epoch, when there is no longer interesting time variation of the signals.

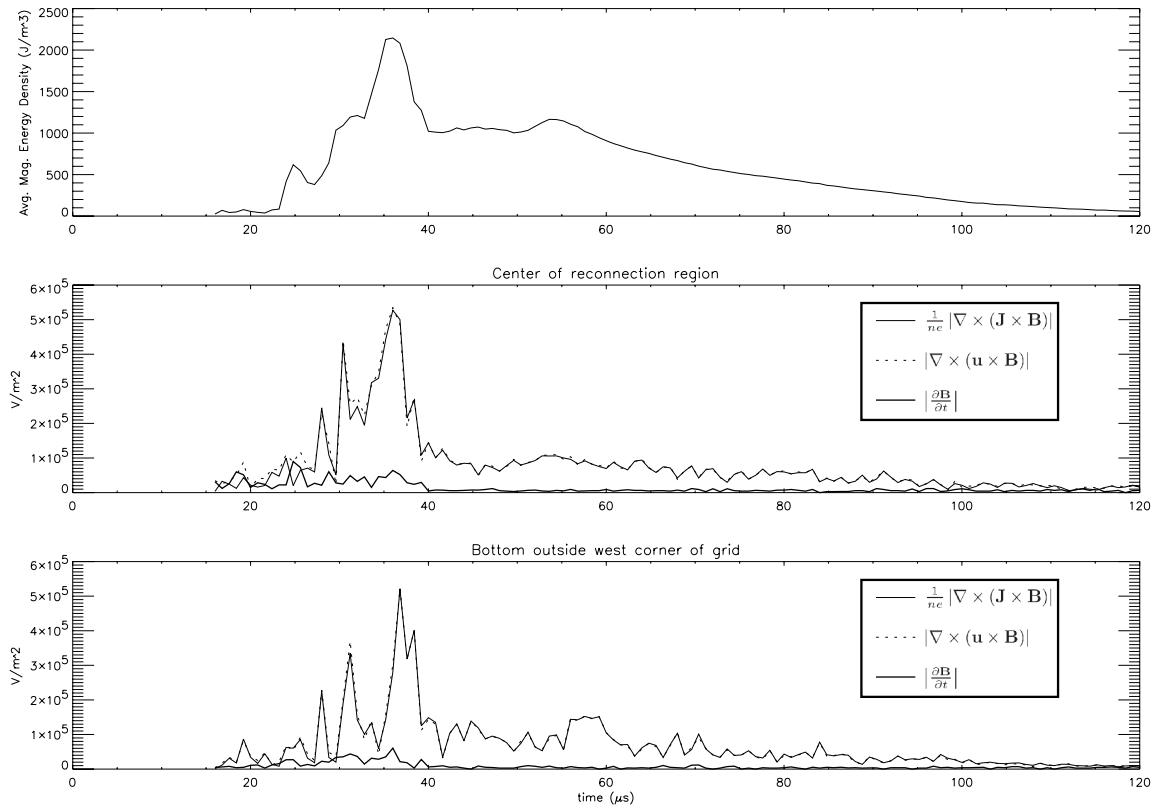


**Figure 4.17:** The significance of the terms in curl-of-Ohm's law over time, showing that the induction terms is almost completely balanced by the Hall term. Data are for run 2 on 8/9/01. In the first plot, magnetic energy density is shown for comparison. In the lower two plots, terms other than the three shown are too small to be visible. There does not seem to be a significant spatial variation in the relative dominance of each term.

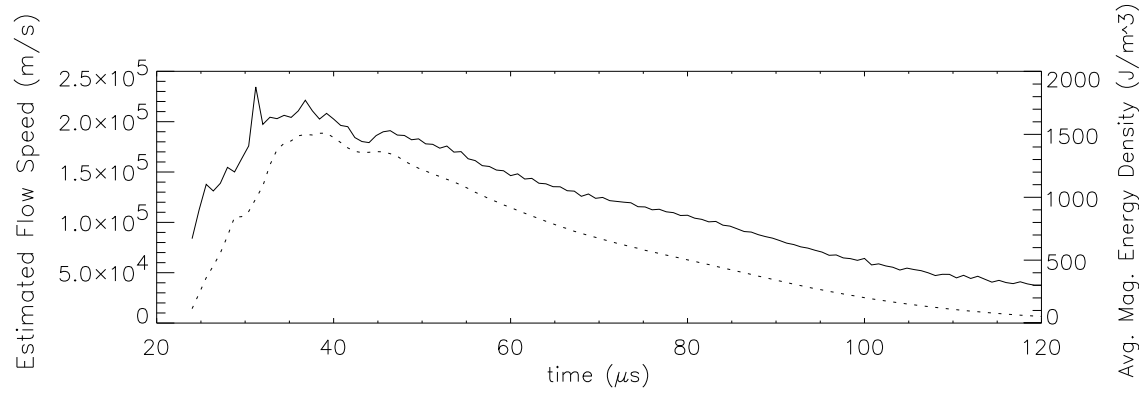


**Figure 4.18:** Estimated flow speed over time, averaged over space, for the 36 shot average data. For comparison, the average magnetic energy density is plotted as the dotted line.

footnote on page 69). We assume

$$|\nabla \times (\mathbf{u} \times \mathbf{B})| \sim \frac{|\mathbf{u}| |\mathbf{B}|}{L} \Rightarrow |\mathbf{u}| \sim \frac{L |\nabla \times (\mathbf{u} \times \mathbf{B})|}{|\mathbf{B}|} \quad (4.7)$$

and use <sup>6</sup>  $L = 4$  cm. We can calculate the right-hand side of Equation 4.7 at each point in the  $4 \times 3 \times 3$  grid, average over space, and plot the results versus time. Figure 4.18 shows the results. The dynamics of the speed seem to be dominated by the magnitude of  $\mathbf{B}$ , since the speed plot tracks the magnetic energy density plot so closely. The peak speed is on the order of the Alfvén speed ( $10^5$  m/s), as expected. There is some spatial variation to the speed, as shown in Figure 4.19. During the early driven period, it seems to peak along a line in the  $(1, -1, 0)$  direction through the center of the volume. Later, during the steady-state period, it appears to be greatest at a central point. This last fact is surprising, as symmetry would suggest that if anything the flow is *slowest* in the exact center of the region. The spatial resolution is so poor and the calculated numbers so far removed computationally from the original  $\mathbf{B}$  measurements that we probably cannot draw firm conclusions from these data.

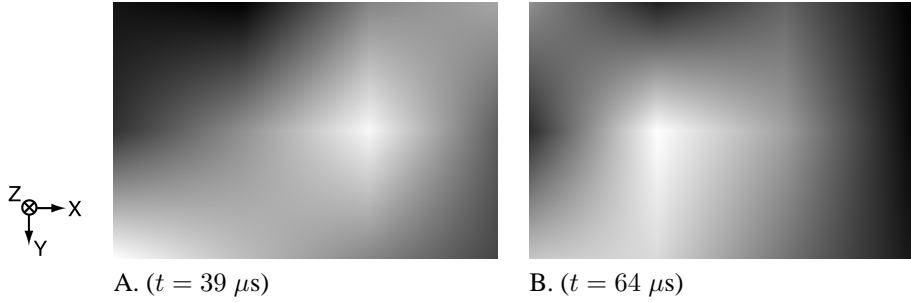


**Figure 4.19:** Spatial variation in the estimated flow speed, as seen in a  $xy$  slice halfway between the flux conservers. The greatest speed in the slice is 100% white and 100% black would be speed=0. Data is for the 36 shot average.

## 4.2.5 Particle Acceleration

Magnetic measurements were compared with RGEA measurements to investigate the acceleration of high-energy particles. Figure 4.20 shows a typical observation. RGEA1, looking normal to the reconnection plane, observes a large early ( $t = 40\mu\text{s}$ ) spike. This is caused by a super-Alfvénic distribution of particles, accelerated by the reconnection electric field and possibly aided by turbulence as in Matthaeus *et al.* RGEA2 observes a smaller, sub-Alfvénic pulse a moment later ( $t = 50\mu\text{s}$ ). It is likely that both groups of particles are generated at the same moment – when the driven reconnection is at its peak – but RGEA2 detects the pulse later because the particles are moving slower.

One interesting feature obtained from magnetics data is that  $\mathbf{J}$  behaves differently in the driven and equilibrium/decay epochs. At the moment of spheromak collision it points up ( $-y$ ) towards RGEA1 and roughly normal to the best-fit reconnection plane (Figure 4.20.A). However, after  $2-3\mu\text{s}$  it points horizontally ( $-x$ ) for the remainder of the shot, at an oblique angle to the best-fit  $\mathbf{B}$  plane (Figure 4.20.B). This evolution can be seen in more detail in Figure 4.21.

This behavior was quantified in other ways in Figure 4.22. In A, the  $\mathbf{J}$  flux is summed over the six sides of the measurement “cube.” The flux is mostly through the horizontal faces, but a vertical flux appears during the driven epoch. In B, the average angle of  $\mathbf{J}$  in the  $xy$  plane was computed over time. It initially points  $50^\circ$  upwards from the horizontal, but relaxes to a horizontal position.

It is hard to know what we *expect*  $\mathbf{J}$  to do, since there are two directions that would seem plausible. First, 2D reconnection models have an out-of-plane  $\mathbf{J}$ , which for SSX corresponds to the initial upward  $\mathbf{J}$  that points towards RGEA1. However, spheromaks are supposed to have  $\mathbf{J} \parallel \mathbf{B}$ , parallel for one spheromak and antiparallel for the other because the helicities are opposite. Thus, the  $\mathbf{J}$  we would expect if no reconnection occurred would be pointed towards

<sup>6</sup>Not only does the scale-length of the fields look like roughly 4 cm, but this value for  $L$  also produces a very good fit for  $|\mathbf{J}| = |\nabla \times \mathbf{B}| = |\mathbf{B}|/L$ .

the central axis ( $-x$ ) and *downward*. We see a small trace of this downward component on the highest- and lowest- $z$  planes of data – those most within the flux conservers. Perhaps the fact that  $\mathbf{J}$  largely points towards  $-x$  is due to a “superposition” of these upward-pointing reconnection vectors with the downward-pointing equilibrium spheromak vectors:  $\nwarrow + \swarrow = \leftarrow$ .

### 4.2.6 Full Merging of Spheromaks

Since the reconnection experiments described in this thesis, the SSX apparatus has undergone several major changes in preparation for a different experimental campaign (see Future Directions, Chapter 5). The first step in this conversion process was the removal of much of the back wall material from the flux conservers, as Figure 4.2.6 shows. With this new configuration, reconnection should in theory occur around the entire ring of contact between the spheromaks. As Figure 4.23 illustrates, this additional reconnection should allow the two plasma rings to join into a single structure in which there is very little remaining toroidal field. This object, known as a Field-Reversed Configuration (FRC), has been previously produced by this same method by Ono *et al.*[60] Much of the motive for creating FRCs in SSX relates to the new experiment rather than to the reconnection studies (see Fefferman [17] and Falk [16]). However, in this intermediate configuration, some interesting data has been taken with relevance to reconnection.

### Typical Shots

It was stated earlier in this thesis that the function of the flux conservers and chevron holes was to allow a controlled amount of reconnection while ensuring the overall reproducibility and stability of the configuration. Looking at typical data taken without the conserver end plates, it is apparent that their stabilizing effect was in fact quite significant. Figure 4.25 shows data from a typical full-merging shot, and it is apparent that the fields are much more dynamic than for partial-merging shots (cf. Figure 4.4). Also, the difference from one shot to the next is much greater than before. In fact, the “typical” shot shown here represents only one of several substantially different possible configurations. Roughly 90-95% of full-merging shots relax to a  $-z$  directed field as shown here, but others reach a  $\pm x$ -directed equilibrium. For the sake of brevity, these pathological cases are not shown here, but they can be found in Appendix F.

### Similarities to Partial-Merging

In actual astrophysical reconnection events there are of course no flux conservers to create a relatively straight and symmetric reconnection geometry, and so the particularly tumultuous full-merging shots are much more representative of “natural” reconnection. The usefulness of the results obtained in the partial-merging shots thus relies on the assumption that the conserver walls to not significantly change the physical processes at work. We hope that by looking at the much more orderly data from partial-merging shots, we can make a direct inference that the same results would hold for FRC formation in SSX, or in solar flares or the magnetosphere. To what extent though do the conserver end plates really affect the physics of reconnection?

We generally believe that the physics is the same in full- and partial-merging reconnection. Figure 4.27 shows fieldlines from one moment in a full-merging shot. The geometrical similarities of the  $\mathbf{B}$  field to the partial-merging case are clear. To be sure, it is hard to find a frame of full-merging data in which the field null region is centered on the probe array as it is here – usually one or two frames in a typical full-merging shot look this good. However, this difficulty is surely due to the fact that the plasma is no longer confined to reconnect right over the probe region, so the reconnection center is usually pushed to one side or the other.

Some critics have suggested that the end plates may reduce the speed of the incoming fluid. Eddy currents in the plates do eventually stop the spheromaks from colliding, but how much does this effect impact the fluid that passes through the chevron holes? Six full-merging and six partial-merging shots were considered in which all of the timing parameters (e.g., East-West gun delay, etc.) were identical. For the full-merging shots, the first 200 G field appeared on

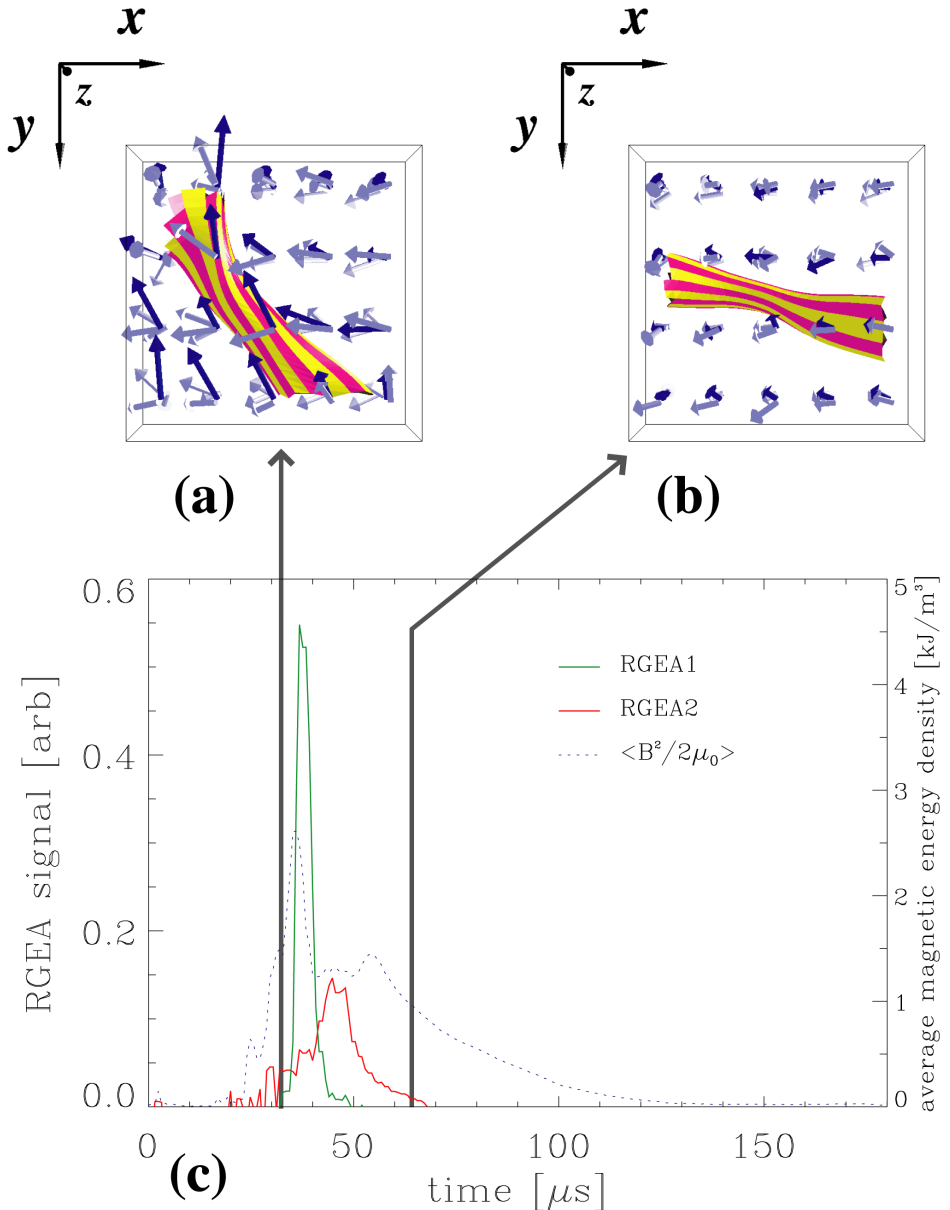


**Figure 4.20:** Comparison of RGEA particle measurements with magnetics data. A and B depict  $\mathbf{J}$  vectors and fieldlines. A. Early in the shot  $\mathbf{J}$  points at RGEA1 for 2-3  $\mu\text{s}$  right at the moment of driven reconnection. This upward-directed  $\mathbf{J}$  is the likely acceleration mechanism for the super-Alfvénic particles. B. For the remainder of the shot, however,  $\mathbf{J}$  points horizontally. C. After the moment of peak reconnection depicted in A, the RGEAs detect a burst of particles.

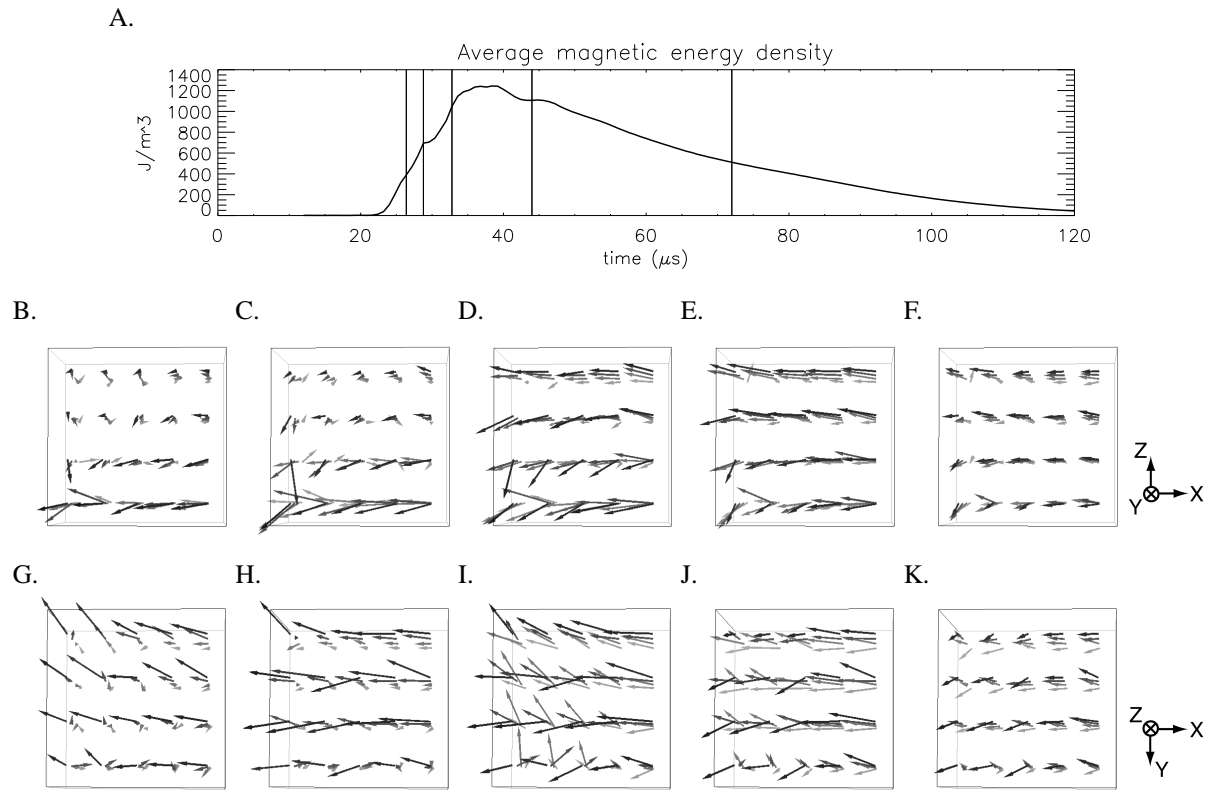
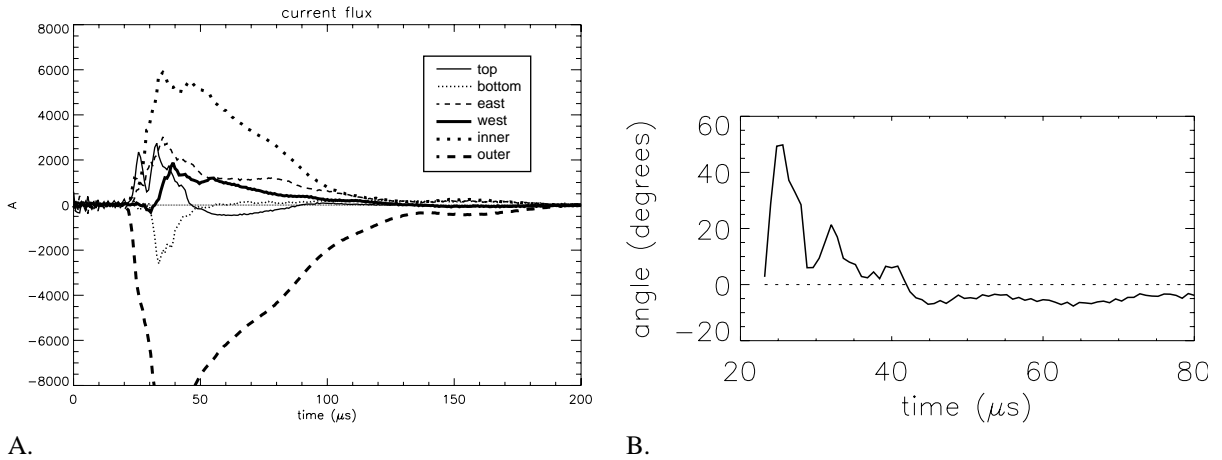


**Figure 4.21:** Evolution of the current  $\mathbf{J}$  in a typical shot. B-F show a top view, and G-K depict a side view. In B, the east spheromak introduces a mostly  $x$ -directed current with some vertical ( $y$ ) component. By C, much of the vertical component has disappeared. In D, the arrival of the west spheromak results in a second upwards current pulse, but this too rapidly disappears (E). Other than these moments, the current is roughly uniform in the  $-x$ -direction for the entire plasma lifetime, although it bends slightly in the  $z$ -direction at the corners. These data are from the 36-shot average;  $\mathbf{J}$  fields from actual shots are similar but noisier.



A.

B.

**Figure 4.22:** Other characterizations of the vertical current pulse which may be responsible for the RGEA signal. A shows current flux *out* of the probe volume through each of its faces over time. Most of the flux is from the outer ( $+x$ ) to the inner ( $-x$ ). However, from  $30 \mu\text{s} < t < 50 \mu\text{s}$  there is a significant flux from the bottom to the top as well, which dies out much faster than the overall signal. B: Average angle of  $\mathbf{J}$  over time, in degrees upwards (towards  $-y$ ) from horizontal ( $-x$ ), again illustrating the “rotation” of  $\mathbf{J}$  between the driven and equilibrium/decay epochs. Data are from the 36-shot average to reduce noise.

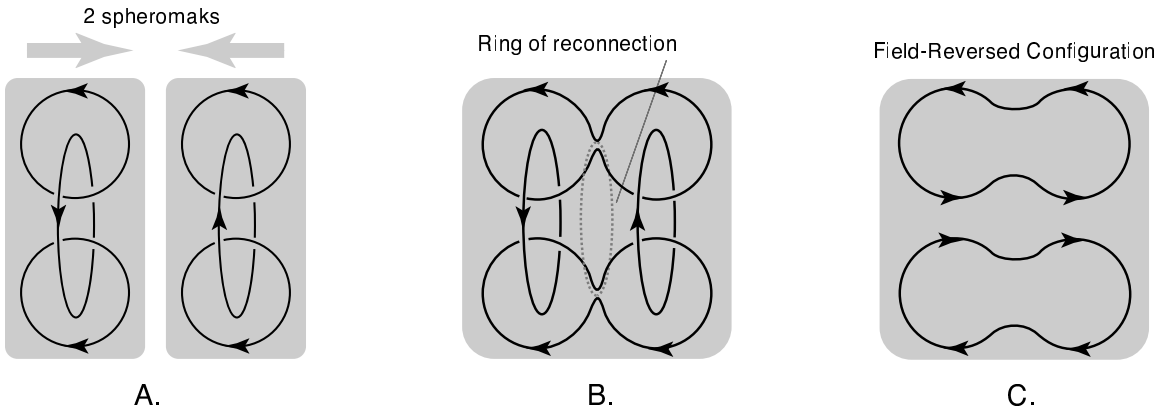


**Figure 4.23:** “Full-merging” of two spheromaks to produce an FRC. A: The initial configuration is exactly as before. B: Now, however, reconnection occurs not just at the two chevron holes but rather in an entire ring. C: The poloidal lines remain, since they “rotate” in the same direction, even though locally they cancel. The toroidal lines, however, completely cancel each other because they rotate in opposite directions.



**Figure 4.24:** The SSX vacuum chamber, split in half along the midplane, after the removal of much of the flux conservator end plates (cf. Figure 3.5.A). A 2" lip remains around the perimeter of each conservator, but otherwise the two spheromaks are free to fully merge.

	E Field	Resistivity	Hall	$e^-$ Inertia	Everything Else
	$ \frac{\partial \mathbf{B}}{\partial t} $	$\eta  \nabla \times \mathbf{J} $	$\frac{1}{ne}  \nabla \times (\mathbf{J} \times \mathbf{B}) $	$\frac{m_e}{ne^2}  \nabla \times \frac{\partial \mathbf{J}}{\partial t} $	$ \nabla \times (\mathbf{u} \times \mathbf{B}) $
run 9, 1/16/02 ( $t = 38 \mu\text{s}$ )	$2.6 \times 10^4$	$5.5 \times 10^2$	$2.2 \times 10^5$	$8.2 \times 10^0$	$2.1 \times 10^5$
run 3, 1/16/02 ( $t = 36 \mu\text{s}$ )	$2.4 \times 10^4$	$8.8 \times 10^2$	$2.2 \times 10^5$	$5.5 \times 10^1$	$2.3 \times 10^5$

**Table 4.3:** Relative magnitudes for terms in the curl-of-Ohm's-law for full-merging shots at times in which the reconnection surface appears to cross the probe volume. Values the norm of the vector at the central grid location. The numbers correspond well with Table 4.2. Unfortunately, data corresponding to later in the shot is not possible since the reconnection surface quickly moves out from the probe volume.

the east-most  $xy$  plane between 23-25  $\mu\text{s}$  into the shot, marking the arrival of the east spheromak. The east spheromak also arrived between 23-25  $\mu\text{s}$  in the six partial-merging shots<sup>7</sup>. Similarly, the first 200 G field appeared in the central  $xy$  plane between 24-26  $\mu\text{s}$  in both the full-merging and partial-merging shots. Thus, the flux conservers did not noticeably slow the spheromaks as they approached the midplane, and they did not even slow the plasma as it flowed through the chevrons. Consequently, the inflow speed should be the same for full- and partial-merging reconnection.

Another comparison we can make between full- and partial-merging is to compare the magnitudes of Ohm's law terms. Table 4.3 illustrates the results for the curl-of-Ohm's-law, at times which are comparable to the top two rows in Table 4.2. These numbers quantify what is apparent from watching these full-merging shots: they are very similar to shots with the end plates in place. A similar comparison can be attempted with the un-curved Ohm's law terms, but this is not very trustworthy because the slow-flow assumption used to calculate  $\nabla p_e$  is probably not correct. As in the curl-of-Ohm's-law table, the terms look very comparable to the partial-merging data (Table 4.1). The time dependence of the terms and the speed function also look comparable, but are not displayed here for brevity.

Another question we may ask is if the thickness of the reconnection layer is determined by the physics of the reconnection process, or rather by the size of the chevron holes. This question can be addressed by comparing the layer width in full- and partial-merging shots, as shown in Figure 4.28.

Unfortunately, this comparison is not as easy as it first sounds. We cannot measure the layer width without seeing

<sup>7</sup>It is harder to precisely define the arrival time for the west spheromak, because the east spheromak (which arrives first in all the partial-merging shots, since no time delay was used) contributes to the field in the western-most  $xy$  plane. The somewhat chaotic interaction on this  $xy$  plane means that some arrows switch direction before others. In any event, to answer our question it is enough to look at just one side.

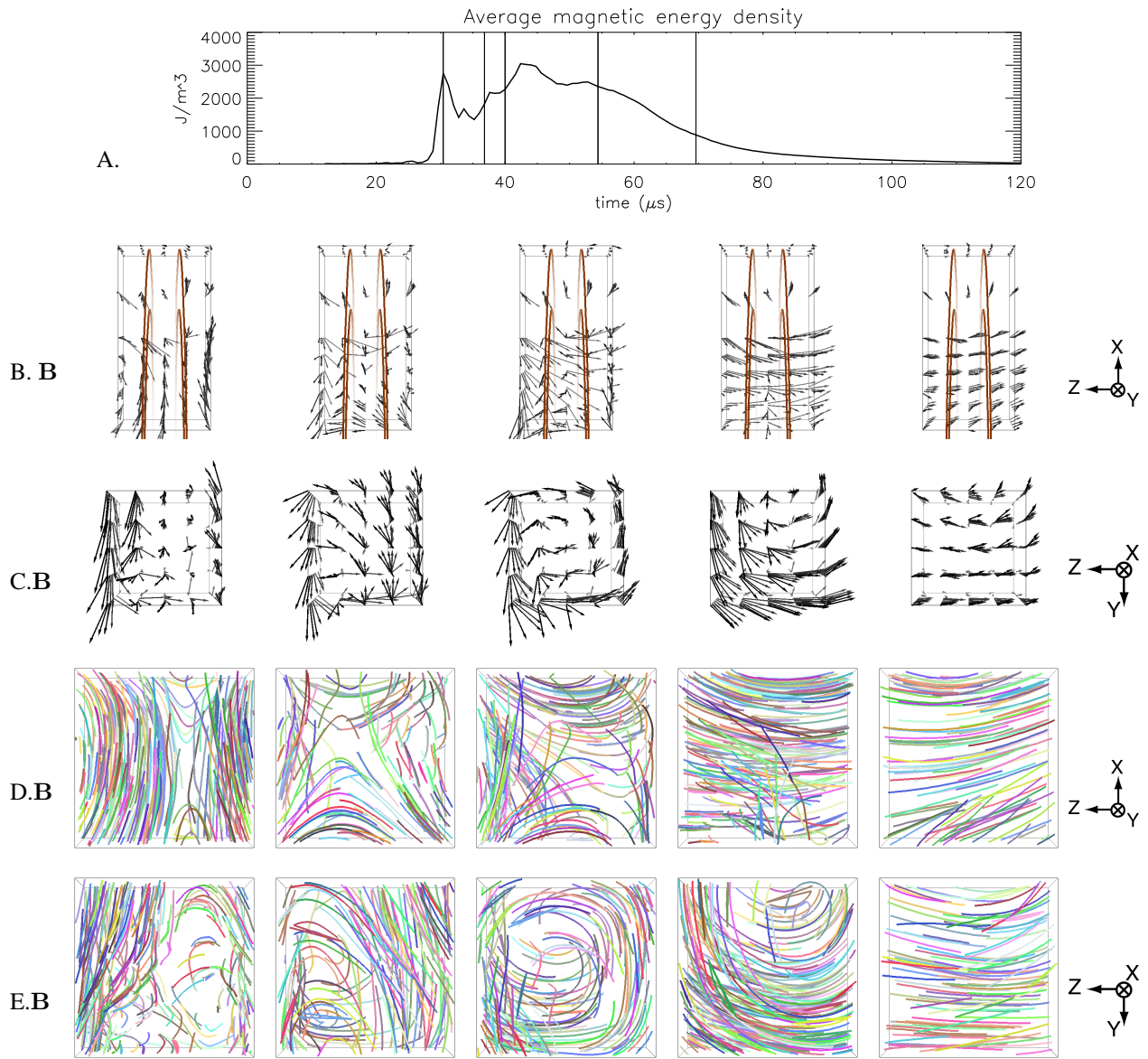


**Figure 4.25:** Run 9, 1-16-2002. A typical full-merging shot. The left-most frame looks quite like a typical shot from before the flux conserving end-plates were removed. However, here the reconnection layer curls up into a cylindrical “tube” supported by a strong  $-x$ -directed current. The tube then moves up and east, and the  $\mathbf{B}$  field straightens until it is roughly uniform in the  $-z$  direction.

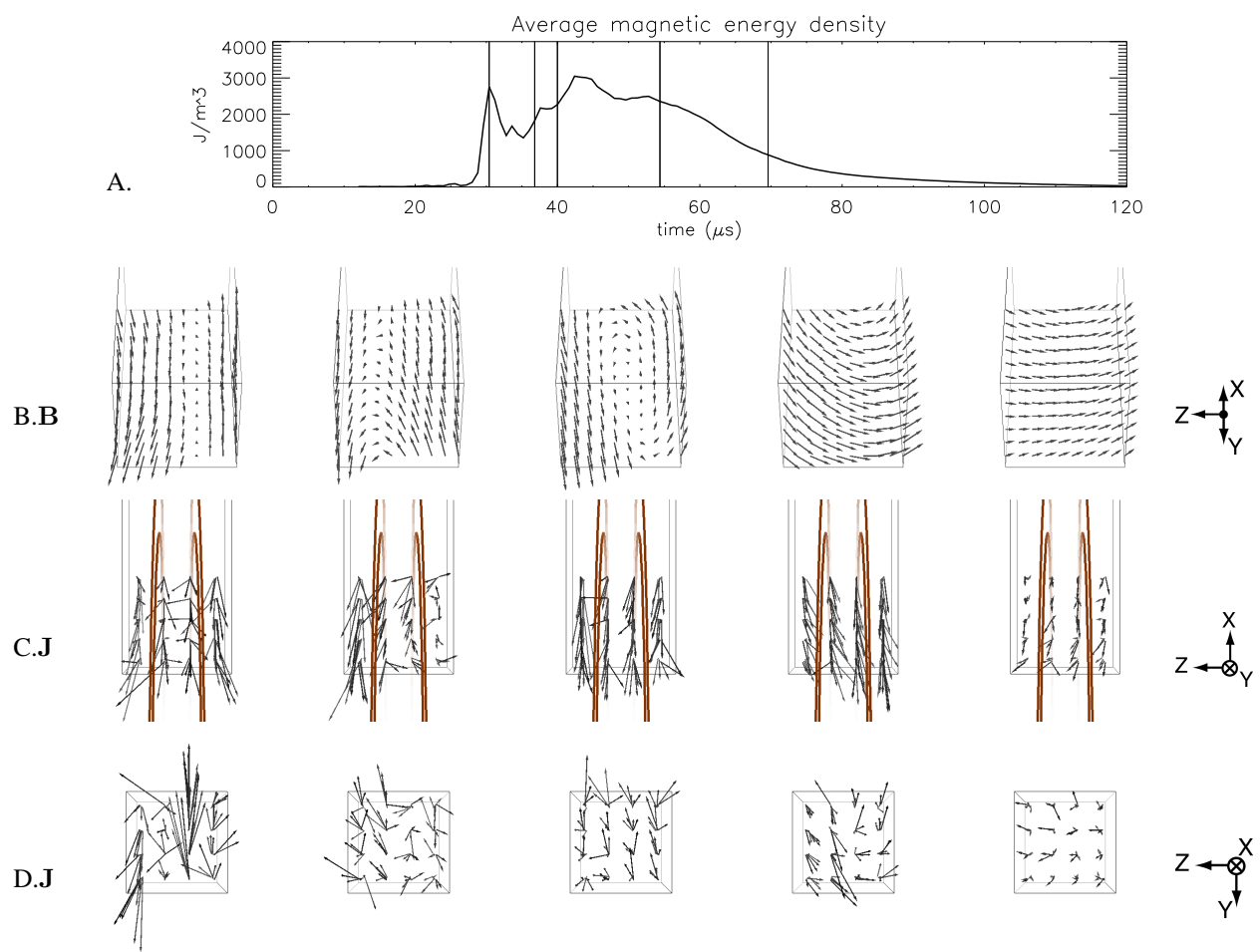


**Figure 4.26:** Run 9, 1-16-2002. More images from the same typical full-merging shot.

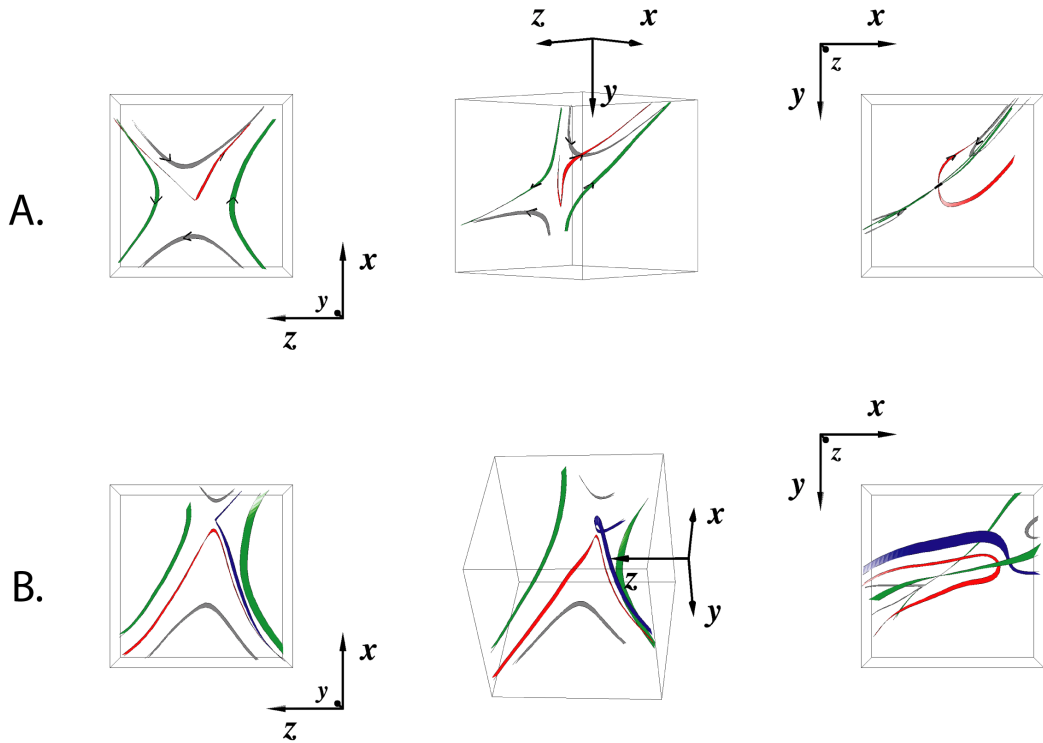


**Figure 4.27:** Comparison of a partial-merging shot (A) and a full-merging shot (B) to illustrate the qualitative similarities. From Cothran *et al.*[11]

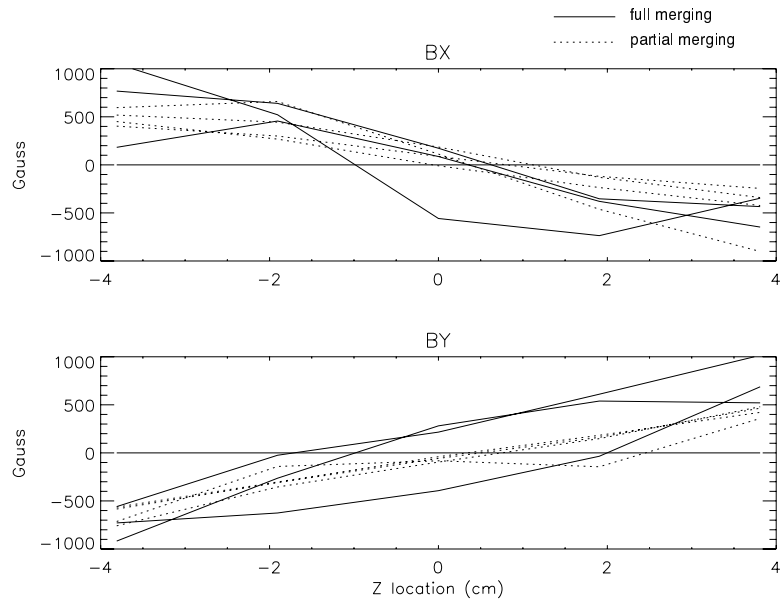


**Figure 4.28:** Components of  $\mathbf{B}$  along a line through the reconnection layer, for both full- and partial-merging shots. We do not see enough of the layer to put an upper bound on the layer width (c.f. Figure 3.12), but it does not seem significantly different between the two kinds of shots.

where  $\mathbf{B}$  plateaus on either side of the layer (where the incline “rolls over” to the horizontal), which is apparently outside of the probe volume. You might recall that earlier experiments on SSX *did* measure the layer width (see Section 3.2.3). One contributing factor to the 3D probe’s failure in this regard is that its extent in the  $z$  direction is slightly less (3 inches instead of 3.5 inches). However, 1D probe experiments indicated a layer width as small as 2 cm early in the spheromak merging; this small layer thickness should be discernable even in the smaller 3D probe, and yet it is not. A likely reason why the layer appears thicker using the 3D probe is that the larger mass of metal in the reconnection layer excludes or slows some of the incoming plasma. This hypothesis is consistent with other observations we will discuss shortly.

As we do not have enough information to calculate layer widths for each shot, we cannot eliminate all doubt that the layers are equally thick in full and partial merging. However, if the layer would be any different in full merging it would be *thinner*, since the conserver walls are not present to “pull back” on the plasma. We *can* firmly say that the full-merging layer does not seem much thinner than the partial merging layer, consistent with our other observations that the conserver end-plates do not affect the reconnection physics. It seems, then, that even in the partial-merging case the layer width is determined by physics, and not by the chevron hole size.

## What Is this Structure?

Although there are similarities between full- and partial-merging shots – arrival times, fieldline topology during several frames, Ohm’s law terms, and layer widths – the global magnetic dynamics are fundamentally different. In the partial merging shots, we have a good understanding of the spheromak equilibrium in each conserver (see Geddes [20]), and with the three-dimensional probe array we can see in detail the magnetic configuration between the conservers. However, in a full-merging shot we cannot assume that the plasma outside of the probe volume remains in a stable spheromak equilibrium, and indeed, the global magnetic dynamics seem different. What exactly is the evolution of the magnetic topology in a full-merging shot?

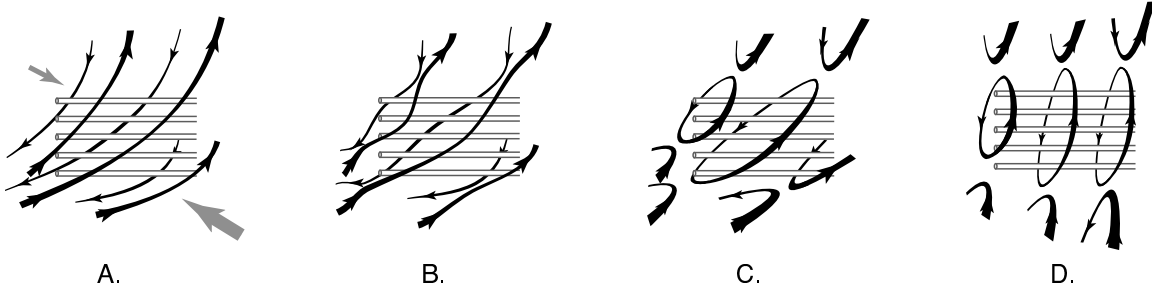


**Figure 4.29:** Possible mechanism for creation of the “roll” in a full-merging shot, as seen from a side view (looking  $+z$ ). A: Spheromak fieldlines come in from either side (cf. Figure 4.6.D) B: The stainless steel probe tines - which are more resistive than the copper but still somewhat conductive - slightly slow the incoming plasma near the probe. C: Consequently, reconnection occurs initially just outside the probe region, leaving reconnected rings of  $\mathbf{B}$  around the stalks. D: The rings equilibrate to form the roll.

Consider the first three columns in Figure 4.25. Initially we see the appearance of oppositely-directed fields, much as in the partial-merging case. However, in the next two frames the fields curl around into a loop-like structure around the probe stalks. No such loop structure was seen in partial-merging experiments. Recall that without the conserver end-plates, SSX is completely axisymmetric – except for the probe array itself. Thus, the plasma must be influenced in a non-trivial way by the presence of the probe. We need not discard our earlier assertion that the probe’s presence *fundamentally alters* the plasma, however. It is possible that the plasma is subject to some kind of instability which would lead to the “roll” structure somewhere, and a small perturbation from the probe makes the roll *tend* to appear around the stalks. Figure 4.29 illustrates such a scenario.

Some other noteworthy features of full-merging shots include the following:

- The “roll” structures tends to move upwards (towards  $-y$ ) from the probe region, as seen in the rightmost 3 columns of data in Figure 4.25.
- For most full-merging shots, the fields end up pointing in the  $-z$  direction for the final decay period
- FRC decay is consistently faster than decay in a partial-merging shot. This fact can be seen by comparing the magnetic energy density plot atop Figure 4.25 with similar plots from partial-merging shots.
- As one can see in Figure 4.23, and FRC has a field null, a radius at which the direction of the field reverses ( $\mathbf{B} = +z$  for  $r > r_0$ ,  $\mathbf{B} = -z$  for  $r < r_0$ ). However, this reversal has never been observed using the 3D probe. Yet, a reversal point is *consistently* observed with new magnetic measurements made with a less intrusive “distributed probe array.” This fact strengthens the evidence that the original probe array has a non-negligible impact on the plasma dynamics.
- Current studies by Fefferman[17] show that the FRC-like object formed in full-merging is susceptible to a “tilt instability” that may rotate the plasma within the flux conservers. One might try to explain the roll structure by saying that the central axis of the FRC has rotated on top of the probe array, but this conclusion is unlikely given the time at which these phenomena occur. The tilt instability is typically observed to begin around  $t = 60 \mu\text{s}$  and reach a maximum around  $80 \mu\text{s}$ , while the roll shown in Figure 4.25 is fully developed by  $40 \mu\text{s}$ .

## Chapter 5

# Future Directions and Concluding Remarks

The work described in this thesis is for now the last to be performed related to the direct study of magnetic reconnection in SSX. Now operating under a new grant, the laboratory has shifted focus to instead study the stability of FRCs produced in a new flux conserver that allows for full merging of the two spheromaks. This work focuses on the stability of the resulting equilibria, not on the reconnection process by which these equilibrium states are formed, and will be described in upcoming papers and theses [17, 16]. Even with this change in emphasis, data from the new Mach probe and soft X-ray diagnostics should help to flesh out our understanding of the now-retired SSX partial-merging configuration.

This change of focus is by no means due to a lack of directions for further study. One particular experiment is begging to be performed. The 3D probe in SSX was not used to measure any of the topologically novel configurations that the theorists refer to when they speak of “3D reconnection.” Rather, in SSX the probe measured a skewed version of standard 2D reconnection. There was no attempt to produce spines, fans, or exotic separators. Instead, SSX provided little more than a bent version of the standard 2D Sweet-Parker picture, not one of the topologically unique structures to which theorists refer when they say “3D reconnection.” To achieve the full potential of the 3D probe array, it could be placed in a situation with more of the random 3D topology that typifies the true complexity of, say, the solar corona.

A second important experimental direction would be a campaign to test the predictions of the collisionless reconnection models of Shay *et al.* SSX could not test the prediction of the magnetic quadrupole due to the curvature inherent in spheromak fields, so the device would have to be constructed with a Cartesian rather than cylindrical geometry to more closely approximate 2D.

Another direction of research that could be fruitful would be to model the FRC formation process. The 3D probe has provided the world’s first 3D dataset of the complicated process of full spheromak merging. It would be a tremendous achievement to have a code that could be trusted to accurately reproduce the internal behavior of the plasma during this process. If the code were able to reproduce the observed magnetic field in the small volume for which we *have* data, the code’s prediction for the fields and other quantities in the *rest* of the volume would be very believable. We are already pushing the limits of technology to acquire data in our small probe volume, so only a computer model would be able to give us a global perspective on the dynamics of full merging. Figure 4.29 seems like a reasonable explanation for the formation of the “roll” structure observed, but a computer model could provide a more global perspective on the process. A model would also be particularly interesting in light of the new focus of the laboratory on FRC formation and stability. It might not be too difficult to modify the existing SSX TRIM code [36] for this purpose.

Perhaps SSX will return to the study of reconnection in the coming years, but even if not there will undoubtedly be other laboratory studies of the phenomenon. The past years of work on SSX have provided a multifaceted picture of a particular reconnection configuration. Measurements of the magnetic field, temperature, density, velocity, and

other quantities will provide theorists with numbers to match as they investigate which non-ideal effects are important in allowing reconnection to occur. The technology of 3D probe should be useful in exploring the exotic geometrical forms exhibited by reconnection in nature.

## Appendix A

# Why the Displacement Current can be Neglected

Maxwell's corrected version of Ampère's law is

$$\nabla \times \mathbf{B} = \mu_0 \mathbf{J} + \mu_0 \epsilon_0 \frac{\partial \mathbf{E}}{\partial t} \quad (\text{A.1})$$

On several occasions, however, we have wanted to make the simplifying assumption that the rightmost term – the one corresponding to the “displacement current” – is insignificant compared to the other two:

$$\nabla \times \mathbf{B} \approx \mu_0 \mathbf{J} \quad (\text{A.2})$$

We can show this to be a valid approximation with a method of order-of-magnitude estimation that is common in plasma physics. We begin by taking a ratio of the term-we-want-to-show-to-be-small over some other term in the equation which is expected to be more significant. We will first compare the displacement current to the leftmost term in A.1, and later we will compare it to the second term. So,

$$\frac{|\mu_0 \epsilon_0 \partial \mathbf{E} / \partial t|}{|\nabla \times \mathbf{B}|} = ? \quad (\text{A.3})$$

We evaluate the order of magnitude of the two derivatives by considering the scales over which these quantities change in the situation of interest. For example, if a 4 T magnetic field varies with space in a way such that it *changes direction* over a distance of 2 m, then it is a reasonable guess that  $\nabla \times \mathbf{B}$  is on the order of  $4 \text{ T}/2 \text{ m} = 2 \text{ T/m}$ . Now it *could* be the case that the magnetic field is in fact perfectly curl-free, so that its *actual* magnitude everywhere is zero. However, the chance that a given “randomly selected” field is curl-free is very small. If we have no reason to suspect that the derivative is identically zero<sup>1</sup>, then this order of magnitude guess is probably a reasonable one.

Let us then introduce  $\tau$ , a typical time for the fields to change, and  $L$ , a typical length over which the fields change. Then we have

$$\frac{|\mu_0 \epsilon_0 \partial \mathbf{E} / \partial t|}{|\nabla \times \mathbf{B}|} \sim \frac{\mu_0 \epsilon_0 E L}{B \tau} \sim ? \quad (\text{A.4})$$

For SSX we do not have as good a sense for what the electric field is as we do for the magnitude of the magnetic field (which we know very well from the 3D probe!). Thus, we can apply a similar order-of-magnitude argument to Faraday's law to “solve” for  $E$ :

$$\nabla \times \mathbf{E} = -\frac{\partial \mathbf{B}}{\partial t} \Rightarrow \frac{E}{L} \sim \frac{B}{\tau} \Rightarrow E \sim \frac{BL}{\tau} \quad (\text{A.5})$$

---

<sup>1</sup>We could, for example, use similar reasoning to suggest that the order of magnitude of  $\nabla \cdot \mathbf{B} \approx 2 \text{ T/m}$ . However, we know there are no magnetic monopoles, so this expression cannot be anything but zero! In the case of  $\nabla \times \mathbf{B}$  however we have no *a priori* reason to suspect it must vanish.

Plugging this latest result into equation A.4 we arrive at:

$$\begin{aligned}\frac{|\mu_0\epsilon_0 \partial\mathbf{E}/\partial t|}{|\nabla \times \mathbf{B}|} &\sim \frac{\mu_0\epsilon_0 E L}{B\tau} \sim \frac{\mu_0\epsilon_0 (BL/\tau)L}{B\tau} \sim \frac{\mu_0\epsilon_0 L^2}{\tau^2} \\ &\sim \frac{(4\pi \times 10^{-7} \text{ T m A}^{-1})(8.85 \times 10^{-12} \text{ C m}^{-1}\text{V}^{-1})(0.02 \text{ m})^2}{(2 \times 10^{-6} \text{ s})^2} \\ &\sim 1 \times 10^{-9}\end{aligned}$$

In the last step we have inserted typical values for SSX near the reconnection region. The magnetic field seems to vary smoothly on a distance scale of a few centimeters, and the most rapid changes in the magnetic fields, during the arrival and collision of the spheromaks at the reconnection region, occur in one or two of the 800 ns frames of 3D probe data. Some variations in the magnetic field take much longer than 2  $\mu\text{s}$ , but a larger value for  $\tau$  would only *lessen* the resulting “significance factor” of our term. It is an assumption that the distance and time scales for the *electric* field are similar to those of the magnetic field, for we have used the same  $\tau$  and  $L$  to refer to both.

Since the displacement current term is so much smaller than the  $\nabla \times \mathbf{B}$  term, we will probably be able to ignore it. For completeness, however, we can use a similar procedure to compare the displacement current term to the *other* term in Ampère’s law:

$$\frac{|\mu_0\epsilon_0 \partial\mathbf{E}/\partial t|}{|\mu_0\mathbf{J}|} \sim \frac{\epsilon_0 E}{\tau J} \sim \frac{(8.85 \times 10^{-12} \text{ C m}^{-1}\text{V}^{-1})(10^3 \text{ V m}^{-1})}{(2 \times 10^{-6} \text{ s})(10^6 \text{ A m}^{-2})} \sim 4 \times 10^{-9} \quad (\text{A.6})$$

Above, we have plugged in typical SSX values for  $E$  and  $J$ . Since the displacement current term is nine orders of magnitude smaller than the other terms in Ampère’s law, it can be discarded as insignificant.

Although SSX values were used here, the fact that the displacement current is negligibly small also follows from the assumptions of MHD. Thus, a general argument like the one above can be made for *any* plasma in the MHD regime.

## Appendix B

# Derivation of Ohm's Law for Plasmas

### The Continuity Equation

As a first step towards deriving Ohm's law, let us begin by deriving a well-known and relatively simple result, the continuity equation. This equation expresses the idea that if more of a vector field is flowing out of a box than into it, then some of the quantity must be accumulating in the box. We probably could take the result as given, but the derivation will lead us through an easier version of a tricky argument we will need later, so it will be good practice. Let us then see how to formalize this notion of continuity with some vector calculus!

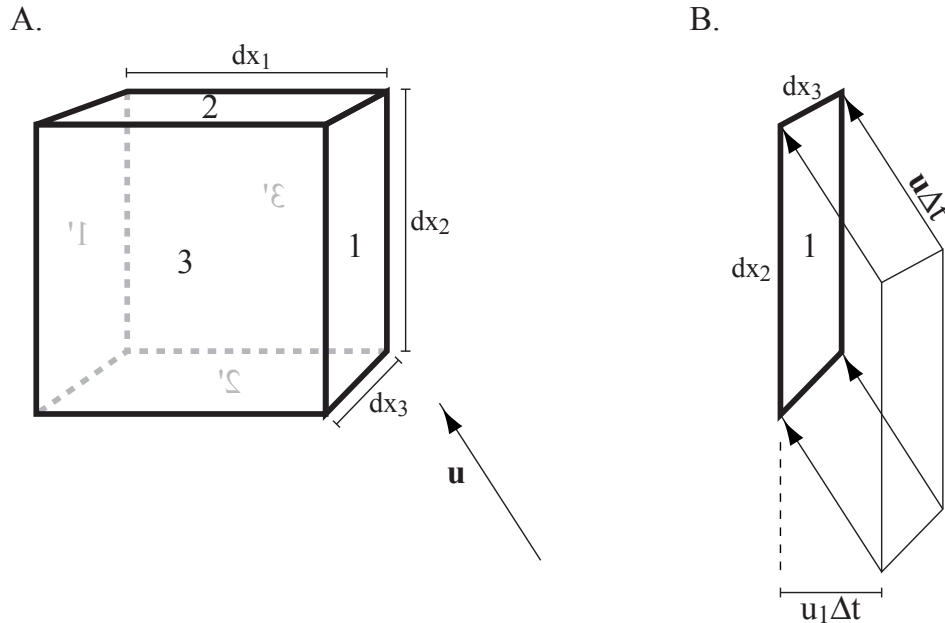


**Figure B.1:** Derivation of the continuity equation. A. A fluid volume element, through which the plasma flows with velocity  $\mathbf{u}$ . The primed surfaces are on the opposite side of the cube as the equivalent unprimed surface. B. The particles within this parallelepiped will pass through face 1 in time  $\Delta t$ .

Consider a differential rectangular volume at the point  $(x_1, x_2, x_3)$  and with sides of length  $dx_1$ ,  $dx_2$ , and  $dx_3$ , as

shown in Figure B.1.A. In a timestep  $\Delta t$  we know

$$\Delta(\# \text{ particles in box}) = (\# \text{ crossing in on face 1}) - (\# \text{ leaving out 1'}) \quad (\text{B.1})$$

$$+ \text{similar terms for } 2, 2', 3, 3' \quad (\text{B.2})$$

The number of particles crossing into the cube through face 1 can be thought of as the number of particles inside a certain parallelepiped bordering face 1, as shown in Figure B.1.B, formed by extruding face 1 through the vector  $-u_1\Delta t$ . It is exactly the particles in this volume that will move across face 1 in the timestep  $\Delta t$ . If we denote the velocity of the fluid in the  $x_1$ -direction by  $u_1$  then the volume of this region is  $dx_2 dx_3 u_1\Delta t$ . The *number* of particles in this region is just this volume times the density:  $n dx_2 dx_3 u_1\Delta t$

Now, we are really interested in the *difference* between the number of particles crossing in on side 1 and the number of particles crossing out along side 1'. These two values are almost the same, since the number crossing out along 1' can be expressed by a formula similar to the one we just obtained for side 1. However,  $n$  and  $u$  are functions of position, so they might change a small amount across the distance  $dx_1$  that separates the two sides. We must thus be careful about *where* we are evaluating  $n$  and  $u_1$ . We evaluate them at the *center* of each face, although it would turn out that to first order that anywhere on the appropriate face would be okay. Consequently,

$$\begin{aligned} (\# \text{ in 1}) - (\# \text{ out 1'}) &= nu_1 dx_2 dx_3 \Delta t|_{(x_1, x_2 + \frac{dx_2}{2}, x_3 + \frac{dx_3}{2})} - \\ &\quad nu_1 dx_2 dx_3 \Delta t|_{(x_1 + dx_1, x_2 + \frac{dx_2}{2}, x_3 + \frac{dx_3}{2})} \end{aligned} \quad (\text{B.3})$$

where the subscripted coordinates indicate where to evaluate  $n$  and  $u_1$ . The expression simplifies if we express the change in  $nu_1$  by its derivative:

$$\begin{aligned} (\# \text{ in 1}) - (\# \text{ out 1'}) &\approx nu_1 dx_2 dx_3 \Delta t|_{(x_1, x_2 + \frac{dx_2}{2}, x_3 + \frac{dx_3}{2})} - \\ &\quad \left( nu_1|_{(x_1, x_2 + \frac{dx_2}{2}, x_3 + \frac{dx_3}{2})} + dx_1 \frac{\partial(nu_1)}{\partial x_1} \right) dx_2 dx_3 \Delta t \end{aligned} \quad (\text{B.4})$$

$$= - \left( \frac{\partial(nu_1)}{\partial x_1} \right) dx_1 dx_2 dx_3 \Delta t \quad (\text{B.5})$$

The *total* change in the number of particles in our box in  $\Delta t$  is a sum of three such terms, one for each coordinate direction. We can identify this sum of three derivatives as a gradient.

$$\Delta(\# \text{ in box}) = -(\nabla \cdot (n\mathbf{u})) dx_1 dx_2 dx_3 \Delta t \quad (\text{B.6})$$

What do we get if we divide this equation through by  $dx_1 dx_2 dx_3 \Delta t$ ? The left-hand side will then be the *rate of change per volume in the number of particles present*, which is the time derivative of the density. Thus, we find a compact equation to express continuity:

$$\frac{\partial n}{\partial t} = -\nabla \cdot (n\mathbf{u}) \quad (\text{B.7})$$

## Momentum Balance

Now that we have seen the origin of the continuity equation, let us move on to the *momentum balance equation*. This equation is really nothing more than Newton's second law,  $\mathbf{F} = m\mathbf{a}$ . While Newton's second law is easy enough to write down for one particle, it is a tricky process to port the concept to a fluid. If we consider one particular particle in the plasma, there is only one force to speak of – the Lorentz force – at least if we ignore collisions. However, our eventual goal is to write down some expressions for the dynamics of the plasma as a sort of homogeneous fluid, with no reference to the particles that compose it on a microscopic level. Thus, what we really want is not  $\mathbf{F} = m\mathbf{a}$  for a single particle, but rather an equivalent expression for a fluid. Recall that *in general* a force is not necessarily equal to  $m\mathbf{a}$  if the mass is changing, but rather  $\mathbf{F} = \frac{\partial(m\mathbf{v})}{\partial t}$ , the rate of change of momentum. Since the mass density of a plasma can easily change with time, we will need to consider this more general version of the second law. Finally,

a last consideration is that with fluids we are interested in the local dynamics of properties such as *mass density* and *force density*, not some sort of *total* mass and force. Thus, what we really need to write down is an expression for the *rate of change of momentum density* for the plasma:

$$\left( \frac{\partial(mn\mathbf{u})}{\partial t} \right)_{\mathbf{x}} = ? \quad (\text{B.8})$$

The  $\mathbf{x}$  subscript is used here as it was on the introductory section on the convective derivative (Section 2.1.1). It simply emphasizes that the derivative is being taken with respect to a box fixed in space, not with respect to a particular particle.

Rather than dive right into a general momentum balance equation for any plasma, let us attack a simple system first, and we will go back to add the details later. Let us consider a fluid of only one species of particle, rather than the usual set of ions and electrons. Furthermore, let us simplify the situation by setting  $\mathbf{E}$  and  $\mathbf{B}$  to 0, so there is no Lorentz force. Then if we fix a location  $\mathbf{x}$  in space, what is the rate of change of momentum density at that point? A nonzero value can be created due to the motion of the fluid particles. For example, there may be a large density of upward moving particles immediately below the box. In this case, we expect a large positive rate of change of momentum density in the upward direction.

Suppose we focus on a particular component of the momentum derivative, say  $\partial(nmu_i)/\partial t$ . We are interested in how much momentum of this  $i$ -direction flows into and out of the box in a given time step  $\Delta t$ . Again applying the basic notion of continuity,

$$\begin{aligned} \Delta(nmu_i)dx_1 dx_2 dx_3 &= (\text{i-momentum in through face 1}) \\ &\quad - (\text{i-momentum out face } 1') \\ &\quad + \text{other terms for } 2, 2', 3, 3' \end{aligned} \quad (\text{B.9})$$

How much i-momentum crosses each face? Let us pick face 1 as a particular case. We will need to introduce the phase-space density of the gas,  $f(\mathbf{x}, \mathbf{v})$ , which is normalized such that  $\int f d^3\mathbf{v} = n$  =density. Then the *number of particles* which cross face 1 is

$$\Delta t dx_2 dx_3 \int d^3\mathbf{v} f v_1 \quad (\text{B.10})$$

We wrote down a similar but simpler equation above in discussing the continuity equation (recall Figure B.1.B). There, we had “already” performed the  $f$  integral to replace it with  $nu_i$ , where  $u_i$  was the *mean* velocity in the  $x_i$ -direction. Here we have kept the integral because we will need to take an expected value in a moment, and this requires an integral over the phase space density. Now to find the *amount of i-momentum* transferred into the box by these incoming particles, we simply insert the momentum of a particle ( $mv_i$ ) inside the integral.

$$(\text{i-momentum in through face 1}) = \Delta t dx_2 dx_3 \int d^3\mathbf{v} f v_1 mv_i \quad (\text{B.11})$$

We recognize this integral as an expected value for  $v_1 v_i$  and thus obtain that the i-momentum flow in through face 1 is  $\Delta t dx_2 dx_3 nm\langle v_1 v_i \rangle|_{(x_1, x_2 + \frac{dx_2}{2}, x_3 + \frac{dx_3}{2})}$ . Here, the subscripted coordinates tell us where to evaluate  $n, v_1$ , and  $v_i$ : on the center of face 1. The total i-momentum through all six faces is a sum of six such terms:

$$\begin{aligned} \Delta(nmu_i)dx_1 dx_2 dx_3 &= \Delta t dx_2 dx_3 nm\langle v_1 v_i \rangle|_{(x_1, x_2 + \frac{dx_2}{2}, x_3 + \frac{dx_3}{2})} \\ &\quad - \Delta t dx_2 dx_3 nm\langle v_1 v_i \rangle|_{(x_1 + dx_1, x_2 + \frac{dx_2}{2}, x_3 + \frac{dx_3}{2})} \\ &\quad + \Delta t dx_1 dx_3 nm\langle v_2 v_i \rangle|_{(x_1 + \frac{dx_1}{2}, x_2, x_3 + \frac{dx_3}{2})} \\ &\quad - \Delta t dx_1 dx_3 nm\langle v_2 v_i \rangle|_{(x_1 + \frac{dx_1}{2}, x_2 + dx_2, x_3 + \frac{dx_3}{2})} \\ &\quad + \Delta t dx_1 dx_2 nm\langle v_3 v_i \rangle|_{(x_1 + \frac{dx_1}{2}, x_2 + \frac{dx_2}{2}, x_3)} \\ &\quad - \Delta t dx_1 dx_2 nm\langle v_3 v_i \rangle|_{(x_1 + \frac{dx_1}{2}, x_2 + \frac{dx_2}{2}, x_3 + dx_3)} \end{aligned}$$

where the terms are for faces 1, 1', 2, 2', 3, and 3' respectively. As we saw in the continuity equation derivation, this expression does *not* evaluate to zero even though the terms look similar because  $n$  and the  $v$ s are functions of position and can change between face 1 and 1', between 2 and 2' etc. Examining for a moment only the 1, 1' pair (the top line in the above equation) we can again express the difference between the 1 and 1' faces by expanding the difference to first order using a derivative (like we did in Equations B.3-B.4):

$$\begin{aligned}
\Delta(nmu_i)dx_1 dx_2 dx_3 &= \Delta t dx_2 dx_3 nm\langle v_1 v_i \rangle|_{(x_1, x_2 + \frac{dx_2}{2}, x_3 + \frac{dx_3}{2})} - \\
&\quad \Delta t dx_2 dx_3 m \left( n \langle v_1 v_i \rangle|_{(x_1, x_2 + \frac{dx_2}{2}, x_3 + \frac{dx_3}{2})} + dx_1 \frac{\partial(n \langle v_1 v_i \rangle)}{\partial x_1} \right) \\
&\quad + (2, 2', 3, 3' \text{ terms}) \\
&= -\Delta t dx_1 dx_2 dx_3 m \frac{\partial(n \langle v_1 v_i \rangle)}{\partial x_1} - \Delta t dx_1 dx_2 dx_3 m \frac{\partial(n \langle v_2 v_i \rangle)}{\partial x_2} \\
&\quad - \Delta t dx_1 dx_2 dx_3 m \frac{\partial(n \langle v_3 v_i \rangle)}{\partial x_3} \\
&= -\sum_{j=1}^3 \frac{\partial(nm \langle v_i v_j \rangle)}{\partial x_j}
\end{aligned}$$

Dividing by  $\Delta t dx_1 dx_2 dx_3$  we obtain  $\frac{\Delta(nmu_i)}{\Delta t}$ , the *change in momentum density per unit time*, which is exactly what we were looking for. We used  $\Delta$ s above, but since this ratio of deltas was constructed for a specific position we can turn them into a partial derivative.

$$\left( \begin{array}{c} \text{change in i-momentum density} \\ \text{per unit time} \end{array} \right) = \frac{\partial(nmu_i)}{\partial t} = -\sum_{j=1}^3 \frac{\partial(nm \langle v_i v_j \rangle)}{\partial x_j} \quad (\text{B.12})$$

At this point, we are going to do something which will not make immediate sense. We will add and subtract a term, causing the formula to look needlessly complicated. Furthermore, we will call one of the resulting terms a “pressure-like term” without explanation for now why this term has anything to do with pressure (more on that in the next section!). Bear with us for now; terms will cancel and we will end up with terms that are easier to recognize than the ugly meaningless sum we currently see. Here goes:

$$\frac{\partial(nmu_i)}{\partial t} = -\sum_{j=1}^3 \frac{\partial(nm(\langle v_i v_j \rangle - \langle v_i \rangle \langle v_j \rangle))}{\partial x_j} - m \sum_{j=1}^3 \frac{\partial(n \langle v_i \rangle \langle v_j \rangle)}{\partial x_j} \quad (\text{B.13})$$

$$= -(\text{pressure term})_i - m \sum_{j=1}^3 \frac{\partial(n \langle v_i \rangle \langle v_j \rangle)}{\partial x_j} \quad (\text{B.14})$$

where

$$(\text{pressure term})_i \equiv \sum_{j=1}^3 \frac{\partial}{\partial x_j} mn(\langle v_i v_j \rangle - \langle v_i \rangle \langle v_j \rangle) \quad (\text{B.15})$$

Recall that we distinguished between  $\mathbf{v}$  and  $\mathbf{u}$  throughout this thesis:  $\mathbf{u} = \langle \mathbf{v} \rangle$ . In other words,  $\mathbf{u}$  is the mean velocity, while  $\mathbf{v}$  indexes the possible velocities of a single particle within the distribution. We can then replace the  $\langle v_i \rangle$ s with

$u_i$ s on the right hand side of Equation B.14. Applying the product rule, we find that

$$\frac{\partial(nmu_i)}{\partial t} = -( \text{pressure term})_i - m \sum_{j=1}^3 \frac{\partial(nu_i u_j)}{\partial x_j} \quad (\text{B.16})$$

$$mn \left( \frac{\partial u_i}{\partial t} \right) + mu_i \left( \frac{\partial n}{\partial t} \right) = -( \text{pressure term})_i$$

$$-mu_i \sum_{j=1}^3 \frac{\partial(nu_j)}{\partial x_j} - mn \sum_{j=1}^3 u_j \frac{\partial u_i}{\partial x_j}$$

$$\quad \quad \quad (\text{B.17})$$

On the left hand side, we will now use the continuity equation to replace  $\partial n / \partial t$ . On the right side, we recognize one of the sums as a component-free expression.

$$mn \frac{\partial u_i}{\partial t} - mu_i (\nabla \cdot (n\mathbf{u})) = -( \text{pressure term})_i$$

$$-mu_i (\nabla \cdot (n\mathbf{u})) - mn \sum_{j=1}^3 u_j \frac{\partial u_i}{\partial x_j}$$

$$\quad \quad \quad (\text{B.18})$$

Now, cancel the equivalent gradient terms from each side. Until now we have only had an equation for the  $i$ -th component of momentum, but we might as well put all three components together in a vector equation. After doing this and bringing the last term to the left hand side we obtain

$$nm \left( \frac{\partial \mathbf{u}}{\partial t} + (\mathbf{u} \cdot \nabla) \mathbf{u} \right) = -( \text{pressure term}) \quad (\text{B.19})$$

Note that the quantity in parentheses on the left is the convective derivative of  $\mathbf{u}$ . In fact, what we have done in this section is a more thorough version of what we did in Section 2.1.1 on the convective derivative – promoting  $\mathbf{F} = m\mathbf{a}$  for a particle into a fluid version. In this more precise derivation, we can see why we must include the “pressure term” as one of the forces on the fluid elements, as discussed in a footnote in the convective derivative discussion.

Almost done! There are two last things we need to add to this equation to form a complete momentum balance equation for each species. We began this section by looking for a momentum balance equation for a fluid with no external forces ( $\mathbf{E} = \mathbf{B} = 0$ ). However, if we want a general expression for a plasma that does experience these forces, it is quite easy to add such a term in. To all of our equations for  $\partial(\text{momentum density})/\partial t$  we would have to add the *local force density* for a species with charge  $q$ :  $nq(\mathbf{E} + \mathbf{u} \times \mathbf{B})$ . Secondly, the flow of each species of particle is affected by collisions with the other species. Collisions effectively subtract a quantity of momentum from the balance equation of one species and add that same amount (a result of momentum conservation) to the equation of the other species. We will investigate this collision term more in the following sections, but for now let us simply denote by  $\mathbf{R}_{\alpha\beta}$  the rate of momentum per volume transferred from species  $\beta$  to species  $\alpha$ . Had we wanted to consider these two additional terms from the start we would have simply added them to the right hand side in the very beginning at equation B.12. They would sit there idly for the entire derivation and would still remain on the right hand side now. Thus, our completed momentum balance equation for each species  $\alpha$  is:

$$n_\alpha m_\alpha \left( \frac{\partial \mathbf{u}_\alpha}{\partial t} + (\mathbf{u}_\alpha \cdot \nabla) \mathbf{u}_\alpha \right) = -( \text{pressure term})_\alpha + n_\alpha q_\alpha (\mathbf{E} + \mathbf{u}_\alpha \times \mathbf{B}) + \mathbf{R}_{\alpha\beta} \quad (\text{B.20})$$

Unfortunately from here on out we will need subscripts to indicate both the components of a vector and also the species of particle; the context should be enough to identify which meaning is intended.

## The Pressure Tensor

Let us discuss the “pressure term” we defined earlier to see how it relates to pressure. The term looks like:

$$(\text{pressure term})_i \equiv \sum_{j=1}^3 \frac{\partial}{\partial x_j} mn(\langle v_i v_j \rangle - \langle v_i \rangle \langle v_j \rangle) \quad (\text{B.21})$$

Let us focus on the bit inside the derivative. We can split the above equation into:

$$(\text{pressure term})_i \equiv \sum_{j=1}^3 \frac{\partial}{\partial x_j} P_{ij} \quad (\text{B.22})$$

$$P_{ij} \equiv mn(\langle v_i v_j \rangle - \langle v_i \rangle \langle v_j \rangle) \quad (\text{B.23})$$

It will turn out that the  $P_{ij}$  object is something like the pressure we are used to, although it at first seems to be a complicated multidimensional object. In fact, it happens to be a tensor. We cannot immediately assume that it is a tensor simply because it has two indices, for not just any object with nine components *transforms* like a tensor. Let us check that it is in fact a tensor, then. Suppose we switch to a new reference frame such that the velocity vectors transform to new primed components according to:

$$v'_k \equiv \sum_{l=1}^3 a_{kl} v_l \quad (\text{B.24})$$

Then how does the  $P_{ij}$  object transform? If it is a tensor it will pick up *two* copies of the  $a_{ij}$ s. It turns out that the linearity of expected values does the trick for us:

$$P'_{ij} = mn(\langle v'_i v'_j \rangle - \langle v'_i \rangle \langle v'_j \rangle) \quad (\text{B.25})$$

$$= mn \left[ \left\langle \left( \sum_w a_{iw} v_w \right) \left( \sum_x a_{jx} v_x \right) \right\rangle - \left\langle \sum_y a_{iy} v_y \right\rangle \left\langle \sum_z a_{jz} v_z \right\rangle \right] \quad (\text{B.26})$$

$$= mn \sum_{wxyz} (a_{iw} a_{jx} \langle v_w v_x \rangle - a_{iy} a_{jz} \langle v_y \rangle \langle v_z \rangle) \quad (\text{B.27})$$

$$= \sum_{wx} a_{iw} a_{jx} mn(\langle v_w v_x \rangle - \langle v_w \rangle \langle v_x \rangle) \quad (\text{B.28})$$

$$= \sum_{wx} a_{iw} a_{jx} P_{wx} \quad (\text{B.29})$$

So  $P_{ij}$  is indeed a tensor, and so from now on we will refer to it as  $\underline{P}$ . As an interesting observation, note that its definition in equation B.23 is completely symmetrical under exchange of indices. Thus,  $P_{ij}$  is a *symmetric* tensor.

So what does this object have to do with pressure?

**Theorem 3.** *For a gas with a Maxwellian distribution of particle velocities,  $\underline{P}$  reduces to the familiar  $nkT$  pressure times the identity tensor ( $\underline{P} = p\underline{I}$ ).*

In plasmas the velocity distribution need not be isotropic, and there may be other odd correlations that make the various terms in  $\underline{P}$  useful.

*Proof.* Let us begin by showing that for a gas with a Maxwellian distribution the off-diagonal elements of  $\underline{P}$  are 0. This can be seen by looking at the definition of  $\underline{P}$  in equation B.23 and noting that it is just  $mn$  times the statistical correlation function between  $v_i$  and  $v_j$ . If  $i \neq j$  then this correlation is zero for our gas; a particle's velocity in the x-direction is uncorrelated with its velocity in the y-direction.

Now let us examine the diagonal terms in  $\underline{P}$ .  $P_{ii} = mn(\langle v_i^2 \rangle - \langle v_i \rangle^2) = mn\text{Var}(v_i)$ , the statistical variance of the velocity in the i-th coordinate direction. This variance may not be a value you remember off the top of your head, so let us quickly derive it. Recall that the probability density  $f(v_i)$  is proportional to a Boltzmann factor in  $E_i$ , the energy due to motion in the  $i$ -th direction:

$$f(v_i) \propto \exp(-\beta E_i) = \exp\left(-\left(\frac{1}{kT}\right)\left(\frac{1}{2}mv_i^2\right)\right) \quad (\text{B.30})$$

$$= \exp\left(-\frac{v_i^2}{2(kT/m)}\right) \quad (\text{B.31})$$

Recognizing that this is a Gaussian distribution, and recalling that the variance of a Gaussian is just the factor between the parentheses in the denominator, we find that  $\text{Var}(v_i) = kT/m$ . Consequently,

$$P_{ii} = mn \left( \frac{kT}{m} \right) = nkT \quad (\text{B.32})$$

and  $nkT$  is exactly the standard definition of pressure in a gas.  $\square$

Thus, not only is  $\underline{\mathbf{P}}$  isotropic for a Maxwellian gas, but also its value is exactly the standard pressure times  $\underline{\mathbf{I}}$ . Incidentally, the derivative of this pressure tensor that appears in the balance equation happens to be the way that the *divergence of a tensor* is defined. Thus, from now on our equations will use  $\nabla \cdot \underline{\mathbf{P}}$  for the “pressure term”.

## Simplifications, Round 1

Our momentum balance equation for the electrons now looks like this:

$$n_e m_e \left( \frac{\partial \mathbf{u}_e}{\partial t} + (\mathbf{u}_e \cdot \nabla) \mathbf{u}_e \right) = -\nabla \cdot \underline{\mathbf{P}}_e - n_e e(\mathbf{E} + \mathbf{u}_e \times \mathbf{B}) + \sum_{\beta \neq e} \mathbf{R}_{e\beta} \quad (\text{B.33})$$

Note that this is one of the equations (2.12) we listed as one of the exact dynamical equations for a plasma in the section first introducing MHD. At this point, we will begin to apply the MHD simplifications to reduce the complexity of the system. Eventually this equation above will become Ohm’s law. Rather than eliminate all the non-zeroth-order effects in one fell swoop with an order-of-magnitude argument, we will proceed slowly to see where some of the other terms in our “generalized Ohm’s law” come from.

**Simplification 1.** *The plasma consists of fully ionized monoatomic hydrogen ( $H^+$  and  $e^-$ ).*

The sum in the rightmost term above reduces to  $\mathbf{R}_{ei}$ .

**Simplification 2.** *The separation of charge is negligible, i.e.,  $n_e \approx n_i$ .*

As a result we will henceforth use  $n$  to refer to the density of *both* the electrons and ions, since the values are assumed to be only negligibly different. This assumption is a reasonable one since any separation of charge cannot persist for very long; the rapidly moving electrons react to cancel it. Charges cannot be felt beyond a few Debye lengths, so in effect MHD is assuming the system is much larger than a Debye length.

**Simplification 3.** *The electron mass is small compared with the ion mass:  $m_e \ll m_i$*

This is a fine simplification for any plasma, since  $m_e/m_i < 10^{-3}$ . To 0th order, then, the momentum of the overall plasma is simply the momentum of the ions. Consequently we will begin to call the ion velocity  $\mathbf{u}_i$  simply  $\mathbf{u}$ .

Note that with our simplifications, the current density has the form

$$\mathbf{J} \approx ne(\mathbf{u} - \mathbf{u}_e) \quad (\text{B.34})$$

## Collisions and the Resistivity Term

What can we say about the collision factor  $\mathbf{R}_{ei}$ ?

**Simplification 4.** *The momentum  $\mathbf{R}_{ei}$  transferred to the electrons from the ions is parallel to  $(\mathbf{u} - \mathbf{u}_e)$*

This could certainly be false: two billiard balls that collide with some impact parameter certainly exchange a momentum that is not parallel to their velocity difference. However, for our two superimposed streams of particles here, this assumption is a reasonable one to make. If we imagine one electron passing through a sea of fixed protons, the rate at which it encounters protons will be proportional to its velocity relative to the proton field. In a complex plasma where all particles are moving, motion is restricted by magnetic orbits, and other such complications, this assumption might be less valid. For now we will ignore these concerns. Now, note that the *current density*  $\mathbf{J}$  is *also* proportional to  $(\mathbf{u} - \mathbf{u}_e)$ . In other words,  $\mathbf{R}_{ei} \parallel \mathbf{J}$ . These two quantities are thus related by a proportionality constant, which we can call  $\alpha$ :  $\mathbf{R}_{ei} = \alpha \mathbf{J}$ . Is there anything interesting we can say about this  $\alpha$ ? Suppose we were applying the momentum balance equation to a very boring plasma, one in which there was no magnetic field ( $\mathbf{B} = 0$ ), homogenous pressure ( $\nabla \cdot \underline{\mathbf{P}} = 0$ ), and the mean velocity of each species was 0. In this case the momentum balance equation is greatly simplified:

$$0 = -ne\mathbf{E} + \alpha\mathbf{J} \quad (\text{B.35})$$

or,

$$\mathbf{J} = \frac{ne}{\alpha}\mathbf{E} \quad (\text{B.36})$$

This last equation looks quite similar to a traditional Ohm's law we might find for a resistive solid:

$$\mathbf{J} = \frac{1}{\eta}\mathbf{E} \quad (\text{B.37})$$

Comparing these last two equations, then, we see that it makes some sense to use  $\eta n_e e$  instead of  $\alpha$  as our proportionality constant between  $\mathbf{R}_{ei}$  and  $\mathbf{J}$ . We can call  $\eta$  the "resistivity" of the plasma. If we do, then in the case where we turn off the magnetic fields and bring the plasma to a static equilibrium this  $\eta$  value will equal the resistivity we are used to from electrodynamics. However, it is not so clear what a resistivity is in a more complicated plasma. In the Ohm's law for solids we *defined* resistivity as the proportionality constant between the applied electric field in a material and the resulting current that flowed. However, we can see in the momentum balance equation that we cannot expect a nice linear relationship in the case of a complicated plasma. Instead we will use a *different definition* of resistivity when referring to plasmas than we did in solids, but one that reduces to the old definition of resistivity in the case of "boring" plasmas. The definition, as we have already stated, is "whatever value, when multiplied by  $n_e e \mathbf{J}$ , yields the rate of momentum density transferred from the ions to the electrons ( $\mathbf{R}_{ei}$ ).

## Simplifications, Round 2

At this point, our electron momentum balance equation has become:

$$nm_e \left( \frac{\partial \mathbf{u}_e}{\partial t} + (\mathbf{u}_e \cdot \nabla) \mathbf{u}_e \right) = -\nabla \cdot \underline{\mathbf{P}}_e - ne(\mathbf{E} + \mathbf{u}_e \times \mathbf{B}) + ne\eta\mathbf{J} \quad (\text{B.38})$$

From here on, we will start to throw away terms. To do so rigorously, we must argue that they are of a much lower order than some other term in the expression, just as we argued away the displacement current in the previous Appendix. Whereas in that case we ultimately plugged in SSX values to show a ratio of terms was very small, here we would instead turn the ratio into something held to be small in the MHD other assumptions (e.g.,  $u/c \ll 1$ ). The details are very tedious and will not be reproduced here.

**Simplification 5.** *The  $nm_e(\mathbf{u}_e \cdot \nabla) \mathbf{u}_e$  term is negligible.*

so,

$$nm_e \left( \frac{\partial \mathbf{u}_e}{\partial t} \right) = -\nabla \cdot \underline{\mathbf{P}}_e - ne(\mathbf{E} + \mathbf{u}_e \times \mathbf{B}) + ne\eta\mathbf{J} \quad (\text{B.39})$$

We would like at this point to eliminate the last traces of the electron fluid velocity  $\mathbf{u}_e$ , which we can do by rearranging our expression for  $\mathbf{J}$ :

$$\mathbf{u}_e = \mathbf{u} - \frac{1}{ne} \mathbf{J} \quad (\text{B.40})$$

Substituting this expression into our latest version of the momentum balance equation yields

$$m_e n \frac{\partial(\mathbf{u} - \mathbf{J}/ne)}{\partial t} = -ne \left( \mathbf{E} + \left( \mathbf{u} - \frac{1}{ne} \mathbf{J} \right) \times \mathbf{B} \right) - \nabla \cdot \underline{\mathbf{P}}_e + \eta ne \mathbf{J} \quad (\text{B.41})$$

**Simplification 6.** *The  $\frac{\partial \mathbf{u}}{\partial t}$  term in the above equation is negligible.*

After this term is removed and some rearrangement, we finally arrive at one of the standard forms of Ohm's law:

$$\mathbf{E} + \mathbf{u} \times \mathbf{B} = \eta \mathbf{J} - \frac{1}{ne} \nabla \cdot \underline{\mathbf{P}}_e + \frac{1}{ne} \mathbf{J} \times \mathbf{B} + \frac{m_e}{ne^2} \frac{\partial \mathbf{J}}{\partial t} \quad (\text{B.42})$$

Another common form – the one used often in this thesis – is obtained by the following simplification:

**Simplification 7.** *The electron pressure is isotropic.*

Thus,

$$\mathbf{E} + \mathbf{u} \times \mathbf{B} = \eta \mathbf{J} - \frac{1}{ne} \nabla p_e + \frac{1}{ne} \mathbf{J} \times \mathbf{B} + \frac{m_e}{ne^2} \frac{\partial \mathbf{J}}{\partial t} \quad (\text{B.43})$$

If we continue to eliminate every term that can possibly be eliminated by the MHD assumptions, we can eventually show that the whole right-hand side of Ohm's law is negligible. At the end of this process we are left at last with the ideal MHD Ohm's law:

$$\mathbf{E} + \mathbf{u} \times \mathbf{B} = 0 \quad (\text{B.44})$$

## Appendix C

# Multiplexer timing circuitry

The operation of the multiplexing system requires that the digitizers and multiplexer boards be synchronized within only a few tens of nanoseconds. In particular, each multiplexer board must be on the first channel at precisely the same moment that the digitizers begin to acquire data. Otherwise, there would be no way to know which probe position corresponded to the first point in the timeseries uploaded to the computer, and thus no way to de-multiplex the data. If the system *is* in fact synched so that probe position 0 corresponds with the first value in the timeseries, then the de-multiplexing software can simply associate value 0 with probe position 0, value 1 with position 1, and in general value  $n$  with position  $n \bmod 8$ . The timing situation is complicated by the fact that each of the 10 DSP digitizer modules – each of which has eight inputs – accepts signals from several multiplexer boards, and so *every* multiplexer board must be synched with *every* DSP.

Several custom circuits for timing coordination were attempted by the author, Dr. Cothran, and Mr. Radcliffe. The circuit which finally produced consistent results, designed by Dr. Cothran, is shown in Figures C.1 - C.3.

The system accepts a 10 MHz clock input from a function generator (*not* from the DSPs) and also a copy of the trigger pulse which fires the high-voltage ionizing current. It reproduces the clock signal so that every multiplexer and DSP is driven with a copy of the original input. Also, a “gate pulse” is sent to each multiplexer and DSP. The rising edge of the gate pulse acts as a trigger for the DSPs to start acquiring data. It also tells the multiplexers to begin multiplexing from channel zero. The gate pulse is derived from the trigger signal, but delayed using a flip-flop until the first following falling edge of the clock. This ensures that the multiplexer boards have a full half clock cycle (50 ns) to switch to multiplexing mode. The length of the gate pulse is not critical, as long as it exceeds the interval over which data is acquired (otherwise the multiplexers stop multiplexing). Thus, the gate remains high until the end of the 350  $\mu$ s trigger pulse – much longer than the timescale of plasma dynamics.

In order to produce the required 35 gate and clock output signals without voltage droop, a series of TTL logic buffers was used. An important design consideration is that all the outputs pass through roughly the same number of buffer stages from the input to the output. Otherwise, the small (10s of ns) delay from the input to the output of the buffers can be enough to put the various components out of synchrony. Note that it is not critical that the output gates and clocks be synchronized with the input trigger and clock respectively (i.e., it is not important that the multiplexing start within 100 ns of the high-voltage pulse), only that the outputs be synchronized with respect to each other.

Chips used were 7408 AND gates, 74LS08 AND gates (marked with ‘LS’ on the schematics here), 74LS07 buffers, 75138 coax cable drivers, and 74LS74 flip-flops.

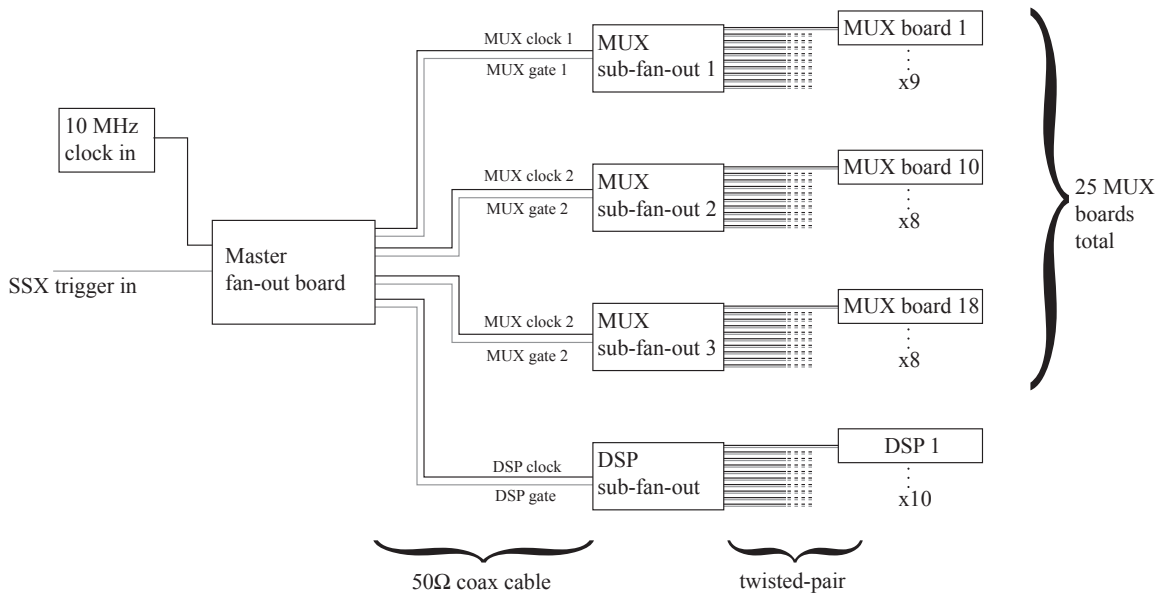


**Figure C.1:** Components of the multiplexer custom timing circuitry.

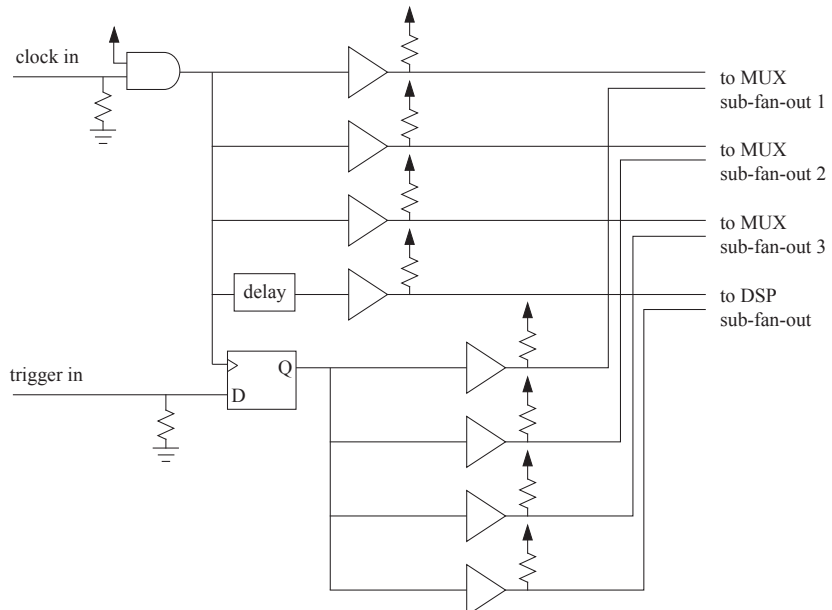


**Figure C.2:** Components of the multiplexer master fan-out board. Resistors are 50Ω unless otherwise specified. Up arrows indicate a connection to +5VDC. Buffers on this board are the 75138 coax cable drivers.

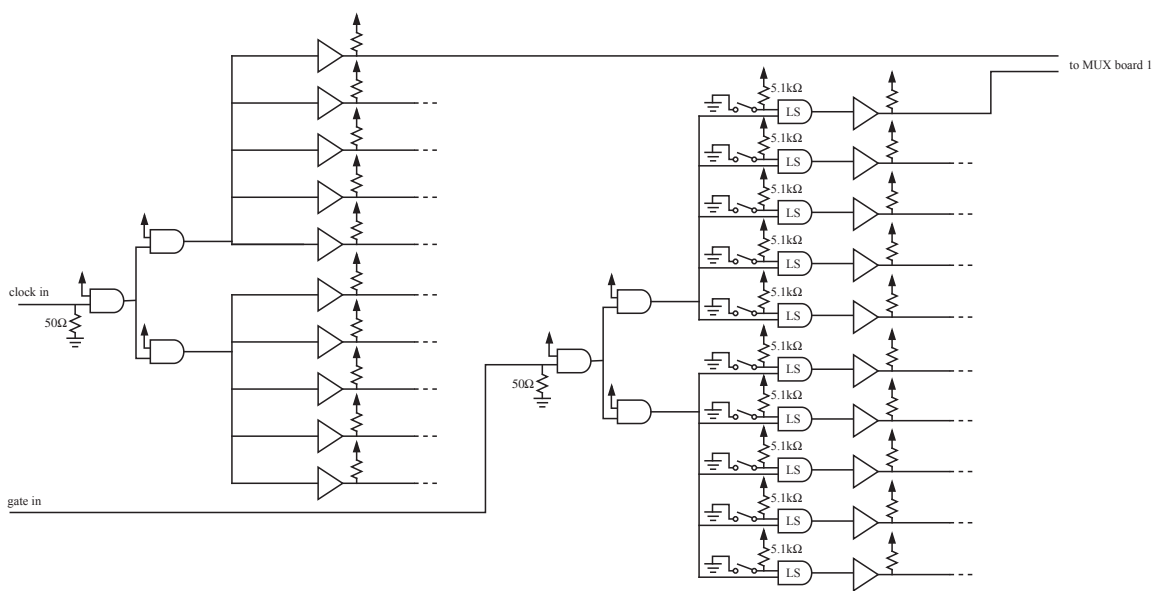


**Figure C.3:** Components of the multiplexer subordinate fan-out boards. Resistors are  $150\Omega$  unless otherwise specified. Up arrows indicate a connection to +5VDC. Buffers on this board are the 74LS07 chips.

## Appendix D

# Demonstration of 3D probe on simple vacuum fields

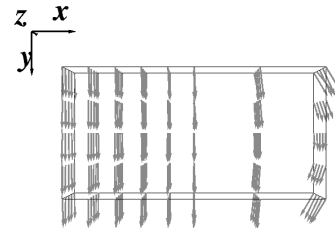
In this Appendix, we present data taken with the 3D magnetic probe taken *outside* of SSX. To check that the probe gave sensible results, a number of fields were produced using long straight wires and the Helmholtz coil aligned in various geometries. These results are a nice verification that magnetostatics works the way one expects. Figure 4.3 also illustrates the  $\mathbf{B}$  field and current obtained for several vacuum fields in this series.



A.



B.



C.

**Figure D.1:** As a result of the calibration procedure described in Section 3.2.2, the data displayed for a shot with the Helmholtz coil in the  $x$ ,  $y$ , or  $z$  direction will be *by definition* correct. Each coil is calibrated so that the data from a Helmholtz shot along a coordinate direction matches a theoretical model for such a field. The model actually finds the exact field vector - it does not merely assume a uniform field. This precision can be seen in this figure, which shows a Helmholtz calibration shot and the corresponding “data” (which is really the analytical model, not data). At the probe locations on the far right, proximity to the wire results in a non-uniformity of the field. A and C are in the same side-view perspective, while B is a birds-eye view.

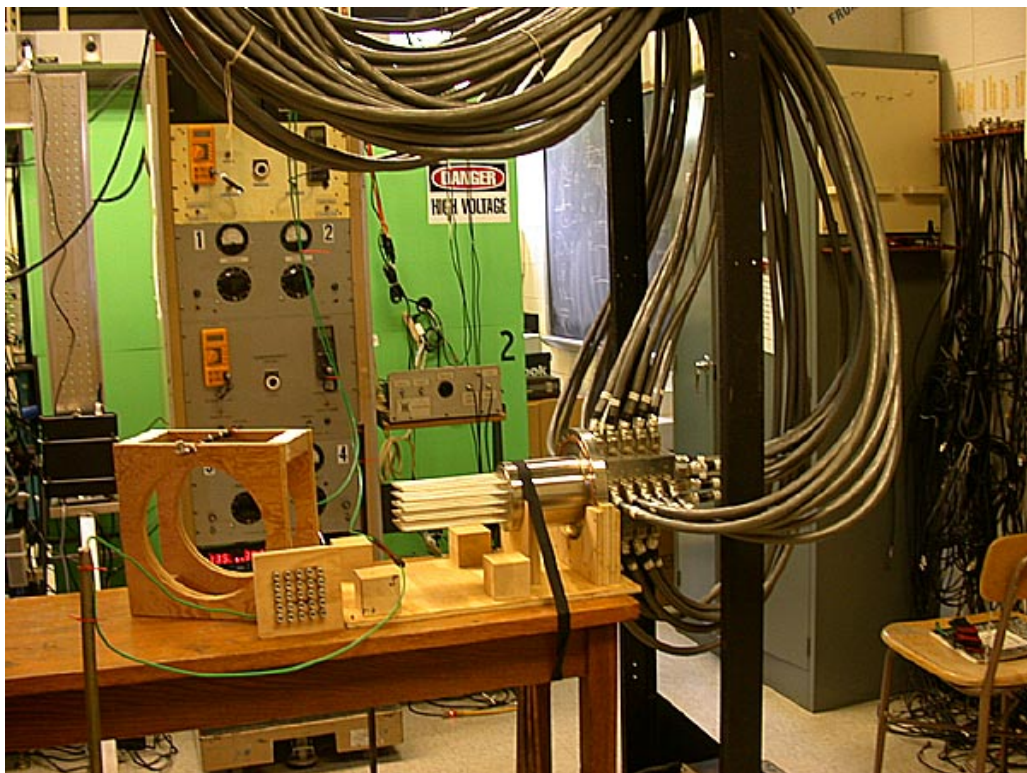


**Figure D.2:** The apparatus used for these vacuum field measurements. On the table are the Helmholtz coil, the “squasher” (see Figure D.6), and the “quasi-infinite” wire. The probe is not set up to measure any particular field at this point.

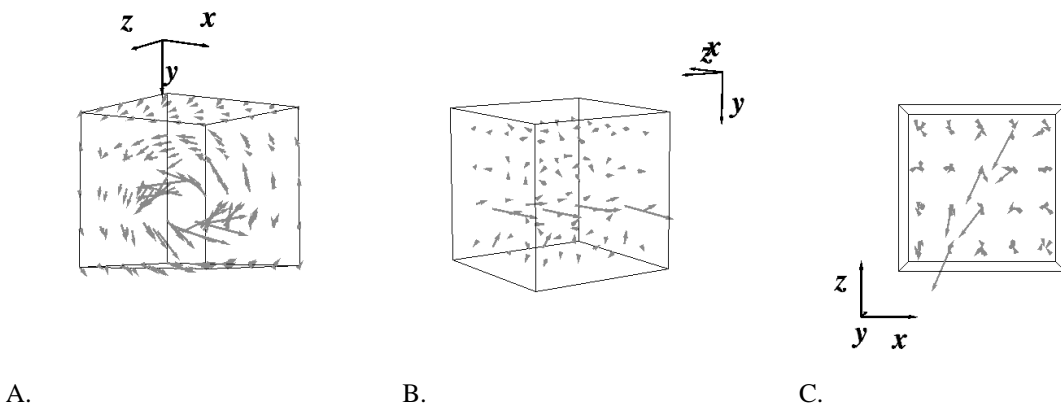


**Figure D.3:** Here, a long straight wire is run through the array at an angle in the  $xz$  plane. Unfortunately, no photograph was taken of the configuration. A: The magnetic field circles around the wire. B and C show the current, obtained by taking  $\nabla \times \mathbf{B}$ . As expected, we see a strong signal pointed along the line of the wire, and negligible signal elsewhere.

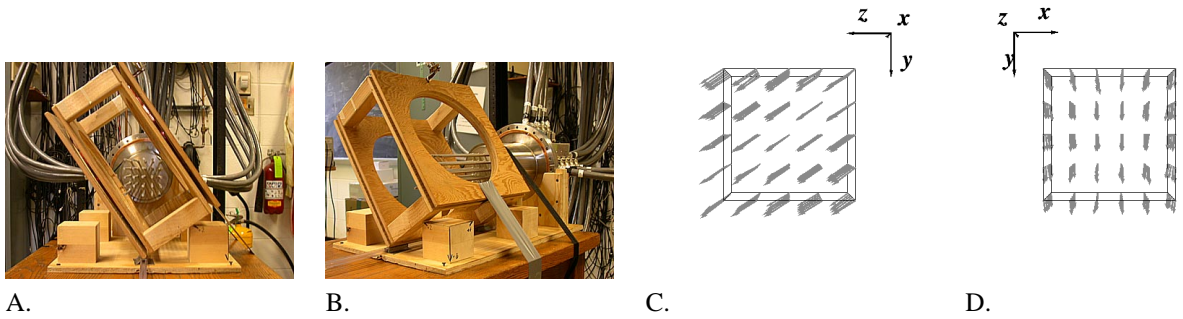


**Figure D.4:** In this setup, the Helmholtz coil is directed at an angle so that its axis points in the  $(0, 1, 1)$  direction. A and B show two different views of the configuration. C and D show the data, which is approximately uniform as desired. A and C are roughly the same perspective. D shows a side view.

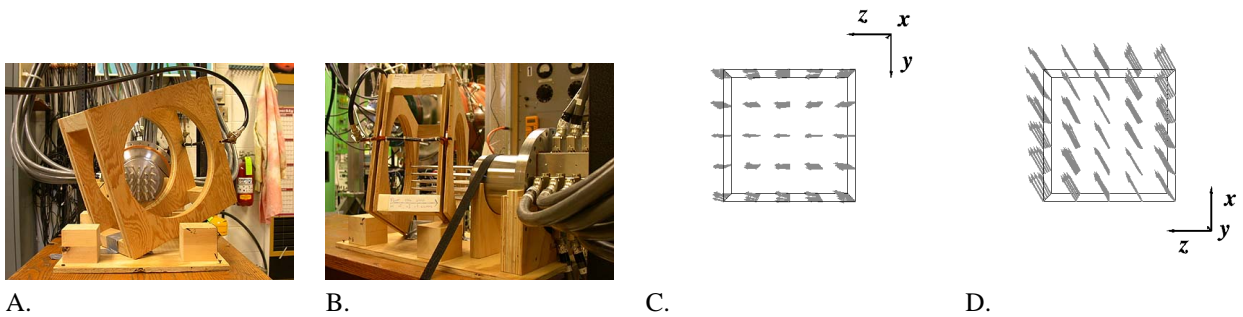
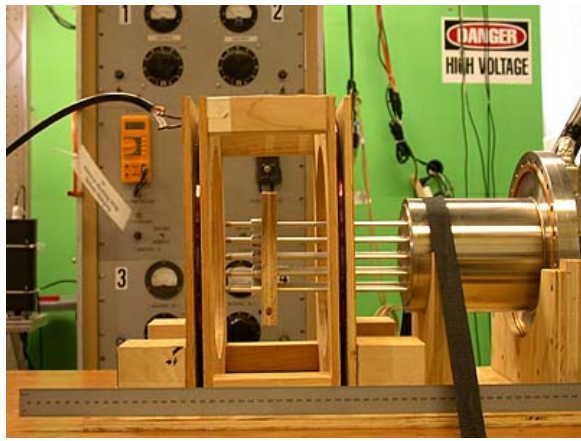
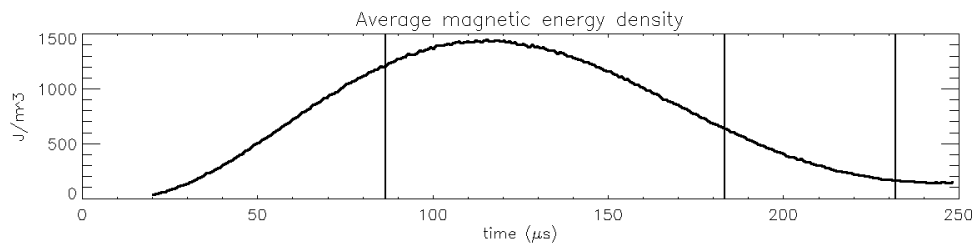


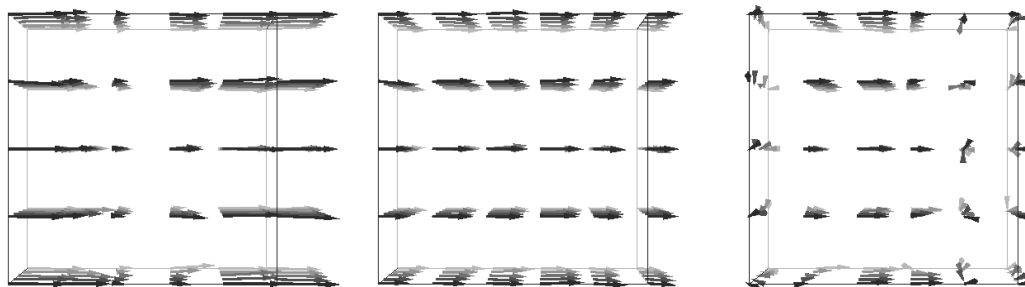
**Figure D.5:** This run is very much like the previous one, except the Helmholtz coil is adjusted to point in a new direction- along  $(1, 0, 1)$ . A and B show two different views of the configuration. C and D show the data, which is approximately uniform as desired. A and C are roughly the same perspective. D shows a bird-eye view.



A.



B.



C.

D.

E.

**Figure D.6:** A: The “squasher” is a piece of plywood with a  $5 \times 5$  array of hollow aluminum cylinders feeding through it. The squasher can be placed over the tines of the probe, and fits snugly over them. The metal in the squasher causes a roughly  $100 \mu\text{s}$  soak time for the magnetic field to penetrate the plane of probes which it shields. C-E show data for a shot like the one photographed in A from the same perspective. In C, the unshielded probe locations experience a field, but it has not soaked through to the third layer. By the time of D, the field has soaked through, meaning circular currents are flowing in the cylinders of the squasher. While the rest of the field dies away, in E, these eddy currents maintain the field for the probe locations inside the squasher cylinders.

## Appendix E

# Visualization Software

Visualization software was indispensable for comprehension of the massive three-dimensional datasets produced by the magnetic probe array. Fortunately, the IDL language has a powerful set of 3D graphics rendering functions, which enabled custom applications to be rapidly built for SSX. This Appendix expands on the discussion of Section 3.2.4 and presents the details of several of these programs. Coding of these routines was done primarily by the author, with much assistance on PLOTTER3D\_XP.PRO from Chris Cothran.

### PLOTTER3D.PRO

This first visualization application, pictured earlier in Figure 3.13, was developed in tandem with the multiplexer timing circuitry, so that sense could be made of the first tests of the probe with vacuum fields from line currents and the Helmholtz coil. At this point we anticipated only the first few objects we would want to display:  $\mathbf{B}$  vectors,  $\mathbf{J} = (1/\mu_0)\nabla \times \mathbf{B}$  vectors, magnetic energy surfaces, and fieldlines. The program was designed to be highly interactive, enabling users to rapidly gain an intuitive overall sense of the data.

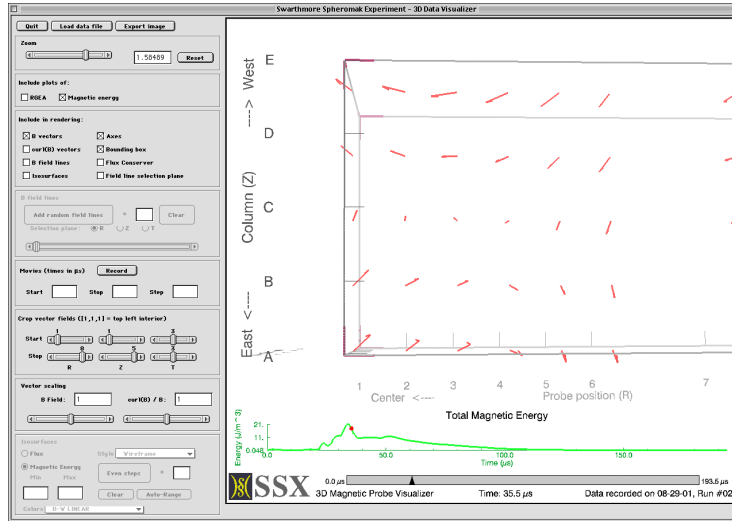


**Figure E.1:** PLOTTER3D.PRO allows the user to crop the volume so that a more manageable number of vectors are displayed. An arbitrary rectangular subset of the  $8 \times 5 \times 5$  grid can be shown. The user can scan forward and backwards through the shot in real time using the slider at the bottom. It is also possible to rotate, pan, and zoom in real time. A box outlines the region in which the magnetic pickup loops are arranged. The average magnetic energy density plot can be turned on at the bottom of the screen.

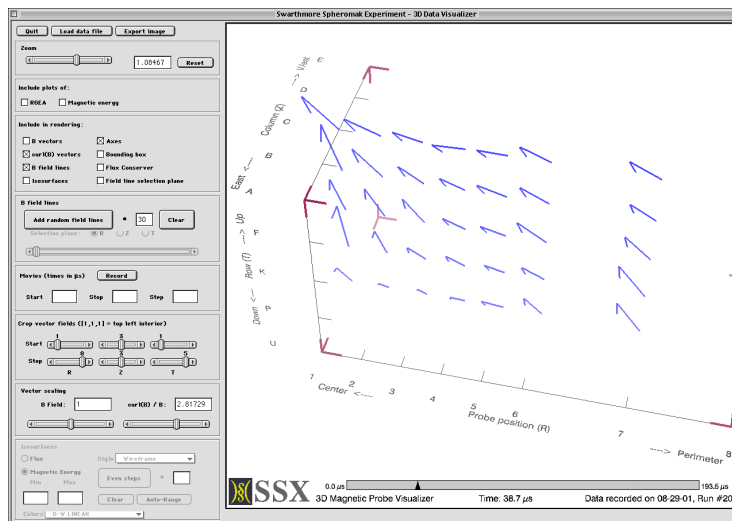


**Figure E.2:** Here, the program displays  $\mathbf{J}$  vectors computed from the  $\mathbf{B}$  data. Axes can be displayed which give orientation information, such as "West", "Up", etc. The letters visible on the axes refer to a convention in which the 25 probe stalks are named "A" through "Y" in normal left-right, top-down reading order as seen from the back of the array.

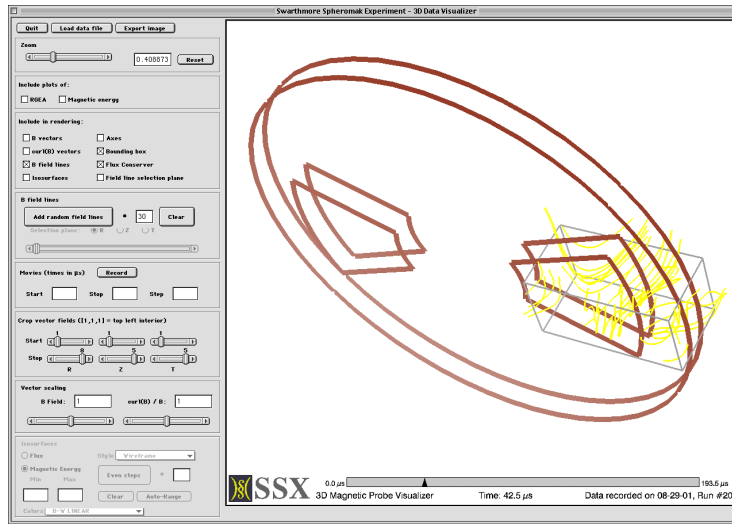


**Figure E.3:** The outlines of the flux conserving midplanes can be displayed, helping to put the data volume in context. Here, several fieldlines are displayed as well. The screen interface allows to user to add an arbitrary number of fieldlines at random locations.

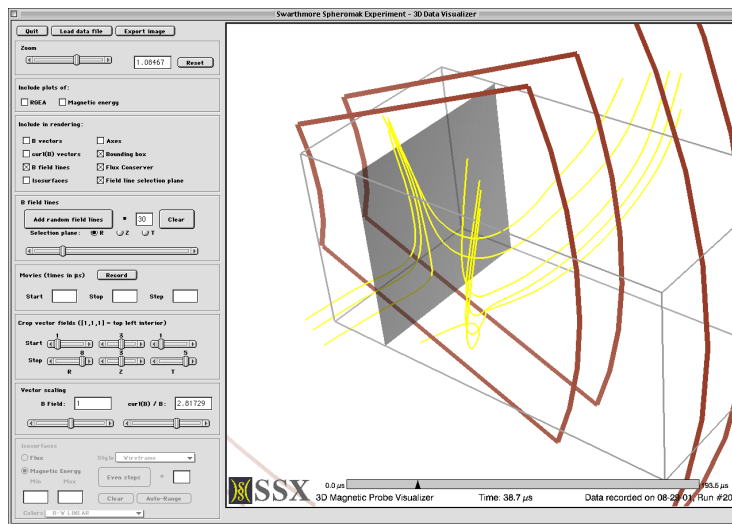


**Figure E.4:** It is also possible to interactively add fieldlines anchored at specific locations. To do this, a translucent plane is turned on. When the user clicks the mouse on the plane, the three-dimensional location where the mouse and plane intersect is used as the anchor point. The fieldline is traced forwards and backwards from that location until it exits the volume or a maximum length is reached. The plane can be switched to be normal to any of the three cardinal directions, and can be interactively positioned anywhere in the probe volume.

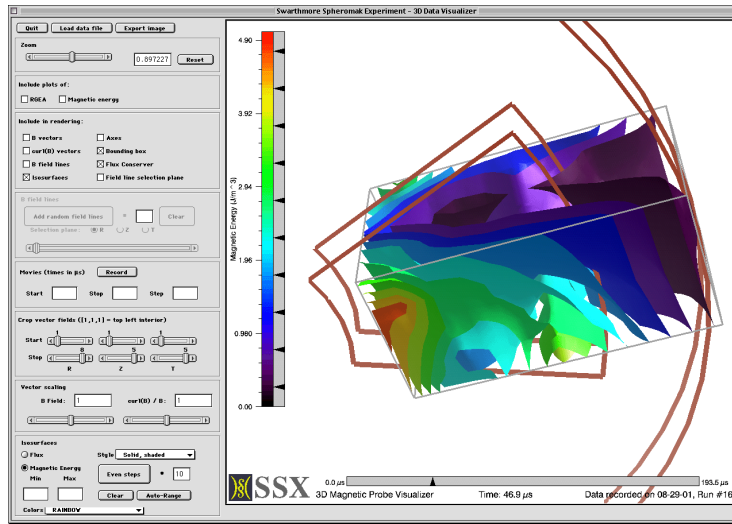


**Figure E.5:** The visualizer can also display surfaces of constant magnetic energy density. Here, the software has generated 10 equally spaced surfaces over a range determined automatically from the maximum and minimum in the volume. The surfaces can be made solid or wireframe. As one can see on the control panel at left, movies can be saved by inputting the start time, stop time, and number of frames desired. Images can also be exported.

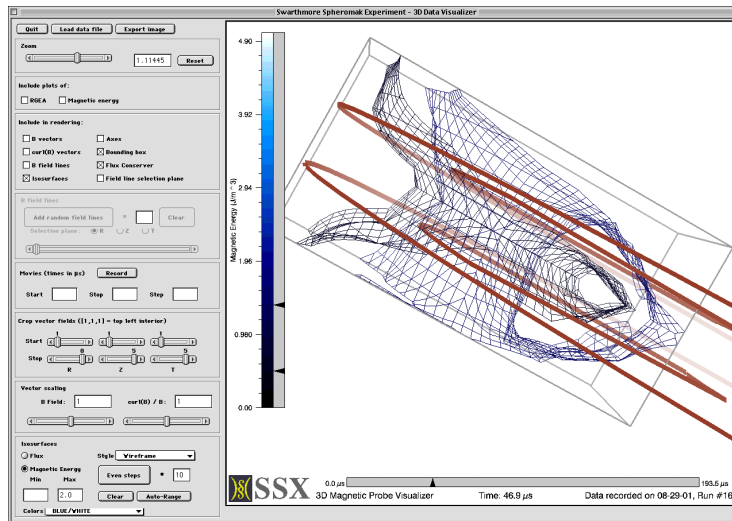


**Figure E.6:** The user can also manually add arbitrary surfaces at any value interactively by clicking on the vertical scale. By dragging the triangles on it, the surfaces change value in real time. All features such as vectors, surfaces, and fieldlines change in real time as the time is scrolled, although fieldline recalculation is somewhat slow.

## PLOTTER3D\_XP.PRO

The original visualization package was quite interactive. This was helpful for gleaning some intuition about the overall dynamics of the shot, but the code for these features made the program grow quite long. In order to create simple, clear figures for publication, and in order to add the many new calculated objects we desired (Ohm's law terms, pressure surfaces, etc.) a second generation of software was developed. The core program eventually became known as PLOTTER3D\_XP.PRO. A separate copy was saved for each figure destined for publication, so the code could be tweaked to reproducibly generate the desired image. While this program was not as interactive as its forerunner, dozens of new calculated objects could be easily and quickly added to it. Many of these objects can be seen in the figures throughout this thesis, including  $\mathbf{B}$ ,  $\mathbf{J}$ , and  $d\mathbf{u}/dt$  vectors, energy density surfaces, best-fit reconnection and normal-to-the-x-line planes, theoretical spheromak equilibrium fields, slices of the  $\mathbf{B}$  field, and  $\mathbf{B}$  fieldlines. In this section, we present some of the features which did not appear earlier in this thesis.

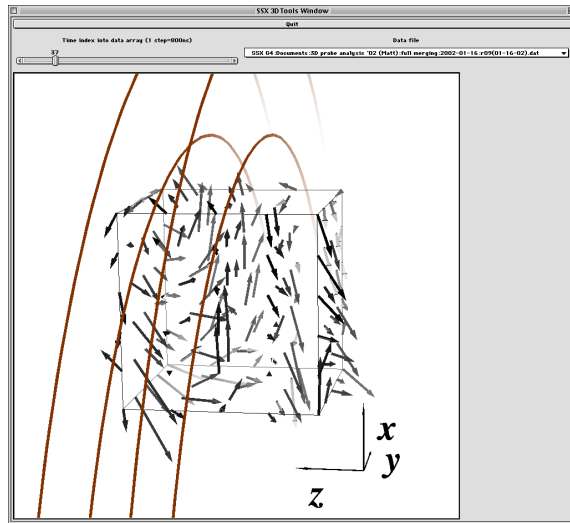


**Figure E.7:** Many vector fields were computed that did not end up being particularly useful. Here we see  $\partial\mathbf{B}/\partial t$ , along with the flux conserving rims after the bulk of the endplates was removed. Some of the other fields which were calculated included all the terms in Ohm's law and the curl-of-Ohm's-law derivable from  $\mathbf{B}$ , measured  $\mathbf{B}$  minus theoretical spheromak equilibrium  $\mathbf{B}$ ,  $\mathbf{J}$  fieldlines, and surfaces of constant flow speed. With the slider visible at the top, the user could scan through time as with the previous application. It is also possible to rotate the image in real time.

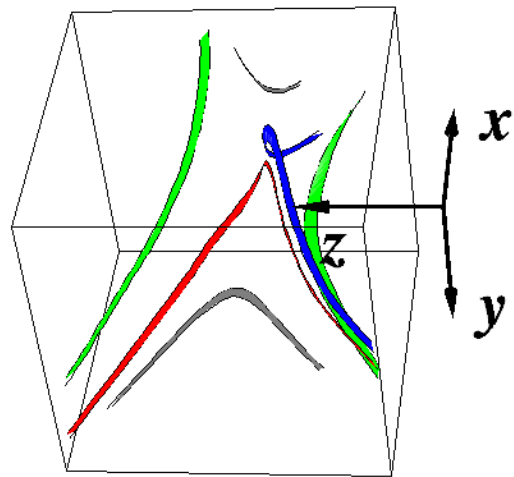


**Figure E.8:** Field *ribbons* could be computed by picking two nearby points, tracing the fieldlines through them, and connecting the resulting lines with a surface. Each ribbon could be arbitrarily colored to emphasize the topological difference between regions of the field.

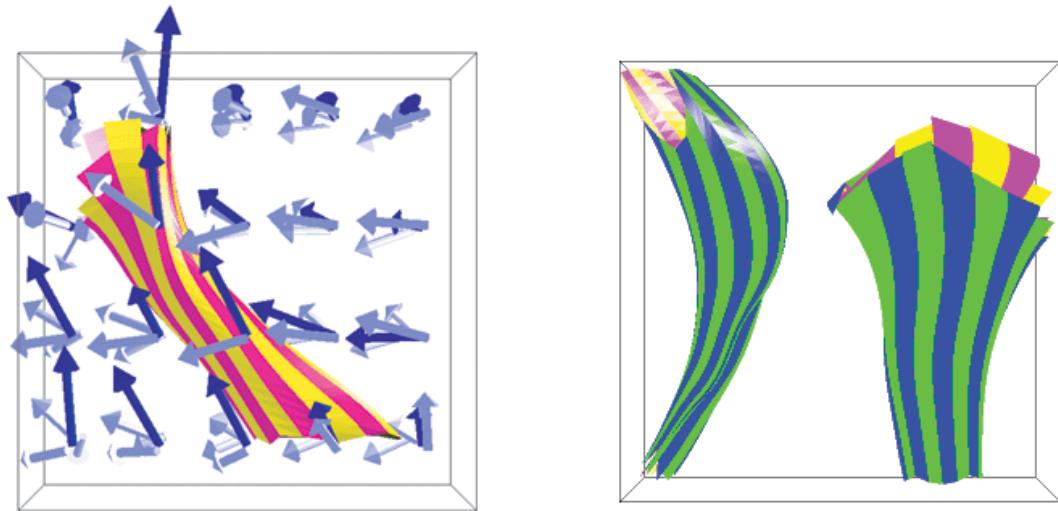


**Figure E.9:** A series of field ribbons can be traced from an initial circle of points. The result is a flux tube, as shown here. The color is alternated between adjacent ribbons so the twisting of the field can be seen.

## Field Line Plotting

It is particularly challenging to draw fieldlines in an intuitive way. One expects some kind of continuity from one moment of time to the next, but as we have seen there is no way to associate two fieldlines at different points in time unless the plasma is ideal (so lines freeze to the fluid) *and* we know the fluid flow velocity. In our case we know neither, so from one moment to the next we cannot easily show the “movement of a line.” The two options that have been employed at SSX are drawing random fieldlines at each moment in time, or else holding an “anchor point” constant over time and at each moment drawing whatever line passes through that point.

Secondly, we expect the *density* of fieldlines to represent the magnitude of the field. If we fix anchor points, as described above, there is no way to control the apparent density of lines in the volume. One good compromise method is illustrated here, and has been used earlier in this thesis. For a given frame, PLOTTER3D\_XP.PRO picks random starting points for the lines such that the density of start points reflects the field intensity. The start points must be recalculated at each moment in time to ensure they reflect the new field density, so the method of fixing anchor points described above cannot be used if we wish the field intensity to be represented.

Fieldlines are calculated using a fourth-order Runge-Kutta method, and trilinear interpolation of the  $\mathbf{B}$  data.

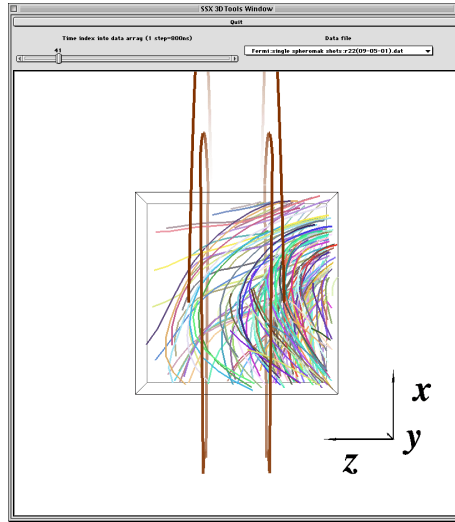


**Figure E.10:** The above image is from a single-bank shot, and uses this randomized method to reflect field intensity. It is evident that the field is much stronger on the side that contains a spheromak.

## PLANE.PRO

On several occasions we wished to look at the component of a field normal to the reconnection plane. For this purpose, a new application was developed for taking arbitrary slices of the dataset. The program can be configured to display components of the  $\mathbf{B}$ ,  $\mathbf{J}$ , or  $\nabla p$  fields.

The screen was divided in two. The left half contained an interactive image of the full dataset, as in PLOTTER3D\_XP.PRO, together with a slicing plane. However the user had three options for the effect the mouse would have in this window: it could rotate the entire image, rotate only the slicing plane while the rest of the image remained fixed, or it could translate the plane while the rest of the image remained fixed.

The right screen displayed the normal component of one of the fields, with red indicating one direction and blue the other. Any changes made to the slicing plane by interacting with the right screen would translate to changes on this left screen in real time. A system of large vectors on the left window helps the user orient the directions in that window to directions on this right screen.

Fine adjustments can be made with buttons at the bottom for arbitrary rotations and translations of the plane. They can be performed relative to any of the three fixed data axes, or relative to any of three axes which move with the slicing plane.

Figure E.11 displays a screen shot. The normal component of the  $\mathbf{B}$  field evident in the slice at right is responsible for the swept/sheared fieldlines in the center of the reconnection region discussed in Section 4.2.2. Also, the sign of the normal component varies in the four quadrants according to  $(\begin{smallmatrix} - & + \\ + & - \end{smallmatrix})$ . This is the quadrupole moment observed due to the inherent curvature in spheromak equilibrium fields.

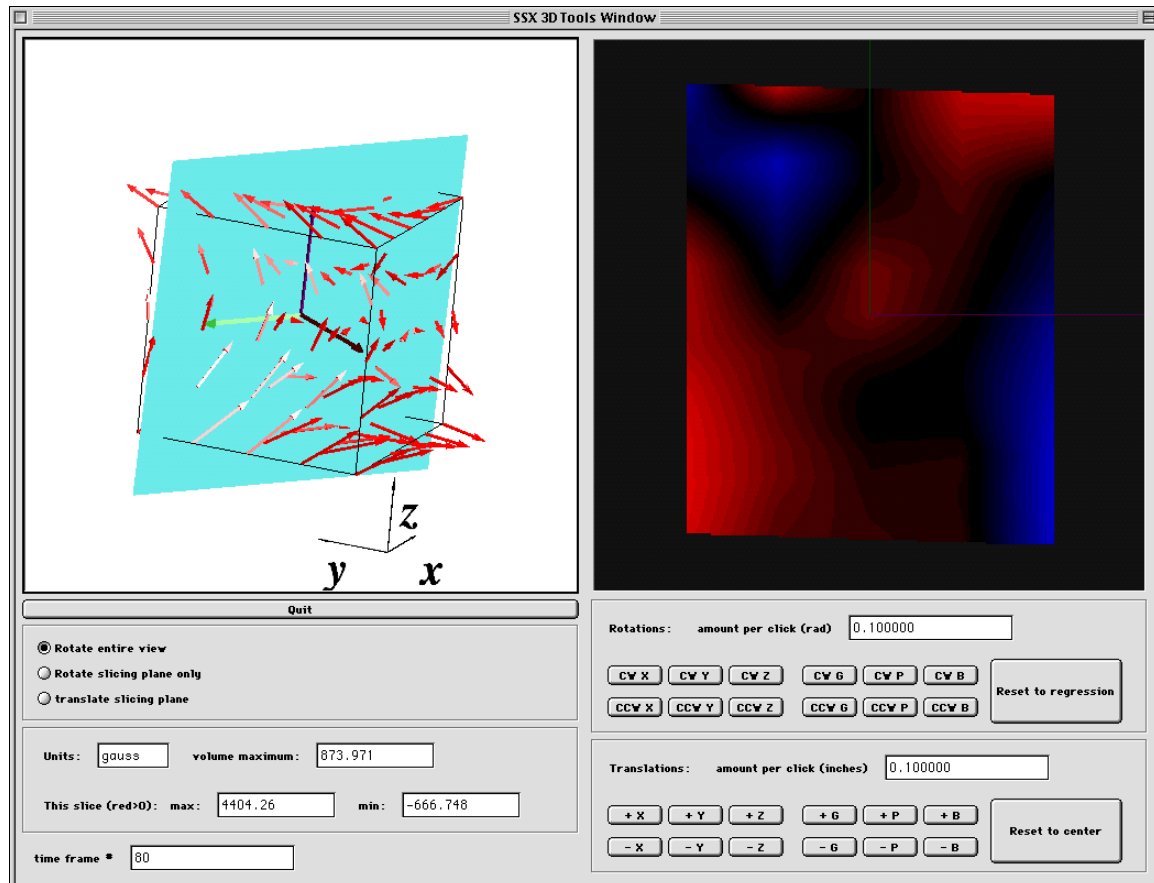


**Figure E.11:** A screen shot from PLANE.PRO.

## **STORYBOARD.PRO**

For publication in this thesis and for presentations, it is useful to generate tables of “movie frames” of the data, showing how  $\mathbf{B}$ ,  $\mathbf{J}$ , and other quantities evolve in time. One such image is shown on page 58. STORYBOARD.PRO was developed to generate these images efficiently. It is based on PLOTTER3D\_XP.PRO, but allows the user to specify different viewing angles and different objects ( $\mathbf{B}$  arrows, fieldlines, etc.) to display for each of an arbitrary number of rows. The user also specifies the time of each frame to display. STORYBOARD.PRO then generates all the images automatically, including the magnetic energy plot with the time of each frame marked, and saves a L<sup>A</sup>T<sub>E</sub>X file with the layout to be cut and pasted into other documents.

## **Appendix F**

# **Additional Details of Shot Evolution**

### **F.1 Single-Bank Shots**

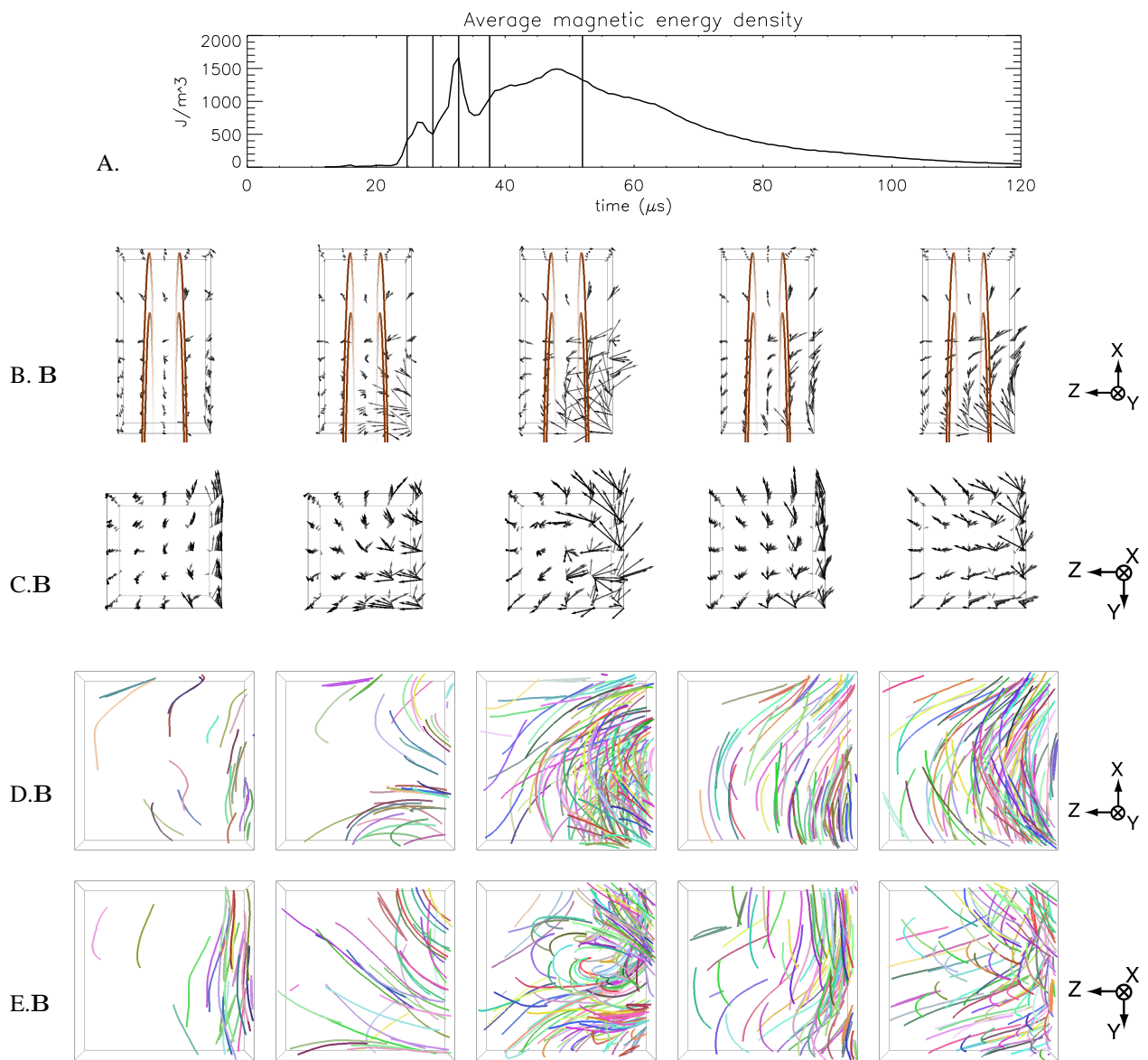


**Figure F.1:** Run 22, 9-5-2002. A typical single-bank shot, in which only the east plasma gun is discharged. The average magnetic energy density is roughly half of that for a two-spheromak shot, as expected. B-C: Magnetic field vectors. D-E: Magnetic fieldlines

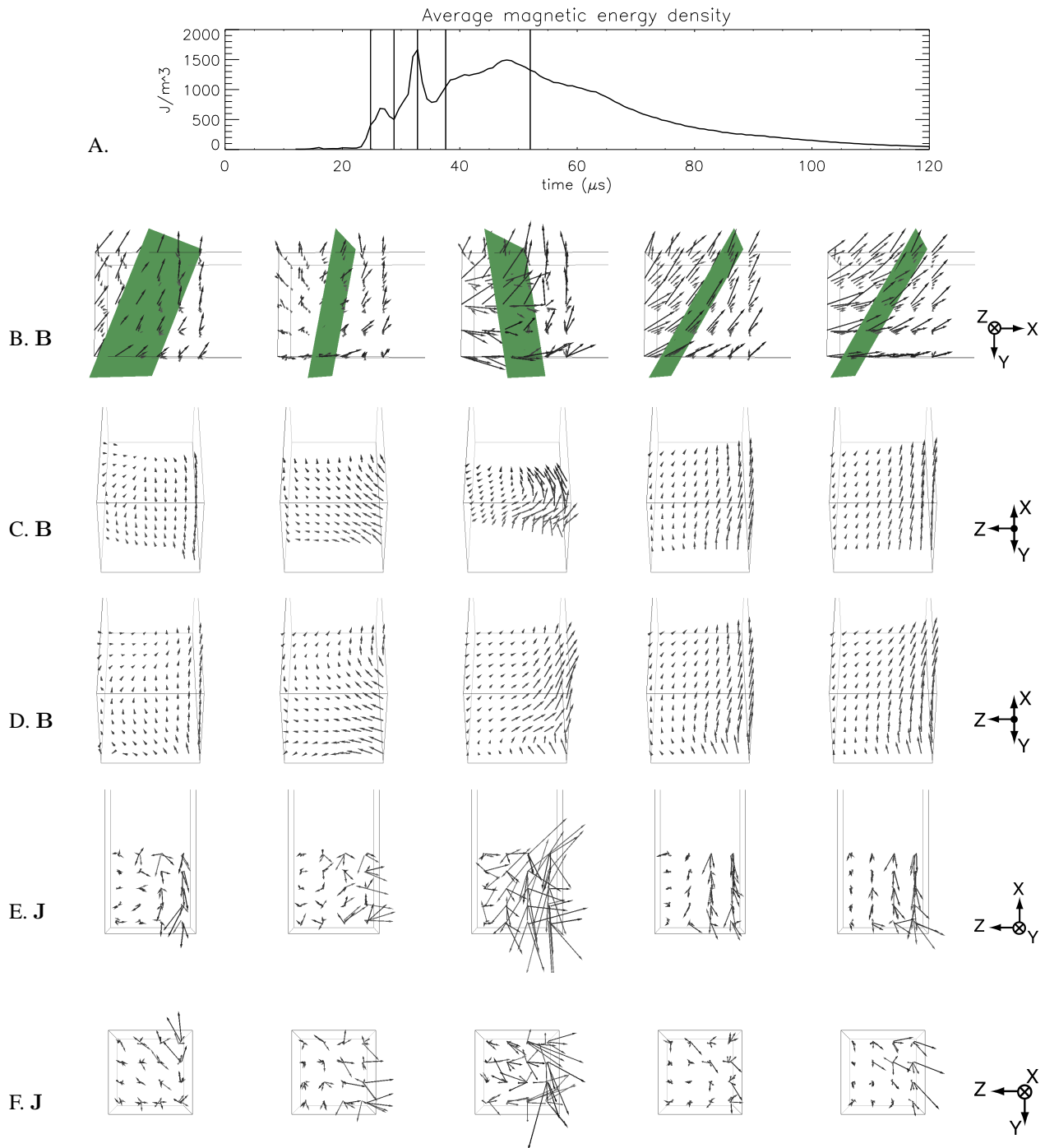


**Figure F.2:** Run 22, 9-5-2002. More images from the same single-bank shot. B: A side view of the magnetic field vectors, showing the best-fit plane. It is harder to fit a plane for one-spheromak shots because the incline of the field changes as the plasma moves in and out of the chevron hole. C: Magnetic field vectors in the best-fit plane, as seen from roughly normal to that plane. D-E: Current density vectors.

## F.2 Full Merging of Spheromaks

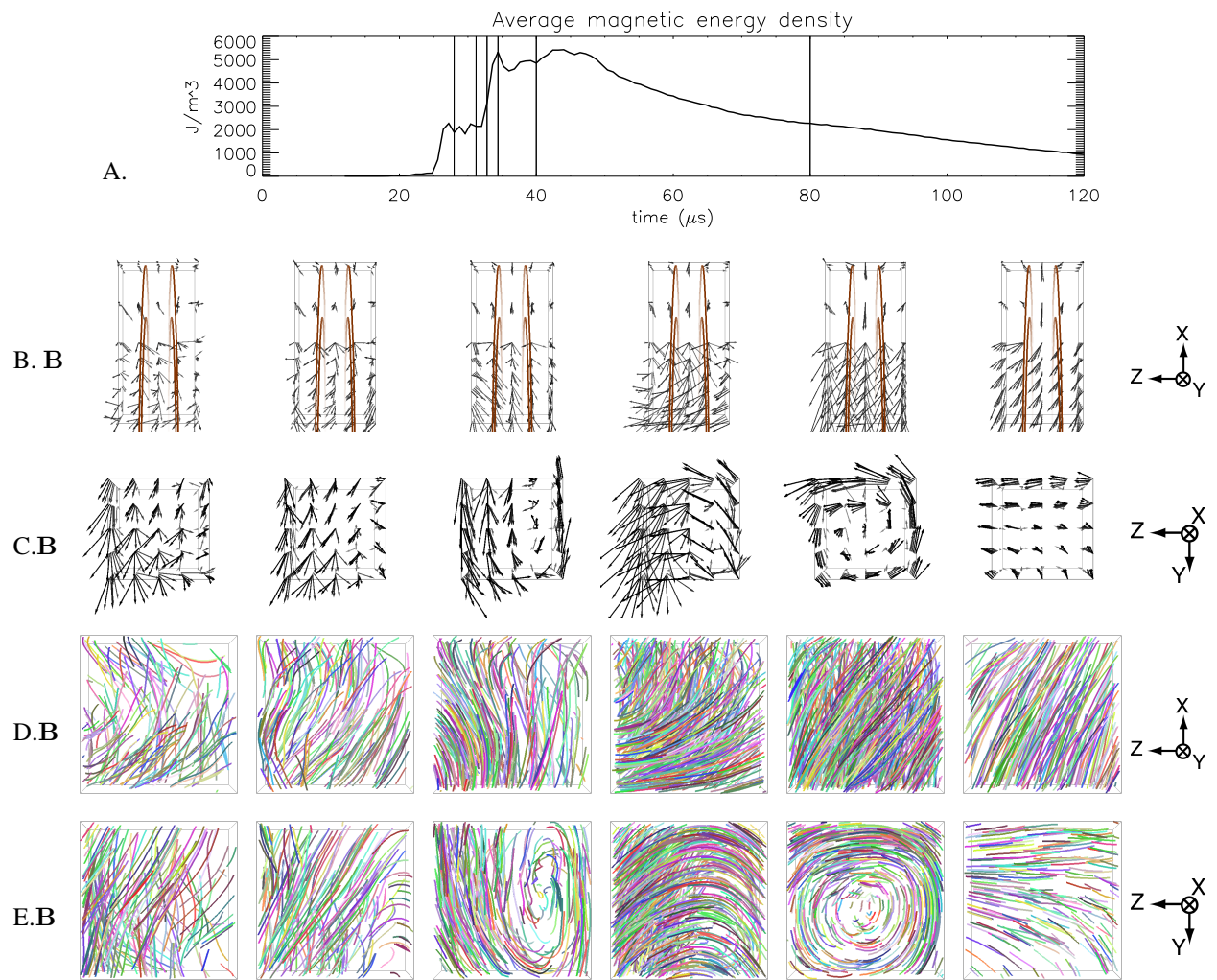


**Figure F.3:** Run 7, 1-25-2002. A full-merging shot in which the plasma appears tilted relative to the typical configuration. Observe that in this shot the final configuration is a  $\mathbf{B}$  field which is mostly directed in the  $-x$  direction, rather than the more usual  $-z$  direction (cf. Figure 4.25).

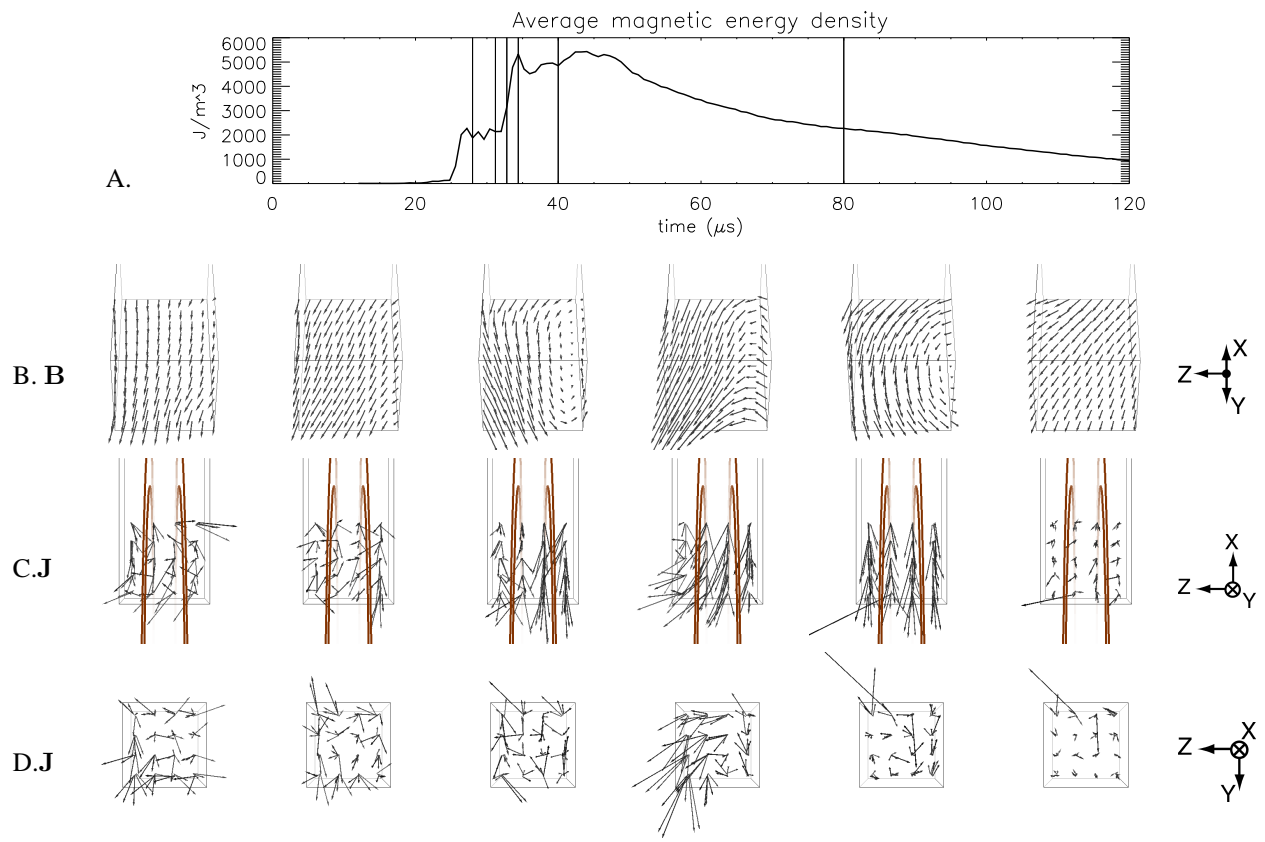


**Figure F.4:** Run 7, 1-25-2002. More images from the same “tilted” full-merging shot. B: Magnetic field vectors from a  $45^\circ$  plane. C-D: Current density vectors.

## **Appendix G**

### **Acknowledgements**

The author deeply wishes to thank his advisor Michael Brown for his guidance and remarkable talent as a teacher and researcher. Chris Cothran also provided invaluable advice, ideas, and assistance. The work of Steve Palmer and Dave Radcliffe was also of great help. Tom Kornack and Mark Kostora were responsible for much of the initial design of the probe system. Thanks also to Bill Matthaeus, Slava Lukin, and Andrea Stout, and to fellow researchers Andrew Fefferman and Abram Falk, for their valuable conversations and ideas. Financial support has been provided by the Department of Energy (grant numbers DE-FG02-00ER54604 and ER54654).

# Appendix H

## Notation

### Latin Alphabet

<b>A</b>	Magnetic vector potential
<b>B, <math>B</math></b>	Magnetic field
$c$	Speed of light
$e$	Magnitude of electron and proton charge
<b>E, <math>E</math></b>	Electric field
<b>J, <math>J</math></b>	Current density
$k$	Boltzmann's constant
$L$	Characteristic length scale; sometimes the reconnection layer length in particular
$m$	Mass of some species of particle
$M$	Normalized reconnection rate ( $u_{in}/u_{Alf}$ )
$m_e$	Electron mass
$n$	Number density
<b>P, <math>P_{ij}</math></b>	Pressure tensor
$p, p_e$	Pressure, electron pressure
$q$	Charge of some species of particle
$S$	Lundquist number (ratio of convective term to diffusive term for a reconnection plasma)
$t$	Time
$T$	Temperature
$T_e, T_i$	Temperature of the electrons, ions
<b>u, <math>u</math></b>	Fluid velocity (in the MHD approximation that there is one fluid)
$u_{Alf}$	Alfvén speed
<b>u<sub>e</sub></b>	Velocity of the electron fluid
<b>v</b>	Velocity of some specific particle
<b>x</b>	Position

### Greek Alphabet

$\beta$	Ratio of thermal to magnetic pressure
$\delta$	Reconnection layer thickness
$\epsilon_0$	Permittivity of free space
$\eta$	Resistivity
$\mu_0$	Permeability of free space
$\rho$	Mass density
$\Phi$	Magnetic flux

# Bibliography

- [1] J. Ambrosiano, W. H. Matthaeus, M. L. Goldstein, and D. Plante. Test particle acceleration in turbulent reconnecting magnetic fields. *Journal of Geophysical Research*, 93:14383, 1988.
- [2] A. Bhattacharjee and Z. M. Ma. Recent developments in collisionless reconnection theory: Applications to laboratory and space plasmas. *Physics of Plasmas*, 8:1829, 2001.
- [3] D. Biskamp. Collisional and collisionless magnetic reconnection. *Physics of Plasmas*, 4:1964, 1997.
- [4] D. Biskamp. *Magnetic Reconnection in Plasmas*. Cambridge University Press, Cambridge, 2000.
- [5] Dieter Biskamp. Magnetic reconnection in plasmas. *Astrophysics and Space Science*, 242:165, 1997.
- [6] M. R. Brown. Experimental studies of magnetic reconnection. *Physics of Plasmas*, 6:1717, 1999.
- [7] M. R. Brown. Magnetic reconnection notes. National Undergraduate Fellowship Presentation, 2001.
- [8] M. R. Brown, C. D. Cothran, M. Landreman, D. Schlossberg, and W. H. Matthaeus. Experimental observation of energetic ions accelerated by three-dimensional magnetic reconnection in a laboratory plasma. *The Astrophysical Journal*, 577:L63, 2002.
- [9] M. R. Brown, C. D. Cothran, M. Landreman, D. Schlossberg, W. H. Matthaeus, G. Qin, V. S. Lukin, and T. Gray. Energetic particles from three-dimensional magnetic reconnection events in the swarthmore spheromak experiment. *Physics of Plasmas*, 9:2077, 2002.
- [10] F. F. Chen. *Introduction to Plasma Physics and Controlled Fusion*. Plenum Press, New York, 1984.
- [11] C. D. Cothran, A. Falk, A. Fefferman, M. Landreman, M. R. Brown, and M. J. Schaffer. Spheromak merging and frc formation at ssx. *Physics of Plasmas (submitted)*, 2003.
- [12] C. D. Cothran, M. Landreman, W. H. Matthaeus, and M. R. Brown. Three dimensional structure of magnetic reconnection in a laboratory plasma. *Geophysical Review Letters*, 2003. To appear.
- [13] S. Cowley. Magnetohydrodynamics. National Undergraduate Fellowship Notes, 2001.
- [14] S. Curtis. The magnetospheric multiscale mission...resolving fundamental processes in space plasmas. Technical Memorandum TM-2000-209883, NASA, 1999.
- [15] Charles Day. Spacecraft probes the site of magnetic reconnection in earth's magnetotail. *Physics Today*, 54(10):16, 2001.
- [16] Abram Falk. Dynamics of field-reversed configuration in ssx. Undergraduate thesis, Swarthmore College, June 2003.
- [17] Andrew Fefferman. Formation and stability of spheromak / field reversed configuration (frc) hybrids in ssx-frc. Undergraduate thesis, Swarthmore College, June 2003.
- [18] R. P. Feynman, R. B. Leighton, and M. Sands. *The Feynman Lectures on Physics*. Addison-Wesley, Reading, Massachusetts, 1989.

- [19] C. G. R. Geddes, T. W. Kornack, and M. R. Brown. Scaling studies of spheromak formation and equilibrium. *Physics of Plasmas*, 5:1027, 1998.
- [20] Cameron G. R. Geddes. Equilibrium studies on ssx. Undergraduate thesis, Swarthmore College, June 1997.
- [21] W. Gekelman, R. L. Stenzel, and N. Wild. Magnetic field line reconnection experiments. *Physica Scripta*, T2/2:277, 1982.
- [22] R. J. Goldston and P. H. Rutherford. *Introduction to Plasma Physics*. Institute of Physics Pub., Philadelphia, Pennsylvania, 1995.
- [23] D. J. Griffiths. *Introduction to Electrodynamics*. Prentice Hall, Upper Saddle River, New Jersey, 1999.
- [24] S. C. Hsu, T. A. Carter, G. Fiskel, H. Ji, R. M. Kulsrud, and M. Yamada. Experimental study of ion heating and acceleration during magnetic reconnection. *Physics of Plasmas*, 8:1916, 2001.
- [25] S. C. Hsu, G. Fiskel, H. Ji, R. M. Kulsrud, and M. Yamada. Local measurement of nonclassical ion heating during magnetic reconnection. *Physical Review Letters*, 84:3859, 2000.
- [26] Hiroaki Isobe, Takaaki Yokoyama, Masumi Shimojo, Taro Morimoto, Hiromichi Kozu, Shigeru Eto, Noriyuki Narukage, and Kazunari Shibata. Reconnection rate in the decay phase of a long duration event flare on 1997 may 12. *The Astrophysical Journal*, 566:528, 2002.
- [27] H. Ji, M. Yamada, S. Hsu, and R. Kulsrud. Experimental test of the sweet-parker model of magnetic reconnection. *Physical Review Letters*, 80:3256, 1998.
- [28] T. W. Kornack, P. K. Sollins, and M. R. Brown. Experimental observation of correlated magnetic reconnection and alfvènic ion jets. *Physical Review E*, 58:36, 1998.
- [29] Thomas W. Kornack. Magnetic reconnection studies on ssx. Undergraduate thesis, Swarthmore College, June 1998.
- [30] N. A. Krall and A. W. Trivelpiece. *Principles of Plasma Physics*. McGraw-Hill, New York, 1973.
- [31] R. M. Kulsrud. Magnetic reconnection in a magnetohydrodynamic plasma. *Physics of Plasmas*, 5:1599, 1998.
- [32] R. M. Kulsrud. Magnetic reconnection: Sweet-parker versus petschek. Princeton Plasma Physics Laboratory, 2000.
- [33] M. Landreman, C. D. Cothran, M. R. Brown, M. Kostora, and J. T. Slough. Rapid multiplexed data acquisition: application to three-dimensional magnetic field measurements in a turbulent laboratory plasma. *Review of Scientific Instruments*, 74, 2003. To appear.
- [34] Y. Lau and J. M. Finn. Three-dimensional kinematic reconnection in the presence of field nulls and closed field lines. *The Astrophysical Journal*, 350:672, 1990.
- [35] V. S. Lukin, G. Qin, W. H. Matthaeus, and M. R. Brown. Numerical modeling of magnetohydrodynamic activity in the swarthmore spheromak experiment. *Physics of Plasmas*, 8:1600, 2001.
- [36] Vyacheslav S. Lukin. Modeling ssx spheromak plasmas. Undergraduate thesis, Swarthmore College, June 2000.
- [37] W. H. Matthaeus, J. J. Ambrosiano, and M. L. Goldstein. Particle acceleration by turbulent magnetohydrodynamic reconnection. *Physical Review Letters*, 53:1449, 1984.
- [38] W. H. Matthaeus and Stan L. Lamkin. Turbulent magnetic reconnection. *Physics of Fluids*, 29:2513, 1986.
- [39] F. S. Mozer, S. D. Bale, and T. D. Phan. Evidence of diffusion regions at a subsolar magnetopause crossing. *PRL*, 89:015002, 2002.
- [40] Y. Ono, M. Inomoto, T. Okazaki, and Y. Ueda. Experimental investigation of three-component magnetic reconnection by use of merging spheromaks and tokamaks. *Physics of Plasmas*, 4:1953, 1997.

- [41] Y. Ono, M. Yamada, T. Akao, T. Tajima, and R. Matsumoto. Ion acceleration and direct ion heating in three-component magnetic reconnection. *Physical Review Letters*, 76:3328, 1996.
- [42] E. N. Parker. Sweet's mechanism for merging magnetic fields in conducting fluids. *Journal of Geophysical Research*, 62:509, 1957.
- [43] C. E. Parnell. Magnetic reconnection and some solar applications. *Phil. Trans. R. Soc. Lond. A*, 358:669, 2000.
- [44] H. E. Petschek. Magnetic field annihilation. In W. N. Hess, editor, *Physics of Solar Flares*, page 425. NASA SP-50, 1964.
- [45] E. Priest and T. Forbes. *Magnetic Reconnection: MHD Theory and Applications*. Cambridge University Press, Cambridge, 2000.
- [46] E. R. Priest and C. J. Schrijver. Aspects of three-dimensional magnetic reconnection. *Solar Physics*, 190:1, 1999.
- [47] E. R. Priest and V. S. Titov. Magnetic reconnection at three-dimensional null points. *Phil. Trans. R. Soc. Lond. A*, 354:2951, 1996.
- [48] M. J. Schaffer. Exponential taylor states in circular cylinders. *Physics of Fluids*, 30:160, 1987.
- [49] David Schlossberg. Energetic particle studies on ssx. Undergraduate thesis, Swarthmore College, June 2001.
- [50] C. J. Schrijver and A. M. Title. Today's science of the sun. *Sky & Telescope*, page 34, February 2001.
- [51] M. A. Shay and J. F. Drake. The role of electron dissipation on the rate of collisionless magnetic reconnection. *Geophysical Research Letters*, 25:3759, 1998.
- [52] M. A. Shay, J. F. Drake, R. E. Denton, and D. Biskamp. Structure of the dissipation region during collisionless magnetic reconnection. *Journal of Geophysical Research*, 103:9165, 1998.
- [53] M. A. Shay, J. F. Drake, B. N. Rogers, and R. E. Denton. The scaling of collisionless, magnetic reconnection for large systems. *Geophysical Research Letters*, 26:2163, 1999.
- [54] M. A. Shay, J. F. Drake, B. N. Rogers, and R. E. Denton. Alfvénic collisionless magnetic reconnection and the hall term. *Journal of Geophysical Research*, 106:3759, 2001.
- [55] G. Sigl. Ultrahigh-energy cosmic rays: Physics and astrophysics at extreme energies. *Science*, 291:73, 2001.
- [56] R. L. Stenzel and W. Gekelman. Experiments on magnetic-field-line reconnection. *Physical Review Letters*, 42:1055, 1979.
- [57] R. L. Stenzel and W. Gekelman. Magnetic field line reconnection experiments: 1. field topologies. *Journal of Geophysical Research*, 86:649, 1981.
- [58] V. M. Vasyliunas. Theoretical models of magnetic field line merging. *Review of Geophysics Space Research*, 13:303, 1975.
- [59] M. Yamada, H. Ji, S. Hsu, T. Carter, R. Kulsrud, Y. Ono, and F. Perkins. Identification of y-shaped and o-shaped diffusion regions during magnetic reconnection in a laboratory plasma. *Physical Review Letters*, 78:3117, 1997.
- [60] M. Yamada, Y. Ono, A. Hayakawa, M. Katsurai, and F. W. Perkins. Magnetic reconnection of plasma toroids with cohelicity and counterhelicity. *Physical Review Letters*, 65:721, 1990.